



UNIVERSITY
OF
JOHANNESBURG

COPYRIGHT AND CITATION CONSIDERATIONS FOR THIS THESIS/ DISSERTATION

 creative
commons



- Attribution — You must give appropriate credit, provide a link to the license, and indicate if changes were made. You may do so in any reasonable manner, but not in any way that suggests the licensor endorses you or your use.
- NonCommercial — You may not use the material for commercial purposes.
- ShareAlike — If you remix, transform, or build upon the material, you must distribute your contributions under the same license as the original.

How to cite this thesis

Surname, Initial(s). (2012) Title of the thesis or dissertation. PhD. (Chemistry)/ M.Sc. (Physics)/ M.A. (Philosophy)/M.Com. (Finance) etc. [Unpublished]: [University of Johannesburg](https://ujcontent.uj.ac.za/vital/access/manager/Index?site_name=Research%20Output). Retrieved from: https://ujcontent.uj.ac.za/vital/access/manager/Index?site_name=Research%20Output (Accessed: Date).

**Modelling of the Multiphase Interactions in a Hydrocyclone using
Navier-Stokes and Lattice Boltzmann Based Computational
Approaches**

by

MUAAZ BHAMJEE

A thesis submitted in partial fulfilment of the requirements for the degree of

DOCTOR INGENERIAE

in the

DEPARTMENT OF MECHANICAL ENGINEERING SCIENCE

in the

FACULTY OF ENGINEERING AND THE BUILT ENVIRONMENT

at the

UNIVERSITY OF JOHANNESBURG

SUPERVISOR: PROF. S.H. CONNELL

CO-SUPERVISOR: PROF. A.L. NEL

AUGUST 2016

Declaration

I “Muaaz Bhamjee” hereby declare that this dissertation is wholly my own work and has not been submitted anywhere else for academic credit either by myself or by another person. I understand what plagiarism implies and declare that this dissertation is my own ideas, words, phrases, argument, figures, results and organisation except where reference is explicitly made to another’s work. I understand that any unethical academic behaviour, which includes plagiarism, is seen in a serious light by the University of Johannesburg and is punishable by disciplinary action.

Signed _____

Date _____

UNIVERSITY
OF
JOHANNESBURG

Abstract

Coupled Navier-Stokes (NS) and Discrete Element Method (DEM) based models have been applied to capture the complex multiphase interactions in hydrocyclones. However, the application of the Lattice Boltzmann Method (LBM) is sparse and is mostly limited to the modelling of single phase flow in hydrocyclones. Thus, the aim in this study was to compare the predictions of NS and LBM models of a hydrocyclone to study and understand their performance when benchmarked to experimental measurements. Both approaches were implemented to incorporate air-core formation, particle-fluid, particle-particle and particle-wall interactions. The NS models used to model the air-core were the Volume-of-Fluid (VOF), Algebraic Slip Mixture and Eulerian-Eulerian models while the LBM models used were the LBM-VOF and LBM-VOF two-fluid models. NS-DEM models and the LBM coupled with the Point and Verlet particle classes were used to capture the particle interactions.

The LBM model predictions were comparable to the NS model for single phase flow. The LBM-VOF model could not predict air-core formation. The NS-DEM based models predict surging and air-core suppression. The results indicate that the underflow PSD and water mass flow split are comparable to experiment. The separation efficiency and overflow PSD predictions require more modelled flow-time than was used in this study to match experimental measurements. The LBM-VOF Verlet particle model provided more accurate separation predictions than the NS-DEM models. The Eulerian-Eulerian Dense Discrete Phase Model (DDPM) coupled with the DEM provided similar predictions to the VOF-DEM model. The LBM was more computationally efficient for single phase flow and for air-core modelling. The LBM-VOF Particle models were comparable to the VOF-DEM model, whilst the Eulerian DDPM-DEM was the least computationally efficient.

Based on the results from this study it is recommended that the LBM model should be used for single phase flow modelling, that the Eulerian-Eulerian model should be used for air-core modelling and that the LBM-VOF Verlet particle model should be used to model the particle interactions and separation. The particle models should be run for at least 16s of flow-time to potentially predict the full recovery from surging and provide accurate predictions of the separation efficiency which is eight times the maximum particle residence time for this specific hydrocyclone. Turbulence should be modelled using the Renormalization Group Theory k - ϵ turbulence model on course meshes. On fine meshes the Reynold Stress Model (RSM) should be used. The Large Eddy Simulation (LES) model may require significantly finer meshes than used in this study to produce results comparable to the RSM. However, the LES model is suitable for use in the LBM models on all mesh sizes.

Future work that can be done to overcome some of the problems discovered in this study includes the development of a stable LBM-VOF two-fluid model, when modelling high-Reynolds number flows and the incorporation of an off-lattice pressure boundary condition for the LBM-VOF two-fluid model to predict air-core formation in hydrocyclones. It is recommended that, in future work, that at least 16s of flow-time should be modelled to investigate if the NS-DEM models predict a complete recovery from surging and the subsequent re-formation of the air-core.

Acknowledgements

- In the name of Allah (God), the Beneficent, the Merciful. You are the All - Knowing, All - Wise. All that is correct herein is due to the knowledge that you have granted me. All that is incorrect herein is due to the knowledge that you have kept from me.
- Allah! Shower Your mercy on Muhammad (Peace Be Upon Him) and his family and followers as You showered Your mercy on Abraham (Peace Be Upon Him) and his family and followers. Surely you are the Praiseworthy and Most High.
- I would like to express my love for my wife Naiefa and my sons Khalid and Yousha. You are the light of my eyes. May Allah reward you abundantly for your help and support.
- Sincere gratitude is due to my family for supporting me in this venture. May Allah reward you abundantly.
- Thanks are due to my supervisor Prof. Simon H. Connell and and co-supervisor Prof. Andre' L. Nel for the guidance and support (during our long and frequent discussions) given for this Doctoral Study and beyond.
- Further gratitude is expressed to Prof. Alan Nurick and Dr. Pieter Henning. Your constant motivation and support was invaluable in helping me complete this study.
- Gratitude is due to the University of Johannesburg for providing me with the Next Generation Scholarship. In addition, sincere thanks to the UJ Research Committee for funding a large part of the equipment and resources acquired for this research.

- The financial assistance of the National Research Foundation (NRF) towards this research is hereby acknowledged. Opinions expressed and conclusions arrived at, are those of the author and are not necessarily to be attributed to the NRF.
- The Centre for High Performance Computing (CHPC) is acknowledged for the use of the CHPC cluster facilities.
- The support and encouragement of Multotec Pty Ltd in the pursuit of this research is also acknowledged.



Contents

Declaration	i
Abstract	iii
Acknowledgements	iv
Contents	xi
List of Figures	xix
List of Tables	xxi
Nomenclature	xxii
1 Introduction	1
1.1 Problem Statement	7
1.2 Aim and Objectives	11
1.3 Study Methodology	11
1.4 Preview	12



<i>CONTENTS</i>	vii
2 Literature Review	14
2.1 Overview of the Current Status of CFD Modelling of Process Equipment	14
2.2 The Physics of Cyclonic Flows	16
2.3 Available Research on Hydrocyclones and Similar Process Equipment	17
2.3.1 Experimental Studies and Empirical Models	17
2.3.2 NS based Models of Hydrocyclones and Similar Process Equipment	20
2.3.3 LBM based Models of Hydrocyclones and Similar Process Equipment	23
2.4 Advances in Particle Interaction Modelling	25
3 Coupled Navier-Stokes Based Computational Fluid Dynamics and Discrete Element Method Models	29
3.1 Overview of the Navier-Stokes based Finite Volume Method	30
3.2 Model Geometry and Mesh	31
3.3 Governing Equations	32
3.3.1 Conservation of Mass, Conservation of Momentum and Turbulence	32
3.3.2 Air-Core	37
3.3.3 Particles	46
3.4 Boundary Conditions	49
3.5 Solver Setup	51

4	Lattice Boltzmann Method Based Models	53
4.1	Overview of the Lattice Boltzmann Method	54
4.2	Overview of Palabos	57
4.3	LBM Model Geometry and Domain Voxelisation	58
4.4	LBM Governing Equations	61
4.4.1	LBM-VOF Model for Air-Core Formation	65
4.4.2	LBM Particle Model	67
4.5	Boundary Conditions	69
4.6	Notes on Solver Setup	70
5	Experimental Setup and Results	72
5.1	Overview of the Experimental Setup	72
5.2	Measured Variables, Instrumentation and Data Acquisition . .	76
5.2.1	Feed Pressure Measurements	76
5.2.2	Solids Loading and Mass Fraction Measurements . . .	76
5.2.3	Mass Flow Rate Measurements	78
5.2.4	Particle Size Analysis	79
5.3	Experimental Procedure	79
5.4	Experimental Results	81
5.4.1	Mass and Volume Fraction Measurements	81
5.4.2	Mass Flow Rate Measurements	84

<i>CONTENTS</i>	ix
5.4.3 Particle Size Analysis	87
5.5 Air-Core Formation	93
6 Simulation Results and Discussion	96
6.1 Air-Core Formation	96
6.1.1 NS Based Models Predictions	96
6.1.2 Numerical Stability and Convergence of the Eulerian Model	106
6.1.3 LBM-VOF Model Predictions	115
6.1.4 Computational Efficiency Comparison for Single Phase and Air-Core Models	125
6.2 Particle Model Predictions	130
6.2.1 Effect of Particles on the Air-Core and Water Phase . .	130
6.2.2 PSD and Separation Efficiency Predictions	142
6.2.3 Eulerian DDPM-DEM and LBM-VOF Particle Model Predictions	147
6.2.4 Computational Efficiency Comparison for Particle Mod- els	153
6.2.5 Linearisation of the DPM Source Terms in the NS Based Models	156
6.3 Summary	156
7 Conclusions and Recommendations	161
7.1 Outcomes from the Study	163

<i>CONTENTS</i>	x
7.2 Validation of Research Hypothesis and Answers to Research Questions	167
7.3 Contributions Arising from the Study	169
7.4 Recommendations and Future Work	170
Bibliography	187
Appendices	188
A Malvern Mastersizer Particle Size Analyser Performance Verification Certificate	189
B The Effect of Surface Tension on Air-Core Formation	196
B.1 Model, Boundary Conditions and Solver Setup	197
B.2 Results and Conclusions	198
C Mesh Sensitivity Study	202
C.1 NS based Air-Core Models	202
C.2 NS based Particle Models	206
D List of Does and Don'ts when Modelling Hydrocyclones	209
D.1 Meshing Guidelines	209
D.1.1 NS based Models	209
D.1.2 LBM based Models	210
D.2 Physics Specification	210

CONTENTS

xi

D.2.1 NS based Models	210
D.2.2 LBM based Models	211
D.3 Solver Setup	211
D.3.1 NS based Models	211
D.3.2 LBM based Models	211



UNIVERSITY
OF
JOHANNESBURG

List of Figures

1.1	Isometric view of a cyclone separator	3
3.1	Hydrocyclone geometry	32
3.2	Computational grid (mesh)	32
4.1	Two-dimensional lattice labelling and velocity vectors based on the D2Q9 lattice structure	56
4.2	Wall surface and domain construction via STL - a) hydrocyclone and b) bounding box around the hydrocyclone	59
4.3	Section of the voxelised domain	60
4.4	Cell Tagging	61
4.5	D3Q19 Lattice (adapted from [99])	63
5.1	Isometric view of the test rig (Adapted from an image courtesy of Multotec Pty Ltd)	73
5.2	Agitation mechanism used to prevent solids settling in the feed bin	74
5.3	Plastic curtains used for spill containment	74
5.4	Half scale perspex hydrocyclone model	75

5.5	Inlet pressure gauge	77
5.6	Underflow spray shapes: a) roping, b) cylindrical and c) conical	80
5.7	Feed PSD - cumulative passing	90
5.8	Underflow PSD - cumulative passing	90
5.9	Overflow PSD - cumulative passing	91
5.10	Feed Rosin-Rammler fit	91
5.11	Underflow Rosin-Rammler fit	92
5.12	Overflow Rosin-Rammler fit	92
5.13	Image stills from video of air-core formation	94
5.14	Image stills from video of air-core formation with dye	95
6.1	Iso-Surface of volume fraction of air from the NS based Model at flow-time $t = 2s$: a) VOF with RNG $k - \epsilon$, b) VOF with RSM, c) VOF with LES, d) Mixture with RNG $k - \epsilon$, e) Mixture with RSM, f) Mixture with LES, g) Eulerian with RNG $k - \epsilon$ and h) Eulerian with RSM	100
6.2	Air-core in perspex half scale hydrocyclone - green dye added to reveal air-core	101
6.3	“Quasi”-steady behaviour at the overflow as illustrated by overflow mass flow rate as predicted by the NS based models	102
6.4	“Quasi”-steady behaviour at the underflow as illustrated by underflow mass flow rate as predicted by the NS based models	102
6.5	Overflow mass flow rate as predicted by the NS based models - mesh size 5mm	103

6.6	Underflow mass flow rate as predicted by the NS based models - mesh size 5mm	103
6.7	Overflow mass flow rate as predicted by the NS based models - mesh size 2.5mm	104
6.8	Underflow mass flow rate as predicted by the NS based models - mesh size 2.5mm	104
6.9	Overflow mass flow rate as predicted by the NS based models - mesh size 1.25mm	105
6.10	Underflow mass flow rate as predicted by the NS based models - mesh size 1.25mm	105
6.11	Turbulent kinetic energy as a function of the normalised z - co-ordinate two time steps before divergence for the Eulerian model compared to stable VOF and ASM based predictions .	108
6.12	Turbulent dissipation rate as a function of the normalised z - co-ordinate two time steps before divergence for the Eulerian model compared to stable VOF and ASM based predictions .	108
6.13	Axial velocity as a function of the normalised z -co-ordinate two time steps before divergence for the Eulerian model com- pared to stable VOF and ASM based predictions	109
6.14	Turbulent viscosity ratio as a function of the normalised z - co-ordinate two time steps before divergence for the Eulerian model compared to stable VOF and ASM based predictions .	109
6.15	Cells with aspect ratio equal to or above 10 on mesh with cell size a) 5mm and b) 5mm with reduced aspect ratio	111
6.16	High velocity region for Eulerian RNG model on mesh with cell size a) 5mm, b) 2.5mm and c) 5mm with reduced aspect ratio	113
6.17	Comparison of the velocities in the core of the hydrocyclone in a) original Eulerian RSM model and b) Eulerian RSM model with shifted overflow boundary	114

6.18	Comparison of air-core surface in a) original Eulerian RSM model and b) Eulerian RSM model with shifted overflow boundary	114
6.19	“Quasi”-steady behaviour at the overflow as illustrated by overflow mass flow rate as predicted by the Eulerian models for different overflow boundary positions	115
6.20	Iso-Surface of volume fraction of air from the LBM-VOF model at flow-time a) $t = 0.0s$, b) $t = 0.5s$ and c) $t = 2.0s$	116
6.21	Contours coloured by velocity magnitude ($ u m/s$) on the plane $x = 0$ from the LBM-VOF model at flow-time a) $t = 0.5s$, b) $t = 2.0s$	117
6.22	Iso-Surface of volume fraction of air from the LBM-VOF model: a) $\alpha_{air} = 0.5$ at $t = 0.5s$, b) $\alpha_{air} = 0.5$ at $t = 1s$, c) $\alpha_{air} = 0.5$ at $t = 2s$, d) $\alpha_{air} = 1$ at $t = 0.5s$, e) $\alpha_{air} = 1$ at $t = 1s$ and f) $\alpha_{air} = 1$ at $t = 2s$	119
6.23	Overflow mass flow rate as predicted by the LBM based models for α_{air} at the outlets set at 1 and 0.5	120
6.24	Underflow mass flow rate as predicted by the LBM based models for α_{air} at the outlets set at 1 and 0.5	120
6.25	Pathlines reversed from the overflow and contours coloured by velocity magnitude ($ u m/s$) on the plane $x = 0$ at $t = 0.25s$ for the a) LBM single phase model and b) NS single phase model	123
6.26	Contours coloured by velocity magnitude ($ u m/s$) on the planes $x = 0$, $y = 0$, $z = 0.25$ $t = 0.25s$ for the a) LBM single phase model and b) NS single phase model	123
6.27	Low pressure region, as predicted by the LBM, in the core of the hydrocyclone from single phase simulation on the planes $x = 0$, $y = 0$, $z = 0$ at $t = 2s$: a) full pressure distribution and b) clipped low pressure region	124
6.28	RAM usage for the LBM-LES and NS-LES single phase models	126

6.29 MCUPS based performance for the LBM-LES and NS-LES single phase models	126
6.30 Walltime in seconds for the LBM-LES and NS-LES single phase models (on similar hardware)	127
6.31 RAM usage for the air-core models	127
6.32 MCUPS based performance for the air-core models	128
6.33 MCUPS based performance for the NS based air-core models (expanded view of part of Figure 6.32)	128
6.34 Walltime in seconds for the air-core models (on similar hardware)	129
6.35 Overflow water mass flow rate as predicted by the NS based VOF-DEM models	132
6.36 Underflow water mass flow rate as predicted by the NS based VOF-DEM models	132
6.37 Iso-Surface of volume fraction of air from the VOF-DEM models at flow-time 4s: a) RSM and b) LES.	134
6.38 Iso-Surface of particle concentration above 600 kg/m^3 from the VOF-DEM models at flow-time 4s: a) RSM and b) LES.	134
6.39 Contours coloured by velocity magnitude, on the planes $x = 0$, $y = 0$ and $z = 0$ from the VOF-DEM models at flow-time 4s: a) RSM and b) LES.	135
6.40 Contours coloured by static pressure, on the planes $x = 0$, $y = 0$ and $z = 0$ from the VOF-DEM models at flow-time 4s: a) RSM and b) LES.	135
6.41 Positions where profiles were investigated.	136
6.42 a) Static and b) dynamic pressure (Pa) as a function of the normalised z co-ordinate.	137

6.43 a) Tangential and b) axial velocities (m/s) as a function of the normalised y co-ordinate at various heights as reported in literature (adapted from [114]).	137
6.44 a) Tangential and b) axial velocities (m/s) as a function of the normalised y co-ordinate at various heights.	139
6.45 Vorticity magnitude ($1/s$) for the a) RSM and LES models and b) the RSM model as a function of the normalised y co-ordinate at various heights.	140
6.46 Euler Number for the a) air-core models and b) the particle models as a function of the normalised y co-ordinate at various heights.	141
6.47 Underflow PSD - Comparison between Fluent predictions and experimental measurements	144
6.48 Overflow PSD - Comparison between Fluent predictions and all experimental measurements	144
6.49 Feed PSD - Comparison between Fluent predictions and average experimental measurements	145
6.50 The Accumulation of particles	146
6.51 VOF-DEM (RSM) separation efficiency predictions	146
6.52 Extrapolation of the separation efficiency predictions	147
6.53 Overflow water mass flow rate as predicted by the VOF-DEM models, with RSM, for different mesh sizes	148
6.54 Underflow water mass flow rate as predicted by the VOF-DEM models, with RSM, for different mesh sizes	148
6.55 Contours coloured by velocity magnitude ($ u m/s$) on the planes $x = 0$, $y = 0$, $z = 0$ from the VOF-DEM (RSM) model at flow-time = 4s for the a) 5mm, b) 3.75mm and c) 2.5mm mesh sizes	149

6.56	Contours coloured by velocity magnitude ($ u $ m/s) on the planes $x = 0, y = 0, z = 0$ at $t = 1.5$ s from the a) VOF-DEM (RSM), b) Eulerian DDPM-DEM (RSM), c) LBM-VOF Verlet particle and d) LBM-VOF Point particle models	150
6.57	Underflow PSD - Comparison between Eulerian DDPM-DEM, VOF-DEM (RSM) and LBM-VOF particle models with experimental measurements	152
6.58	Overflow PSD - Comparison between Eulerian DDPM-DEM, VOF-DEM (RSM) and LBM-VOF particle models with experimental measurements	152
6.59	RAM usage for the particle models	154
6.60	MCUPS based performance for the particle models	154
6.61	MCUPS based performance for the NS based particle models (expanded view of part of Figure 6.60)	155
6.62	Walltime in seconds for the particle models	155
7.1	Summary of computational models used in the study	162
B.1	Contours coloured by volume fraction of air (α_{air}), on the plane $x = 0$, for the case with a) no surface tension b) reduced surface tension and c) surface tension of pure water	198
B.2	Contours coloured by velocity magnitude ($ \mathbf{u} $ (m/s)), on the plane $x = 0$, for the case with a) no surface tension b) reduced surface tension and c) surface tension of pure water	199
B.3	mass flow rate at the a) underflow and b) overflow	200
C.1	VOF model mesh sensitivity - overflow mass flow rate	203
C.2	VOF model mesh sensitivity - underflow mass flow rate	203
C.3	Mixture model mesh sensitivity - overflow mass flow rate	204

C.4 Mixture model mesh sensitivity - underflow mass flow rate . . . 204

C.5 Eulerian model mesh sensitivity - overflow mass flow rate . . . 205

C.6 Eulerian model mesh sensitivity - underflow mass flow rate . . . 205

C.7 VOF-DEM model mesh sensitivity - total efficiency 207

C.8 VOF-DEM model mesh sensitivity - overflow mass flow rate . 208

C.9 VOF-DEM model mesh sensitivity - underflow mass flow rate 208



List of Tables

3.1	VV100 Hydrocyclone dimensions	32
3.2	Fluid properties	40
3.3	Flow Boundary conditions	50
5.1	Operating Pressures for Test 1, 2 and 3.	81
5.2	Water and Solids Densities for Test 1, 2 and 3.	81
5.3	Overflow Mass and Volume Fraction Measurements	82
5.4	Underflow Mass and Volume Fraction Measurements	83
5.5	Overflow Mass Flow Rates	85
5.6	Underflow Mass Flow Rates	86
5.7	Feed Mass Flow Rates, Volumetric Flow Rates, Mass Fractions and Volume Fractions	87
5.8	Feed PSD - Cumulative Passing	88
5.9	Underflow PSD - Cumulative Passing	88
5.10	Overflow PSD - Cumulative Passing	88
5.11	Accuracy of the Size Measurements	89

5.12 Rosin-Rammler Distribution Parameters 89

6.1 NS Air-Core Mass Flow Rate Model Comparisons 98

6.2 NS Air-Core Model Mass Flow Rate Comparisons 2.5mm Mesh 98

6.3 NS Air-Core Model Mass Flow Rate Comparisons 1.25mm Mesh 98

6.4 Air-Core Model Mass Flow Rate Comparisons for LBM-VOF
Model 118

6.5 NS-DEM Water Mass Flow Rate Model Comparisons 131

B.1 Old VV100 Hydrocyclone dimensions 197



Nomenclature

A	Area, m^2
\mathbf{A}	Area Vector, m^2
A_i	Interfacial Area, m^2
a	Inlet width, m
a_i	Spherical drag law coefficient constants $\forall i = 1, 2, 3$
B_i	Body force components $\forall i = x, y, z$
b	Inlet height, m
C_D	Drag coefficient
C_{ij}	Transport of the Reynolds stresses by convection
C_s	Smagorinsky constant
C_{vm}	Virtual mass factor
$C_{1\epsilon}, C_{2\epsilon}, C_{3\epsilon}$	RNG $k - \epsilon$ model constants
c	Speed of sound, m/s
\mathbf{c}_i	Lattice vector
c_s	Lattice speed of sound, <i>lattice units per second</i> (lu/s)
CFL	Courant-Friedrichs-Lewy number
D	Spatial dimension
D_c	Barrel diameter, m
D_H	Hydraulic diameter, m

$D_{L,ij}$	Transport of the Reynolds stresses by molecular diffusion
$D_{T,ij}$	Transport of the Reynolds stresses by turbulent diffusion
d	Diameter, m
d_w	Distance from the point in the flow field to the closest wall, m
\bar{d}	Mean diameter, m
E_T	Total efficiency, %
Eu	Euler number,
\bar{e}	Set of discrete velocities, m/s
\bar{e}_i	Discrete velocity component at lattice node i , m/s
\bar{e}_{ij}	Unit distance vector from particle i to particle j , m
$f(\bar{r}, \bar{\xi}, t)$	Single-particle distribution function
f^{eq}	Equilibrium distribution function
f_i	Single-particle distribution function at lattice node i
\bar{F}	Force, N
F_{CSS}	Surface tension force, N
\bar{F}_{drag}	Drag force, N
$\bar{F}_{friction}$	Friction force, N
\bar{F}_g	Gravitational force, N
F_{ij}	Transport of the Reynolds stresses by production by system rotation
\bar{F}_{ij}	Force exerted on particle i by particle j , N
\bar{F}_{lift}	Lift force, N
$\bar{F}_{pressure}$	Pressure gradient force, N
\bar{F}_{other}	Other particle interaction forces, N
\bar{F}_{td}	Turbulent dispersion force, N
\bar{F}_{vm}	Virtual mass force, N
\bar{F}_{wl}	Wall lubrication force, N

f_{loss}	Loss factor
G_b	Generation of turbulence kinetic energy due to buoyancy
G_{ii}, G_{ij}	Transport of the Reynolds stresses by buoyancy production
G_k	Generation of turbulence kinetic energy due to the mean velocity gradients
\mathbf{g}	Gravitational vector, m/s^2
g	Gravitational constant, m/s^2
H	Hydrocyclone height, m
h	Cone height, m
I_{turb}	Turbulence intensity, %
I	Unit tensor
\bar{I}	Identity tensor
K	Spring constant, N/m
K_{pq}	Interphase momentum exchange coefficient
k	Turbulence kinetic energy, J/kg
L_s	Mixing length
l	Vortex finder height, m
M_t	Turbulent Mach Number
m	Mass, kg
m	Number of discrete lattice nodes (or directions)
m_i	Mass of arbitrary particle i , kg
m_{ij}	Reduced mass of arbitrary particles i and j , kg
\dot{m}	Mass-flow rate, kg/s
N	Number of discrete size bins
N_{faces}	Number of faces
n	Rosin-Rammler distribution spread parameter
N	Spatial Dimension

\hat{n}	Unit surface normal vector
\bar{n}	Volume fraction gradient
\hat{n}_w	Unit normal vector at the wall
P	Pressure, kPa
P_a	Atmospheric pressure, kPa
P_{ii}, P_{ij}	Transport of the Reynolds stresses by stress production
\bar{p}	Mean pressure, Pa
p	Instantaneous pressure, Pa
p'	Fluctuating pressure due to turbulence, Pa
p_{gauge}	Gauge pressure, kPa
R_g	Gas constant, J/(mol K)
R_{pq}	Interphase momentum exchange force, N
R_ϵ	RNG $k - \epsilon$ model R term
r	Radius, m
\bar{r}	Space co-ordinate, m
Re	Reynolds Number
\mathbf{S}	Strain-rate tensor
s	Spigot height, m
$ \mathbf{S} $	Tensor norm of strain-rate tensor
\mathbf{S}_{ij}	Rate-of-strain tensor for the resolved scale
S_M	Momentum source term
$S_{M,i}$	x, y and z momentum source terms respectively
S_k	Turbulence kinetic energy source term
S_ϵ	Turbulence dissipation rate source term
$S_{\overline{\rho u_i u_j}}$	Reynolds stresses source term
S_ϕ	x, y Generalised scalar source term
T	Temperature, K
T	Surface stress tensor due to surface tension, Pa
t	Time, s
t_{coll}	collision time scale, s

\hat{t}_w	Unit tangential vector at the wall
Δt	Time step size, s
δt	Discrete time unit, s
u, v and w	x, y and z velocities respectively, m/s
u	Speed, m/s
$\bar{\mathbf{u}}$	Mean velocity vector, m/s
\mathbf{u}_{eq}	Equilibrium velocity, m/s
\bar{u}_i	Mean velocity components $\forall i = x, y, z$, m/s
\mathbf{u}	Velocity vector, m/s
$ \mathbf{u} $	Velocity vector magnitude, m/s
\mathbf{u}_{wall}	Wall velocity vector, m/s
u'_i	Fluctuating velocity components $\forall i = x, y, z$, m/s
u_i	Instantaneous velocity components $\forall i = x, y, z$, m/s
V	Volume, m ³
V_c	Computational cell volume, m ³
v_i	Velocity of arbitrary particle i , m/s
v_{ij}	Relative velocity of arbitrary particles i and j , m/s
v_{pq}	Slip velocity between phase p and q , m/s
v_θ	Tangential velocity, m/s
w	Mass fraction
w_i	Lattice weights
x, y, z	Cartesian co-ordinates, m
x_i	Cartesian directions $\forall i = x, y, z$, m
\bar{x}_i	Position of particle i , m
Δx	Lattice spacing, m
Y_d	Mass fraction of particles with diameter greater than d
Y_M	The contribution of the fluctuating dilatation in compressible turbulence to the overall dissipation rate
$\mathbf{0}$	Zero vector
<i>Greek Symbols</i>	
α	Volume fraction

$\alpha_k, \alpha_\epsilon$	Inverse effective Prandtl numbers for k and ϵ respectively
Γ	Diffusion coefficient
γ	Damping coefficient, (Ns)/m
δ	Particle overlap due to collision, m
δ_{ij}	Kronecker Delta
$\Delta\rho$	Density difference, kg/m ³
ϵ	Turbulence dissipation rate, m ² /s ³
ϵ_D	Fraction of the particle diameter for allowable overlap
ϵ_{ij}	Transport of the Reynolds stresses by dissipation
η	coefficient of restitution, $0 < \eta < 1$
θ_w	Contact angle at the wall
$\kappa(\bar{x}, t)$	Surface curvature
κ	von Kármán constant
λ	Bulk viscosity, kg/(m s)
μ	Viscosity, kg/(m s)
μ	Surface friction coefficient
μ_{eff}	Effective viscosity, kg/(m s)
μ_t	Turbulent (eddy) viscosity, kg/(m s)
ν	Kinematic viscosity, m ² /s
$\bar{\xi}$	Microscopic velocity, m/s
$\overline{\rho u'_i u'_j}$	Reynolds stresses (tensor notation), Pa
ρ	Density, kg/m ³
σ	Surface tension coefficient, N/m
σ_{ij}	Stress tensor due to molecular viscosity, Pa
σ_k	Turbulent Prandtl Number for k
τ	Relaxation time, s
τ_0	Relaxation time, s

τ_p	Particle relaxation time, s
τ_t	Turbulent (LES) relaxation time, s
τ_*	Effective relaxation time, s
τ_{ij}	Filtered sub-grid scale stress tensor, Pa
$\overline{\overline{\tau}}_q$	Phase shear stress-strain tensor, Pa
ϕ	Generalised scalar
ϕ_{ij}	Transport of the Reynolds stresses by pressure strain

Subscripts

<i>air</i>	Air
<i>ave</i>	Average
<i>dr</i>	Drift
<i>exp</i>	Experiment
<i>f</i>	Face
<i>G</i>	Local gas
<i>m</i>	Mixture
<i>max</i>	Maximum
<i>min</i>	Minimum
<i>over</i>	Overflow
<i>overflow</i>	Overflow
<i>p</i>	Particles or solids
<i>p, q</i>	Phase indices
<i>r</i>	Relative
<i>t</i>	Total
<i>under</i>	Underflow
<i>underflow</i>	Underflow
<i>w</i>	Water

Superscripts

T Transpose

Abbreviations

ASM	Algebraic Slip Mixture
BGK	Bhatnagar-Gross-Krook
CFB	Circulating Fluidised Bed
CFD	Computational Fluid Dynamics
CGD	Computational Granular Dynamics
CHPC	Centre for High Performance Computing
CPU	Central Processing Unit
CSS	Continuum Surface Stress
DDP	Dense Discrete Phase
DEM	Discrete Element Method
DMC	Dense Medium Cyclone
DNS	Direct Numerical Simulation
DPM	Discrete Phase Model
FDM	Finite Difference Method
FLOPS	Floating Operations per Second
FVM	Finite Volume Method
GB	Gigabyte
GPU	Graphical Processing Unit
IB	Immersed Boundary
IGES	Initial Graphics Exchange Specification
LBM	Lattice Boltzmann Method
LDA	Laser Doppler Anemometry
LES	Large Eddy Simulation
LGA	Lattice Gas Cellular Automaton
LOR	Line of Response

LPT	Lagrangian Particle Tracking
MCMP	Multi-Component Multiphase
MCUPS	Mega Cell-site-Updates per Second
MD	Molecular Dynamics
MLUPS	Mega Lattice-site-Updates per Second
MPI	Message Passing Interface
NS	Navier-Stokes
PEPT	Positron Emission Particle Tracking
PET	Positron Emission Tomography
PIV	Particle Image Velocimetry
PSD	Particle Size Distribution
RAM	Random Access Memory
RANS	Reynolds Averaged Navier-Stokes
RNG	Renormalization Group Theory
RSM	Reynolds Stress Model
SGS	Sub-grid Scale
SRT	Single Relaxation Time
STL	Stereo-lithography
VOF	Volume-of-Fluid
VTI	Visualisation Toolkit Image Data
VTK	Visualisation Toolkit Data

Chapter 1

Introduction

Cyclone separators are used in the metal and mineral processing industry as well as in the chemical industry [1–3]. Hydrocyclones are used to separate solid particles or liquid droplets by size or by density [1]. In the case of density based separation, as opposed to size based separation, the hydrocyclone is called a dense medium cyclone (DMC) [2]. Gas cyclones are used to remove dust from a gas, via separation, as well as for product recovery [3].

Cyclone separators have very simple geometrical structures [1–3]. As illustrated in Figure 1.1, most cyclone separators have an inlet that is tangential to the cylindrical section, which is referred to as the barrel. The barrel has a cylindrical insert, known as the vortex finder, which forms an annulus region in the barrel. At the top of the vortex finder is the upper outlet (overflow). The barrel is connected to a conical section which is in turn connected to the spigot. The spigot leads to the lower outlet (underflow).

In some cases, the inlet is axial (concentric) with the main body of the cyclone, more specifically with the vortex finder [4]. The swirl is generated by stationary guide vanes between the vortex finder and the intake head [4]. In the case of an axial inlet the cyclone is known as a swirl tube. However, the focus of this study is on tangential inlet cyclones, thus, the swirl tube will not be discussed further.

The gas/liquid stream with entrained particles is pumped through the inlet and separates, in the barrel, into two secondary streams. The first of the secondary streams consists of a high volume (and high mass) fraction

of gas/liquid and a low volume (and low mass) fraction of solids/droplets. This stream contains the smaller/less dense particles/droplets. The other secondary stream consists of a high volume (and high mass) fraction of solids/droplets and a low volume (and low mass) fraction of gas/liquid. This stream contains the larger/denser particles/droplets.

The combination of gravitational and centrifugal forces causes both secondary streams to swirl forming spiral flow structures. The first stream is forced into the core of the barrel through the vortex finder and exits through the overflow. The second stream is forced to the walls of the separator via centrifugal forces. Due to gravity the second stream flows to the underflow.

Both the underflow and the overflow are open to atmosphere while the gas/liquid stream is pumped into the inlet at a pressure higher than atmospheric [1–3]. In the case of a hydrocyclone, including all DMCs, air flows into the underflow and overflow via the pressure gradient between the inlet and the respective outlets as well as from air that is entrained in the feed [1]. This results in a rotating column of air, known as the air-core, forming in the center (core) of the hydrocyclone [1]. However, if the pressure difference between the inlet and atmosphere is not sufficiently high, an air-core may not form [1].

Despite the geometric simplicity of cyclone separators, the flow structures and multiphase interactions in cyclone separators are complex [1–3]. The flow structures in cyclone separators consists of:

- highly swirling turbulent flows,
- flow separation with resulting secondary flows and
- multiphase interactions.

The interactions are multiscale in the sense that the time and length scale of the flow field of each phase is different relative to same scale for the other phases [5].

Due to the importance of hydrocyclones, in metal and mineral processing as well as chemical operations, they have been the topic of increased research in recent years [2, 6–9]. The complexity of the flow structures in cyclone

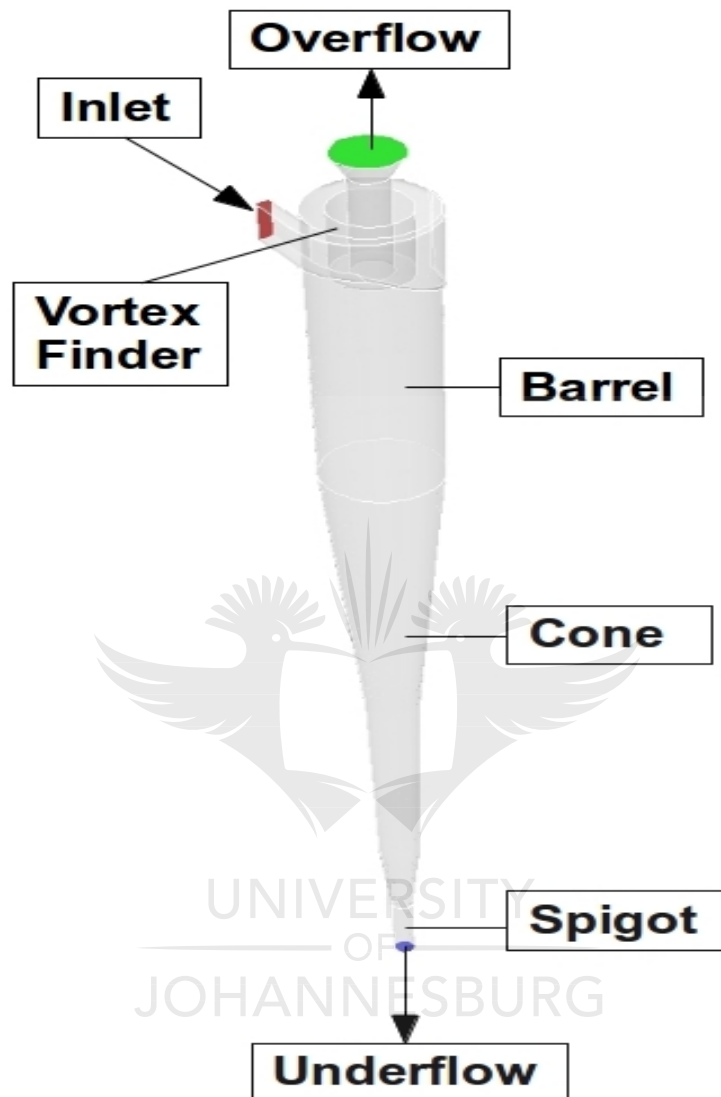


Figure 1.1: Isometric view of a cyclone separator

separators makes design optimisation by experiment a tedious and financially costly exercise. Furthermore, design optimisation by experiment does not provide a holistic view of the flow structures and multiphase interactions in a cyclone separator.

Simulation techniques such as Computational Fluid Dynamics (CFD) have become an attractive means to characterise the complex flow structures and

multiphase interactions in cyclone separators [1–3, 6–12]. This is due to the large scale availability of powerful computational resources at relatively low cost and the relative maturity of the multiphase models used in CFD [5, 10, 11].

Traditionally CFD provided two approaches to model granular (fluid-solid) flows [11, 13], the Eulerian-Lagrangian, otherwise known as Lagrangian Particle Tracking (LPT), and the Eulerian-Eulerian Granular multiphase models [11, 13].

The LPT model treats the solid (discrete) phase as discrete particles that follow the fluid (liquid/gas) path [11, 13]. The major shortcoming of this model is that the particles have no interaction with each other as well as with the wall [13]. Furthermore, the particle-fluid interaction is limited to empirical drag correlations for flow around a cylinder/sphere/object, virtual mass, thermophoretic, Saffman lift, Brownian motion and pressure gradient forces [11, 13]. Furthermore, the fluid flow is modelled at length scales larger than the smallest particle diameter and in some cases the largest particle diameter. Thus, the effect of the particle on the actual fluid flow around the particles is not captured.

Flows with non-uniform particle sizes or densities can be modelled by grouping particles by effective diameters or densities and modelling each group as a separate phase [11, 13]. In the case of non-uniform size the particle size distribution is described by a statistical distribution such as the Rosin-Rammler distribution [13, 14].

The Eulerian-Eulerian Granular model treats both the fluid and solid phases as inter-penetrating continua [11, 13]. Flows with non-uniform particle sizes (or densities) can be modelled by grouping particles by effective diameters (or densities) and modelling each group as a separate phase [11, 13]. In this way particle-particle and particle-fluid interactions can be specified by interaction between the phases [11]. This approach still poses the problem, as in the LPT model, of the effect of the particles on the flow field.

Because the LPT model neglects particle-particle and particle-wall interactions it is applicable to flows with solid volume fractions below 10% [13]. However, the Eulerian-Eulerian Granular model is applicable to flows with higher solid volume fractions [13]. Most process equipment such as hydrocyclones and cyclone separators have regions where the solid volume fraction is high (solids settling) as well as regions where the solid volume fraction is

low (fluidisation).

In the case of packed and fluidised beds the solids volume fraction is high ($\gg 10\%$) [13, 15]. Thus, the Eulerian-Eulerian Granular multiphase model has yielded good results in terms of the modelling of such systems [15]. However, in the case of hydrocyclones and cyclone separators the volume fraction is low ($< 10\%$) in the core of the separator and high ($> 30\%$) near the walls of the separator as well as in the conical section near the underflow [16].

Due to the low solids volume fraction in the core of a hydrocyclone the LPT model has been widely used in the literature to model hydrocyclones [12, 16–20]. However, the LPT model breaks down in the region where the solids volume fraction exceeds ten percent such as in the cone and near the wall.

CFD models (LPT) of cyclone separators, with results comparable to experiment, have been presented in the literature [12, 16–20]. However, the models present significant error in the areas where the solids tend to group together and near the wall. This problem is exacerbated by the fact that the particles in cyclone separators tend to group in a spiral strand near the wall region [2, 3, 21]. The reason for such error is due to the neglected particle-particle and particle-wall interaction [3]. Various researchers have considered, as an alternative, the discrete element method (DEM) to have the potential to address this shortcoming [2, 3, 22].

DEM is traditionally used in bulk solids handling simulations where particle-particle and particle-wall interaction is significant; and is based on Newton's equations of motion [2, 3, 22]. DEM incorporates particle-particle interaction via a description of the normal and tangential forces that act on a particle by the other particles [2, 3, 22]. In both cases, normal and tangential forces, the contact and viscous damping components are defined [2, 3, 22]. In addition, the torque generated by the tangential forces and the rolling friction torque is included in the model [2, 3, 22]. The tangential and normal forces are used to calculate the particle-wall interaction forces. In the case of CFD-DEM models, particle-fluid interaction is incorporated via the viscous drag and pressure gradient forces as defined in the LPT model [2, 3, 22]. CFD-DEM has been used to model gas-solid cyclones and DMC's as in [3] and [2] respectively.

Due to the importance of the air-core in hydrocyclones [1, 6, 7] significant research [2, 6–9, 12] has been done on modelling of air-cores in hydrocyclones.

Research on air-core formation in hydrocyclones has been driven by the need for an improvement in the understanding of hydrocyclone behaviour and performance. According to Narasimha, Brennan and Holtham [1], when the feed pressure in a hydrocyclone is sufficiently low, as demonstrated in reference [1], an air-core does not form. However, when the feed pressure is sufficiently high an air-core does form and cannot be ignored. In the study done by Bhaskar *et al.* [20] the air-core was neglected which resulted in a difference of up to 20% between the experimental results and the CFD predictions.

According to Narasimha, Brennan and Holtham [6], the Algebraic Slip Mixture (ASM) and Volume of Fluid (VOF) models have been used, amongst other less effective models, to predict air-core formation in hydrocyclones. The VOF is the most commonly used approach due to its simplicity and its relatively low computational cost [2,6–9,12]. The accuracy of the VOF model in predicting air-core formation has been experimentally proven in numerous studies such as in [2,6–9,12]. There is presently no available literature on the comparison of the different approaches to the modelling of air-core formation in hydrocyclones.

The Lattice-Boltzmann Method (LBM) uses a “simplistic” version of a Molecular Dynamics (MD) description of the fluid motion [23–25]. This is done using the kinetic theory of gases, the Boltzmann equation in particular [23–25]. In this way the fluid motion is described by the movement and interaction of the fluid molecules [23]. Using the Chapman-Enskog expansion it has been proven that the LBM recovers Navier-Stokes behaviour for general compressible and incompressible fluids [23–25]. Thus, the macroscopic fluid dynamics are recovered using the LBM.

Due to the fact that the LBM is used to simulate fluid behaviour it is classified under CFD. The LPT and CFD-DEM models mentioned earlier are Navier-Stokes (NS) based methods. Hence, to differentiate between the approaches used in this study, the LPT and CFD-DEM will be classified under the NS based methods and the LBM will be classified separately. Thus, CFD models to be used refer to NS based methods.

The LBM has gained popularity as an alternative method, to the Navier-Stokes (NS) based Finite Volume Method (FVM), for simulating fluid flow [5,26–28]. Furthermore, with its high level of parallelism [28] it has significant advantages over the NS based FVM in terms of computational cost. Thus, it has major potential for applications in industry. The popularity of the LBM,

however, remains within the academic sphere and has made slow progress in becoming a commonly used technique in industry in relation to the NS based FVM [5]. It has proven to be particularly adept at solving multiphase and discrete phase problems which is of particular interest in simulating process equipment such as cyclone separators [5, 26–28]. However, the literature on the application of the LBM to hydrocyclones, and cyclone separators in general, is sparse [28–30].

Gronald and Derksen [28] have shown that for single phase flow the LBM is comparable to the NS based FVM with regards to hydrocyclone modelling. However, Gronald and Derksen [28] provide insufficient information on how they applied the LBM. Thus, it is not possible to reconstruct a working model of a hydrocyclone from the published work of Gronald and Derksen [28].

Pirker *et al.* [29] used a hybrid of the NS based FVM and LBM to model a gas-cyclone short-cut flow. The hybrid model used in [29] comprised of the NS based FVM which was used to model the cyclone except the annulus region (intake). The annulus region at the top of the cyclone was modelled using the LBM [29]. The LBM used in Pirker *et al.* [29] includes the Large Eddy Simulation (LES) turbulence model. The NS based FVM model was used in a separate case, throughout the domain, to compare with the LBM. The LBM showed superior predictions to the NS based FVM relative to experimental data [29]. Thus, it may be of benefit to model an entire hydrocyclone using the LBM.

The use of coupled CFD (LPT) and DEM [2, 3, 22, 23, 31] models as well as LBM [5, 23] models have been illustrated in recent literature. Both the CFD-DEM coupled model and LBM have been shown to capture key flow features in process equipment such as downers [22], gas-solid [3] and dense medium [2] cyclone separators as well as fluidised beds [5]. These models incorporate particle-particle and particle-wall interaction, albeit at different scales [23].

1.1 Problem Statement

Both the CFD-DEM and the LBM models have drawbacks [23]. In the case of the CFD-DEM model, the fluid motion is described macroscopically at length scales larger than the particle size [23]. Thus, in the case of CFD-

DEM, models with reasonably large length scales ($0.1m$) and quantity of particles in the range of 10^5 can be simulated [23]. As a result this leads to a weak description of the flow field around the particle, and thus a weak description of the particle-fluid interaction. On the contrary, in the LBM, fluid motion is described microscopically at length scales smaller than the particle size [23]. This provides an accurate description of the flow field around the particle, and thus an accurate description of the particle-fluid interaction [23]. Due to the detail provided by the LBM and computational restrictions much smaller models and less particles (≈ 500), than the CFD-DEM model, can be simulated [23].

When simulating multiphase flows particularly liquid-gas-solid flows, as in a hydrocyclone, there is usually a trade off between accuracy and computation effort. This poses a problem in the simulation of such flows in industrial equipment such as hydrocyclones. In the case of hydrocyclones either the flow field in the entire system is modelled while sacrificing accuracy or only a limited portion of the system is modelled while preserving accuracy. The accuracy is usually sacrificed by excluding the important multiphase interactions, namely particle-particle and particle-wall interactions as well as the liquid/gas interactions due to air-core formation. Thus, there is a need for models that preserve accuracy by capturing the multiphase interactions, at the various length and time scales, whilst remaining computationally efficient so that the entire system can be modelled.

While the LBM has been applied to modelling of hydrocyclones as in [28,29], it has only been used to model single phase flow. However, due to the proven accuracy and computational efficiency of the LBM in modelling multiphase flow, as proven in studies such as [5,26,27,32], it may be beneficial to model the full multiphase interactions in a hydrocyclone using the LBM. It may be beneficial to compare the predictions and computational efficiency of the LBM to the NS based FVM models, namely the CFD-DEM model of a hydrocyclone.

This leads to the primary research hypothesis, which is:

The LBM can adequately resolve the multiphase interactions, thus predicting separation, in a hydrocyclone with greater accuracy and computational efficiency than CFD-DEM.

Thus, the null-hypothesis is:

The LBM cannot adequately resolve the multiphase interactions, thus predicting separation, in a hydrocyclone with lower accuracy and computational efficiency than CFD-DEM.

The research hypothesis is extended in the form of a number of research questions. The research questions are as follows:

- Can the CFD-DEM and LBM accurately resolve the multiphase interactions in a hydrocyclone?
- Can the CFD-DEM and LBM provide accurate predictions of separation in a hydrocyclone?
- Can the LBM give more accurate predictions, than CFD-DEM, of separation in a hydrocyclone?
- Is the LBM more computationally efficient, than the CFD-DEM, in predicting multiphase interactions and separation in a hydrocyclone?

Additional research questions, regarding the modelling of air-core formation, will be addressed as a by-product of the testing of the hypothesis:

- From the VOF, mixture, algebraic slip, Eulerian-Eulerian multiphase, Eulerian-Eulerian VOF, LBM-VOF and LBM two-fluid VOF models which provides the most accurate predictions of air-core formation in a hydrocyclone?
- Based on NS CFD models, does surface tension have a significant effect on air-core formation in hydrocyclones?

The term accuracy in the above questions relate to the accuracy of the model predictions against experimental observations. Computational efficiency of the models will be measured against a range of factors, namely, central processing unit (CPU) usage, random access memory (RAM) usage, simulation run-time as well as convergence rate (number of iterations per time step to reach convergence).

Traditionally the number of floating point operations per second (FLOPS) is used to gauge computational efficiency. However, FLOPS is a more appropriate metric to gauge computational efficiency of hardware than of simulation

per sé. The simulations will often be limited, in terms of FLOPS, by the hardware being used. In addition it may be the case that a model achieves higher FLOPS, in relation to another model, but requires significantly more floating operations to reach convergence.

Based on the above two it is not appropriate to use FLOPS as a measure of computational efficiency in this study. To assess the computational efficiency of the model, it is appropriate to consider the factors of CPU usage, RAM usage, simulation run-time as well as convergence rate. This approach will objectively determine which model has a higher computational efficiency based on all the underlying factors. This approach is also of benefit to industrial stakeholders as the results can be used as a benchmark for selecting appropriate hardware as well as to benchmark expectations on time lines for simulations to complete. In addition, industrial stakeholders are not concerned with FLOPS as the only information of relevance to them are “how quickly can a result be obtained?” and “what sort of hardware is required to run the simulations?”

Multiple hardware configurations were used in this study, namely:

- Core i7 Desktop with 8 threads and 24GB RAM,
- Core i7 Laptop with 8 threads and 6GB RAM,
- the Nehalem cluster at the Centre for High Performance Computing (CHPC)
- the Westmere cluster at the Centre for High Performance Computing (CHPC)

Due to the difference in architecture used the bias of the hardware (CPU availability) and other factors that affect convergence rate, such as time step size and cell count are removed by introducing the metric Mega Cell-site-Updates per Second (MCUPS) which represents the number of cell/lattice time step updates per second, which is congruent with the performance metric used in [33]. Thus, computational efficiency was measured using RAM usage, simulation run-time (walltime) and MCUPS.

1.2 Aim and Objectives

The aim in this study is to compare the predictions of the CFD-DEM and LBM in the case of a hydrocyclone. Furthermore, the aim is to determine if either or both of the approaches produce results which are comparable to experimental results. The CFD-DEM and LBM models will be compared in terms of accuracy and computational efficiency to determine which approach is more suitable to modelling hydrocyclones. Both approaches will incorporate air-core formation, particle-fluid, particle-particle and particle-wall interactions.

1.3 Study Methodology

The methodology to be used in the research project is a combination of simulation and experiment. CFD-DEM and LBM numerical simulation based approaches will be used to model a hydrocyclone. The CFD-DEM models will be implemented in a commercial CFD code, namely ANSYS Fluent [34]. The LBM models will be implemented in the Palabos open-source LBM libraries [35]. The experimental work will be used to validate the models.

ANSYS Fluent will be used to compare different models used to predict air-core formation. The different models will include the VOF, mixture, algebraic slip, Eulerian-Eulerian multiphase and the Eulerian-Eulerian VOF models.

A turbulence sensitivity study will be conducted using the Renormalization Group-Theory (RNG $k - \epsilon$), RSM and LES models. For the LBM only the LES model will be used. A full mesh sensitivity study will be done on the both approaches.

The accuracy and computational efficiency of both approaches will be discussed and compared.

A key component in solving the above problem is experimental validation of the models to ensure that the models are physically accurate, both quantitatively and qualitatively. Thus, the models will be experimentally validated. The aim, in terms of the experimental work is to validate both approaches and to determine which method is more accurate in predicting the separation

curve of a hydrocyclone. In addition, the experimental work will provide the operating parameters that will be used as the boundary conditions for the models. The experimental work will be done on a full scale purpose built experimental setup.

1.4 Preview

The rest of the report includes:

Chapter 2 : Literature Review

The literature that was reviewed and the information obtained from the literature is discussed and critically analysed in this chapter.

Chapter 3: Coupled Navier-Stokes Based Computational Fluid Dynamics Model and Discrete Element Modelling Approach

In this chapter the coupled NS based CFD and DEM model is presented. Furthermore, a comparison of the performance of various multiphase models, to incorporate the air-core, is also given. The CFD-DEM model used in this research to capture the fluid-particle, particle-particle interactions, particle-wall interactions and air-core formation is presented in this chapter.

Chapter 4: Lattice Boltzmann Method based Model

The LBM model used in this research to capture the fluid-particle, particle-particle interactions, particle-wall interactions and air-core formation is presented in this chapter.

Chapter 5 : Experimental Setup and Results

The experimental setup, that was designed and used in this research, is described in this chapter. Furthermore, the experimental procedure is outlined in this chapter. The results from the experiments are presented in this chapter.

Chapter 6: Results and Discussion

The results from the CFD-DEM and LBM models are presented in this chapter. The different approaches are validated against the experimental results. The two approaches are compared based on accuracy and computational efficiency.

Chapter 7: Summary, Conclusions and Recommendations

A summary of the research as well as conclusions and recommendations derived from the research is presented in this chapter.



Chapter 2

Literature Review

2.1 Overview of the Current Status of CFD Modelling of Process Equipment

Increasing global competition and a drive towards lower energy footprints dictates that the chemical, metal and mineral processing industries develop technologies that are cheaper to manufacture and operate, are safer, have higher efficiencies with lower waste and have a reduced negative environmental impact [11]. According to Joshi and Ranade [11], to achieve the above and to maximise the industrial benefit of these industries the design of chemical, metal and mineral processing equipment needs to be optimised and advanced. Joshi and Ranade [11] state that this can be achieved by “manipulating the underlying fluid dynamics” in processing equipment. This in turn requires advances in the scientific knowledge and modelling of fluid dynamic systems [5, 11].

A greater understanding of the physics in granular dynamics is needed due to the large scale presence of granular materials in mineral processing. Granular materials have complex physical behaviours which can be characteristic of fluids under certain conditions and characteristic of solids under different conditions [36]. Despite significant advances in the field of granular dynamics, the theory on granular matter and granular dynamics is still not as well developed and generalised as that of liquids, gases and solids [36].

It is evident from the literature that significant advances in the theory of fluid and granular dynamics would have a positive bearing on the advancement of the industrial value of chemical, metal and mineral processing industries [5, 11, 36]. According to Joshi and Ranade [11] CFD is a technology that can be used to achieve these advances from the fluid dynamics perspective. In the same light, Pöschel and Schwager [36] assert that computational granular dynamics (CGD) is also necessary to achieve these advances. Based on the advances in both fields it is clear that a combination of both is required to make the necessary leaps in technology required to achieve the above.

Noteworthy advances in turbulence modelling for two-phase flow highlight the importance and progress made on attempts to devise a full multiscale strategy for modelling turbulent two-phase flows [5]. The most notable shift forward is the move from RANS based models to LES based and ultimately DNS based approaches. Van den Akker [5], further highlights the progress made and importance of LBM based models. Joshi and Ranade [11] gave an overview of the then current status of CFD for single and multiphase flow and the path forward for CFD. The study by Joshi and Ranade [11] also covered free surface, dispersed phase and reactive flows. Whilst many of the items listed under the path forward in [11] are now standard in CFD, a number of the shortcomings still remain. Based on the suggestions of [11] notable outstanding advances relevant to hydrocyclones are:

- Free Surface flows (air-core formation):
 - hysteresis in contact angle for wall adhesion in free surface flows
 - characterisation of wetting and drop dynamics on different surfaces
 - momentum transport at the interface - continued progress is needed in this area
- Dispersed multiphase flows (solids transport):
 - Experimental data to provide drag, lift and virtual mass coefficients for multi-particle systems - analysts still rely on basic empirical formulae for single particle systems

Advances made in CFD and CGD have a positive bearing on the modelling of hydrocyclones, however, research is needed on combining these advances

to the application of hydrocyclone modelling. Hydrocyclone behaviour is characterised by multiscale multiphase interactions namely: liquid-gas, fluid-particle, particle-particle and particle-wall interactions. The modelling of these interactions have been predominantly done using CFD [1–3, 6–12]. However, hydrocyclones present behaviour, such as jamming, characterised by granular dynamics. Thus, to effectively model hydrocyclones the above multiscale interactions and granular behaviour needs to be captured.

A general solution to the full turbulent NS equations combined with a unifying theory for granular flow would negate the need for the above. However, in the absence of such breakthroughs advances in CFD and CGD are essential.

2.2 The Physics of Cyclonic Flows

The flow structures in cyclone separators consists of highly swirling turbulent flows, flow separation with resulting secondary flows and multiphase interactions [1–3]. The multiphase interactions comprise of particle-fluid, particle-particle and particle-wall interactions [2, 3, 6]. In the case of hydrocyclones and DMC's an additional interactions occur at the air-water interface resulting in air-core formation [2, 3, 6].

The flow field in a hydrocyclone consists of a swirling turbulent flow that forms a spiral pattern [37]. The primary stream is a spiral that flows from the inlet to the underflow, along the wall [37]. The primary flow separates, as it moves downwards, into a secondary spiral that flows to the centre of the hydrocyclone and upwards through the vortex finder and to the overflow [37]. The secondary stream is further fed by short-cut flow that separates from the inlet stream and flows towards the centre of the hydrocyclone into the overflow via the vortex finder [37]. According to Chiang, He and Feng [37] in [38], the short-cut flow can account for as much as 15% of the feed flow. The mass-flow rate of water at the overflow exceeds that of the underflow [37].

Due to the the pressure drop between the inlet and the outlets (overflow and underflow) and the rotational motion of the fluid a low pressure region forms in the core of the hydrocyclone along its' central axis [6, 37]. This low pressure region leads to air ingress from the underflow and the overflow, which combined with air entrained in the feed of the hydrocyclone, is entrained in the main flow and forms an upward rotating column of air in the area of

the low pressure region [6, 37]. This is known as air-core formation [6, 37]. According to Chiang, He and Feng [37] in [38], the air-core stabilizes the vortex flow pattern within the hydrocyclone. However, the air-core itself is an unsteady and often unstable flow phenomenon within the hydrocyclone [6].

The particles are initially entrained in the feed flow and separate along with the primary and secondary stream [37]. The fine particles are predominantly entrained in the secondary flow and exit through the overflow whereas the coarse particles are predominantly entrained in the primary stream and flow downwards along the wall to the underflow [37, 39]. The flow exiting the underflow has a high percentage of solids resulting in a dense slurry exiting the underflow [39].

2.3 Available Research on Hydrocyclones and Similar Process Equipment

Extensive research has been done on the modelling of gas-solid cyclones [3, 16–18, 28, 29, 40–42], fluidised beds [15, 43, 44], circulating fluidised beds (CFB's) [45], downers [22], dense medium cyclones [2, 9, 12] and hydrocyclones [1, 6–8, 19, 20, 46, 47]. The research on gas-solid cyclones, dense medium cyclones, fluidised beds, CFB's and downers can be extended to hydrocyclones to capture part of the physics present in hydrocyclones. The above research highlights the use of various approaches, namely: empirical, neural network, LBM, NS based and NS-DEM based models [1–3, 6–9, 12, 15–20, 22, 28, 29, 40–48]. This is not a comprehensive list in the sense that there are thousands of research papers and theses in the field. However, the above literature is indicative of the state of the art in the field.

2.3.1 Experimental Studies and Empirical Models

Experimental studies of cyclone separators have been carried out to extract empirical models to characterise the relevant physics [42, 46, 48]. Hsu *et al.* [48] used experimental data to provide parameters for a model that accounts for particle collection via deposition by centrifugal forces and diffusion in a gas cyclone with liquid droplets. Cortés and Gil [42] presented a review of the models developed to characterise the velocity profile and pressure drop in gas-

solid cyclones as well as an overview of the CFD models proposed for gas-solid cyclones. Nagaeswararao, Wiseman and Napier-Munn [46] proposed a revised Plitt model for hydrocyclones showing that the revised model should replace the Plitt model as the standard used in industry. Whilst empirical models as presented in [42, 46, 48] give the designer insight into the effect of certain parameters on the performance of gas-solid cyclones and hydrocyclones, the empirical models do not reveal the deeper flow features that need to be manipulated to optimise designs.

Traditionally models of hydrocyclones are validated using a black box approach such as in [2, 3, 12]. In such cases the pressure drop between the inlet and outlet(s) of the system, the outlet(s) mass flow rate(s) as well as the particle size distribution (PSD) at the outlet(s) are measured [2, 3, 12]. These measurements are compared to the predictions from the models and thus the models are validated. However, the use of laser Doppler anemometry (LDA) and particle image velocimetry (PIV) have been used to provide data of the particle and fluid velocities [49].

Both, LDA and PIV, are techniques based on light scatter [49]. Thus, it is necessary that the system be constructed out of a translucent material [49]. This limits the tests to short time periods if particles are used in the tests to ensure that the system does not wear significantly. The issue of wear can be overcome by using fluid only but in that case the particle behaviour and its' subsequent interactions with, and effects on, the fluid are ignored. Another disadvantage of LDA and PIV is that only point-by-point measurements and planar measurements can be taken at any given time [49].

Positron Emission Particle Tracking (PEPT) is an experimental technique that is used to track particles in flow field [49–57]. It has been used to experimentally track particles in fluidised beds [50–52], hydrocyclones [21], L-shaped valves [53], Circulating Fluidised Beds (CFB) [54, 55] amongst other process equipment [49]. The PEPT method has proven successful in tracking single particles with large diameters ($> 50\mu\text{m}$) [49]. Most readers may not be familiar with PEPT, at least not on the level of LDA or PIV. However, PEPT is an important technique for the experimental investigation of process equipment.

PEPT is a technique based on Positron Emission Tomography (PET) [49–57]. In brief, a tracer particle that is radioactively labelled (ideally as a pure γ - emitter) is released into the flow field with other non-labelled particles [49–57]. The tracer particle undergoes β -decay, thus leading to the emission

of a positron from the nucleus [49–57]. The positron annihilates with an electron, thus, releasing energy (dominantly) in the form of emitted back-to-back 511keV γ -rays emitted in coincidence [49–57].

PET detectors mounted around the system detect the distinct 511keV γ -ray energy signals and record the spatial impact points [49–57]. A line, known as a line of response (LOR), can be drawn between the detectors. In a small time frame, usually 4ns - 1ms, hundreds of such emissions occur, thus, resulting in hundreds of LOR's in time slices of a few ns -ms. Through triangulation the position of the particle is determined [49–57]. The time period is sufficiently small to ensure that the particle does not move a significant distance. This is done for many sequential time slices. Thus, the full 3D trajectory of the particle is detected [49–57]. By differentiating the trajectory the full 3D velocity field can be obtained [49–57].

PEPT has the potential to overcome the limitations of LDA and PIV. Furthermore PEPT can be used to provide greater insight into the deeper physics in process equipment. Insight needed to extract continuum laws for granular dynamics and possible solutions for the governing equations for fluid dynamics. At the minimum PEPT could be used as a tool to distil more detailed empirical models for process equipment. Chang *et al.* [21] successfully used PEPT to study a hydrocyclone. However, the results were not used to validate CFD models nor was the data used to distil more detailed empirical models.

Despite the advances made in the use of PEPT, work is needed in terms of using the technique for validating models of equipment such as hydrocyclones. For such applications, the use of multiple tracer particles needs to be used [49] as opposed to single tracer particles as used in [50–55]. According to [49], algorithms for multiple tracers are available in literature. However, it appears that multiple tracer particle have not been used extensively in studies of equipment such as gas-solid cyclone separators.

Furthermore, it is stated in [49] that there is a need for improvement of PEPT, particularly in source preparation, so as to incorporate the use of smaller tracer particles ($< 50\mu\text{m}$). Despite PEPT not being the focus of this study, it deserves mention as it has the potential to address the shortcomings in knowledge as outlined by [5, 11, 36]. PEPT will be incorporated in the future scope of this ongoing research project.

2.3.2 NS based Models of Hydrocyclones and Similar Process Equipment

CFD modelling of gas-solid cyclones have been studied in depth in the literature [3, 16–18, 40–42]. The NS based approach is used by [3, 16–18, 40–42] with the LPT model for particle tracking. The particle-fluid interactions are predominantly limited to the drag and gravitational forces with only [16] accounting for drag, gravitational, Saffman lift, thermophoretic and Brownian motion forces. The particle-fluid momentum exchange was incorporated as either one-way transfer (fluid to particle) [41] or two-way coupled transfer (fluid to particle and particle to fluid). Additional coupling should be included via the particle collisions, particularly when the solids concentration is high, resulting in a four-way coupled system.

Particle-particle collisions are either neglected as in [16, 41] or via a DEM collision rule that accounts for normal and tangential forces as well as particle rotation. The normal and tangential forces account for the contact and damping components [3]. Particle-wall collisions are accounted for using the DEM model [3] or via a particle reflection condition at the wall [16].

Turbulence is modelled either using the RSM [3, 16, 18] or LES models [41]. Based on the findings from [41] turbulence causes re-entrainment of particles, thus, the choice of turbulence model is critical for accurate prediction of collection efficiency in gas-solid cyclones and by inference it would be critical for predicting separation efficiency in hydrocyclones. According to the results from [41], which were compared against the RSM model predictions from [28], the LES model is the most suitable for modelling turbulence in gas-solid cyclones. However, the accuracy of predictions using the LES model is reliant on the use of fine grids [13, 14, 28, 41].

In all cases the particle tracking was implemented using the unsteady particle tracking approach with particles being injected at the fluid flow time step [3] or at discrete intervals of the fluid flow time step [41]. De Souza, Salvo and Martins [41] illustrated that the analytical and trapezoidal integration schemes (for the particle equations of motion) produced the best results against experiment. This is because the Euler scheme is sensitive to particle time step size whereas the analytical and trapezoidal schemes are not [41]. Based on the literature the unsteady segregated solver is to be preferred over a coupled approach. The equations were discretised using the QUICK scheme with a time step size in the $\Delta t = (10^{-5}) - (10^{-4})$ s range [3, 16–18, 22, 41, 42].

The approaches used to model gas-solid cyclones are applicable for hydrocyclone modelling, however, a multiphase or free surface model needs to be included to account for air-core formation. Research has been done on the modelling of hydrocyclones [1,6,7,7,8,19,20,20,47,58] and DMC's [2,9,12,59] with focus on both the particle interactions and the air-core formation. The air-core is modelled using either the mixture, ASM and the VOF models [1,6,7,7,8,19,20,20,47,58]. The particle tracking and interaction modelling follows the same approaches as in the literature on gas-solid cyclone modelling [2,3,12].

The predominant topic of the literature regarding air-core formation has been on establishing a model to predict the air-core diameter and shape as well as the effect of the air-core on the slurry [2,6–9,12]. However, Narasimha, Brennan and Holtham [6] investigated the effect of the slurry viscosity, inlet flow rate and spigot diameter on the air-core. Delgadillo and Rajamani [7] also investigated the effect of varying hydrocyclone geometries on the air-core.

The effect of the turbulence model on CFD predictions of hydrocyclones has been investigated in the literature [6,8,9]. According to Narasimha, Brennan and Holtham [6] and Narasimha *et al.* [9] the LES is more accurate than the RSM in the modelling of air-cores. However, Brennan, Holtham and Narasimha [8] found that in the case of a coarse mesh the RSM is more accurate. Narasimha, Brennan and Holtham [6], found that, for the RSM, the linear and quadratic pressure strain assumptions are not suitable for air-core modelling. A clear comparison of the performance of the ASM and VOF models, in terms of computational efficiency and accuracy, has not been done in the literature.

Despite the progress made in modelling of air-core formation and particle collisions and interactions, the models suffer from certain limitations. The major assumption of the LPT model is that the particles' volume fraction is less than 10%.¹ Thus, the LPT approach does not consider the effect of the volume fraction of solids on the fluid. As a result, the effect of particle loading towards the packing limit in the conical section of a hydrocyclone (and a DMC) is neglected. This, unmodelled effect may have a negative

¹ANSYS Fluent [13] stipulates that the discrete phase must have a low volume fraction loading even though high mass loading is acceptable. However, they do not assign a numerical value to the maximum volume fraction that is still acceptable. The value of 10% is one based on experience in using the LPT model for a wide range of problems and it is supported by literature such as [60].

impact on model predictions in the cone and at the underflow. The Eulerian granular model has the potential to overcome this limitation.

The Eulerian multiphase model is a true multiphase model in the sense that the different phases are modelled as separate inter-penetrating continua, albeit they do share a single pressure [13]. Due to the above, the continuity and momentum equations are solved for each phase. Based on preliminary simulations from this study, the pressure gradient at the water-air interface (air-core surface) can be in the region of 3 - 7 kPa [61]. This is a significant pressure difference between the phases. Thus, the assumption of a shared single pressure for both phases is not valid in the case of hydrocyclones.

The advantage of the Eulerian multiphase model is that the phases each have their own velocity field. Furthermore, due to the Dense Discrete Phase model, the Eulerian model can incorporate the LPT model while accounting for the effect of the solids volume fraction on the liquid and gas phase in a hydrocyclone, which is not possible to account for in the VOF and ASM models. In addition, the Eulerian granular approach can be used to incorporate the kinetic theory of granular materials to account for effects such as solids pressure, solids shear stress, bulk viscosity and the granular temperature.

The Eulerian granular approach has been successfully applied to fluidised beds [15, 43–45] and compared to LPT based models in [43, 44]. Cornelissen *et al.* [15] illustrated the successful application of an Eulerian granular model to a liquid-solid fluidised bed. The model proposed in [15] models the liquid and solid as inter-penetrating continua (two-fluids) with granular interactions between the two phases. The approach used in [15] is now a standard in CFD to model fluid-solid systems with a large volume fraction ($> 10\%$) of solids. Ibsen *et al.* [45], illustrated that the LPT model provided more accurate results than the Eulerian granular model, but that, the Eulerian granular model was more computationally efficient than the LPT approach.

The application of an Eulerian model to cyclones has been limited to modelling of gas-solid cyclones [40, 62]. In both cases the Eulerian model was applied to gas-solid cyclones. In the case of [40], the gas was modelled as the primary phase and the solids as the secondary phase. Meier, Vegini and Mori [62] modelled the gas as the primary phase and the solids as three separate secondary phases (one for each characteristic particle diameter).

A hydrocyclone could be modelled using the Eulerian model with water as a primary phase, air as a secondary phase and the solids as a third phase.

To alleviate the need to model an extra phase for each characteristic particle diameter a dense discrete phase model can be applied to the solid phase [13, 63]. Using this approach the third phase is modelled using the LPT and DEM and adding granular behaviour such as solids pressure, solids shear stress, bulk viscosity, the granular temperature and the solids volume fraction [13, 14, 63].

2.3.3 LBM based Models of Hydrocyclones and Similar Process Equipment

Gronald and Derksen [28] applied the LBM to model the single phase flow in a gas cyclone. The particles and subsequent interactions were not modelled. The focus of the study was to capture the turbulent swirling gas flow in the cyclone. In the study the NS based approach was compared to the LBM. The RSM and LES turbulence models were used for the NS based approach whereas for the LBM the LES model was used. The results were compared to LDA measurements from literature [28].

For the NS based models the steady and unsteady segregated pressure based solvers were used [28]. The equations were discretised using the QUICK scheme for the RSM model and the bounded central differencing scheme for the LES model [28]. PRESTO! was used for the pressure correction [28]. For the unsteady cases the time step size used was $\Delta t = 10^{-4}$ s for the LES models and $\Delta t = 5 \cdot 10^{-4}$ s for the LES model [28]. Gronald and Derksen [28] provided no details beyond mesh sizing for the LBM model.

On coarse grids the NS based approach with the RSM model provided more accurate predictions, compared against experiment. However, the NS-LES and LB-LES models provided results comparable to experiment within 10% on finer meshes [28]. Gronald and Derksen [28] did not discuss the computational efficiency of the various approaches.

Derksen, Sundrasen and van den Akker [30] used the LBM coupled with an LPT model to study the effect of mass loading in gas-solid cyclone separators. The LBM model was the same as that used in [28]. The particles were modelled using the LPT approach. Particle-fluid interactions were limited to drag and gravitational forces and particle-particle collisions were ignored [30]; the particles were modelled as point particles [30]. Derksen, Sundrasen and

van den Akker [30] illustrated that the presence of the particles reduces the gas swirl intensity and that the gas flow turbulence is reduced; a similar observation was made by [3].

Pirker *et al.* [29] used a hybrid of the NS based FVM and the LBM to model a gas-cyclone short-cut flow. The hybrid model used in [29] comprised of the NS based FVM which was used to model the cyclone except the annulus region (intake). The annulus region at the top of the cyclone was modelled using the LBM [29]. The hybrid model used in Pirker [29] included the LES turbulence model in the LBM section and RSM in the NS section. The NS based FVM model, with the RSM, was used throughout the domain in a separate case to compare with the LBM. No details on solver setup were given for both the NS and hybrid model. The particles were modelled with a one-way coupling (momentum transfer from gas to particle but not particle to gas) LPT approach with no collisions. The momentum transfer from the gas to particle accounted for drag, gravitational and Saffman lift forces [29].

The hybrid model showed superior predictions to the NS based FVM relative to experimental data [29]. Thus, it may be of benefit to model an entire hydrocyclone using the LBM. This conclusion is inferred from the study by Pirker *et al.* [29] and was not made by the authors. According to Pirker *et al.* [29], the particles do not affect separation efficiency. The hybrid model predicts that the short-cut flow is dispersed into the main flow near the outer wall of the vortex finder by unsteady turbulent eddies whereas the NS model predicted a constant short-cut flow to the vortex finder [29]. The hybrid model was 15 times faster, in terms of run-time, than the NS model [29].

Both [28, 29] provide valuable insight into the applicability and benefits of the LBM over the NS based approach for gas cyclones. However, the air-core has a pivotal role in the physics and performance of hydrocyclones, in terms of pressure drop and separation efficiency [6]. Furthermore, neither [28, 29] incorporated the particles and subsequent interaction in the cyclone models. It is clear that the application of the LBM to modelling hydrocyclones would be of benefit given the superior predictions, in relation to the NS based approaches, using the LBM to model hydrocyclones as shown in the literature [28–30].

The LBM has not been applied to the modelling of air-core formation in hydrocyclones. Research has been done on interface tracking schemes using an LBM-VOF approach for metal foams and gases [64–66]. Furthermore, multi-component multiphase (MCMP) models [24, 25] have the potential for

application to air-core formation modelling. The LBM-VOF approach as in [64–66] may be a good starting point for air-core modelling because it does not suffer from the larger computational cost as the MCMP models do.

2.4 Advances in Particle Interaction Modelling

Fluid-solid flows have been modelled in the past using two approaches namely the LPT and Eulerian granular models [11, 13]. Systems with low volume fraction of solids ($< 10\%$) were modelled using the LPT approach which does not consider particle-particles collisions and models particle-wall collisions using a reflection condition at the wall [13]. The Eulerian granular model is used to model systems with a high volume fraction of solids ($> 10\%$). In the Eulerian granular model the fluid(s) and solids are modelled as separate interpenetrating continua [11, 13, 15]. Particle-particle interactions are accounted for via granular interaction terms, derived from the kinetic theory of granular material, such as solids pressure, solids shear stress, bulk viscosity, frictional viscosity and the granular temperature [11, 13, 15].

The DEM overcomes the major shortfall of the LPT model by incorporating particle-particle and particle-wall collisions in granular assemblies [67]. DEM was originally used exclusively in bulk material handling applications [11]. DEM has been increasingly coupled, successfully, with CFD codes to model systems such as gas-solid cyclones, hydrocyclones, DMC's, fluidised beds, downers and slurry flow in pipes [2, 3, 11, 12, 22, 31, 47].

Initially CFD-DEM coupling was, and in many cases still is, done via coupling a pure CFD code with a pure DEM code or coding the DEM collisions into the pure CFD code via user-defined functions [2, 3, 12, 22, 47]. The growth of the use of CFD-DEM coupling has led to major CFD code developers such as ANSYS to incorporate DEM couplings directly into the CFD code [13, 14]. Based on the increased use of CFD-DEM as evidenced by the literature, CFD-DEM can be considered as the standard for modelling systems with low solids volume fraction ($< 10\%$) whereby particle-particle interactions become significant due to a rise in solids volume fraction in parts of the system [2, 3, 11, 12, 22, 31, 47].

Due to the progress made in CFD-DEM coupling, which was initially done using an NS based CFD approach [2, 3, 11, 12, 22, 31, 47], LBM-DEM coupling

has been used, as can now be seen, in the literature [68]. Third and Müller used both the LBM-DEM and NS based CFD-DEM to model a gas fluidised bed. The LBM-DEM showed close agreement with the Ergun equation and the NS based CFD-DEM in predicting the pressure drop across the bed [68]. At larger superficial gas velocities both models diverged significantly from the Ergun equation predictions. The literature on the application of Eulerian granular models illustrates the potential of an Eulerian granular model to overcome the issues experienced in modelling fluid-granular systems using the LBM-DEM and NS based CFD-DEM approaches [15, 43–45].

The major reason for the error in the LBM-DEM and NS based CFD-DEM is that the solids volume fraction is ignored [11, 13]². Neglecting solids volume fraction results in large modelling errors when the solids volume fraction reaches the packing limit which commonly occurs in fluidised beds and in the cone and spigot in gas-solid cyclones, hydrocyclones and DMC's. The Eulerian granular model accounts for the solids volume fraction [13, 15]. However, the shortcoming of the Eulerian granular approach is that particles with different diameters have to be modelled as a separate phase [40, 62]. Thus, in the case of a hydrocyclone where there are n characteristic particle diameters a total of $n + 2$ phases have to be modelled - one phase for the water, one phase for the air and n phases for each characteristic particle diameter [13, 40, 62].

An Eulerian granular - LPT coupled model known as the dense discrete phase (DDP) model can be used to overcome this limitation. The DDP model uses the Eulerian model to model the fluid phases and the LPT model to account for the solids [13, 63]. Granular interactions are incorporated between the fluids and the particles as in the Eulerian granular model and DEM collision rules can be incorporate for particle-particle and particle-wall collisions [13, 63]. The DDP has not been used extensively to model systems such as hydrocyclones despite advice from CFD code developers [63] such as ANSYS recommending its' use for such applications.

Advances, beyond DEM and Eulerian granular models, in the application of the LBM to the modelling of gas-solid flows has been made [26, 27, 69–79]. The work of Ladd [73] and Ladd and Verberg [69] illustrated a significant advance in the modelling of fluid-particle systems by proposing a model to incorporate fluid-particle interactions using a combination of the LBM and

²Some DEM codes do account for solids volume fraction. These models can be classified as Dense Discrete Phase (DDPM) based models. Thus, for clarity in the thesis, DEM codes refer to models where the solids volume fraction is ignored and DDPM codes refer to models the wherein the solids volume fraction is accounted for.

an immersed (moving) boundary method (IBM) on the particle surface.

The LBM is used to model the fluid dynamics and a link-bounce-back boundary condition is placed on the surface of each particle [69, 70, 73, 74]. The particle surface is free to move within the fluid domain, thus, forming a moving boundary on the surface of each particle [69, 70, 73, 74]. The particle surface cuts the links between nodes on the fluid lattice forming new node points. The fluid particles interact with the new nodes (particle surface) via a bounce back condition at the new nodes, thus, affecting the fluid particles population density by a bounce back rule [69, 70, 73, 74].

Thus, the particle surface behaves in a similar way as a wall boundary in the LBM which results in a no-slip boundary condition. In this way the effective momentum exchange between the particles and the fluid is specified, thus, particle-fluid interaction is incorporated in the model [69, 70, 73, 74]. Similarly inter-particle interaction is specified via the effective momentum exchange at the boundary of the particles [69, 70, 73, 74].

The major advantage of this approach is that drag, lift, pressure gradient, virtual mass forces and the effect of turbulence (such as turbulent dispersion) on the particle(s) are resolved and not modelled. Ladd [73] and Ladd and Verberg [69] also outlined how the LBM can be used to account for thermal fluctuations which results in Brownian motion in colloidal suspensions. The approach outlined by Ladd [73] and Ladd and Verberg [69] has been used successfully to model sedimentation of particles at low Reynolds number ($0.025 < Re < 0.1$) [70], sedimentation in turbulent flows [27], creeping flow [74] and spherical particle motion in silicon oil [71].

This approach commonly known as the (immersed boundary) IB-LBM or LBM-IBM has the potential to produce the most accurate results of all the approaches. However, the major limitation of this approach is the large computational cost. Using this approach, less than one thousand particles at low Reynolds Number ($Re \approx 200$) requires months of run-time, per simulation, on a cluster of unspecified size [5, 27, 71, 74]. The computational cost is increased when DNS is used to resolve turbulence as opposed to a turbulence modelling approach such as LES [5].

Hydrocyclones have billions of particles in the system at any given time. Thus, this approach is not a feasible solution, with present hardware, for industry. Despite the computational requirement problem, this approach scales well on cluster environments [27]. Therefore, The IB-LBM approach


has been used to extract drag, lift, virtual mass laws and generalised understanding of the dynamics for single and multiple particle-fluid interactions and systems.

Graphics processing units (GPUs) provides an alternative to CPUs for solving complex numerical algorithms [33, 80, 81]. In many cases, particularly in the case of computational fluid dynamics, GPUs have surpassed CPUs in terms of scalability and computational efficiency [33, 80, 81]. As a result GPU processing has experienced increased integration in commercial CFD packages such as ANSYS Fluent [13, 14, 34].

The LBM has been ported to GPU architectures, using the nVIDIA CUDA framework, as presented in [33,81]. Habich [33] illustrated that the LBM running on all the CUDA cores of the GPU was one order of magnitude more efficient in terms of Mega Lattice-site-Updates per Second (MLUPS/MCUPS) than the CPU version of the program running on all eight threads on the CPU. Govender *et al.* [80] introduced a GPU based DEM code, named BLAZE-DEM, that simulates millions of polyhedral shaped particles whilst providing real time interactive visualisation of the results. Govender *et al.* [80] illustrated that the GPU implementation of the DEM provides linear scaling for millions (50 million) particles. Due to the results from [33, 80] an LBM-DEM approach may prove computationally efficient and a feasible solution to industry for hydrocyclone (and general process equipment) modelling. Furthermore, the IB-LBM may stand to benefit from GPU computing in terms of simulating millions of particles at high Reynolds Numbers, thus, making it a potential solution for modelling of process equipment.

Chapter 3

Coupled Navier-Stokes Based Computational Fluid Dynamics and Discrete Element Method Models



In this study two modelling approaches are used, namely the NS based FVM and the LBM. The NS based approach is the application of numerical methods to solve the NS equations which are the governing equations for fluid flow at a continuum level [10, 82]. The three most commonly used numerical methods are the Finite Difference Method (FDM), Finite Element Method (FEM) and the Finite Volume Method (FVM) [10, 13, 82–84].

The FVM is the most commonly used of the three. The CFD code used for the NS based modelling, in this study, is ANSYS Fluent 15.0 [34], which uses the FVM [13, 14]. Thus, the FVM will be discussed briefly in this chapter followed by a detailed description of the NS based Model with the coupled DEM model.

3.1 Overview of the Navier-Stokes based Finite Volume Method

The governing equations for fluid dynamics at a continuum level, in conservative form, are [10, 13, 82–84]:

$$\frac{\partial \rho}{\partial t} + \nabla \cdot (\rho \mathbf{u}) = 0 \quad (3.1)$$

$$\frac{\partial(\rho u)}{\partial t} + \nabla \cdot (\rho u \mathbf{u}) = -\frac{\partial p}{\partial x} + \nabla \cdot (\mu \nabla u) + B_x + S_{M_x} \quad (3.2)$$

$$\frac{\partial(\rho v)}{\partial t} + \nabla \cdot (\rho v \mathbf{u}) = -\frac{\partial p}{\partial y} + \nabla \cdot (\mu \nabla v) + B_y + S_{M_y} \quad (3.3)$$

$$\frac{\partial(\rho w)}{\partial t} + \nabla \cdot (\rho w \mathbf{u}) = -\frac{\partial p}{\partial z} + \nabla \cdot (\mu \nabla w) + B_z + S_{M_z} \quad (3.4)$$

Equation 3.1 is the equation for conservation of mass otherwise known as the continuity equation. Equations 3.2, 3.3 and 3.4 are the conservation equations for x , y and z momentum, collectively known as the Navier - Stokes equations.

Equations 3.1 to 3.4 can be re-written in the form of a generalised scalar transport equation for the general transport variable named ϕ [10, 13, 82–84]:

$$\frac{\partial(\rho \phi)}{\partial t} + \nabla \cdot (\rho \phi \mathbf{u}) = \nabla \cdot (\Gamma \nabla \phi) + S_\phi \quad (3.5)$$

Integrating Equation 3.5 and using Gauss's Divergence Theorem produces [10, 13, 82–84]:

$$\int_V \frac{\partial(\rho\phi)}{\partial t} dV + \oint \rho\phi\mathbf{u}.d\mathbf{A} = \oint \Gamma\nabla\phi.d\mathbf{A} + \int_V S_\phi \quad (3.6)$$

The FVM entails discretising the computational domain into cells (control volumes) [10, 13, 82–84]. Equation 3.6 is then discretised for each cell which produces [10, 13, 82–84]:

$$\frac{\partial(\rho\phi)}{\partial t} V + \sum_f^{N_{faces}} \rho_f\phi_f\mathbf{u}_f.\mathbf{A}_f = \sum_f^{N_{faces}} \Gamma_f\nabla\phi_f.\mathbf{A}_f + S_\phi V \quad (3.7)$$

The above equation is written for each cell in the computational domain, for each transport variable ϕ [10, 13, 82–84]. The resulting equations are solved for all the transport variables ϕ at the cell center for all cells [10, 13, 82–84]. Thus, providing an approximate solution for the given problem [10, 13, 82–84].

3.2 Model Geometry and Mesh

An isometric view of the hydrocyclone geometry (CFD domain) is shown in Figure 3.1. The hydrocyclone is a VV100 (100mm barrel diameter) hydrocyclone from Multotec Pty Ltd. The salient dimensions of the hydrocyclone are given in Table 3.1.

The mesh in all regions of the domain was constructed using the sweep and multizone meshing schemes resulting in a full hexahedral mesh as seen in Figure 3.2. The initial cell size was 5mm. The cell size was successively halved (to 2.5mm and 1.25mm) for the mesh sensitivity study. Full details of the mesh sensitivity study are given in Chapter 6.

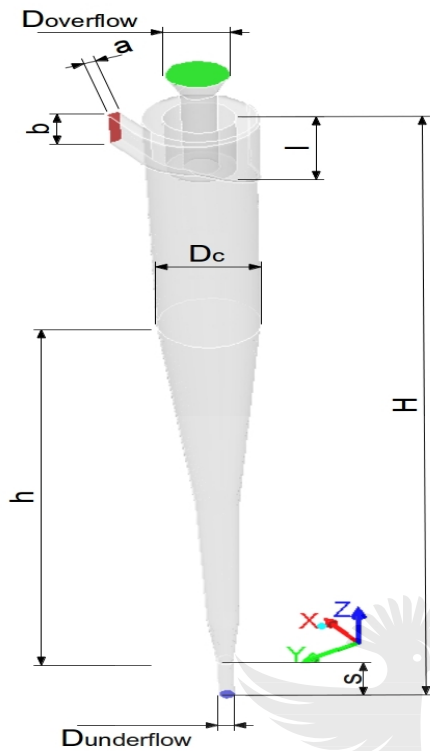


Figure 3.1: Hydrocyclone geometry

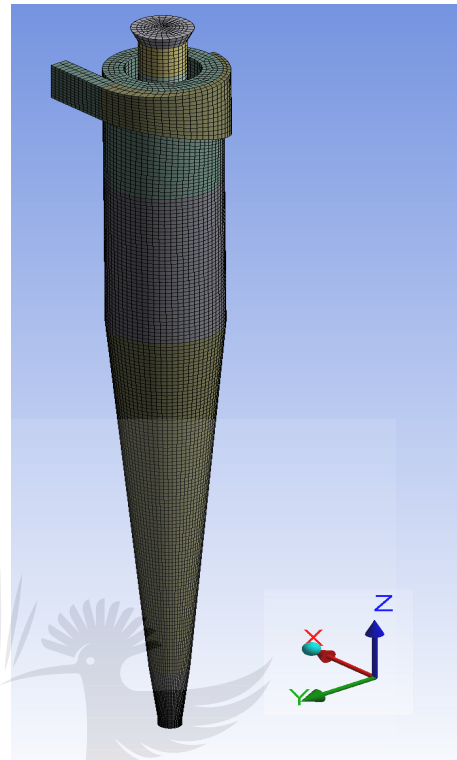


Figure 3.2: Computational grid (mesh)

Table 3.1: VV100 Hydrocyclone dimensions

D_c (mm)	H (mm)	D_{overflow} (mm)	$D_{\text{underflow}}$ (mm)	h (mm)	l (mm)	s (mm)	a (mm)	b (mm)
100	762	74	20	482	129	80	13	45

3.3 Governing Equations

3.3.1 Conservation of Mass, Conservation of Momentum and Turbulence

The governing equations for fluid flow are given by the continuity equation and the Navier - Stokes equations, namely equations 3.1 - 3.4. Turbulence is accounted for in this study using two classes of models, namely the Reynolds

Averaged Navier-Stokes (RANS) and LES.

In the case of the RANS approach the instantaneous velocities and pressure can be written as a superposition of the mean flow and turbulent fluctuating components [10, 13, 82–84]. Thus:

$$u_i = \bar{u}_i + u'_i \text{ and } p = \bar{p} + p'. \quad (3.8)$$

Using Reynolds Averaging of the instantaneous velocities and pressure, and considering an incompressible flow, Equations 3.1 - 3.4 are transformed into the RANS equations. Therefore, the continuity and RANS equations for incompressible flow are given by Equations 3.9 and 3.10, respectively [10, 13, 82–85].

$$\frac{\partial}{\partial x_i}(\bar{u}_i) = 0 \quad (3.9)$$

$$\rho \frac{\partial \bar{u}_i}{\partial t} + \rho \frac{\partial}{\partial x_j}(\bar{u}_i \bar{u}_j) = -\frac{\partial \bar{p}}{\partial x_i} + \frac{\partial}{\partial x_j} \left(\mu \frac{\partial \bar{u}_i}{\partial x_j} \right) - B_i - \rho \frac{\partial}{\partial x_i}(\overline{u'_i u'_j}) + S_M \quad (3.10)$$

for $i, j, k = x, y, z$. Equations 3.9 - 3.10 also includes the assumption of iso-thermal incompressible flow as is the specific case in the analysis of a hydrocyclone.

The turbulence models used, to provide closure to the RANS equations, were the RNG $k-\epsilon$ model and the RSM. For the LES approach the static Smagorinsky LES model was used. A turbulence sensitivity study, as presented in Chapter 6, was done to determine which was the most accurate turbulence model in relation to the experimental results.

3.3.1.1 Renormalization Group-Theory $k - \epsilon$ Model

According to Bakker [86], the RSM is unstable, therefore, it is advisable to provide a stable initial solution using a $k - \epsilon$ class model. The RNG $k - \epsilon$ model was used for this purpose as it generally provides more accurate predictions for highly swirling flows than the standard and realizable $k - \epsilon$ model [13, 86]. Furthermore, Bhaskar *et al.* [20] demonstrated that the RNG $k - \epsilon$ model is between 5 - 10% more accurate than the other $k - \epsilon$ models in hydrocyclone modelling.

The RNG $k - \epsilon$ model is a two equation model that solves for the turbulence kinetic energy (k) and turbulence dissipation rate (ϵ) and uses the Boussinesq hypothesis to calculate the Reynolds Stresses [13, 87]. The RNG $k - \epsilon$ model was used to provide a stable solution that can be used as an initial solution for the RSM. The transport equations for k and ϵ , for incompressible flow, are as follows, respectively [13]:

$$\rho \frac{\partial k}{\partial t} + \rho \nabla \cdot (k \mathbf{u}) = \nabla \cdot (\alpha_k \mu_{eff} \nabla k) + G_k + G_b - \rho \epsilon - Y_M + S_k \quad (3.11)$$

$$\rho \frac{\partial \epsilon}{\partial t} + \rho \nabla \cdot (\epsilon \mathbf{u}) = \nabla \cdot (\alpha_\epsilon \mu_{eff} \nabla \epsilon) + C_{1\epsilon} \frac{\epsilon}{k} (G_k + C_{3\epsilon} G_b) - C_{2\epsilon} \rho \frac{\epsilon^2}{k} - R_\epsilon + S_\epsilon \quad (3.12)$$

The formulae for the additional terms are given in [13]. They are not presented here because of full description would be lengthy. The effective viscosity and turbulent viscosity was solved using the differential equation for turbulent viscosity as opposed to using the empirically-determined value for the standard $k - \epsilon$ model. The RNG $k - \epsilon$ swirl modification as incorporated in ANSYS Fluent 16.0 [34] was used to further improve the model predictions.

The RNG $k - \epsilon$ model uses the Boussinesq hypothesis to calculate the Reynolds Stresses [13, 86]. Using this approach the Reynolds Stresses can be computed, upon solving 3.11 and 3.12, using [13, 86]:

$$-\rho(\overline{u'_i u'_j}) = \mu_t \left(\frac{\partial \overline{u_i}}{\partial x_j} + \frac{\partial \overline{u_j}}{\partial x_i} \right) - \frac{2}{3} \left(\rho k + \mu_t \frac{\partial \overline{u_k}}{\partial x_k} \right) \delta_{ij} \quad (3.13)$$

for $i, j, k = 1, 2, 3$ where the subscripts 1, 2, and 3 represent the $x, y,$ and z components respectively. δ_{ij} is the Kronecker Delta and is given by [13]:

$$\delta_{ij} = \begin{cases} 1 & i = j \\ 0 & i \neq j \end{cases} \quad (3.14)$$

3.3.1.2 Reynolds Stress Model

The RSM is a seven equation model, for three dimensional systems, and is made up of the transport equations for k and the six Reynolds Stresses [13,86,87]. The seven transport equations, in the case of incompressible flow are given by [13,86,87]:

$$\rho \frac{\partial k}{\partial t} + \rho \nabla \cdot (k \mathbf{u}) = \nabla \cdot \left(\mu + \frac{\mu_t}{\sigma_k} \nabla k \right) + \frac{1}{2} (P_{ii} + G_{ii}) - \rho \epsilon (1 + 2M_t^2) + S_k \quad (3.15)$$

$$\rho \frac{\partial \overline{u'_i u'_j}}{\partial t} + C_{ij} = D_{T,ij} + D_{L,ij} - P_{ij} - G_{ij} + \phi_{ij} - \epsilon_{ij} - F_{ij} + S_{\rho \overline{u'_i u'_j}} \quad (3.16)$$

The terms $C_{ij}, D_{T,ij}, D_{L,ij}, P_{ij}, G_{ij}, \phi_{ij}, \epsilon_{ij}, F_{ij}$ and $S_{\rho \overline{u'_i u'_j}}$ represent transport of the Reynolds Stresses by: convection, turbulent diffusion, molecular diffusion, stress production, buoyancy production, pressure strain, dissipation, production by system rotation and sources [13,86,87]. In ANSYS Fluent the terms $C_{ij}, D_{L,ij}, P_{ij}$ and F_{ij} are solved directly [13]. The formulae for the additional terms are not presented here due to their length but can be found in [13,86,87].

The Buoyancy term is zero ($G_{ij} = 0$) in the case of the hydrocyclone because the assumption of iso-thermal flow is used. The terms $D_{T,ij}, \epsilon_{ij}$ and ϕ_{ij} are

modelled as opposed to being solved directly [13]. The Stress-Omega pressure strain term was employed due to its proven accuracy for highly swirling flows and flows over curved boundaries [13]. The formulae for the additional terms are not presented here due to their length but can be found in [13, 86, 87].

3.3.1.3 Large Eddy Simulation Model

The LES model uses a Favré filtered form of the continuity and NS equations as given by Equations 3.17 and 3.18 [13, 86, 87]:

$$\frac{\partial}{\partial x_i}(\bar{u}_i) = 0 \quad (3.17)$$

$$\rho \frac{\partial \bar{u}_i}{\partial t} + \rho \frac{\partial}{\partial x_j}(\bar{u}_i \bar{u}_j) = -\frac{\partial \bar{p}}{\partial x_i} + \frac{\partial \tau_{ij}}{\partial x_j} + \frac{\partial \sigma_{ij}}{\partial x_j} - B_i + S_M \quad (3.18)$$

The stress tensor due to molecular viscosity is σ_{ij} and the filtered subgrid-scale (*SGS*) stress tensor is τ_{ij} . The stress tensor due to molecular viscosity is given by [13]:

$$\sigma_{ij} \equiv \left[\mu \left(\frac{\partial \bar{u}_i}{\partial \bar{x}_j} + \frac{\partial \bar{u}_j}{\partial \bar{x}_i} \right) \right] - \frac{2}{3} \mu \frac{\partial \bar{u}_l}{\partial \bar{x}_l} \delta_{ij} \quad (3.19)$$

and the filtered *SGS* stress tensor is given by [13, 88]:

$$\tau_{ij} \equiv \rho \overline{u_i u_j} - \rho \bar{u}_i \bar{u}_j \quad (3.20)$$

The filtered *SGS* is computed using a the Boussinesq hypothesis [13, 88]:

$$\tau_{ij} - \frac{1}{3}\tau_{kk}\delta_{ij} = -2\nu_t\mathbf{S}_{ij} \quad (3.21)$$

Using the Static Smagorinsky-Lilly Model, the eddy-viscosity is calculated using [13]:

$$\mu_t = \rho L_s^2 |\mathbf{S}| \quad (3.22)$$

where the magnitude of the rate-of-strain tensor is given by $|\mathbf{S}| \equiv \sqrt{2\mathbf{S}_{ij}\mathbf{S}_{ij}}$ and the mixing length $L_s = \min(\kappa d_w, C_s V_c^{1/3})$ [13]. κ is the von Kármán constant, d_w is the distance from the point in the flow field to the closest wall, C_s is the Smagorinsky constant and is taken as 0.14, and V_c is the volume of the computational cell [13].

In the case of the hydrocyclone there are no source terms for the turbulence equations thus they can be removed in all three turbulence models. Furthermore, the body force terms can be expressed as follows [13]:

$$\mathbf{B} = B_x \mathbf{x} + B_y \mathbf{y} + B_z \mathbf{z} \quad (3.23)$$

where $B_x = B_y = 0$ and $B_z = -\rho g$.

$$\therefore \mathbf{B} = B_z \mathbf{z} = -\rho g \mathbf{z} \quad (3.24)$$

3.3.2 Air-Core

For the RANS models a two step approach was used to generate the air-core. Each step was run until steady state was reached before proceeding to the

next step. The first step was to run the model using the RNG $k - \epsilon$ model. This provided a stable initial solution for the second step - running the model using the RSM. Once the air-core was fully formed and the model reached steady state the models were post-processed. The LES model only required a single step as the static Smagorinsky-Lilly LES model was stable.

The commonly accepted process, as per the literature [2, 3, 6–9], is to first model the water flow-field without the air-core. When the model reaches steady state, with a stable reverse flow at the outlet and a stable suction pressure distribution in the core of the hydrocyclone, the multiphase model is turned on to model the air-core [2, 3, 6–9]. When this two step approach was tested in this study, the air-core did not always form and in many cases produced computationally diverged solutions.

Thus, a different approach was developed in this study. In this study, all the models were setup with the multiphase model for the air-core from the outset. The models were initialised with $\alpha_{air} = 1$ to model the real-world case of a hydrocyclone filled with air. The model was then run till steady state. This produced the realistic transient phenomena of air-core formation, which is not seen in the literature. This single step process ensured that the air-core formed in every model without the divergent behaviour observed when using the two-step process as used in [2, 3, 6–9]. The reason for the difference in the predictions between the two step process from the literature and the single step process proposed in this study is that the single step, as observed from experiment in Chapter 5, is a more realistic approximation of air-core formation than the two step process. A detailed explanation of this difference is given in Section 5.5 in Chapter 5.

The air-core was modelled using different modelling approaches. The study compared predictions of the mixture, algebraic slip, VOF, Eulerian-Eulerian multiphase and Eulerian-Eulerian VOF models for air-core formation. The results from the study are presented in Chapter 6.

3.3.2.1 Volume-of-Fluid Model

The VOF multiphase model was used, as in [2, 3, 6–9]. However, the transient coupled solver was used as opposed to the segregated solver used in [2, 3, 6–9].

The VOF model assumes that the different phases are not interpenetrating

continua, thus, only the interface between the phases is tracked [13]. Due to this assumption the continuity and momentum equations are solved for the mixture as opposed to each phase [13]. The flow field for the water-air mixture is described by the continuity equation and the NS equations (Equations 3.9 - 3.10 for RANS and Equations 3.17 - 3.18 for LES) for incompressible flow with gravity as the only body force ($B_x = 0$, $B_y = 0$, $B_z = -\rho g$).

An additional transport equation for the volume fraction for the air phase is solved. The transport equation for the volume fraction, without source terms or mass transfer terms, is as follows [13]:

$$\frac{\partial}{\partial t}(\alpha_{air}\rho_{air}) + \nabla \cdot (\alpha_{air}\rho_{air}\mathbf{u}_{air}) = 0 \quad (3.25)$$

The volume fraction for the water phase is determined from $\alpha_{air} + \alpha_w = 1$ [13]. Cells with $\alpha_{air} = 1$ and $\alpha_w = 0$ are completely occupied by air and water, respectively. If $0 < \alpha_{air} < 1$ then the cell is part of the interface between the water and the air-core [13]. The density in cells with only water or only air is ρ_w or ρ_{air} . The density for the interface cells is a volume-fraction-averaged density and is determined from Equation 3.26 [13]:

$$\rho = \alpha_{air}\rho_{air} + \alpha_w\rho_w \quad (3.26)$$

An interface reconstruction step is applied to all the cells in the vicinity of the interface [13]. The interface reconstruction is an interpolation of the interface shape in the region of the cells that lie near the interface [13]. ANSYS Fluent applies the same order of interpolation as the discretisation used for the other volume fraction equation [13].

A side study, reported in [61], was conducted to determine the effect of changing surface tension when using either hydrophilic or hydrophobic particles. The results of this study are presented in Appendix B. The study shows that there is a noticeable difference in hydrocyclone performance when using hydrophilic or hydrophobic particles, thus, the surface tension coefficient must be specified based on the wettability of the particle type.

Table 3.2: Fluid properties

Fluid	ρ (kg/m ³)	μ (kg/(m.s))
Air	0.964	1.7894(10 ⁻⁵)
Water	1000	1.003(10 ⁻³)

Surface tension was incorporated using the Continuum Surface Stress (CSS) model. The CSS model was used as opposed to the Continuum Surface Force (CSF) model due to the improved accuracy of the CSS model in curved regions [13]. A surface tension force (F_{CSS}) is calculated and added to Equation 3.10 (or 3.18) as a source term (S_M) [13]. Thus:

$$S_M = F_{CSS} = \nabla \cdot (T) \quad (3.27)$$

and

$$T = \sigma \left[|\nabla \alpha| I - \frac{\nabla \alpha \otimes \nabla \alpha}{|\nabla \alpha|} \right] \quad (3.28)$$

The surface tension coefficient was set at $\sigma = 0.073\text{N/m}$. The density and viscosity, specified in the model, for the water and air are given in Table 3.2. Under the assumption of constant surface tension coefficient, as in the model used in this study, the surface tension force is given by Equation 3.29:

$$F_{CSS} = \sigma \nabla \cdot \left(|\nabla \alpha| I - \frac{\nabla \alpha \otimes \nabla \alpha}{|\nabla \alpha|} \right) \quad (3.29)$$

Wall adhesion was added to the model using the option in ANSYS Fluent 16.0. The contact angle was set as a default 90°. The contact angle is used

to modify the surface normal in near wall cells, thus, adjusting the near wall surface curvature [13]. The adjusted local curvature adjusts the body force term when calculating the surface tension [13]. The surface normal is adjusted as per Equation 3.30 [13]:

$$\hat{n} = \hat{n}_w \cos\theta_w + \hat{t}_w \sin\theta_w = \hat{n}_w \cos(90^\circ) + \hat{t}_w \sin(90^\circ) = \hat{t}_w. \quad (3.30)$$

where $\bar{n} = \nabla\alpha$ and $\hat{n} = \bar{n}/|\bar{n}|$ [13].

3.3.2.2 Algebraic Slip Mixture Model

Just as in the case of the VOF model, an assumption of non-interpenetrating continua is used in the mixture model [13]. The ASM model differs from the VOF model in three respects. The first difference is that the mixture model accounts for the relative (slip) velocity between the two phases. The slip velocity is given via the algebraic Manninen et al. model as per [13]:

$$\mathbf{v}_{pq} = \frac{\tau_p}{f_{drag}} \frac{(\rho_{air} - \rho_m)}{\rho_p} \mathbf{a} \quad (3.31)$$

The mixture density (ρ_m) is calculated using Equation 3.26. The Particle relaxation time (τ_p) (for air) and the acceleration (\bar{a}) is given by Equations 3.31 and 3.33, respectively [13]:

$$\tau_p = \frac{\rho_p d_p^2}{18\mu_q} \quad (3.32)$$

$$\mathbf{a} = \mathbf{g} - (\mathbf{u}_m \cdot \nabla) \mathbf{u}_m - \frac{\partial \mathbf{u}_m}{\partial t} \quad (3.33)$$

The mass averaged mixture velocity (\mathbf{u}_m) and the drift velocity ($\mathbf{u}_{dr,air}$) are calculated using Equations 3.34 and 3.35, respectively [13]:

$$\mathbf{v}_m = \frac{\alpha_{air}\rho_{air}\mathbf{u}_{air} + \alpha_w\rho_w\mathbf{u}_w}{\rho_m} \quad (3.34)$$

$$\mathbf{u}_{dr,air} = \mathbf{u}_{air} - \mathbf{u}_m \quad (3.35)$$

In the mixture model, the momentum and continuity equations are solved using the mixture density, viscosity and mass averaged mixture velocity [13]. The individual phase properties are volume weighted [13]. Just as in the VOF model an additional transport equation is solved for the secondary phase (air) volume fraction [13]. However, a different form of the volume fraction transport equation, from the one used for the VOF (Equation 3.25), is used in the mixture model and is given by [13]:

$$\frac{\partial}{\partial t}(\alpha_{air}\rho_{air}) + \nabla \cdot (\alpha_{air}\rho_{air}\mathbf{u}_m) = -\nabla \cdot (\alpha_{air}\rho_{air}\mathbf{u}_{dr,air}) \quad (3.36)$$

The momentum source term for the mixture model is given by Equation 3.37 [13]:

$$S_M = \alpha_{air}\rho_{air}\mathbf{u}_{dr,air}\mathbf{u}_{dr,air} \quad (3.37)$$

The second difference is that the effect of drag between the phases is accounted for by the incorporation of the drag function (f_{drag}) in the slip velocity (Equation 3.31). The drag function is obtained from the drag law. For this study the symmetric drag law was used. According to ANSYS [13], the symmetric drag law provides the best predictions when the secondary phase becomes the primary phase in certain regions in the domain. This is the case in a hydrocyclone because the air, which is the secondary phase, becomes the primary phase in the air-core. As per the symmetric drag law, the drag function is given by:

$$f_{drag} = \frac{C_D Re_m}{24} \quad (3.38)$$

The mixture Reynolds Number is ($Re_m = (\rho_m |\mathbf{v}_{pq}| d_p) / \mu_m$). The mixture viscosity (μ_m) is calculated in the same way as the mixture density. The drag coefficient is given by [13]:

$$C_D = \begin{cases} 24(1 + 0.15Re_m^{0.687}) & Re_m \leq 1000 \\ 0.44 & Re_m > 1000 \end{cases} \quad (3.39)$$

The third difference is that the secondary phase is modelled as particles with a diameter (arbitrarily chosen in this case as $d_p = 10^{-5}$ m). Surface tension is accounted for by specifying the surface tension coefficient. The pressure at the surface of the air bubble is given by well known expression:

$$p = \frac{4\sigma}{d_p/2} \quad (3.40)$$

Wall adhesion is not accounted for in the ASM model in ANSYS Fluent.

3.3.2.3 Eulerian-Eulerian Model

The Eulerian-Eulerian multiphase model is a true multiphase model in the sense that the different phases are modelled as separate interpenetrating continua, albeit they do share a single pressure [13]. Due to the above, the continuity and momentum equations are solved for each phase. The advantage of the Eulerian-Eulerian multiphase model is that the phases each have their own velocity field [13]. Furthermore, due to the DDP model compatibility the Eulerian model can account for the effect of the solids volume fraction on the liquid and gas phase in a hydrocyclone, which is not possible to account for in the VOF and Algebraic slip mixture models. The major drawback of the model is that, in ANSYS Fluent, the Eulerian model cannot be used with the LES model [14]. Thus, for the Eulerian Models only the RNG $k - \epsilon$ model and the RSM were used.

The Eulerian model uses the volume fraction equation used for the VOF (Equation 3.25) and calculates the volume of each phase using Equation 3.41:

$$V_q = \int_V \alpha_q dV \quad (3.41)$$

The effective density of each phase is given by Equation 3.26. The main differences between the Eulerian model and the VOF and the ASM models are that the momentum equations are solved for each phase as opposed to for the mixture and that the source terms in the momentum equation account for more interphase interactions [13].

The continuity and momentum equations for each phase is given as a “mass averaged” form of the continuity equation 3.9 and the momentum equations 3.10¹. Thus, the continuity and momentum equations are given as, respectively, [13]:

$$\nabla \cdot (\alpha_q \mathbf{u}_q) = 0 \quad (3.42)$$

$$\alpha_q \rho_q \frac{\partial \mathbf{u}_{q,i}}{\partial t} + \alpha_q \rho_q \nabla \cdot (\mathbf{u}_{q,i} \mathbf{u}_q) = -\alpha_q \nabla p + \nabla \cdot \bar{\bar{\tau}}_q - \alpha_q \rho_q \mathbf{g} + S_M \quad (3.43)$$

The phase shear stress-strain tensor ($\bar{\bar{\tau}}_q$) is calculated using the following formula [13]:

$$\bar{\bar{\tau}}_q = \alpha_q \mu_q (\nabla \mathbf{u}_q + \nabla \mathbf{u}_q^T) + \alpha_q \left(\lambda_q - \frac{2}{3} \mu_q \right) \nabla \cdot \mathbf{u}_q \bar{\bar{I}} \quad (3.44)$$

The momentum equation for each phase has the following source term [13]:

$$S_{M,q} = (\bar{F}_q + \bar{F}_{lift,q} + \bar{F}_{wl,q} + \bar{F}_{vm,q} + \bar{F}_{td,q}) + \sum_{p=1}^n \bar{R}_{pq} \quad (3.45)$$

¹It should be noted that the Eulerian model, as implemented in ANSYS Fluent, does not use the LES formulation and only allows for the RANS formulation.

Apart from gravity (already accounted for in Equation 3.43) there are no other body forces, thus, $(\bar{F}_q = 0)$. Due to instability inherent in the Eulerian model, particularly experienced in this study, the effects of lift $(\bar{F}_{lift,q})$, wall lubrication $(\bar{F}_{wl,q})$ and turbulence dispersion $(\bar{F}_{td,q})$ forces were neglected². Thus, $(\bar{F}_{lift,q} = 0)$, $(\bar{F}_{wl,q} = 0)$ and $(\bar{F}_{td,q} = 0)$. These forces are computationally expensive to include and contribute significantly towards causing convergence issues [13]. It should be noted that due to the nature of the physics of air-core formation these interactions should be accounted for. Thus, they will be included in future work that forms part of this long term project.

The secondary phase (air) has a much smaller density than the primary phase (water). Thus, the virtual mass force $(\bar{F}_{vm,q})$ must be accounted for [13]. The virtual mass force is calculated using the following equation [13]:

$$\bar{F}_{vm,q} = C_{vm} \alpha_p \rho_q \left[\left(\frac{\partial \mathbf{u}_q}{\partial t} + (\mathbf{u}_q \cdot \nabla) \mathbf{u}_q \right) - \left(\frac{\partial \mathbf{u}_p}{\partial t} + (\mathbf{u}_p \cdot \nabla) \mathbf{u}_p \right) \right] \quad (3.46)$$

where the virtual mass constant $C_{vm} = 0.5$. The drag force is included in the interphase momentum exchange $(\sum_{p=1}^n \bar{R}_{pq})$. The interphase momentum exchange is given by [13]:

$$\sum_{p=1}^n \bar{R}_{pq} = \sum_{p=1}^n K_{pq} (\mathbf{u}_q - \mathbf{u}_p) \quad (3.47)$$

The symmetric model was used to model the interphase momentum exchange coefficient (K_{pq}) and is given by [13]:

$$K_{pq} = \frac{\rho_{pq} f_{drag}}{6\tau_{pq}} d_p A_i \quad (3.48)$$

where τ_{pq} is calculated as per Equation 3.32 using the mixture properties.

²Turbulent dispersion was neglected in the LBM models as well because it was not included as an interaction in the NS models. It was neglected in the NS models because it cannot be included in the VOF model (due to incompatibility in the models) and it was neglected in the Eulerian model so as not to exacerbate the convergence issues in the Eulerian model. Due to its importance it should be included in future work.

The drag function and drag coefficient is calculated in the same way as the mixture model in this study. The interfacial area for the momentum exchange at the air-core interface is calculated using the symmetric model [13]:

$$A_i = \frac{6\alpha_p(1 - \alpha_p)}{d_p} \quad (3.49)$$

For the Eulerian model the turbulence equations can be solved for each phase, for the secondary (dispersed phase) or for the mixture [13]. For stability the mixture option was used in this study. Thus the Equations 3.11, 3.12 and 3.16 were solved using the mixture velocity, mixture density and mixture viscosity [13]. The mixture velocity, mixture density and mixture viscosity were calculated in the same way as in the ASM model [13].

3.3.2.4 Eulerian-Eulerian Multi-Fluid VOF Model

The multi-fluid VOF model provides the option to use the Eulerian model to overcome the shared velocity formulation of the VOF model [13]. This is done by including the discretisation schemes (interface tracking) from the VOF model to be used in conjunction with the Eulerian model [13]. In this study the Geo-Reconstruct interface tracking scheme was used, as was the case in the VOF model.

3.3.3 Particles

The particles are modelled using the discrete phase model (DPM), also known as the Lagrangian particle tracking (LPT) model [13]. The particles are modelled as spherical particles dispersed in the continuous phase(s) [13]. Newton's equations of motion are applied to each particle and particle's velocity fields and the trajectories are obtained from the integration of the equations of motion for the particles [13].

The equation of motion accounts for gravity, drag, pressure gradient and virtual mass effects and other source terms. The particle equation of motion is given as [13]:

$$m_p \frac{d\mathbf{u}_p}{dt} = \bar{F}_{drag} + \bar{F}_g + \bar{F}_{pressure} + \bar{F}_{vm} + \bar{F}_{other} \quad (3.50)$$

The drag, gravitational, pressure gradient and virtual mass force are given by Equation 3.51 [13]:

$$m_p \frac{d\mathbf{u}_p}{dt} = m_p \frac{18\mu C_D Re}{\rho_p d_p^2} (\mathbf{u} - \mathbf{u}_p) + m_p \frac{\mathbf{g}(\rho_p - \rho)}{\rho_p} + m_p C_{vm} \frac{\rho}{\rho_p} \left(\mathbf{u}_p \nabla \mathbf{u} - \frac{d\mathbf{u}_p}{dt} \right) + m_p \frac{\rho}{\rho_p} \mathbf{u}_p \nabla \mathbf{u} + \bar{F}_{other} \quad (3.51)$$

where C_D is as defined by the spherical drag law and is given as [13]:

$$C_D = \sum_{i=1}^3 \frac{a_i}{Re^{i-1}} \quad (3.52)$$

where the coefficients a_i are determined based on the Reynolds Number range as defined in [89]. The particle Reynolds Number is defined as $Re = \rho d_p |\mathbf{u}_p - \mathbf{u}| / \mu$. The drag force is independent of the (local) solids volume fraction.

ANSYS [13, 14] suggests the inclusion of the virtual mass and pressure gradients forces if $\rho/\rho_p > 0.1$. From the experimental tests as per Chapter 5 $\rho/\rho_p \approx 0.3$. Thus, these forces were added to the particle equation of motion. The virtual mass factor $C_{vm} = 0.5$ [13].

The dispersion of particles was accounted for using the stochastic tracking method. In this way the particle trajectories are calculated by using the instantaneous fluid velocities instead of the mean fluid velocities in the integration of the equation of Motion [13].

Two way coupling, between the continuous phase(s) and the particles was implemented. The effect of the fluid flow field is already accounted for in Equation 3.51 via the continuous phase(s) velocity and density. The effect of the particle momentum, as it passes through each control volume, on the

continuous phase(s) is added as a momentum source term in the momentum equations for the continuous phase(s). The momentum source term is given as [13]:

$$F = \sum \left(\frac{18\mu C_D Re}{\rho_p d_p^2} (\mathbf{u} - \mathbf{u}_p) + F_{other} \right) \dot{m}_p \Delta t \quad (3.53)$$

Particle-particle and particle-wall collisions are added using a DEM implementation in ANSYS Fluent 15.0. The forces generated via particle-particle and particle-wall collisions are added to the F_{other} term in Equation 3.51. The normal forces arising from the collisions are modelled as a spring-dashpot system and the tangential forces are modelled via a friction collision law [13].

The normal forces from a collision between arbitrary particle i and j is given Equations 3.54 and 3.55 [13,67]:

$$\bar{F}_{ij} = (K\delta + \gamma(\bar{v}_{ij} \cdot \bar{e}_{ij}))\bar{e}_{ij} \quad (3.54)$$

$$\bar{F}_{ij} = -\bar{F}_{ji} \quad (3.55)$$

The spring constant (K) is determined from Equation 3.56 [13]:

$$K = \frac{\pi |\bar{v}_{ij}|^2}{3\epsilon_D^2} d_p \quad (3.56)$$

The damping coefficient γ is given by 3.57 [13]:

$$\gamma = -2 \frac{m_{ij} \ln(\eta)}{t_{coll}} \quad (3.57)$$

where $\bar{v}_{ij} = \bar{v}_i - \bar{v}_j$ and $\bar{e}_{ij} = (\bar{x}_i - \bar{x}_j) / \|\bar{x}_i - \bar{x}_j\|$. The other parameters are calculated using Equations 3.58 - 3.60 [13]:

$$m_{ij} = \frac{m_i m_j}{m_i + m_j} \quad (3.58)$$

$$t_{coll} = f_{loss} \sqrt{\frac{m_{ij}}{K}} \quad (3.59)$$

$$f_{loss} = \sqrt{\pi^2 + ln^2(\eta)} \quad (3.60)$$

The tangential (friction) force is calculated from Equation 3.61 [13]:

$$\bar{F}_{friction} = \mu \bar{F}_{ij} \quad (3.61)$$

where μ is the friction coefficient between the two colliding particles. The particle-wall collisions are modelled in the same way as particle-particle collisions except that the wall has different material properties from the particle. This approach is congruent with the approach used in [2, 3] whereby the particle-wall collisions were modelled using the same collision laws for the particle-particle interactions. Particle rotation was neglected because it was neglected in the LBM model.

Chu *et al.* [2] and Chu *et al.* [3] used a different set of collision laws than the ones used in this study. Chu *et al.* [2] and Chu *et al.* [3] also included particle rotation in their models. A comparison of the DEM model used in this study and the one used in [2, 3] will be done as part of future work in this long term research project.

3.4 Boundary Conditions

The salient boundary conditions for the CFD model are detailed in Table 3.3. Atmospheric Pressure (P_a) is taken as $P_a = 82.5\text{kPa}$, which is realistic for Johannesburg. The mass flow rate and pressure values are based on the experimental data as presented in Chapter 5.

The inlet mass flow rate is a superposition of the water and particle mass flow rates at the inlet. The water mass fraction and particle mass fraction are 76.05% and 23.95%. In the literature [2, 6–9, 12] a velocity boundary is

Table 3.3: Flow Boundary conditions

Boundary Name	Boundary Type	Pressure (kPa)	α_{air}	\dot{m} (kg/s)	D_H (m)	I_{turb} (%)
Inlet	mass flow inlet	$P_a + 67.5$	0	6.875	0.02	8.86
Underflow	Pressure outlet	P_a	1 (backflow)	N/A	0.02	10
Overflow	Pressure outlet	P_a	1 (backflow)	N/A	0.075	10

often used to model the inlet. For incompressible flow the velocity and mass flow inlet boundary conditions are equivalent [13].

The particles were injected at the inlet via a surface injection with the injection direction set to face-normal. The particle mass flow rate was specified as the mass fraction of the total mass flow rate in Table 3.3. The particle velocity was set as the mean water inlet velocity (calculated from the water inlet mass flow rate). The particle size distribution (PSD) was specified at the inlet. The PSD was determined from the experimental data as presented in Chapter 5. The Rosin-Rammler distribution was used to model the PSD at the inlet³.

Initially the inlet was set as a particle escape zone. This led to the smaller particles escaping from the inlet just as they enter the domain due to particle-particle collisions. This led to unrealistic behaviour because the smaller particles eventually were not entering the domain for long enough to exit via the underflow or overflow. Thus, the inlet was set as a particle reflection zone to ensure that particles are not pushed out of the inlet due to particle-particle collisions. The particle collisions partner was set as the particle material. This was done to model particles, that are pushed to the inlet via downstream particle-particle collisions, being pushed back into the domain via upstream particle-particle collisions. The walls were set as a reflection zones for the particles. The particle collision partner was set as the wall material. All particle-particle and particle-wall collisions are governed by the DEM collision rules given in subsection 3.3.3 (Equations 3.54 - 3.61).

³The Rosin Rammler distribution with the parameters are given in Equation 5.8 and Table 5.12, respectively.

The outlets had a backflow volume fraction of air specified as per Table 3.3 to account for reverse flow of air due to the low pressure region formed at the outlets. The outlets were set as an escape zone for the particles. The particle size distributions (PSD's) were recorded at the outlets. A radial equilibrium pressure distribution is applied at the underflow and overflow to ensure an accurate calculation of the pressure distribution at the outlets. Thus, the gauge pressure ($p_{gauge} = 0\text{kPa}$) is applied at the centre of both the outlets. The static pressure on the rest of the boundary is calculated using [14]:

$$\frac{\partial p}{\partial r} = \frac{\rho v_{\theta}^2}{r} \quad (3.62)$$

The no-slip condition was specified, for the fluid, at the wall boundaries, therefore:

$$\mathbf{u}_{wall} = \mathbf{0} \quad (3.63)$$

The near wall velocity gradients were not resolved down to the wall. Instead, the wall function approach was used to capture the near wall gradients. The standard wall function was used. The formulae for the standard wall function are not presented here due to their length but can be found in [13].

3.5 Solver Setup

The ANSYS Fluent three-dimensional, unsteady, double precision solver was used for all models. The pressure based coupled solver was used. The discretisation scheme used for the momentum, energy, turbulent kinetic energy and Reynold stress equations was the Quadratic Upwind Interpolation for Convection Kinetics (QUICK) scheme, which is a third order accurate scheme [13,90]. The PREssure STaggering Option (PRESTO!) was used for the pressure discretisation scheme, which is used to calculate the staggered face pressure [13,90]. The volume fraction equation was discretised using the Geo-Reconstruct scheme, which is an interface reconstruction method which

uses geometrical information to track the inter-phase interface [13]. Gradient reconstruction was done using the least squares cell based method.

The implicit body force treatment was used for the VOF body force formulation. ANSYS [14] advises the use of the implicit body force treatment, when surface tension is included, for the VOF model. According to [14], this results in the accurate inclusion of the partial equilibrium of the pressure gradient and surface tension forces in the momentum equations, this in turn leads to improved convergence.

The under-relaxation factors were kept at their default settings as per [14]. The fixed time step size was varied for different cases as per Chapter 6. The time step size was chosen to ensure that the models converged in 5 - 15 iterations per time step. Larger time step sizes results in a *CFL* number greater than 0.7 which leads to instability and divergence. The transient formulation was bounded second order implicit.

The acceptable residual limits for continuity, x , y and z momentum, turbulent kinetic energy and Reynold stresses were $< 10^{-3}$ [13, 14]. Monitors for mass flow rate on the overflow and underflow were used to determine when steady state conditions were reached.

ANSYS Fluent allows steady and unsteady particle tracking in unsteady simulations [13]. The literature, such as [2, 3, 12], makes use of steady tracking. However, in this study the unsteady particle tracking approach was used. Originally the particles time step size was set to be equal to the fluid flow time step size. This caused instability and significant computational cost⁴. Thus, the particle time step size was set to be equal to 100 times the fluid flow time step size. Thus, particles were injected once every 100 fluid flow time steps. The particle step length factor and the maximum number of steps was set at the Fluent default. However, if the number of incomplete particle trajectories rises significantly, through the calculation, these values can be increased. The DPM source terms were updated every flow iteration. The implicit and trapezoidal integration schemes were used for the integration of the particles' equations of motion.

⁴A 500 000 cell model ran for 50 days on 120 cores with 150GB RAM to produce 4s flow time.

Chapter 4

Lattice Boltzmann Method Based Models

According to Guo and Shu [24], fluid dynamics can be modelled at three different scales, namely the molecular scale, the mesoscopic scale and the macroscopic scale. The molecular scale is modelled using microscopic models often referred to as molecular dynamics (MD) whereas the macroscopic scale is modelled using continuum models such as the Navier-Stokes equations [24, 25]. The mesoscopic scale is between the molecular and macroscopic scale and the models used to describe this scale are based on the kinetic theories [24, 25, 91].

The dynamics of fluid molecules are characterised by strong inhomogeneity and fluctuations whereas the macroscopically averaged dynamics of the fluid molecules is homogeneous and continuous [24]. In the case of MD models the dynamics (position, momentum and thermodynamic state) for each fluid molecule is tracked [24, 25]. In the case of the NS based model, the dynamics of the fluid is tracked by treating the fluid as a continuum [24, 25]. The mesoscopic models fall in between the MD and continuum models in the sense that it does consider the dynamics of the fluid molecules albeit at a “coarser” scale than MD and the macroscopic dynamics of the fluid is recovered through macroscopically averaging the microscopic dynamics of the fluid [5, 24, 25, 91].

The LBM falls in the class of mesoscopic models [5, 24, 25, 91]. The LBM offers an alternative CFD approach to the well known NS based approach [5, 91].

While the NS based approach to CFD is widely known and used in both the academic and industrial community, the LBM is primarily restricted to use in academia [91]. Despite its' relatively small presence in industry the LBM offers a different approach to CFD with significant advantages in modelling fluid dynamics phenomena [5, 24, 25]. The LBM is especially powerful in modelling multiphase flow which forms the majority of the complex problems encountered in chemical and process engineering applications [5, 91, 92].

4.1 Overview of the Lattice Boltzmann Method

The precursors to the LBM were lattice gas cellular automaton models (LGA) [24,25,91]. However, the LGA displays chaotic, aperiodic and noisy behaviour which leads to considerable difficulty in the modelling of fluid dynamics [25, 91]. The LBM was developed to overcome the issues of the LGA [91].

The continuous Boltzmann equation from kinetic theory describes the dynamics of the fluid molecules based on the evolution of the single particle distribution function $(f(\bar{r}, \bar{\xi}, t))$ [24, 25, 91]. Based on kinetic theory, the single particle distribution function contains the full information of the statistical distribution of a fluid [24, 91]. The Boltzmann equation is given as [24, 25, 91]:

$$\frac{\partial f(\bar{r}, \bar{\xi}, t)}{\partial t} + \xi \cdot \nabla f(\bar{r}, \bar{\xi}, t) + \mathbf{g} \cdot \nabla_{\xi} f(\bar{r}, \bar{\xi}, t) = \left(\frac{\partial f(\bar{r}, \bar{\xi}, t)}{\partial t} \right)_{collision} \quad (4.1)$$

This describes the dynamics of the single particle distribution function based on streaming (collisionless motion of fluid particles) and the collisions of particles [24, 25, 91]. The terms on the left hand side are the streaming terms and the term on the right is the collision dissipation term [24, 25, 91]. The collision dissipation term is a complex double integral and can be approximated using as:

$$\left(\frac{\partial f(\bar{r}, \bar{\xi}, t)}{\partial t} \right)_{collision} = -\frac{1}{\tau_*} (f(\bar{r}, \bar{\xi}, t) - f^{eq}) \quad (4.2)$$

where f^{eq} is the Maxwellian distribution function and τ is the relaxation time. The Maxwellian distribution function is the analytical solution to the Boltzmann equation for a single-component monatomic gas and it is given by [24, 25, 91]:

$$f^{eq} = \frac{\rho}{(2\pi R_g T)^{D/2}} \exp\left(-\frac{(\bar{\xi} - \mathbf{u})^2}{2R_g T}\right) \quad (4.3)$$

where D is the spatial dimension. By substituting Equations 4.2 and 4.3 into Equation 4.1, the Boltzmann-Bhatnagar-Gross-Krook (Boltzmann-BGK) equation is obtained:

$$\frac{\partial f(\bar{r}, \bar{\xi}, t)}{\partial t} + \xi \cdot \nabla f(\bar{r}, \bar{\xi}, t) + \mathbf{g} \cdot \nabla_{\xi} f(\bar{r}, \bar{\xi}, t) = -\frac{1}{\tau_*} (f(\bar{r}, \bar{\xi}, t) - f^{eq}) \quad (4.4)$$

In a similar fashion as the NS based FVM the Boltzmann-BGK equation is solved numerically. This is done by discretising the domain into regular lattices. A two-dimensional example of such a lattice is seen in Figure 4.1. Each lattice is denoted in the form $DnQm$, where n is the spatial dimension and m is the number of discrete lattice nodes/directions.

By discretising the domain into lattices as in Figure 4.1 the particles are limited to move in only the discrete lattice directions with the microscopic velocity ξ discretised into the set of discrete velocities $\bar{e} = \{\bar{e}_0, \bar{e}_2, \dots, \bar{e}_{m-1}\}$ [24, 25, 91, 92]. The discrete velocity set \bar{e} is defined based on the lattice dimension n and the number of discrete directions m [24, 25, 91, 92]. The discrete velocity \bar{e}_0 is at the centre of Figure 4.1 and it represents a stationary particle [24, 25, 91, 92].

The Boltzmann-BGK equation as given in Equation 4.4 is temporally discretised using either the FDM [24, 25, 91, 92] or in special cases the FVM [93, 94]. The discretised equations are solved for the updated single particle distribution functions at each lattice node [24, 25, 91–94].

The macroscopic fluid density on the lattice is the sum of the single particle distribution functions at the lattice nodes [25]:

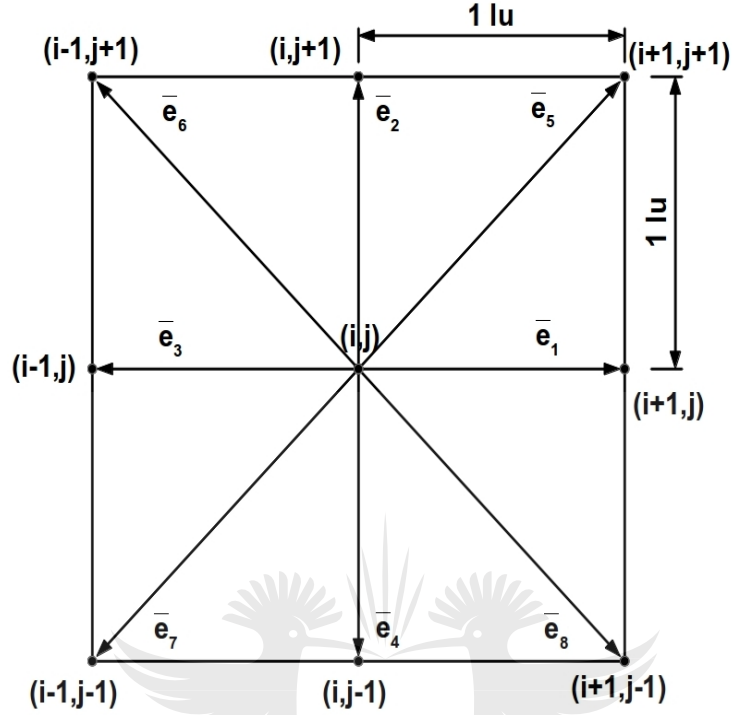


Figure 4.1: Two-dimensional lattice labelling and velocity vectors based on the D2Q9 lattice structure

$$\rho = \sum_{i=0}^{m-1} f_i \quad (4.5)$$

and the macroscopic fluid velocity on the lattice is the weighted average of the discrete velocity set with the single particle distribution functions as the weights [25]:

$$\mathbf{u} = \frac{1}{\rho} \sum_{i=0}^{m-1} f_i \bar{\mathbf{e}}_i \quad (4.6)$$

Via the Chapman-Enskog expansion the Boltzmann-BGK equation (Equation 4.4) as well Equations 4.5 and 4.6 simplifies to the NS equations [24]. The Chapman-Enskog expansion is a multiscale analysis that is implemented

by expanding each term in Equation 4.4 using zeroth, first and second order Taylor series expansions and substituting the resulting expansions into Equations 4.4, 4.5, 4.6. By simplifying the resultant equations, from the above expansions and substitutions, the NS equations are obtained [24, 25, 91, 92].

The maximum order of expansion is second order, thus, the LBM is regarded by researchers as a second-order scheme for solving the NS equations [24]. Others may argue that the NS equations are, thus, a second-order approximation of the Boltzmann equation for generalised fluid flow. The full Chapman-Enskog analysis is too lengthy to present here¹. It should be noted that the Maxwellian distribution function is applicable to single component monatomic gases which would imply that the LBM is only applicable to this class of gases [24, 25, 91, 92]. However, the Chapman-Enskog expansion recovers the NS equations from the Boltzmann equation. Thus, the LBM models general compressible and incompressible fluid behaviour [24, 25, 91, 92]².

4.2 Overview of Palabos

The LBM models were implemented in Palabos [35]. Palabos is an open-source LBM based CFD solver which uses the FDM. Palabos was originally developed as a research tool under the name OpenLB Project [95]. Palabos forked from the OpenLB Project to provide an open-source package with commercial support to cater for both the academic and industrial community. Palabos is maintained and developed under a joint venture, Flowkit Ltd., between the Federal Institute of Technology of Lausanne and the University of Geneva, Switzerland.

Unlike ANSYS Fluent, Palabos is not a Graphical User Interface (GUI) package. Instead Palabos is a c++ library. The user has to write end code in c++ using the Palabos library and functions to implement the model. Parallelisation is native via the distributed memory protocol Message Passing Interface (MPI) or the shared memory protocol OpenMP with MPI being the most used to ensure compatibility when running the code on a laptop or

¹The interested reader can refer to Guo and Shu [24] for the full Chapman-Enskog analysis.

²The above discussion is meant only as a brief introduction to the LBM. The interested reader can consult texts such as [5, 24, 25, 91–94], amongst others, for a detailed presentation of the LBM.

desktop and a cluster. Palabos runs natively on UNIX environments but can be used under a Windows environment.

Pre-processing is described in the next section. It should be noted that the user can hard-code the domain geometry in the end code as opposed to the STL specification method outlined in detail in the next section. The end code is setup by the user to output the data in Visualization Toolkit Image Data (VTI)/ Visualization Toolkit Data (VTK) files as well as Comma Separated Variables (CSV) files as per the user requirements. Post-processing (visualisation) of the VTI/VTK files is done using the open-source package Paraview [96] or equivalent packages.

4.3 LBM Model Geometry and Domain Vox- elisation

The LBM models were implemented using the Palabos open-source libraries [35]. Palabos does not have a dedicated pre-processor for geometry creation and voxelisation (the LBM equivalent of meshing). Thus, three separate codes were used to generate the geometry and voxelise the computational domain. The first step was to export the geometry created in the ANSYS Fluent pre-processor (DesignModeller) as an initial graphics exchange specification (IGES) file. The IGES file was imported into Solidworks [97] and converted to a stereo-lithography (STL) file as seen in Figure 4.2.

The STL file contains a triangular mesh representation of the surface of the hydrocyclone including the inlet and outlets. Palabos requires that the STL file have holes instead of surfaces for the inlet and outlets. Thus, MeshLab [98] was used to create holes (open faces) in the place of the inlet and outlets. MeshLab was also used to check for any non-manifold faces or vertices in the STL file as well as to repair any holes created by the STL export from Solidworks.

A bounding box, as seen in Figure 4.2, was created around the STL file to specify the computational domain. This operation along with the domain

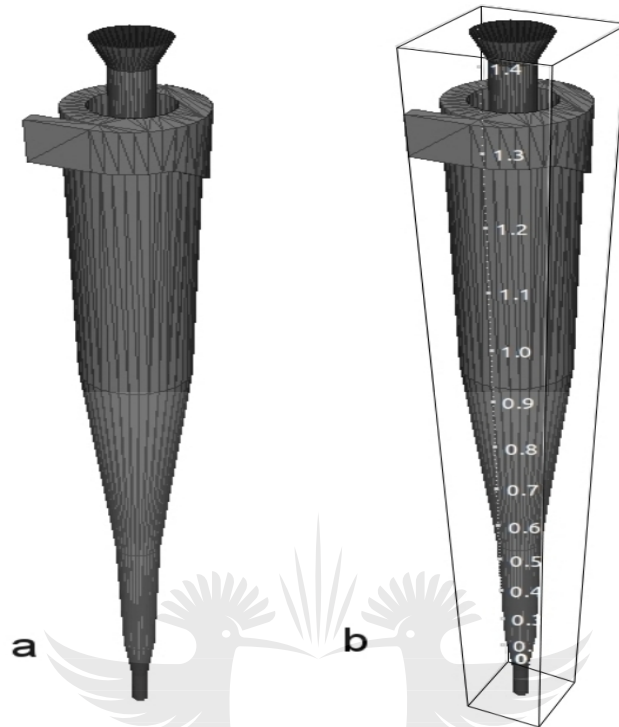


Figure 4.2: Wall surface and domain construction via STL - a) hydrocyclone and b) bounding box around the hydrocyclone

voxelisation is done using Palabos. These steps are done as part of the simulation by specifying the x , y and z resolution (grid spacing) which creates a voxelised domain within the bounding box.

The sectioned voxelised domain is shown in Figure 4.3. Each cubic voxel (cell) in Figure 4.3 is a lattice that is connected to each neighbouring lattice. Figure 4.3 was generated using Paraview [96]. The STL file is used by Palabos to define the domain, wall boundaries as well as the inlet and outlets.

The LBM does not make use of body-fitted meshes (grids) as in the NS based FVM. Instead the LBM makes use of Cartesian meshes (grids), which results in stair-stepped curved walls. Thus, some voxels (cells) lie inside the domain, outside the domain and some voxels have the walls of the domain inside the respective voxel. Thus, the voxels in the bounding box are tagged as either fluid voxels (cells within the hydrocyclone), inner border voxels (cells on the fluid side of the wall), outer border voxels (cells on the non-fluid

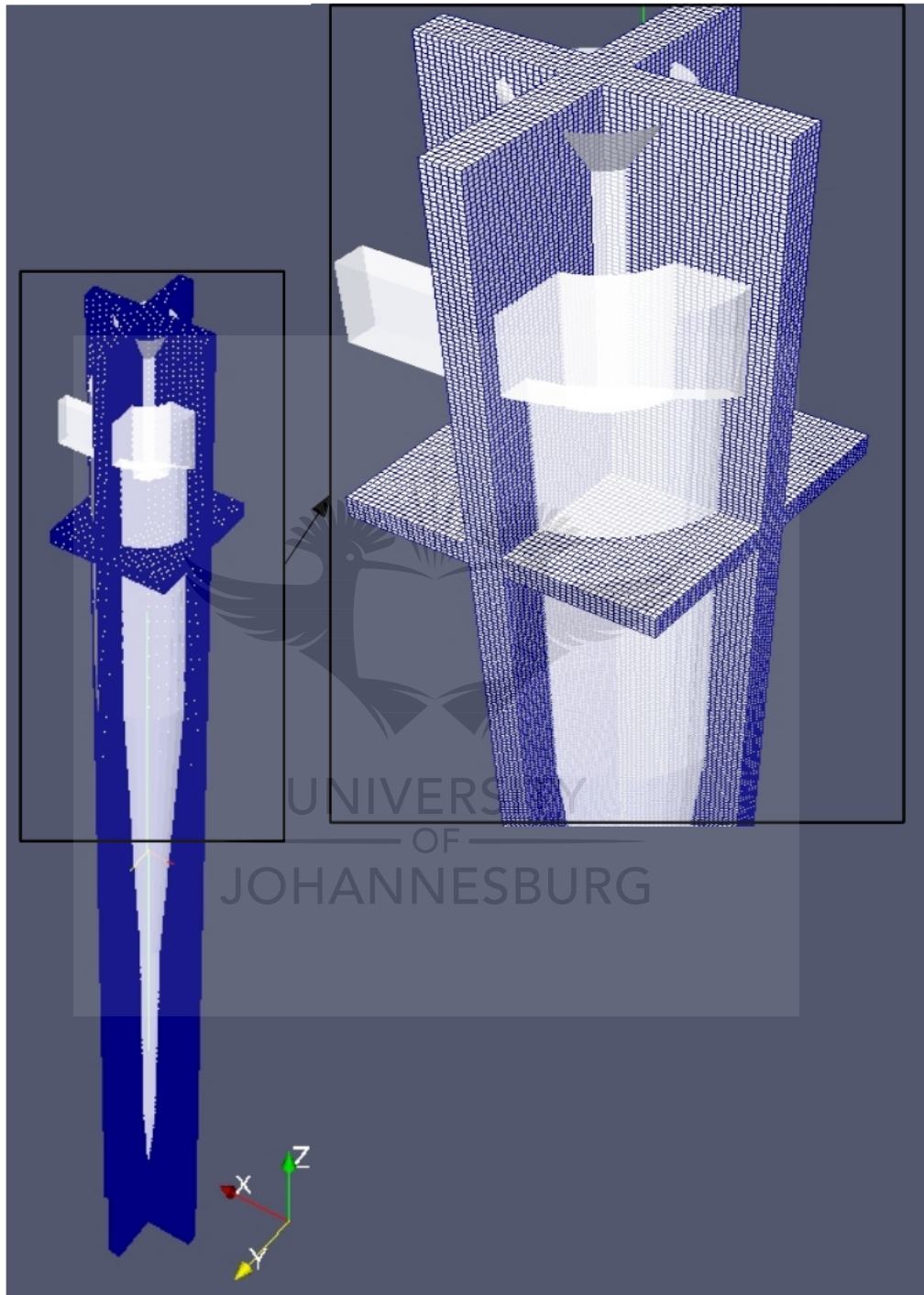


Figure 4.3: Section of the voxelised domain

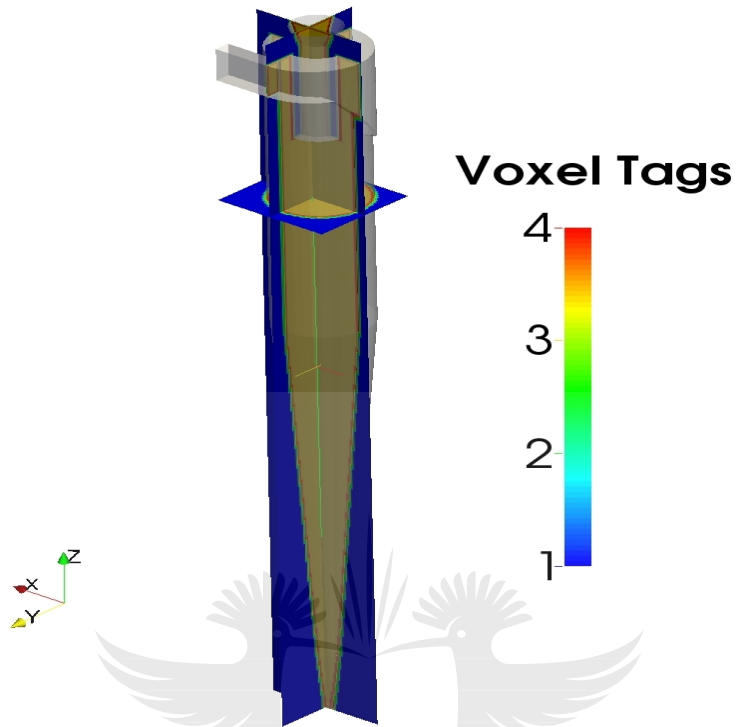


Figure 4.4: Cell Tagging

side of the wall) and outer voxels (cells on the outside of the hydrocyclone). These tagged voxels are shown in Figure 4.4. The tag numbers in Figure 4.4 relate to voxel types with the voxel tags 1 corresponding to outer voxels, 2 corresponding to outer-border voxels, 3 corresponding to inner border voxels and 4 corresponding to fluid voxels. These voxel tags are used to assign different dynamics to each voxel group.

4.4 LBM Governing Equations

The single relaxation time (SRT) - BGK LBM model is used. This is commonly referred to as the BGK-LBM. Thus, the Boltzmann equation is given as [5, 24, 25, 91, 92]:

$$\frac{\partial f(\bar{r}, \bar{\xi}, t)}{\partial t} + \xi \cdot \nabla f(\bar{r}, \bar{\xi}, t) + \mathbf{g} \cdot \nabla_{\xi} f(\bar{r}, \bar{\xi}, t) = -\frac{1}{\tau_*} (f(\bar{r}, \bar{\xi}, t) - f^{eq}) \quad (4.7)$$

Dropping the external force term in Equation 4.7 results in:

$$\frac{\partial f(\bar{r}, \bar{\xi}, t)}{\partial t} + \xi \cdot \nabla f(\bar{r}, \bar{\xi}, t) = -\frac{1}{\tau_*} (f(\bar{r}, \bar{\xi}, t) - f^{eq}) \quad (4.8)$$

The equilibrium distribution function is given by the Maxwellian distribution function as shown in Equation 4.3 [99]. In the LBM the truncated Taylor expansion of the Maxwellian distribution function is used:

$$f^{eq} = w_i \rho \left[1 + \frac{\mathbf{c}_i \cdot \mathbf{u}}{c_s^2} + \frac{(\mathbf{c}_i \cdot \mathbf{u})^2}{2c_s^4} - \frac{u^2}{2c_s^2} \right] \quad (4.9)$$

Gravitational force does constitute an external force, however, gravity is included via a modified velocity term in the equilibrium distribution function (Maxwellian distribution function). By replacing the velocity term in Equation 4.9 with the equilibrium velocity proposed by [25]:

$$\mathbf{u}_{eq} = \mathbf{u} + \Delta \mathbf{u} = \mathbf{u} + \frac{\tau(m\mathbf{g})}{\rho} \quad (4.10)$$

gravity is incorporated into the LBM.

The LBM model, as with the NS based model, was 3D, thus, the $D3Q19$ lattice was used [99]. The $D3Q27$ lattice was not used because it has been shown that for complex high-Reynolds Number flows, which is the case in the hydrocyclone, the $D3Q19$ and $D3Q27$ lattice provide comparable results [100, 101]. The $D3Q27$ lattice has an advantage in terms of stability and accuracy in the case of low Reynolds Number and wall bounded flows [102] and it is necessary to use the $D3Q27$ to solve the energy equation, as in heat transfer problems, using the LBM [24]. The lattice structure for the $D3Q19$ lattice is shown in Figure 4.5 [24, 91, 99] with lattice weights as given in Equation 4.11:

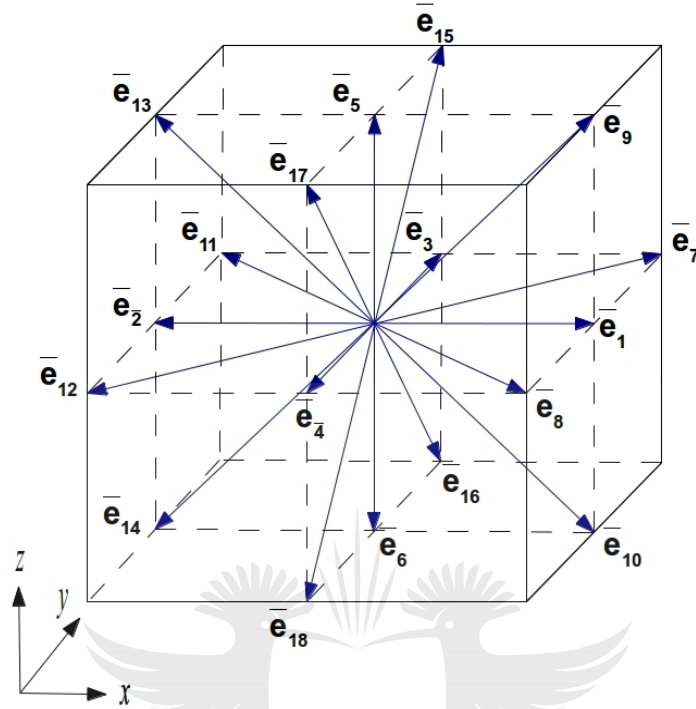


Figure 4.5: D3Q19 Lattice (adapted from [99])

$$w_i = \begin{cases} \frac{12}{36} & i = 0 \\ \frac{2}{36} & i = 1 \dots 6 \\ \frac{1}{36} & i = 7 \dots 18 \end{cases} \quad (4.11)$$

The discrete velocity \bar{e}_0 is in the centre of the lattice and, as in the case of $D2Q9$ lattice, it represents a stationary particle. In the LBM the pressure is $p = c_s^2 \rho$ [99] where, on the D3Q19, lattice $c_s = 1/\sqrt{3}c$. In the SRT BGK-LBM model the relaxation time is given by [24, 25, 91, 92, 99, 103]:

$$\tau_0 = \left(\frac{\nu}{c_s^2} + \frac{1}{2} \right) \quad (4.12)$$

Common RANS turbulence models such as the $k-\epsilon$ and RSM can be imple-

mented as per the method proposed in [104]. However, the implementation of the static and dynamic LES models have been the predominant focus of the literature as in [103, 105–107]. Because the LES model allows for subgrid scale modelling the LES model is incorporated here.

Turbulence is accounted for in the LBM for by using a modified relaxation time [103–107]. The modified relaxation time for turbulence is included in the LBM model via a viscosity correction to include the static Smagorinsky LES model as per [103, 106, 107]:

$$\nu_t = C_s^2 |\mathbf{S}| \quad (4.13)$$

where the magnitude of the rate-of-strain tensor is given by $|\mathbf{S}| \equiv \sqrt{2\mathbf{S}_{ij}\mathbf{S}_{ij}}$.

The viscosity correction results in a turbulent component of the relaxation time as given in [103, 106, 107]:

$$\tau_t = \left(\frac{(C_s \Delta x)^2}{c_s^2 \delta_t} |\mathbf{S}| \right) \quad (4.14)$$

where $C_s = 0.14$. The total relaxation time is a superposition of the two components of the relaxation times (Equation 4.12 and 4.14). Thus, the relaxation time is given by Equation 4.15

$$\tau = \tau_0 + \tau_t = \left(\frac{\nu}{c_s^2} + \frac{1}{2} \right) + \left(\frac{(C_s \Delta x)^2}{c_s^2 \delta_t} |\mathbf{S}| \right) \quad (4.15)$$

This model is sufficient for single phase flow. The air-core is included via a VOF free-surface LBM implementation that is coupled with the above model. Similarly the particle model is included via a Verlet particle model that is coupled with the VOF free-surface model. These extensions will be discussed in the following sub-sections.

4.4.1 LBM-VOF Model for Air-Core Formation

The interaction between the water and air (air-core) was implemented using the LBM-VOF free-surface model in Palabos which is based on the work of [64–66]. The model was developed by [64–66] to simulate the gas-fluid interface between a metal foam (liquid) and a gas. However, the model has broader applicability to modelling the interface between a general liquid and a gas.

The premise of the model is similar to that of the VOF model used in the NS based model with one significant distinction. The LBM-VOF model as proposed in [64–66] is an interface tracking scheme. The voxels (cells) are categorised as either fluid, gas or interface voxels [64–66] based on the volume fraction (α). If the entire volume of the voxel is filled with liquid it is a fluid voxel, and if it is entirely filled with gas then it is a gas voxel [64–66]. Voxels that are partially filled with liquid and gas are part of the interface [64–66]. The interface in the LBM-VOF is only a single layer of interface voxels between the fluid and gas voxels [64–66].

The voxels filled with gas are tagged as ‘empty’ voxels and the voxels filled with liquid are tagged as ‘fluid’ voxels. The ‘empty’ voxels are assigned no-dynamics in the sense that no fluid equation (Equation 4.7) is solved in those voxels and the volume fraction in these voxels is zero [64–66]. The ‘fluid’ voxels are assigned dynamics based on the model described above and the volume fraction is one [64–66]. This is the main difference in the LBM-VOF free surface model and the NS based VOF model. The NS based VOF model is a two fluid model which is an interface tracking scheme but also solves the fluid (NS) equations for both the liquid and gas phase [13].

This will have an effect on the particle behaviour near the liquid-gas interface. If a particle is in a ‘fluid’ cell near the interface or if it is in the interface then the particle will be transported as expected. However, if a such a particle experiences a collision with another particle forcing it to the ‘empty’ region the particle will become stationary as it has no local fluid velocity to transport it. It will then remain in the same location which will result in unrealistic behaviour. A realistic model would ensure that the particle is acted upon by gravity and it’s previous velocity (due to conservation of momentum). However, once it enters the ‘empty’ region, the particle has no momentum transfer from any external source such as drag and lift from the surrounding fluid or body forces such as gravity because no transport equations are solved

in the ‘empty’ region. To overcome this issue a boundary condition can be set at the interface to detect such occurrences and force the particle back to a neighbouring ‘fluid’ cell.

According to Körner *et al.* [66] the layer of interface voxels do not allow advection of f from the fluid to the gas and gas to fluid voxels. In this way the interface layer forms a closed boundary [64–66]. Mass is transferred from fluid to interface voxels and vice versa to ensure mass conservation [64–66]. No mass transfer occurs between gas and interface voxels [64–66]. All voxels can change their state but a fluid voxel cannot change directly to a gas voxel directly and vice versa [64–66]. A change from fluid to gas or vice versa occurs via an intermediary change to an interface voxel first [64–66]. This poses a limitation when modelling the sudden change of a region from gas to fluid, and vice versa, as in the case of the sudden burst of a bubble.

Surface tension effects are added by modifying the locally acting gas pressure as outlined in [64–66]. The locally acting gas pressure is given by Equation 4.16 [64–66]:

$$\rho_G = 3P_G + 6\sigma\kappa(\bar{x}, t) \quad (4.16)$$

where $\kappa(\bar{x}, t)$ is the surface curvature.

The disadvantages of the model are that a fluid equation is not solved for the gas region and that a backflow volume fraction of gas cannot be specified at the outlets. These disadvantages have an impact on the application to hydrocyclones. Firstly, when a particle passes the interface from a liquid to a gas voxel it will no longer move. The particle model depends on the velocity of the fluid for motion. Because (in the gas region) there is no velocity the particle will not move. Secondly, unlike in the NS based VOF model, a backflow volume fraction of gas cannot be specified. Thus, reverse flow of air at the underflow and overflow cannot be modelled. This is an essential phenomena that leads to air-core formation in hydrocyclones.

The LBM-VOF two fluid model, implemented in Palabos, has the potential to overcome the problems mentioned above. The LBM-VOF two fluid model is similar to the LBM-VOF free surface model with the addition of a fluid equation being solved for the gas phase. The implementation of this model in Palabos is still in the early stages and is unstable for high Reynolds Number

flows such as in a hydrocyclone³. This model was implemented and preliminary tests were done. However, it was unstable and produced unphysical results. An example of this is presented in Chapter 6. Thus, the LBM-VOF free surface model was implemented. For a more detailed description of the model the reader can consult [64–66].

4.4.2 LBM Particle Model

The three major particle types (classes) available in Palabos are the point particle, Verlet particle and a particle based on the IBM as discussed in Chapter 2. The point-particle type is a massless particle with no associated diameter [36]. The point particle has a one-way coupling with the fluid in the sense that it inherits the local fluid velocity and no other fluid-particle interaction is considered. Newton's equations of motion are not solved for the particle [36] because the particle inherits the local fluid velocity and the particle has no associated mass and volume. This massless one-way coupling approach is easy to implement, from a coding perspective, but is not sufficient to capture the physics of particle motion in the fluid in the hydrocyclone.

The IBM particle, based on the work of [69], can be defined so that it has an associated mass, diameter, density and shape. The particle occupies a volume in the domain and a no-slip boundary is applied at the surface of the particle [69]. In this way, full two-way coupling is incorporated and the fluid flow around each particle is captured. Furthermore, full fluid-particle, particle-wall and particle-particle interaction is modelled. This is a promising method when coupled with the LBM, however, it does have the limitation of (high) computational cost and as a result the ability to simulate only a few particles (on the scale of a few hundred particles at a time) in the domain [69].

The Verlet particle is similar to the point-particle in the sense that it does not have an associated mass, diameter or density [36]. However, the Verlet particle just as is the case with the NS based particle model, as described in Chapter 3, can account for mass, size and density by applying an equation (Newtonian) of motion to each particle and solving for the particle position and velocity [36]. As a result the Verlet particle does not cause a local disturbance to the flow field - due to a lack of physical size - and is therefore an approximation with the following shortcomings:

³This limitation has been confirmed by the Palabos development team.

- momentum transfer between the fluid and particle, such as drag and lift, is calculated via a model as opposed to being resolved directly and
- the effect of mass fraction of particles on the fluid flow field is not accounted for, or modelled, as opposed to being resolved directly.

It was decided that the Verlet particle class in Palabos would be used to model the particles because the two-way coupling in the Verlet particle class matches the two-way coupling in the NS based models. Furthermore, the size range of the particles used in this study are below $1mm$ which is smaller than the smallest cell/voxel resolution used in the models in this study. Thus, to resolve the local disturbance of the particles on the flow field, the IB-LBM approach must be used on meshes with cells/voxel below $1mm$, which is beyond the scope of this study.

The Verlet particle position and velocity is obtained by solving the Newton equations of motion for each particle. The equation of motion as a standard in Palabos only includes the effect of gravity and drag. This ‘particle interaction’ force was modified to account for gravity, drag, pressure gradient and virtual mass effects. Furthermore, particle-wall interaction (collisions) and particle-particle collisions are included as linear elastic collisions. The particle equation of motion, just as in the NS based model, is given as [13]:

$$\frac{d\mathbf{u}_p}{dt} = F_D(\mathbf{u} - \mathbf{u}_p) + \frac{\mathbf{g}(\rho_p - \rho)}{\rho_p} + C_{vm} \frac{\rho}{\rho_p} \left(\mathbf{u}_p \nabla \mathbf{u} - \frac{d\mathbf{u}_p}{dt} \right) + \frac{\rho}{\rho_p} \mathbf{u}_p \nabla \mathbf{u} \quad (4.17)$$

where F_D is as defined in Chapter 3. Equation 4.17 defines the particle acceleration based on the forces per unit particle mass [13].

Particles with different diameters are added by modifying the particle diameter in the drag coefficient (F_D) in Equation 4.17. The Verlet class does not directly have an option to specify a PSD. Thus, particles with different diameters are added as a separate particle field with an associated mass and ‘particle interaction’ force. The number of particles injected, from each field, into the domain was determined from the Rosin-Rammler distribution and hard-coded⁴. Particle counters were setup at the outlets for each particle field to reconstruct the PSD’s at the outlets.

⁴As future work, the Verlet particle class will be modified to directly specify a PSD and in turn only use one particle field. This can be done because the user has access to

Particle-wall collisions are implemented via a simple strategy in Palabos. Motionless particles are placed at the nodes of the vertices of the STL file. These particles are assigned a tag number of 0. Moving particles are assigned a tag number corresponding to the particle diameter in μm . When the distance between a moving particle reaches a specified value a collision is assumed and the moving particle is pushed (bounced back) into the domain. In this way particle-wall collisions are modelled. The algorithm that is used, in Palabos, to determine the proximity of particles is the link-cell algorithm [36]. The link cell algorithm is discussed in detail in [36].

Particle-particle collisions are implemented using a linear elastic collision rule. Complex collision rules such as the DEM rule used in Chapter 3 can be implemented in Palabos via the link-cell algorithm which can be used to determine the proximity of the moving particles and collision detection. This would form the basis for modelling particle-particle collisions. The above would lead to an LBM-DEM model. However, the implementation of an LBM-DEM model was not done in this study and has been reserved for future work.

4.5 Boundary Conditions

The cells, within the bounding box, that were outside of the hydrocyclone domain were assigned no-dynamics. Thus, the distribution functions for the no-dynamics cells were set to zero. The cells inside the domain were assigned the relevant dynamics.

Initially the wall boundaries were assigned using the Guo off-lattice boundary scheme proposed by Guo, Chuguang and Baochang [108], which reproduced a no-slip boundary at the walls and has improved predictions for curved boundaries. This was done for the single phase models [109]. The Guo off-lattice boundaries could not be used when the VOF model was added due to the incompatibility of the two models⁵. Thus, the wall boundaries in the

the source code for Palabos. Thus, a modified Verlet particle class can be developed by the user without the input of the Palabos developers.

⁵The Guo off-lattice boundary scheme should be used when modelling a gas cyclone or a hydrocyclone with no air-core due the improved predictions, in comparison to the bounce-back node option, for curved boundaries. Furthermore, the Guo off-lattice scheme provides for more versatile, from a coding perspective, inlet(s) and outlet(s) boundary specification.

final models were specified as on-lattice boundaries with bounce-back nodes specified for the voxels on the outside-border and outside tagged cells.

Via the bounce-back condition, a fluid particle is bounced back to the node that the fluid particle was at before the streaming step [24, 25, 91, 92, 108]. In this way a wall boundary is asserted at the relevant position. Furthermore, a no-slip condition at the wall is reproduced [24, 25, 91, 92, 108]. The solid particle-wall collisions are implemented as outlined in Section 4.4.2 which leads to a linear elastic collision.

The inlet was specified as a velocity inlet with the velocity specified to obtain the mass flow rate given in Table 3.3 and with the inlet pressure matching that in Table 3.3. The outlets were specified as pressure outlets⁶ matching that in Table 3.3.

4.6 Notes on Solver Setup

Palabos does not provide solver options analogous to those discussed in Section 3.5. All variables such as velocity, pressure and density have to be scaled to lattice units. The fluid properties and boundary values were specified in metric units and the scaling is done in the end code by an implementation of the algorithm as proposed by [110]. The accuracy of the LBM model is defined predominantly by the specification of the relaxation time as well as the mesh resolution and time step size. The effect of mesh resolution and time step size are discussed in detail in Chapter 6.

The maximum time step size that kept the relaxation time in the range $0.5 < \tau < 1$ was used as an initial estimate for the time step size. The initial estimate was successively reduced by half until convergence and numerical stability was achieved. The time step sizes used in the LBM models are reported for each LBM model and mesh refinement in Chapter 6.

The LBM model as presented in [109] was part of the preliminary LBM models in this study. The results from [109] highlights that to obtain results from the LBM that are comparable to that from the NS based model the LBM requires a mesh resolution that is 2 to 15 times finer, in terms of computational cells/lattices, than the mesh for the NS based model. The

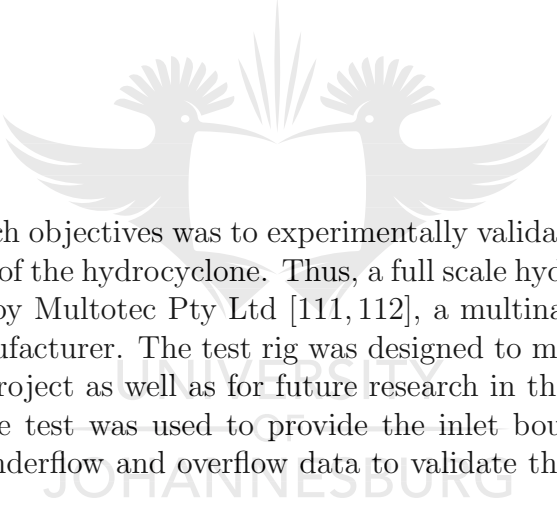
⁶This was done by fixing the density and via the equation of state fixing the pressure.

time step size required should also have a similar relationship to the time step required for the NS based models [109]. Despite the requirement for finer mesh resolution and smaller time step sizes the LBM could easily run on smaller hardware requirements as illustrated in [109].



Chapter 5

Experimental Setup and Results



One of the research objectives was to experimentally validate the CFD-DEM and LBM models of the hydrocyclone. Thus, a full scale hydrocyclone test rig was constructed by Multotec Pty Ltd [111, 112], a multinational separation technologies manufacturer. The test rig was designed to meet the objectives of this research project as well as for future research in this area. The data obtained from the test was used to provide the inlet boundary conditions and to provide underflow and overflow data to validate the CFD-DEM and LBM models.

5.1 Overview of the Experimental Setup

The test rig, as seen in Figure 5.1 was designed to test a full scale 100mm hydrocyclone under standard operating conditions, hence, it contained a VV100 (100mm barrel diameter) hydrocyclone from Multotec Pty Ltd. The hydrocyclone was the same as the one modelled in Chapters 3 and 4. Three support brackets were used to limit hydrocyclone vibration. As seen in Figure 5.1 the support brackets, which were attached to the side frame of the rig, were positioned at the overflow elbow, spigot and at the barrel.

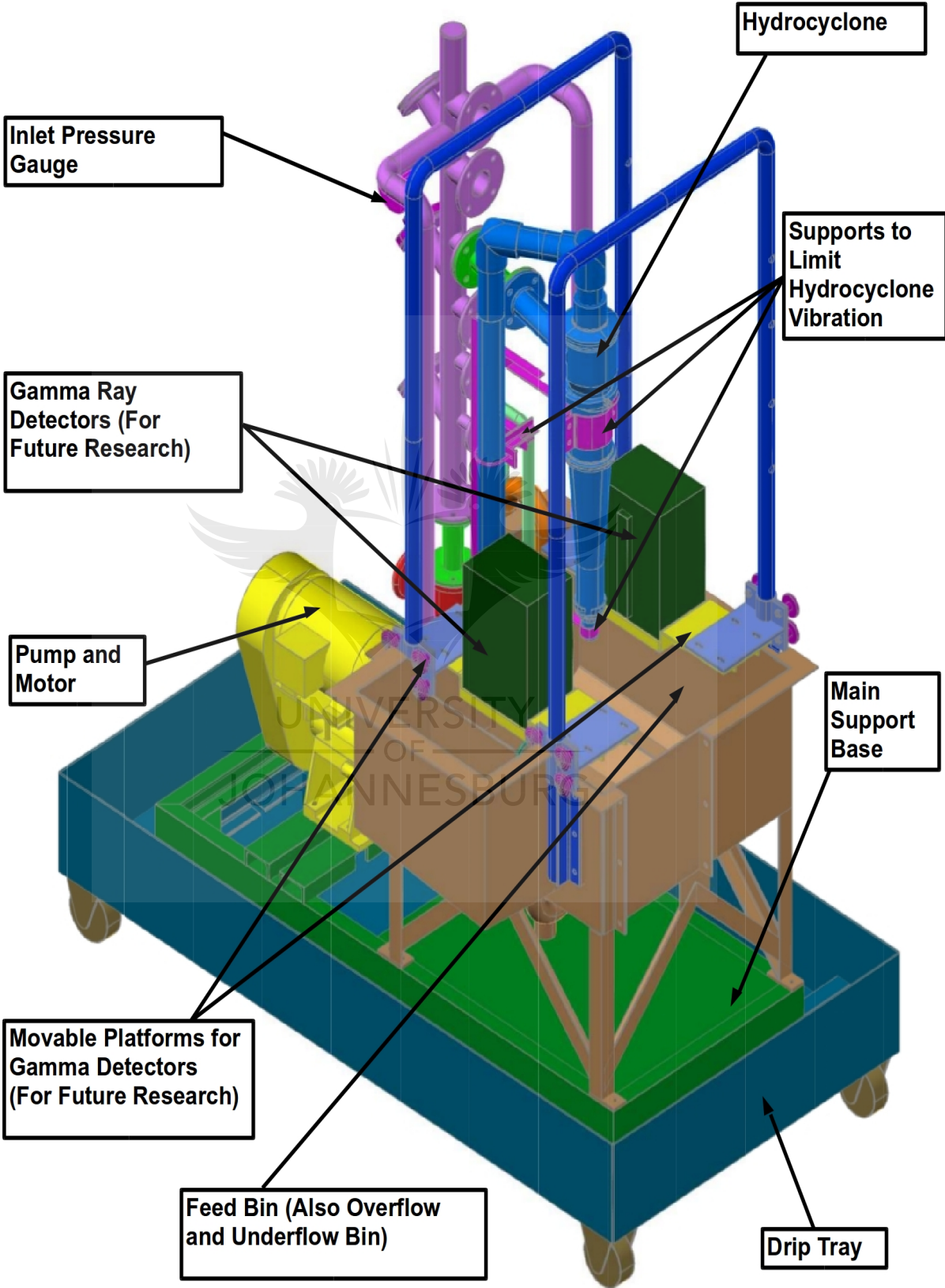


Figure 5.1: Isometric view of the test rig (Adapted from an image courtesy of Multotec Pty Ltd)



Figure 5.2: Agitation mechanism used to prevent solids settling in the feed bin

Figure 5.3: Plastic curtains used for spill containment

The feed to the hydrocyclone was from the feed bin via a centrifugal pump which was powered by a 6kW AC motor. The feed pressure was measured using a pressure gauge. Two agitation mechanisms were used to prevent solids settling. The first agitation mechanism was the re-direction of the underflow and overflow into the feed bin. Thus, the feed bin was also used as the underflow and overflow bin. The other mechanism was the re-direction of a fraction of the flow from the pump back into the feed bin, as seen in Figure 5.2. The pump, motor and feed bin were placed on the main support base which in turn was placed on a drip tray.

The test rig was designed to be mobile and compact so that it could be easily transported between the Multotec test facility and iThemba LABS North. The experiments were conducted at the Multotec Pty Ltd. Research and Development Division. However, in the future Positron Emission Particle Tracking (PEPT) studies will be conducted using the test rig. These studies



Figure 5.4: Half scale perspex hydrocyclone model

must be conducted at a radiation safe zone, thus, the PEPT tests will be conducted at iThemba LABS North. Two movable platforms that will be used to mount Gamma-Ray Detectors for future research (PEPT studies) were added to the main structure. The drip tray and plastic curtain, as seen in Figures 5.1 and 5.3, were added to reduce spilling. The spill prevention modifications were added to ensure a clean lab as well as for radiation safety requirements for the future PEPT studies.

A half scale perspex hydrocyclone model, at Multotec Pty Ltd. was used to capture real time video footage of the air-core formation in a hydrocyclone.

The half scale model is shown in Figure 5.4.

5.2 Measured Variables, Instrumentation and Data Acquisition

The four major variables that were measured were feed pressure, solids loading, mass flow rate and particle size distributions (PSD). The solids loading and mass flow rate were measured at the feed, overflow and underflow. Samples were collected at the feed, overflow and underflow for particle size analysis.

5.2.1 Feed Pressure Measurements

The feed pressure was measured using an analog pressure gauge as seen in Figure 5.5. The feed valve was opened steadily until the required inlet pressure was obtained. The gauge was monitored throughout each test to ensure that the feed pressure was steady.

5.2.2 Solids Loading and Mass Fraction Measurements

The solids loading at the inlet and the solids mass fraction at the underflow and overflow were measured in the same way. A sample from the feed, underflow and overflow were taken at the same time using volume marked containers. The samples were weighed and the sample volumes were recorded. The mass and volume measurement for each sample was used to calculate a relative density for the water and solids mixture. The density of the solids and the water is known. Thus, the mass of the solids and the water was then calculated using the approach below:

The total mass (m_t) is the sum of the solids mass (m_p) and the water mass (m_w):



Figure 5.5: Inlet pressure gauge

$$m_p + m_w = m_t \quad (5.1)$$

The total volume (V_t) is the sum of the solids volume (V_p) and the water volume (V_w):

$$V_p + V_w = V_t \quad (5.2)$$

The solids volume (V_p) and the water volume (V_w) is given by the following equations, respectively:

$$V_p = \frac{m_p}{\rho_p} \quad (5.3)$$

and

$$V_w = \frac{m_w}{\rho_w} \quad (5.4)$$

Substituting Equations 5.3 and 5.4 into Equation 5.2 and simplifying produces:

$$\rho_w m_p + \rho_p m_w = \rho_p \rho_w V_t \quad (5.5)$$

Thus, Equations 5.1 and 5.5 form a linear system of equations. Solving the system of equations for the two unknowns (m_p and m_w) provides the following solution:

$$m_p = \frac{\rho_p(m_t - \rho_w V_t)}{\rho_p - \rho_w} \quad (5.6)$$

and

$$m_w = \frac{-\rho_w(m_t - \rho_p V_t)}{\rho_p - \rho_w} \quad (5.7)$$

With the total mass, solids mass and the water mass known, the respective mass fractions can be calculated. The solids mass and water mass can be used to calculate the solids and water volumes and in turn the solids and water volume fractions. The above procedure was done for the feed, underflow and overflow.

5.2.3 Mass Flow Rate Measurements

The mass flow rate was measured for the underflow and overflow. As in the case of the mass fraction measurements, a sample from the underflow and overflow were taken at the same time. Containers were used to take samples for a stipulated time. The samples were weighed and the time was recorded. Thus, the total flow rate for the underflow and overflow were calculated. The mass fractions, calculated using the procedure described above, were

used to calculate the solids mass flow rate and the water mass flow rate for the underflow and overflow. Using conservation of mass, the feed mass flow rates were calculated from the underflow and overflow mass flow rates.

5.2.4 Particle Size Analysis

Multotec Pty Ltd. offered two options for the PSD measurements, namely, laser based measurements using the Malvern Mastersizer Hydro 2000G or a shaker table. The shaker table could not capture the fines properly because the smallest sieve had a grating larger than $100\mu\text{m}$. Another disadvantage of using the shaker table was that the sample had to be dried to ensure all water content had been removed, whereas, with the Mastersizer the wet samples were used in the measurements. Thus, the samples were analysed using the Malvern Mastersizer Hydro 2000G.

The PSD was measured for the feed, underflow and overflow. As in the case of the mass fraction and mass flow rate measurements, a sample from the feed, underflow and overflow was taken and used for the particle size analysis.

The Mastersizer has a particle size measurement range of $0.02 - 2000 \mu\text{m}$ with an accuracy of 1% and a maximum achievable reproducibility of 1% [113]. The Mastersizer was calibrated by Malvern and Micron Scientific in August 2013. The experimental work was done in March 2014. The calibration and performance verification certificate is given in Appendix A.

5.3 Experimental Procedure

The procedure used during the experiments is as follows:

- Fill the feed bin with water and particles, ensuring that the desired solids loading (solids mass fraction is obtained).
- Turn on the pump.
- Ensure that the feed bin is sufficiently agitated.

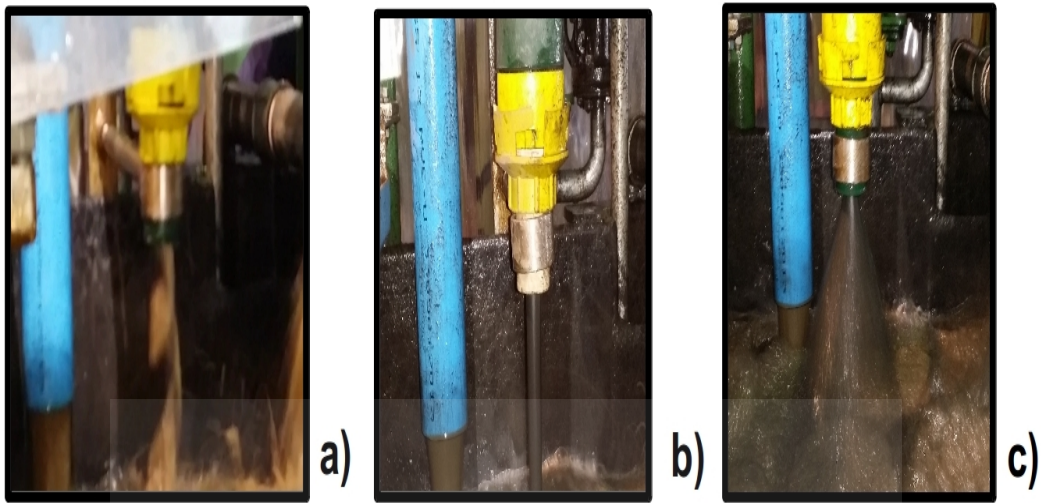


Figure 5.6: Underflow spray shapes: a) roping, b) cylindrical and c) conical

- Open the valve steadily until the required inlet pressure is obtained and that the feed pressure is steady.
- Ensure that the hydrocyclone is not roping and that the slurry exiting the underflow has a conical spray shape. See Figure 5.6 for the difference between roping, cylindrical and full conical spray shapes.
- Run the cyclone for at least two seconds before taking measurements.
- Sample the underflow and overflow a minimum of three times for relative density.
- Sample the underflow and overflow a minimum of three times for mass flow rates.
- Collect samples from the feed, overflow and underflow for particle size analysis.
- Analyse the samples using the Mastersizer to obtain the particle size distributions for the feed, overflow and underflow.
- Repeat the experiment a minimum of three times using the same feed pressure, solids loading and particle type.

Table 5.1: Operating Pressures for Test 1, 2 and 3.

	P (kPa)
Inlet	150
Atmospheric	82.5

Table 5.2: Water and Solids Densities for Test 1, 2 and 3.

	ρ (kg/m ³)
Solids	3330
Water	1000
$\Delta\rho = \rho_p - \rho_w$	2330

5.4 Experimental Results

Three experimental tests were conducted. The solids used for the tests was chromite ore. The tests were all conducted using the same inlet pressure and solids type to obtain a statistically averaged set of data that could be used as inputs and comparison measures for the CFD-DEM and LBM models. The operating pressures are given in Table 5.1. The water and solids densities are given in Table 5.2.

5.4.1 Mass and Volume Fraction Measurements

The solids loading for the feed was kept at approximately 76% water and 24% solids. The measurements data for the mass and volume fraction for the overflow and underflow are given in Tables 5.3 and 5.4, respectively. In each table the descriptive statistics are given. The mean and median in all cases are sufficiently close to each other. Thus, the distributions are not highly skewed. Thus, the mean is an acceptable measure of central tendency. The standard deviations, variance and coefficients of variation are acceptable. The standard deviation can be considered as an indication of the experimental error in the respective measurements because the tests are repeated experiments at the same operating conditions. The mean values will be used for validating the computational models. However, due to the “quasi-steady” nature of the physics in the hydrocyclone, the maximum and minimum values will be used to see if the computational model predictions remain within bounds of the experimental predictions.

It should be noted that the highlighted rows in Table 5.3 represent physical

Table 5.3: Overflow Mass and Volume Fraction Measurements

Test Number	Data Point	m(kg)	V(m ³)	ρ_r (kg/m ³)	m _p (kg)	m _w (kg)	w _p	w _w	α_p	α_w
1	1	1.73	0.00166	1042.17	0.10	1.63	5.78	94.22	1.81	98.19
1	2	1.70	0.00164	1036.59	0.09	1.61	5.04	94.96	1.57	98.43
1	3	1.15	0.00114	1008.77	0.01	1.14	1.24	98.76	0.38	99.62
1	4	1.65	0.00160	1031.25	0.07	1.58	4.33	95.67	1.34	98.66
1	5	1.55	0.00156	993.59	-0.01	1.56	-0.92	100.92	-0.28	100.28
1	6	1.75	0.00176	994.32	-0.01	1.76	-0.82	100.82	-0.24	100.24
2	1	1.88	0.00184	1019.02	0.05	1.82	2.67	97.33	0.82	99.18
2	2	2.03	0.00199	1017.59	0.05	1.97	2.47	97.53	0.75	99.25
2	3	1.63	0.00160	1018.75	0.04	1.59	2.63	97.37	0.80	99.20
3	1	1.87	0.00184	1013.59	0.04	1.83	1.92	98.08	0.58	99.42
3	2	1.55	0.00152	1019.74	0.04	1.51	2.77	97.23	0.85	99.15
3	3	1.32	0.00130	1015.38	0.03	1.29	2.17	97.83	0.66	99.34
	Maximum	2.03	0.00199	1042.17	0.10	1.97	5.78	98.76	1.81	99.62
	Minimum	1.15	0.00114	1008.77	0.01	1.14	1.24	94.22	0.38	98.19
	Mean	1.65	0.00161	1022.28	0.05	1.60	3.10	96.90	0.96	99.04
	Median	1.68	0.00162	1018.89	0.05	1.60	2.65	97.35	0.81	99.19
	Std Dev	0.26	0.00025	10.74	0.03	0.25	1.46	1.46	0.46	0.46
	Variance	0.07	0.00000	115.31	0.00	0.06	2.13	2.13	0.21	0.21
	COE Var	15.86	15.72217	1.05	50.46	15.68	47.01	1.50	48.19	0.47
	Range	0.88	0.00085	33.40	0.09	0.84	4.54	4.54	1.43	1.43

Table 5.4: Underflow Mass and Volume Fraction Measurements

Test Number	Data Point	m(kg)	V(m ³)	ρ_r (kg/m ³)	m _p (kg)	m _w (kg)	w _p	w _w	α_p	α_w
1	1	2.75	0.00148	1858.11	1.82	0.93	66.00	34.00	36.83	63.17
1	2	2.45	0.00132	1856.06	1.61	0.84	65.92	34.08	36.74	63.26
1	3	2.55	0.00138	1847.83	1.67	0.88	65.57	34.43	36.39	63.61
2	1	1.63	0.0009	1811.11	1.04	0.59	64.01	35.99	34.81	65.19
2	2	2.10	0.00116	1806.03	1.34	0.76	63.78	36.22	34.59	65.41
2	3	2.47	0.00138	1789.86	1.56	0.91	63.07	36.93	33.90	66.10
3	1	1.56	0.00088	1767.05	0.96	0.59	62.04	37.96	32.92	67.08
3	2	2.01	0.00114	1758.77	1.24	0.77	61.66	38.34	32.57	67.43
3	3	2.04	0.00112	1821.43	1.31	0.73	64.45	35.55	35.25	64.75
	Maximum	2.75	0.00148	1858.11	1.82	0.93	66.00	38.34	36.83	67.43
	Minimum	1.56	0.00088	1758.77	0.96	0.59	61.66	34.00	32.57	63.17
	Mean	2.17	0.00120	1812.92	1.40	0.78	64.06	35.94	34.89	65.11
	Median	2.10	0.00116	1811.11	1.34	0.77	64.01	35.99	34.81	65.19
	Std Dev	0.39	0.00020	31.40	0.27	0.13	1.38	1.38	1.35	1.35
	Variance	0.17	0.00000	1351.63	0.08	0.02	2.57	2.57	2.49	2.49
	COE Var	17.85	16.94093	1.73	19.09	16.10	2.16	3.84	3.86	2.07
	Range	1.20	0.00060	99.34	0.85	0.35	4.34	4.34	4.26	4.26

data but measurements that cannot be used. These measurements reflect the decrease in water density due to the substantial rise in water temperature. The rise in water temperature is caused by the conversion of the kinetic energy into heat. Thus, the relative density falls below 1000kg/m^3 . In the absence of temperature measurements sampling should stop at this point.

5.4.2 Mass Flow Rate Measurements

The average mass fractions for the overflow and underflow were used to calculate the water and solids mass flow rates at the respective outlets. The measurement data for the mass flow rates for the overflow and underflow are given in Tables 5.5 and 5.6, respectively. In each table the descriptive statistics are given. As in the case of the mass and volume fractions the mean and median in all cases are sufficiently close to each other. Thus, the distributions are not highly skewed and the mean is an acceptable measure of central tendency. The standard deviations, variance and coefficients of variation are acceptable. The standard deviation can be considered as an indication of the experimental error in the respective measurements because the tests are repeated experiments at the same operating conditions. The mean values will be used for validating the computational models. However, due to the “quasi-steady” nature of the physics in the hydrocyclone, the maximum and minimum values will be used to see if the computational model predictions remain within bounds of the experimental predictions.

The mean mass flow rates for the water and solids at the underflow and overflow were added to obtain the feed mass flow rate of water and solids. The feed mass flow rates, volumetric flow rates, mass fractions and volume fractions are given in Table 5.7. The feed mass fractions are close to the original ratio as specified at the beginning of the tests.

Table 5.5: Overflow Mass Flow Rates

Test Number	Data Point	m(kg)	t(s)	\dot{m} (kg/s)	\dot{m}_p (kg/s)	\dot{m}_w (kg/s)
1	1	7.50	1.76	4.26	0.13	4.13
1	2	7.60	1.73	4.39	0.14	4.26
1	3	8.05	1.70	4.74	0.15	4.59
2	1	5.95	1.43	4.16	0.13	4.03
2	2	7.57	1.36	5.57	0.17	5.39
2	3	7.63	1.61	4.74	0.15	4.59
2	4	7.33	1.56	4.70	0.15	4.55
3	2	8.60	2.14	4.02	0.12	3.89
3	2	8.54	2.04	4.19	0.13	4.06
3	2	8.25	1.84	4.48	0.14	4.34
	Maximum	8.60	2.14	5.57	0.17	5.39
	Minimum	5.95	1.36	4.02	0.12	3.89
	Mean	7.70	1.72	4.52	0.14	4.38
	Median	7.62	1.72	4.44	0.14	4.30
	Std Dev	0.80	0.29	0.56	0.02	0.54
	Variance	0.58	0.06	0.20	0.00	0.19
	COE Var	10.44	16.91	12.29	12.29	12.29
	Range	2.66	0.78	1.55	0.05	1.50

Table 5.6: Underflow Mass Flow Rates

Test Number	Data Point	m(kg)	t(s)	\dot{m} (kg/s)	\dot{m}_p (kg/s)	\dot{m}_w (kg/s)
1	1	4.59	1.76	2.61	1.67	0.94
1	2	4.34	1.73	2.51	1.61	0.90
1	3	4.39	1.70	2.58	1.65	0.93
2	1	3.06	1.43	2.14	1.37	0.77
2	2	3.23	1.36	2.38	1.52	0.85
2	3	3.46	1.61	2.15	1.37	0.77
2	4	3.81	1.56	2.44	1.56	0.88
3	1	4.42	2.14	2.06	1.32	0.74
3	2	4.62	2.04	2.26	1.45	0.81
3	3	4.40	1.84	2.39	1.53	0.86
	Maximum	4.62	2.14	2.61	1.67	0.94
	Minimum	3.06	1.36	2.06	1.32	0.74
	Mean	4.03	1.72	2.35	1.51	0.85
	Median	4.37	1.72	2.38	1.53	0.86
	Std Dev	0.58	0.29	0.17	0.11	0.06
	Variance	0.35	0.06	0.04	0.02	0.00
	COE Var	14.39	16.91	7.43	7.41	7.43
	Range	1.56	0.78	0.54	0.35	0.20

Table 5.7: Feed Mass Flow Rates, Volumetric Flow Rates, Mass Fractions and Volume Fractions

Feed Mass Flow Rate Water (kg/s)	5.23±0.54
Feed Mass Flow Rate Solids (kg/s)	1.65±0.11
Feed Water Mass Fraction (%)	76.05±2.01
Feed Solids Mass Fraction (%)	23.95±2.01
Feed Water Volume Fraction (%)	91.36±1.43
Feed Solids Volume Fraction (%)	8.64±1.43

5.4.3 Particle Size Analysis

The PSD measurements produced the PSD for the feed, underflow and overflow as given in Tables 5.8 - 5.10, respectively. The reported sizes and the related experimental error is given in Table 5.11. The PSD data plots with the averaged PSD for the feed, underflow and overflow is given in Figures 5.7 - 5.9, respectively.

5.4.3.1 Rosin-Rammler Distribution Method

The PSD measurements for the feed can be used as an input PSD in the computational models and the underflow and overflow PSDs can be used as a comparison measure for the computational models. Thus, the averaged PSD were measurements were fitted to the Rosin-Rammler distribution as described in [13,14]. The Rosin-Rammler distribution is expressed by Equation 5.8 [14]:

$$Y_d = e^{(-d/\bar{d})^n} \quad (5.8)$$

where Y_d is the mass fraction of particles with diameter greater than d , and \bar{d} is the mean diameter [14]. In this case the mean diameter is the diameter at which $Y_d = e^{-1} \approx 0.368$. The spread parameter n is determined by Equation 5.9 [14].

Table 5.8: Feed PSD - Cumulative Passing

	Percentage Mass Below Sizes (Sizes in μm) - Accuracy $\pm 1\%$												
Sample	2	10	16	38	53	75	106	150	212	300	425	600	850
Test 1	2.65	7.32	8.89	13.44	17.91	25.75	37.10	51.53	67.66	83.03	94.34	99.63	100
Test 2	0.54	3.64	4.91	8.37	11.20	15.97	23.43	35.16	52.29	72.79	90.19	99.01	100
Test 3	0.00	1.00	1.70	4.92	8.20	13.93	22.69	35.52	53.03	73.23	90.21	98.94	100
Average	1.07	3.99	5.17	8.91	12.44	18.55	27.74	40.74	57.66	76.35	91.58	99.19	100

Table 5.9: Underflow PSD - Cumulative Passing

	Percentage Mass Below Sizes (Sizes in μm) - Accuracy $\pm 1\%$												
Sample	2	10	16	38	53	75	106	150	212	300	425	600	850
Test 1	0.18	1.77	2.88	8.04	12.73	20.45	31.35	45.46	62.17	79.40	92.89	99.40	100
Test 2	0.00	0.75	1.38	4.79	8.26	14.05	22.59	35.13	52.63	73.23	90.54	99.14	100
Test 3	0.00	0.41	0.98	4.17	7.39	12.85	21.14	33.58	51.14	71.95	89.70	98.87	100
Average	0.06	0.98	1.75	5.67	9.46	15.78	25.03	38.05	55.31	74.86	91.04	99.14	100

Table 5.10: Overflow PSD - Cumulative Passing

	Percentage Mass Below Sizes (Sizes in μm) - Accuracy $\pm 1\%$												
Sample	2	10	16	38	53	75	106	150	212	300	425	600	850
Test 1	9.99	28.72	34.21	42.63	45.90	50.08	55.84	64.20	75.28	87.21	96.35	100	100
Test 2	5.91	20.65	25.99	36.26	41.49	48.95	58.67	69.60	79.91	88.50	95.13	99.30	100
Test 3	5.82	21.05	26.94	38.90	45.09	53.74	64.38	75.31	84.44	91.22	96.27	99.51	100
Average	7.24	23.48	29.05	39.26	44.16	50.92	59.63	69.71	79.88	88.98	95.92	99.60	100

Table 5.11: Accuracy of the Size Measurements

Reported Size (μm)	Experimental Error (μm)
2	\pm 0.02
10	\pm 0.1
16	\pm 0.16
38	\pm 0.38
53	\pm 0.53
75	\pm 0.75
106	\pm 1.06
150	\pm 1.50
212	\pm 2.12
300	\pm 3.00
425	\pm 4.25
600	\pm 6.00
850	\pm 8.50

$$n = \frac{\ln(-\ln(Y_d))}{\ln(d/\bar{d})} \quad (5.9)$$

As per the procedure outlined in the ANSYS Fluent User Guide [14], the spread parameter n is calculated for each size bin and then averaged. The average n is used in the Rosin-Rammler distribution.

Analysing the PSD data, as per Tables 5.8 - 5.10, produces the parameters, as given in Table 5.12, for the Rosin-Rammler distributions for the feed, underflow and overflow. The comparison between the actual PSDs and Rosin Rammler fitted PSDs are shown in Figures 5.10 - 5.12. It should be noted that the mean diameters are determined from the Figures 5.10 - 5.12.

Table 5.12: Rosin-Rammler Distribution Parameters

Boundary	\bar{d} (μm)	n_{ave}	$d_{\text{min}}(\mu\text{m})$	$d_{\text{max}}(\mu\text{m})$	N
Feed	240	1.3285	2	850	13
Underflow	250	1.5266	2	850	13
Overflow	120	0.7449	2	850	13

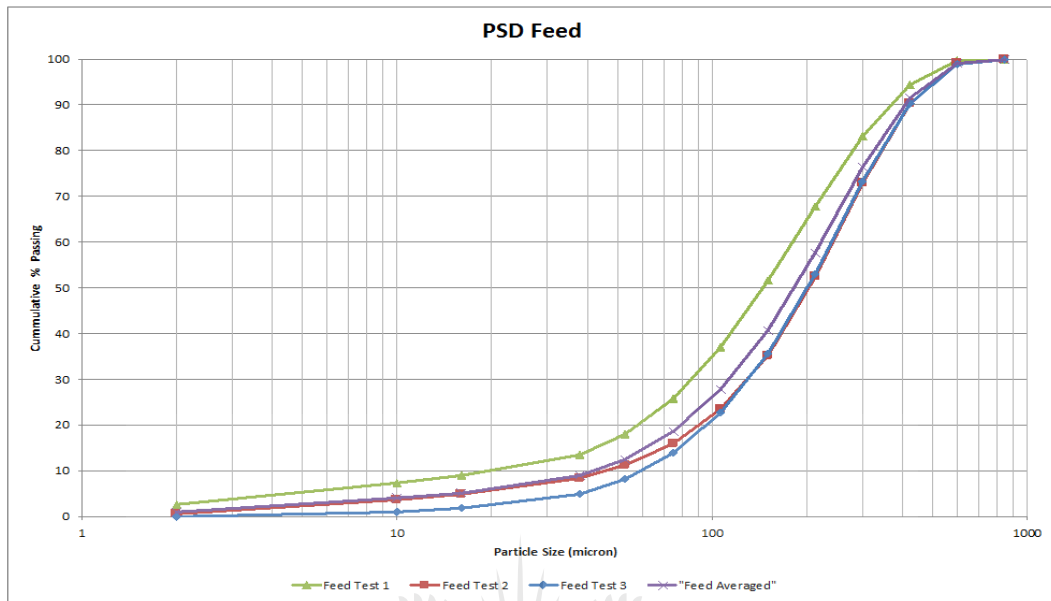


Figure 5.7: Feed PSD - cumulative passing

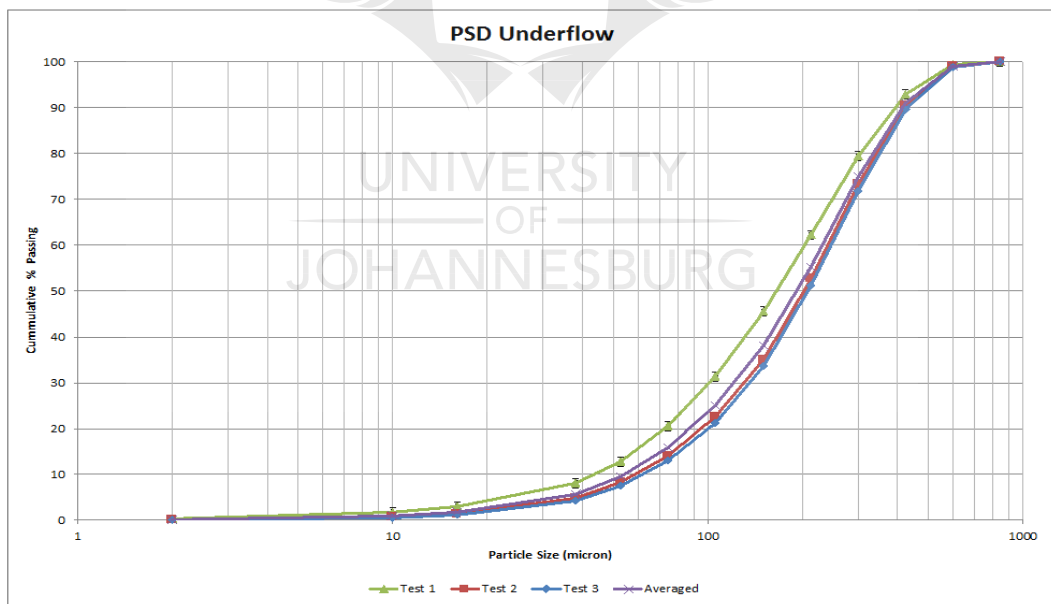


Figure 5.8: Underflow PSD - cumulative passing

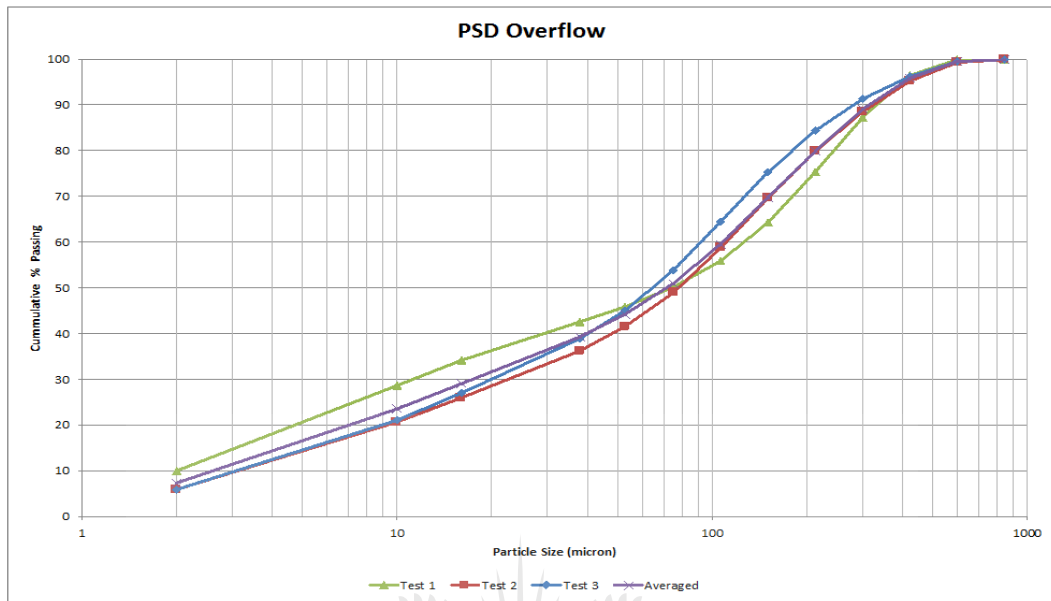


Figure 5.9: Overflow PSD - cumulative passing

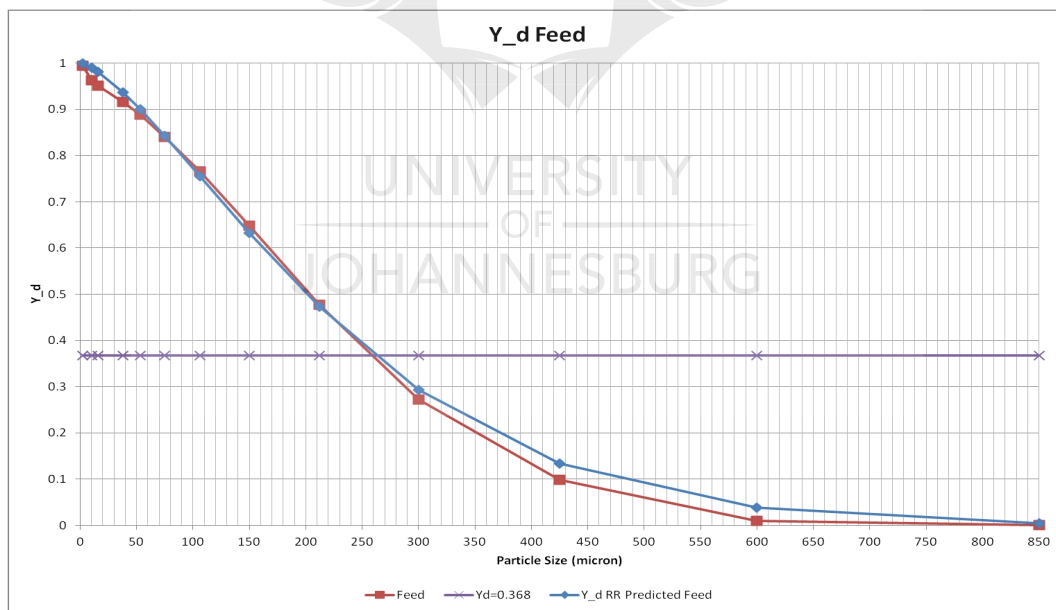


Figure 5.10: Feed Rosin-Rammler fit

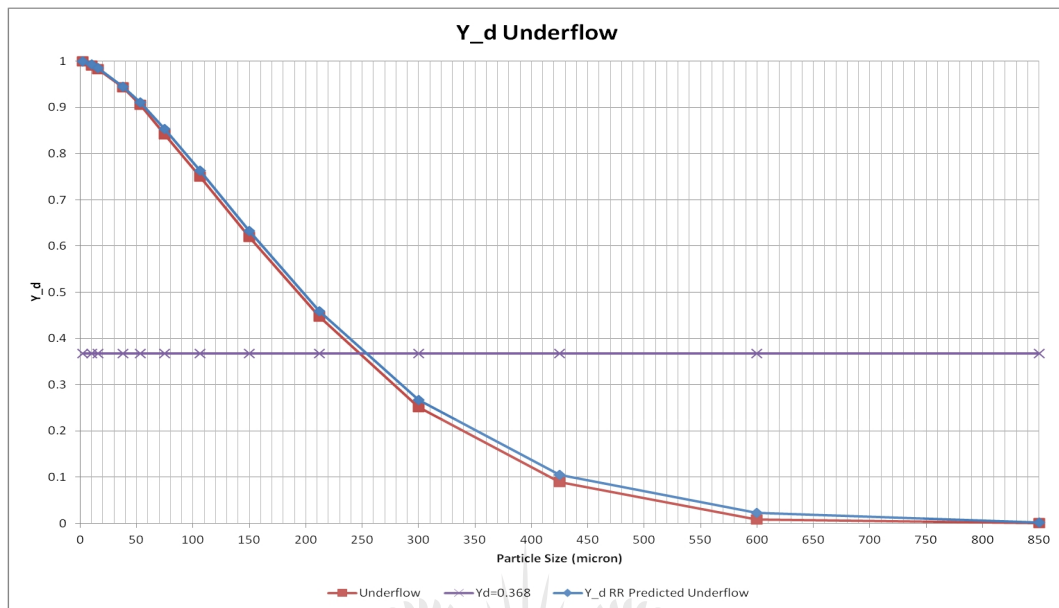


Figure 5.11: Underflow Rosin-Rammler fit

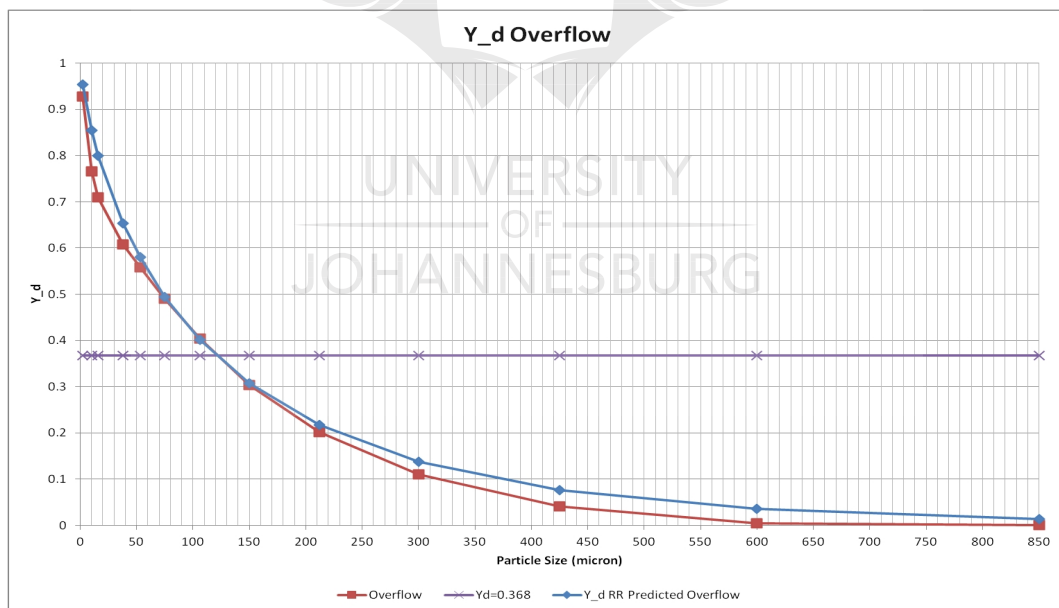


Figure 5.12: Overflow Rosin-Rammler fit

5.5 Air-Core Formation

A video of the air-core formation was taken using the half scale perspex hydrocyclone model, at Multotec Pty Ltd. The video was broken down into an image gallery at 1 frame per second (FPS). The image gallery with time stamps is shown in Figure 5.13. The images run from, time $t = 0\text{s}$ to $t = 13\text{s}$, from the right and vertically. The same was done by adding dye into the test rig. The image gallery is shown in Figure 5.14.

The literature, such as references [2,6–9,12], states that the air-core forms due to reverse flow at the underflow which in turn is caused by the low pressure region in the core of the hydrocyclone. This is contradictory to the results from the video footage. The video footage and image gallery illustrates that the air-core forms as the water enters and occupies the volume that initially is occupied by air. The water fills the hydrocyclone until the air is reduced to a stable rotating column (air-core). It is inferred from the video and the NS based models that the air-core stabilises and does not break up because it is fed with air entering the overflow and underflow due to reverse flow at the respective outlets. The literature also acknowledges reverse flow at the underflow only. However, the preliminary and final NS based models illustrate that the reverse flow is present at both the overflow and underflow, although, it is more significant at the underflow. Initially, the hydrocyclone was modelled with just water until the model reached steady state then the air-core was added. Attempts were made to include both the water and air-core, however, these models either diverged or damped out the air-core. Another model was implemented, inspired by the video footage, where the hydrocyclone volume was initialised with a volume fraction of air ($\alpha = 1$). The water was then introduced at the inlet. This model produced the same physics as described above and seen in the video footage resulting in full air-core formation.

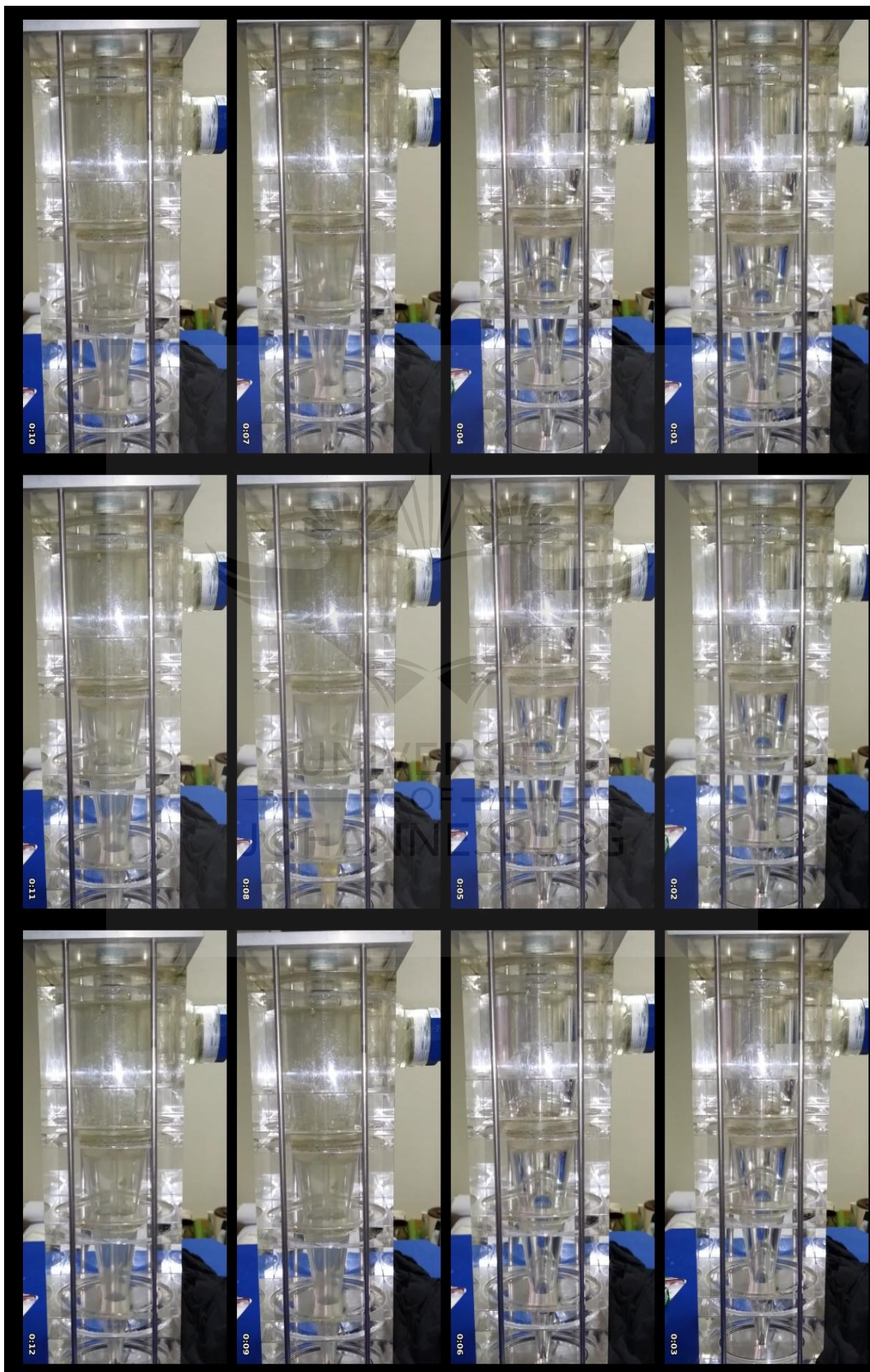


Figure 5.13: Image stills from video of air-core formation



Figure 5.14: Image stills from video of air-core formation with dye

Chapter 6

Simulation Results and Discussion

6.1 Air-Core Formation

The discussion of the simulation results will begin with the air-core formation because the air-core models were used as the initial solution to the particle models. Thus, the air-core models were completed before the particle models. Furthermore, with a detailed insight of the air-core model predictions it would be a natural extension to discuss the effect of the particles on the air-core later.

6.1.1 NS Based Models Predictions

A mesh sensitivity study was conducted for the NS based models and is detailed in Appendix C. Based on the study the VOF and Mixture models (for all turbulence models) reached mesh independence at a cell size of 1.25mm. However, due to stability issues as detailed in 6.1.2, the Eulerian model did not converge on the 1.25mm mesh. The cause of the complications with numerical stability and convergence were investigated and resolved. However, due to time limitations the fine mesh implementation of the Eulerian model was not completed. Thus, the results from the 1.25mm mesh will be reported for the VOF and algebraic-slip mixture models and the results from the

2.5mm mesh will be reported for the Eulerian model. The time step size used in all cases was fixed at $\Delta t = 5(10^{-5})$ s. This time step size was used for the NS-DEM based models as well. It is expected that the time step size should change when the particle phase is included. However, in the case of the NS-DEM models this was not the case and the same time step size could be used. However, at times the convergence rate was slower in the NS-DEM models in comparison to the NS air-core models.

In Tables 6.1 to 6.3 the average mass flow rate at the underflow and overflow as predicted by the different NS based modelling approaches for three levels of mesh refinement are presented. Furthermore, the respective tables present the error between the predictions and experiment for the average mass flow rate at the underflow and overflow. The coarse mesh (5mm cell size), medium mesh (2.5mm cell size) and fine mesh (1.25mm cell size) results are presented in Tables 6.1 to 6.3, respectively.

The Eulerian model provides more accurate predictions than the VOF and ASM models, in comparison to experiment, for all mesh sizes. On the coarse mesh the RNG turbulence model provides more accurate predictions than the RSM and LES. However, on the medium and fine mesh the RSM model provided superior predictions. Close observation of the results presented in Tables 6.2 and 6.3, reveals that the accuracy of the LES model predictions increased whereas the accuracy of the RSM model predictions decreased as the mesh was refined. This indicates that as the mesh is refined further, the LES model may produce superior predictions. This would produce results congruent with the literature [6, 8, 9] related to the RSM and LES models. The difference between the results presented here and those in [6, 8, 9] is that on the coarse mesh the RNG is a better model and not the RSM and on only medium meshes is the RSM superior.

Figure 6.1 shows the air-core surface as predicted by the three NS based models with the different turbulence models. The various approaches approximately predict the same air-core diameter. As seen in Figures 6.1 and 6.2, the RNG $k-\epsilon$ and RSM models predict the bulb in the air-core near the vortex finder as well as the wavy path of the air-core near the underflow.

However, the LES model does not predict the correct air-core features as revealed from the flow visualisation experiment. It is well known that the

Table 6.1: NS Air-Core Mass Flow Rate Model Comparisons

Model	m_{under} (kg/s)	m_{over} (kg/s)	$m_{under,exp}$ (kg/s)	$m_{over,exp}$ (kg/s)	$ Error_{under} $ (%)	$ Error_{over} $ (%)
Mixture (LES)	0.42	4.79	$0.85^{+0.09+0.06}_{-0.11-0.06}$	$4.38^{+1.01+0.54}_{-0.49-0.54}$	51	9
Mixture (RNG)	0.50	4.76	$0.85^{+0.09+0.06}_{-0.11-0.06}$	$4.38^{+1.01+0.54}_{-0.49-0.54}$	41	9
Mixture (RSM)	0.42	4.80	$0.85^{+0.09+0.06}_{-0.11-0.06}$	$4.38^{+1.01+0.54}_{-0.49-0.54}$	50	10
VOF (LES)	0.41	4.78	$0.85^{+0.09+0.06}_{-0.11-0.06}$	$4.38^{+1.01+0.54}_{-0.49-0.54}$	51	9
VOF (RNG)	0.49	4.69	$0.85^{+0.09+0.06}_{-0.11-0.06}$	$4.38^{+1.01+0.54}_{-0.49-0.54}$	42	7
VOF (RSM)	0.43	4.80	$0.85^{+0.09+0.06}_{-0.11-0.06}$	$4.38^{+1.01+0.54}_{-0.49-0.54}$	49	9
Eulerian (RNG)	0.57	4.71	$0.85^{+0.09+0.06}_{-0.11-0.06}$	$4.38^{+1.01+0.54}_{-0.49-0.54}$	32	7
Eulerian (RSM)	0.52	4.71	$0.85^{+0.09+0.06}_{-0.11-0.06}$	$4.38^{+1.01+0.54}_{-0.49-0.54}$	38	7
Multifluid VOF	0.57	4.71	$0.85^{+0.09+0.06}_{-0.11-0.06}$	$4.38^{+1.01+0.54}_{-0.49-0.54}$	32	7

Table 6.2: NS Air-Core Model Mass Flow Rate Comparisons 2.5mm Mesh

Model	m_{under} (kg/s)	m_{over} (kg/s)	$m_{under,exp}$ (kg/s)	$m_{over,exp}$ (kg/s)	$ Error_{under} $ (%)	$ Error_{over} $ (%)
Mixture (LES)	0.19	5.00	$0.85^{+0.09+0.06}_{-0.11-0.06}$	$4.38^{+1.01+0.54}_{-0.49-0.54}$	78	14
Mixture (RNG)	0.19	4.89	$0.85^{+0.09+0.06}_{-0.11-0.06}$	$4.38^{+1.01+0.54}_{-0.49-0.54}$	78	12
Mixture (RSM)	0.32	4.90	$0.85^{+0.09+0.06}_{-0.11-0.06}$	$4.38^{+1.01+0.54}_{-0.49-0.54}$	62	12
VOF (LES)	0.19	5.02	$0.85^{+0.09+0.06}_{-0.11-0.06}$	$4.38^{+1.01+0.54}_{-0.49-0.54}$	78	15
VOF (RNG)	0.20	4.85	$0.85^{+0.09+0.06}_{-0.11-0.06}$	$4.38^{+1.01+0.54}_{-0.49-0.54}$	77	11
VOF (RSM)	0.33	4.85	$0.85^{+0.09+0.06}_{-0.11-0.06}$	$4.38^{+1.01+0.54}_{-0.49-0.54}$	62	11
Eulerian (RNG)	0.29	4.93	$0.85^{+0.09+0.06}_{-0.11-0.06}$	$4.38^{+1.01+0.54}_{-0.49-0.54}$	66	13
Eulerian (RSM)	0.40	4.83	$0.85^{+0.09+0.06}_{-0.11-0.06}$	$4.38^{+1.01+0.54}_{-0.49-0.54}$	53	10

Table 6.3: NS Air-Core Model Mass Flow Rate Comparisons 1.25mm Mesh

Model	m_{under} (kg/s)	m_{over} (kg/s)	$m_{under,exp}$ (kg/s)	$m_{over,exp}$ (kg/s)	$ Error_{under} $ (%)	$ Error_{over} $ (%)
Mixture (LES)	0.21	4.97	$0.85^{+0.09+0.06}_{-0.11-0.06}$	$4.38^{+1.01+0.54}_{-0.49-0.54}$	75	13
Mixture (RNG)	0.13	5.05	$0.85^{+0.09+0.06}_{-0.11-0.06}$	$4.38^{+1.01+0.54}_{-0.49-0.54}$	85	15
Mixture (RSM)	0.28	4.95	$0.85^{+0.09+0.06}_{-0.11-0.06}$	$4.38^{+1.01+0.54}_{-0.49-0.54}$	67	13
VOF (LES)	0.22	4.96	$0.85^{+0.09+0.06}_{-0.11-0.06}$	$4.38^{+1.01+0.54}_{-0.49-0.54}$	74	13
VOF (RNG)	0.15	4.98	$0.85^{+0.09+0.06}_{-0.11-0.06}$	$4.38^{+1.01+0.54}_{-0.49-0.54}$	83	13
VOF (RSM)	0.28	4.89	$0.85^{+0.09+0.06}_{-0.11-0.06}$	$4.38^{+1.01+0.54}_{-0.49-0.54}$	67	12

LES requires finer meshes than RANS models to produce reliable results. Thus, the LES model may require a finer mesh than the 1.25mm mesh to produce accurate predictions. This is substantiated by the trend in Tables 6.1 - 6.3 where it can be seen that the LES predictions improve, in relation to the RANS predictions, as the mesh is refined. The Eulerian model with the RSM turbulence model provides the superior prediction, in comparison to experiment, of the air-core geometrical features.

It should be noted that the Eulerian model produced an air-core with less false diffusion at the air-water interface on a coarser mesh than the VOF and ASM model. Based on Figure 6.1.g. and Figure 6.1.h. the RSM model provided a more-distinct air-water interface than the RNG $k-\epsilon$ model, when coupled with the Eulerian model. It is expected that the Eulerian model would have less false diffusion and a more distinct air-water interface because the Eulerian model solves the velocity field for each phase as separate interpenetrating continua, whereas the VOF and ASM models are based on a shared velocity formulation which will be more susceptible to produce false diffusion.

The underflow and overflow mass flow rate displays a transition from an unsteady to “quasi”-steady behaviour as seen in Figures 6.3 and 6.4. The experimental results from Chapter 5 show that the hydrocyclone shifts from an unsteady to “quasi”-steady behaviour. The average mass flow rates have been used as a primary metric for comparison to experiment. Due to the “quasi”-steady nature of the predictions as well as the actual hydrocyclone behaviour, the maximum and minimum mass flow rates needs to be used to validate and select the most accurate of the approaches. The fluctuating mass flow predictions from the models are line with experiment because the mass flow rates in a real hydrocyclone fluctuates due to an unsteady pressure gradient, between the inlet and outlets, as well as turbulent fluctuations within the hydrocyclone.

Figures 6.5, 6.7 and 6.9, show the mass flow rate at the overflow as a function of time for all the models for the 5mm, 2.5mm and 1.25mm meshes. In all cases the overflow mass flow rates in the “quasi”-steady period (1.5s flow-time onwards) remains within the bounds of the minimum and maximum mass

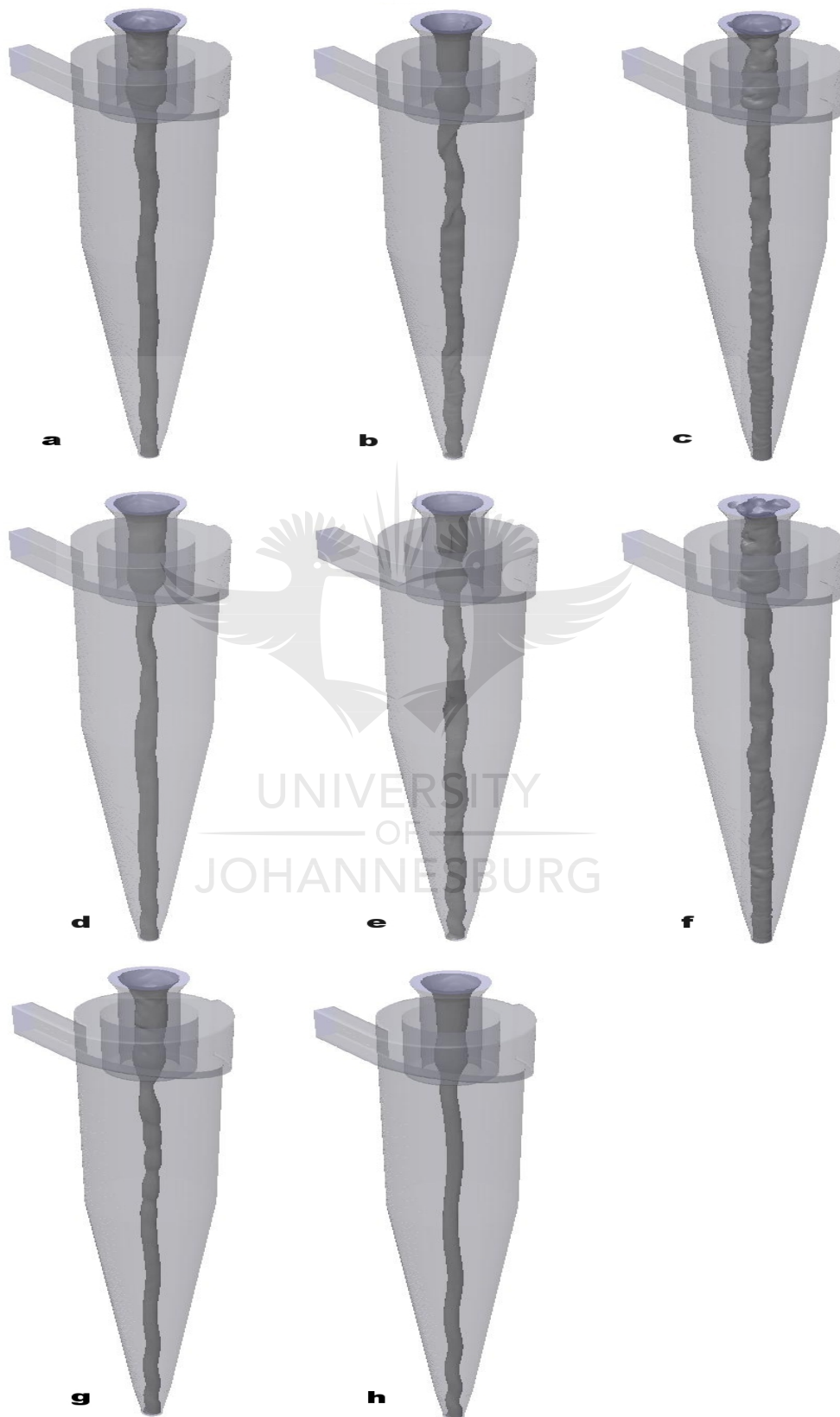


Figure 6.1: Iso-Surface of volume fraction of air from the NS based Model at flow-time $t = 2s$: a) VOF with RNG $k - \epsilon$, b) VOF with RSM, c) VOF with LES, d) Mixture with RNG $k - \epsilon$, e) Mixture with RSM, f) Mixture with LES, g) Eulerian with RNG $k - \epsilon$ and h) Eulerian with RSM



Figure 6.2: Air-core in perspex half scale hydrocyclone - green dye added to reveal air-core

flow rate as determined from the experiment results. Thus, quantitatively all the models provide accurate predictions in relation to the experiments. Another significant outcome is that coarse mesh models can provide accurate initial approximations.

However, this is not the case of the underflow predictions. As seen in Figures 6.6, 6.8 and 6.10, all of the models noticeably under-predict the underflow mass flow rate. Based on the results in Tables 6.1 - 6.3 and Figures 6.5 - 6.10 it would appear that mesh refinement leads to less accurate results which is counter-intuitive. However, the decrease in accuracy of the models with a decrease in cell size is related rather to a decrease in accuracy as a consequence of the decrease in mesh quality rather than mesh size. This will

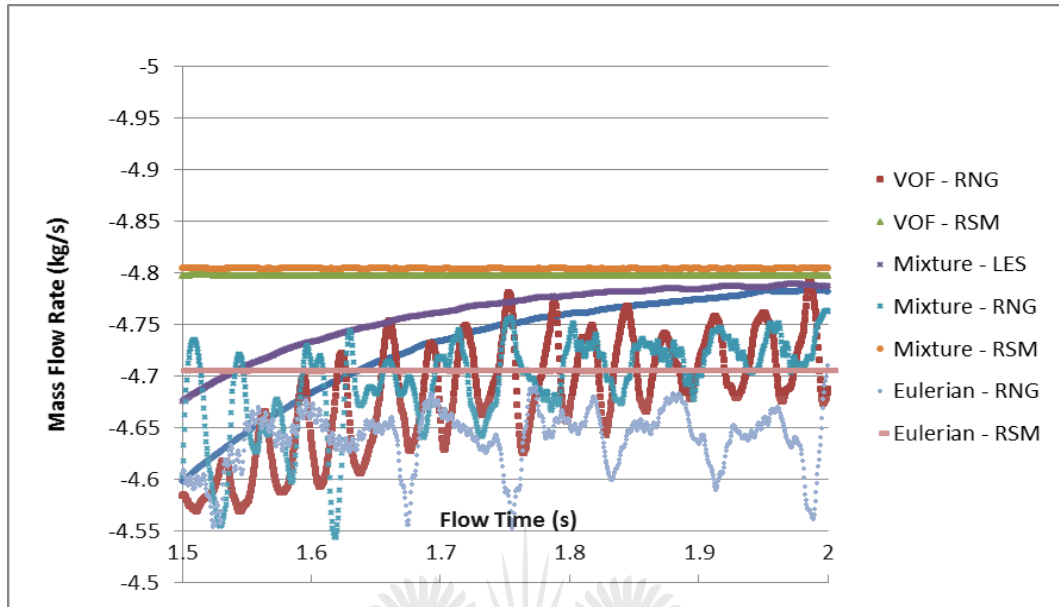


Figure 6.3: “Quasi”-steady behaviour at the overflow as illustrated by overflow mass flow rate as predicted by the NS based models

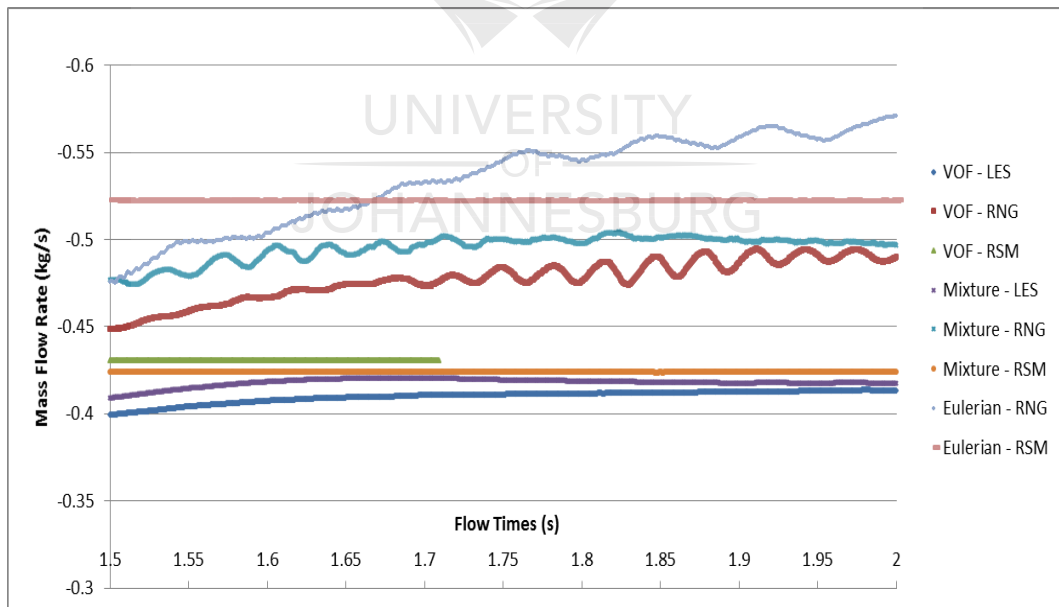


Figure 6.4: “Quasi”-steady behaviour at the underflow as illustrated by underflow mass flow rate as predicted by the NS based models

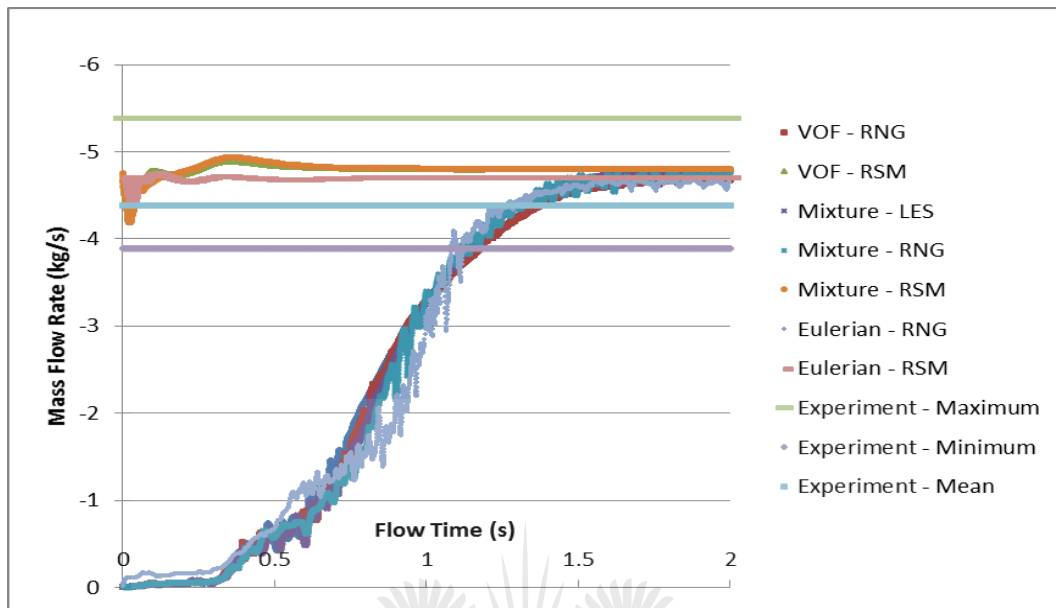


Figure 6.5: Overflow mass flow rate as predicted by the NS based models - mesh size 5mm

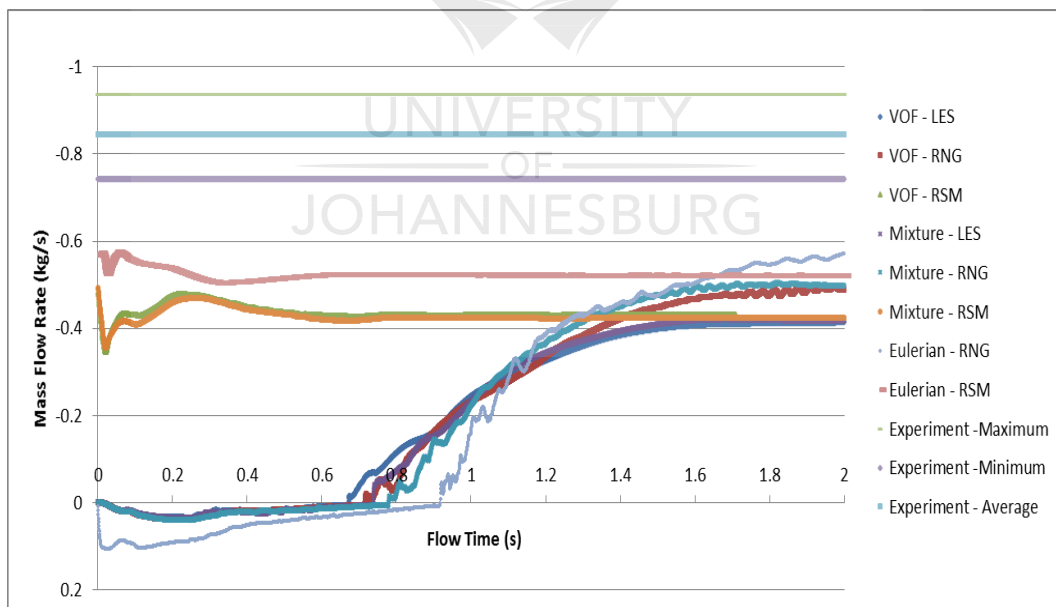


Figure 6.6: Underflow mass flow rate as predicted by the NS based models - mesh size 5mm

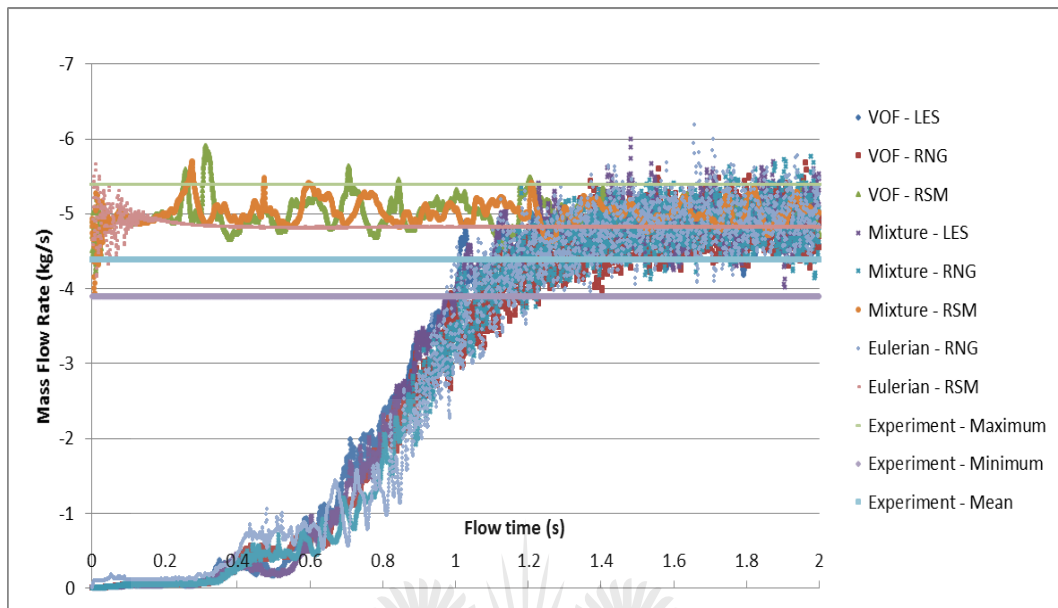


Figure 6.7: Overflow mass flow rate as predicted by the NS based models - mesh size 2.5mm

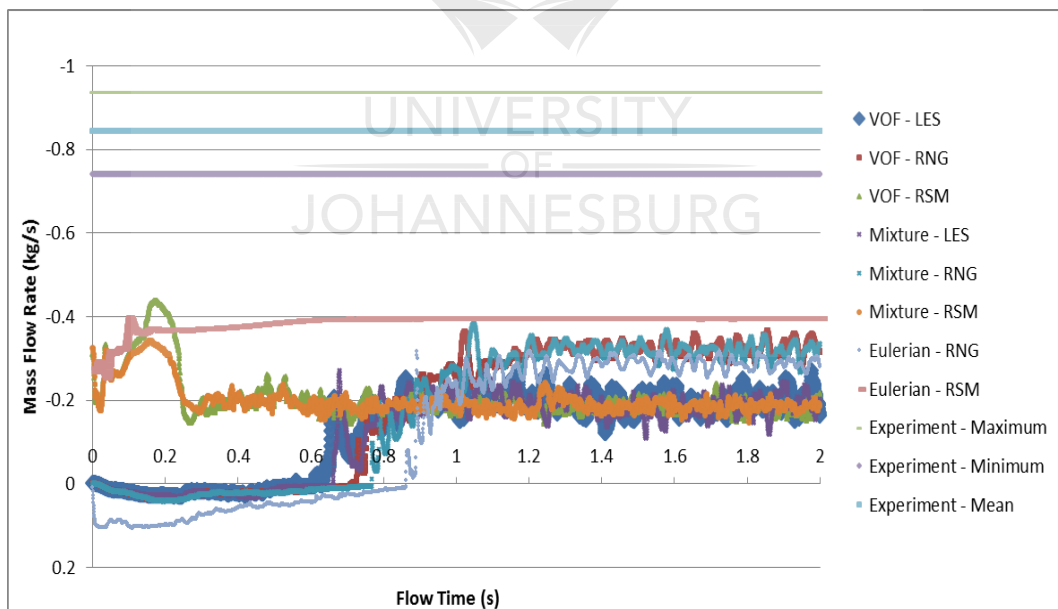


Figure 6.8: Underflow mass flow rate as predicted by the NS based models - mesh size 2.5mm

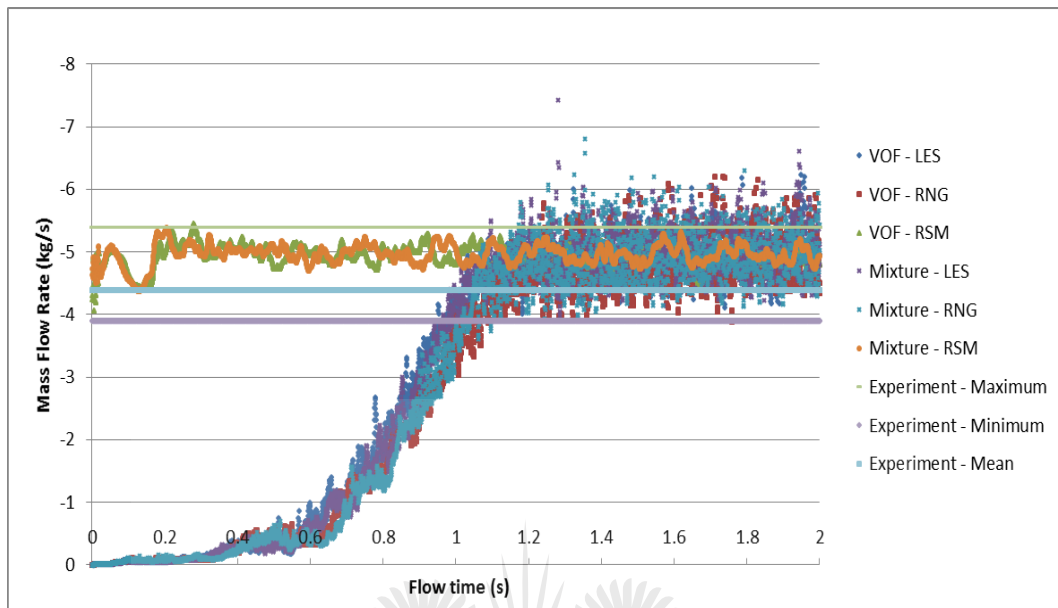


Figure 6.9: Overflow mass flow rate as predicted by the NS based models - mesh size 1.25mm

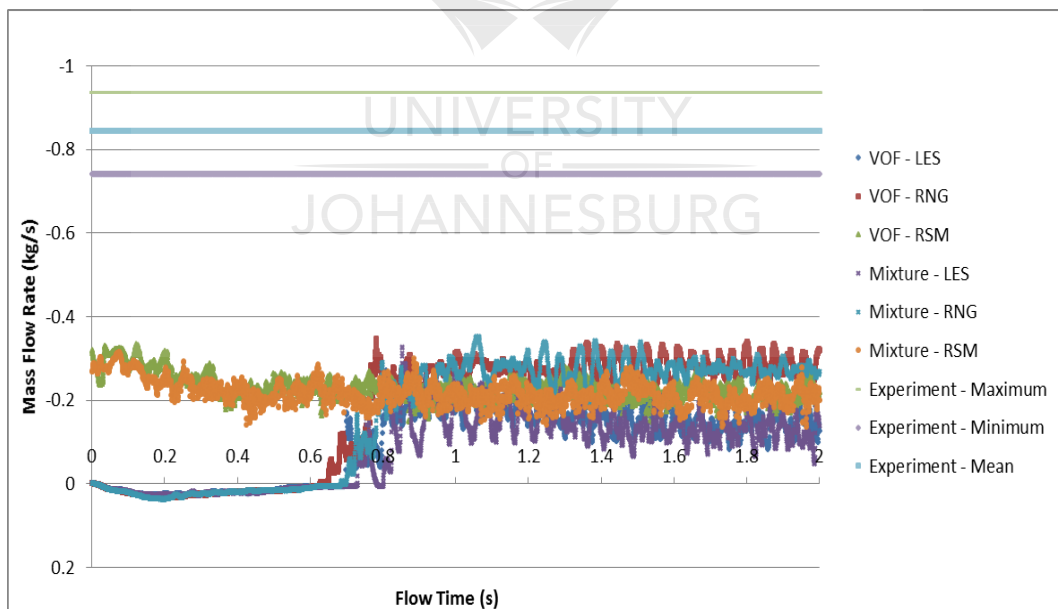


Figure 6.10: Underflow mass flow rate as predicted by the NS based models - mesh size 1.25mm

be discussed in detail in 6.1.2.

The reason for the large error in the underflow mass flow rate predictions is that the particle phase is omitted at this stage in the modelling. The error reduces to 7% for the underflow and 2% for the overflow as reported in Section 6.2. Thus, in summary the reason for the “prohibitively large difference” between the underflow mass flow rate predictions and experiment is that at this point the effect of the particles on the water phase is not captured. Thus, future validation of air-core models should be done using experiments whereby the particles are not included in the experiment. The effect of the particles on the fluid flow is described in detail in Section 6.2.

6.1.2 Numerical Stability and Convergence of the Eulerian Model

The Eulerian model posed significant numerical stability and convergence problems. The numerical stability diminished as the mesh was refined. Initially solver changes were made to improve the stability. The solver changes related to reducing the under-relaxation factors for the pressure, turbulence and continuity variables; reducing the time step size and changing the discretisation scheme to first order upwind. These changes did not improve the numerical stability. An attempt to provide a stable initial mixture model based solution as the initial condition for the Eulerian model was made and did not improve the numerical stability. Thus, an investigation into the numerical stability was done. The investigation focussed on two primary questions, namely:

- What is the underlying cause or source of the numerical instability?
- What methods can be used to overcome the numerical instability?

Closer observation of the models (including the VOF and Mixture models) revealed that a high velocity region ($> 20\text{m/s}$) formed in the core of the hydrocyclone. This high velocity region was independent of the model used. The source of the numerical instabilities is related to how the rise in velocity leads to a rise in the turbulent kinetic energy which in turn leads to a rise in the turbulent viscosity and subsequently the turbulent viscosity ratio (beyond the limit of 10^5).

The turbulent viscosity is given as $\mu_t = \rho C_\mu (k^2/\epsilon)$. In all the multiphase models the density is constant and C_μ is a constant related to the turbulence model. Thus, the turbulent viscosity is directly proportional to the square of the turbulent kinetic energy and inversely proportional to the turbulent dissipation rate. The turbulent viscosity ratio is given as μ_t/μ . The molecular viscosity is constant in all the models. Thus, the turbulent viscosity ratio is also directly proportional to the square of the turbulent kinetic energy and inversely proportional to the turbulent dissipation rate. Thus, a rise in the turbulent kinetic energy due to an increase in the velocity would result in an increase in the turbulent viscosity and viscosity ratio. Thus, the turbulent kinetic energy and turbulent viscosity ratio rises to infinity leading to divergence.

This occurs in the air-core region and is very rapid as it can occur within a period of two time steps. Figure 6.11 - 6.14 shows the turbulent kinetic energy, turbulent dissipation rate, axial velocity and turbulent viscosity ratio as a function of the normalised z -co-ordinate two time steps prior to divergence. The data is plotted in the centre (core) and along the length of the hydrocyclone. The independent variable (the normalised z -co-ordinate) is plotted along the y -axis to illustrate the variation of the dependent variables as a function of the position along the length of the hydrocyclone. At this point all of the above variables are stable. The turbulent kinetic, energy, axial velocity and turbulent dissipation rate are notably higher in the Eulerian model. However, the turbulent viscosity ratio is significantly lower in the Eulerian model. At the point of divergence a rapid rise in axial velocity causes the turbulent kinetic energy and subsequently the turbulent viscosity and viscosity ratio to rise to infinity in the Eulerian model which does not occur in the VOF and ASM models.

The instability of the multiphase models in respect to turbulent viscosity ratio has been noted in the ANSYS Fluent Theory Guide [13] without mentioning the source of the instability. However, ANSYS [13] only makes a recommendation that in the case where the ratio exceeds 10^3 in the VOF model then the compressive interface capturing scheme for arbitrary meshes (CICSAM) should be used instead of the Geo-reconstruct scheme. In this study this issue does not appear in the VOF and ASM model despite the viscosity ratio exceeding 10^3 in those models. In this study the issue arises in the Eulerian-Eulerian models. Thus, the ANSYS proposed solution is not relevant in this case. The Eulerian Eulerian model may be more susceptible

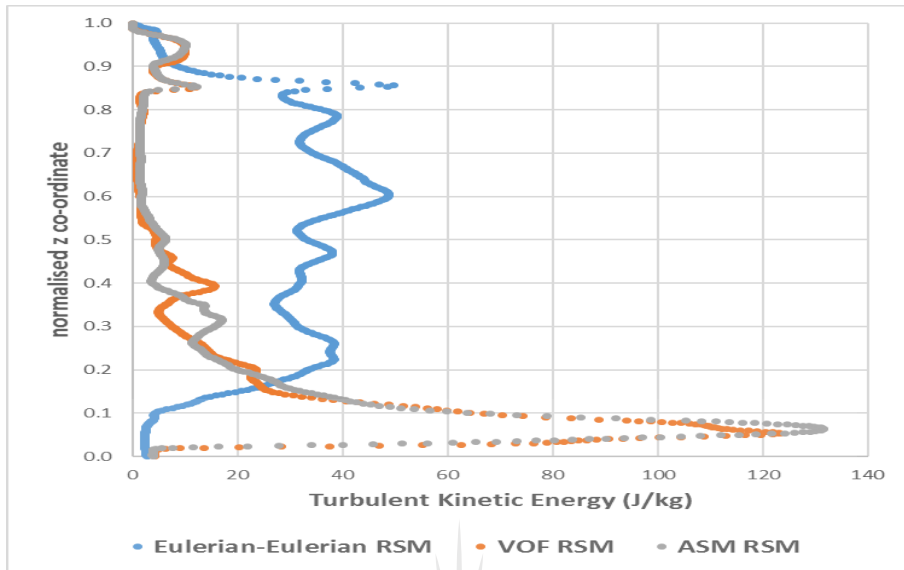


Figure 6.11: Turbulent kinetic energy as a function of the normalised z -co-ordinate two time steps before divergence for the Eulerian model compared to stable VOF and ASM based predictions

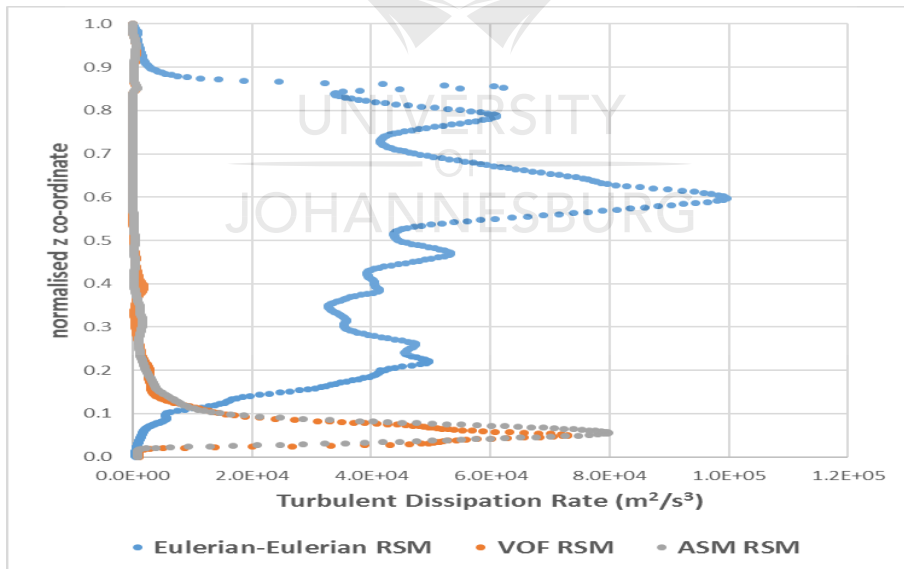


Figure 6.12: Turbulent dissipation rate as a function of the normalised z -co-ordinate two time steps before divergence for the Eulerian model compared to stable VOF and ASM based predictions

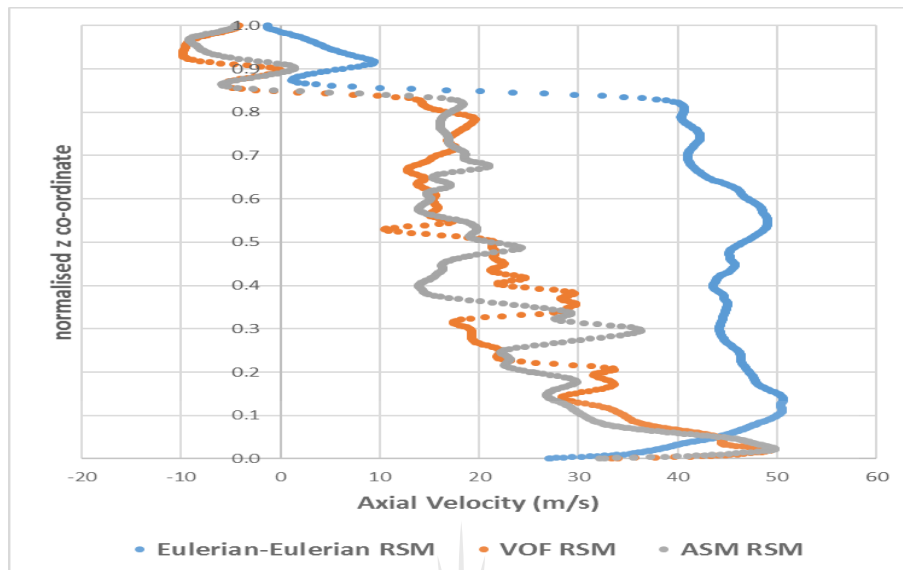


Figure 6.13: Axial velocity as a function of the normalised z -co-ordinate two time steps before divergence for the Eulerian model compared to stable VOF and ASM based predictions

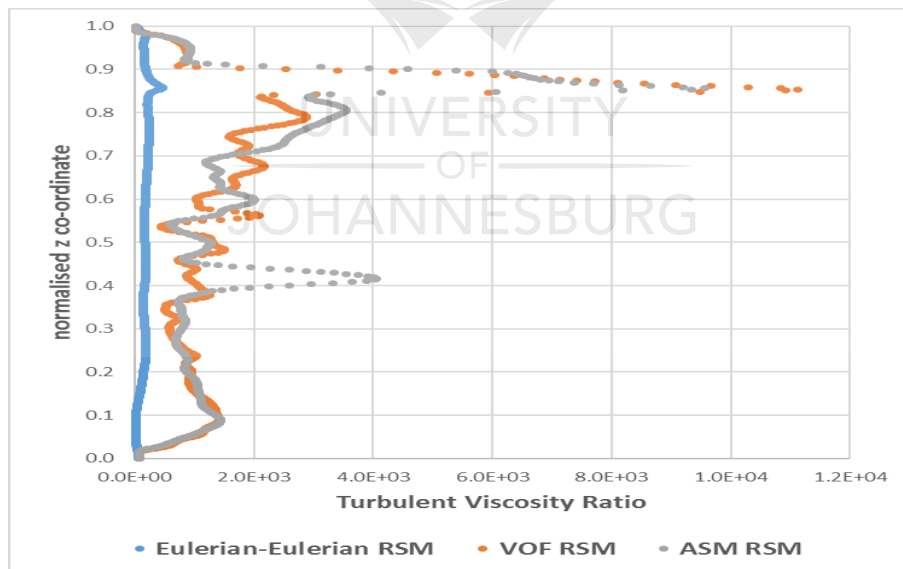


Figure 6.14: Turbulent viscosity ratio as a function of the normalised z -co-ordinate two time steps before divergence for the Eulerian model compared to stable VOF and ASM based predictions

to velocity related instabilities than the VOF and ASM models because it does not use a shared velocity formulation as in the VOF and ASM models. Instead the Eulerian-Eulerian model uses a full multiphase velocity formulation with a shared pressure, thus, the velocity field may behave differently from the VOF and ASM models.

Whilst the VOF and Mixture models produced the same high velocity region, they did not suffer from the numerical instability. However, the VOF, Mixture and Eulerian models underflow predictions were affected by the poor aspect ratios in the core. The increase in aspect ratio with decrease in cell size results in decreased accuracy of the underflow predictions with decreasing cell size. Thus, it is advised that the mesh is constructed to ensure that the aspect ratios must be kept below 10 to ensure stability in the computation and to ensure accurate underflow predictions. If this is not adhered to, an excessively high velocity region forms in the core of the hydrocyclone causing numerical instability and poor underflow predictions.

In the high velocity region region the mesh had high aspect ratios (> 10), which would result in the high velocity predictions in that region. The aspect ratios in that region remained above 10 when the cell size was decreased. ANSYS [13, 14] recommends that the aspect ratios in the far-field are kept below 5 to ensure that the axial velocities predictions are not unphysical. It is common practice to use a mesh with higher aspect ratios than 5 for most flows. However, in the case of the hydrocyclone the high aspect ratios lead to high velocities in the axial direction causing the turbulent viscosity ratio to increase leading to divergence [13, 14]. Furthermore, this could lead to poor predictions of the separation which is prominent at the air-core interface. As seen in Figure 6.15, the high aspect ratio cells (> 10) are prominent in the core of the hydrocyclone and particularly near the underflow.

Thus, a test model was setup for the Eulerian-RNG case. A mesh with the base size of 5mm was constructed with focus placed on reducing aspect ratios in the core of the hydrocyclone. The Eulerian-RNG model was implemented on the original 5mm mesh and the 5mm mesh with reduced aspect ratios. The cell count increased from 106 000 to 211 000 due to reducing the aspect ratios. The maximum aspect ratio in the domain reduced from 32 to 16. In addition, the region with cells with aspect ratio > 10 reduced significantly, as seen in Figure 6.15.

The reduction in aspect ratios resulted in a reduction in the high velocity

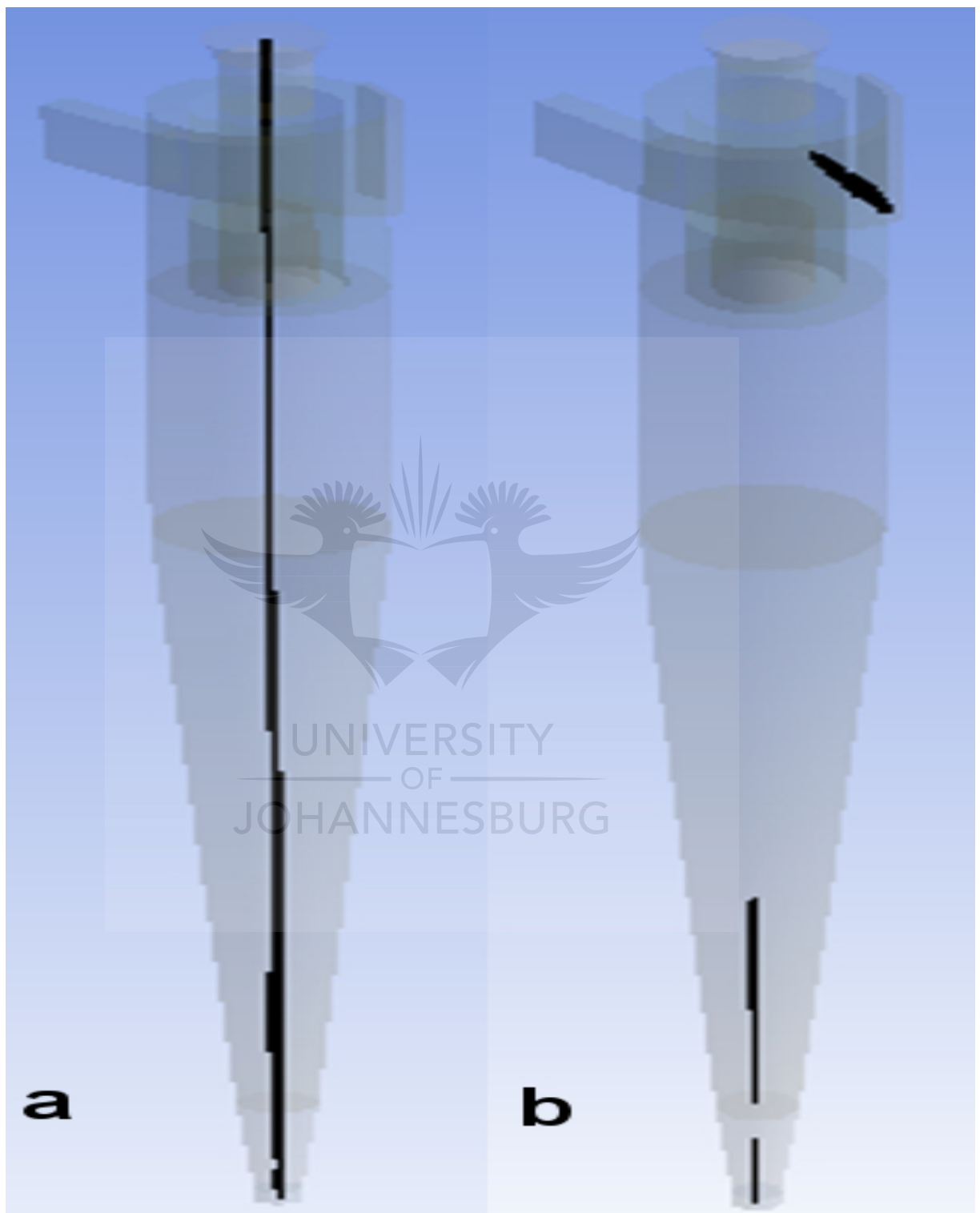


Figure 6.15: Cells with aspect ratio equal to or above 10 on mesh with cell size a) 5mm and b) 5mm with reduced aspect ratio

region in the core, as seen in Figure 6.16.a. and c. Furthermore, the maximum velocity in the core reduced by approximately 20m/s, as seen in Figure 6.16.a. and c. For comparison the 2.5mm mesh produced the largest high velocity region and the highest velocity of the models as seen in Figure 6.16.b. Based on informal discussions with ANSYS support (Qfinsoft Pty Ltd), they control for this by introducing a velocity limiter of 50m/s. The upper limit of 50m/s appears to be the threshold for stability in the sense that if the velocities exceed this limit, in the case of the Eulerian models, the turbulent viscosity ratio exceeds 10^5 which leads to divergence.

The model with the reduced aspect ratio completed without any stability problems and it did not require any changes to the solver. However, the original 5mm and the 2.5mm mesh required a reduction in the under-relaxation factors for the pressure, turbulence and continuity variables and changing the discretisation scheme to first order upwind to ensure convergence.

Thus, two solutions are proposed namely the improvement of mesh quality or by introducing a velocity limiter. The numerical instability was observed to occur when the velocity in the core of the hydrocyclone exceeds 50m/s. This observation was made independently in this study and and by the ANSYS support (Qfinsoft Pty Ltd) without collaboration. Thus, the proposed solution based on the improvement of the aspect ratios of the cells in the core of the hydrocyclone and the proposed solution by the ANSYS support (Qfinsoft Pty Ltd) which is to introduce a velocity limiter are mentioned to contrast the two potential options to resolve the issue.

A potential third solution is to directly limit the turbulent kinetic energy from approaching infinity so that the turbulent viscosity (and subsequently the viscosity ratio) does not reach unstable levels which could cause divergence. This solution has not been tested in this study. However, it would require the limiting of the production of turbulent kinetic energy.

A model was setup by placing the overflow boundary further away. The overflow boundary was placed, arbitrarily, four times the overflow diameter, away from the original position used in the study. This lead to a three times slower convergence rate (iterations required to reach convergence per time step) for the Eulerian-Eulerian RNG $k - \epsilon$ model. The convergence rate was unchanged in the Eulerian-Eulerian RSM model.

In terms of the numerical stability a significant reduction in the velocities in

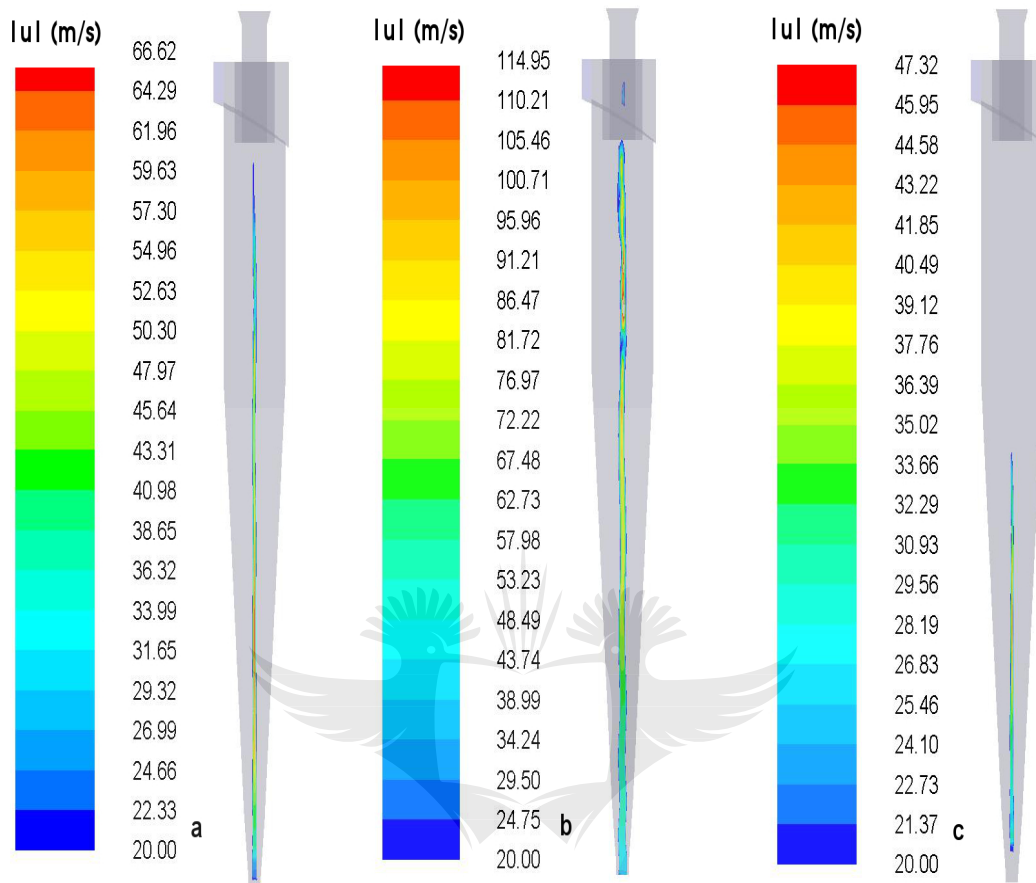


Figure 6.16: High velocity region for Eulerian RNG model on mesh with cell size a) 5mm, b) 2.5mm and c) 5mm with reduced aspect ratio

the core of the hydrocyclone was observed improving numerical stability. The shifting of the overflow boundary lead to a velocity of $< 20\text{m/s}$ in the core for the Eulerian-Eulerian RSM model as seen in Figure 6.17. However, shifting of the overflow boundary attenuated the ingress of air from the overflow leading to incomplete air-core formation as seen in Figure 6.18. Thus, this option is not suitable as a means to improve numerical stability as it leads to incomplete air-core formation.

The placement of the overflow boundary had no impact on the fluctuations (noise) observed in Figure 6.3 The noise is pronounced in the case of the RNG $k - \epsilon$ model regardless of multiphase model used. However, the fluctuations

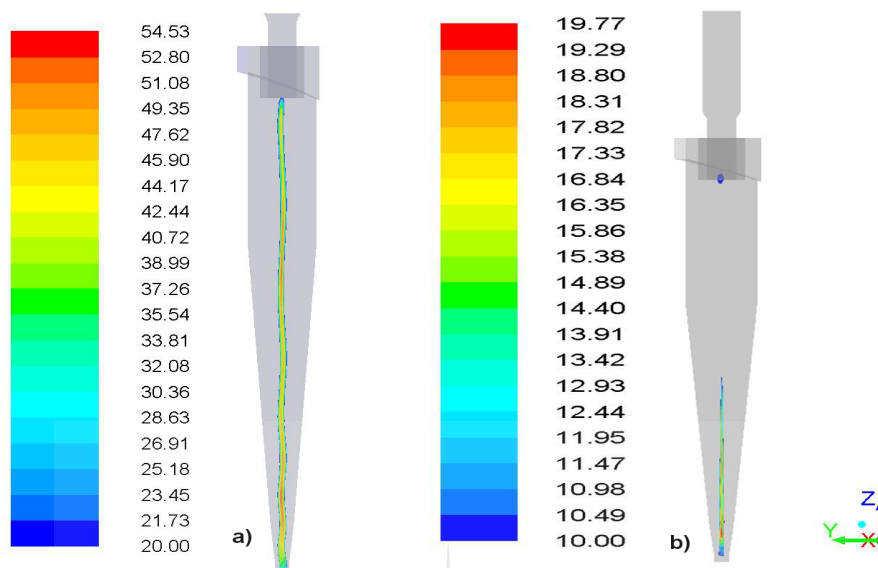


Figure 6.17: Comparison of the velocities in the core of the hydrocyclone in a) original Eulerian RSM model and b) Eulerian RSM model with shifted overflow boundary



Figure 6.18: Comparison of air-core surface in a) original Eulerian RSM model and b) Eulerian RSM model with shifted overflow boundary

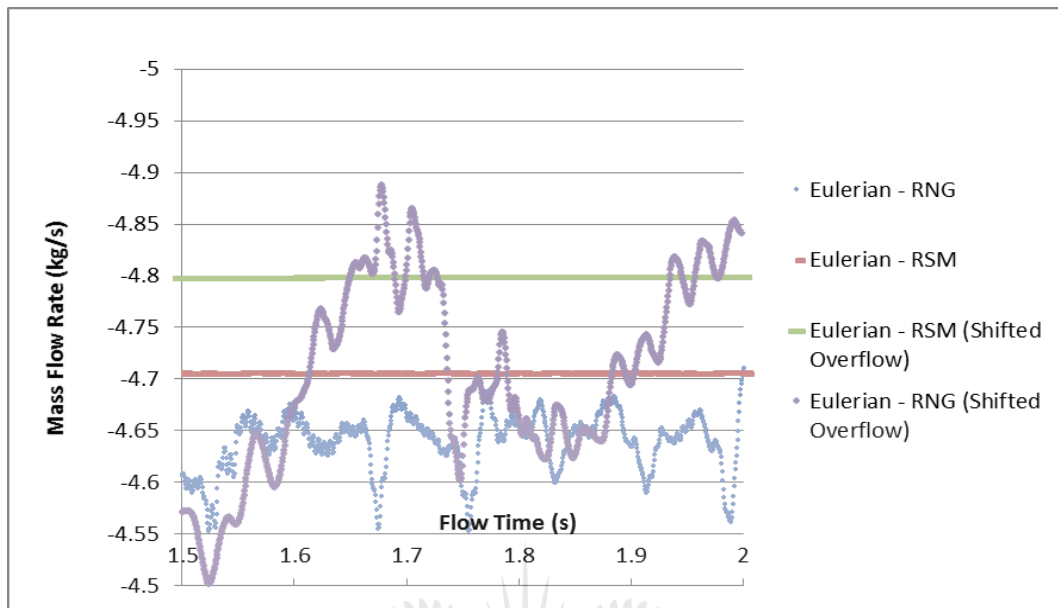


Figure 6.19: “Quasi”-steady behaviour at the overflow as illustrated by overflow mass flow rate as predicted by the Eulerian models for different overflow boundary positions

are far less pronounced when the RSM and LES models are used. This can be seen upon closer inspection of Figure 6.3. Furthermore, the shifting of the overflow boundary still resulted in pronounced fluctuations when the RNG $k - \epsilon$ model is used whilst the fluctuations are far less pronounced when the RSM model is used. The shifting of the overflow boundary increased the fluctuations in the case of the RNG $k - \epsilon$ model. Thus, it can be concluded that the fluctuations are a result of turbulence and not due to boundary related instabilities in the model. A comparison between the fluctuations in Figure 6.3 and the cases with the shifted overflow boundary are given in Figure 6.19.

6.1.3 LBM-VOF Model Predictions

The LBM-VOF model failed to capture air-core formation in the hydrocyclone. Figure 6.20 illustrates the volume of air in the hydrocyclone at three different flow-times. At $t = 0$ s the hydrocyclone is filled with air. As water

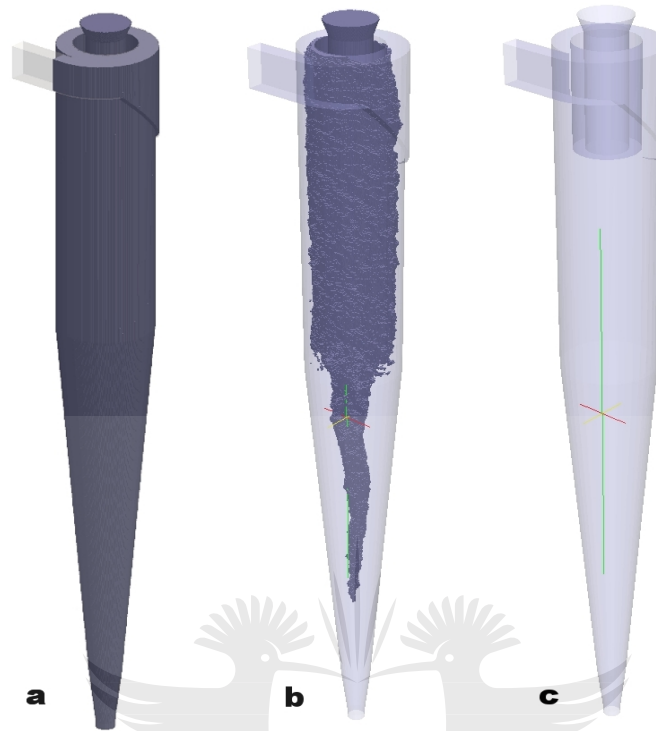


Figure 6.20: Iso-Surface of volume fraction of air from the LBM-VOF model at flow-time a) $t = 0.0s$, b) $t = 0.5s$ and c) $t = 2.0s$.

is pumped into the hydrocyclone, water fills the hydrocyclone pushing the air out of the hydrocyclone as seen at $t = 0.5s$. This continues to occur until the entire hydrocyclone is filled with water (at $t = 2s$).

There are two reasons as to why the LBM-VOF fails to capture air-core formation in the hydrocyclone. Air-core formation occurs due to the hydrocyclone being “fed” with air from reverse flow of atmospheric air at the underflow and overflow due to the suction pressure formed in the core of the hydrocyclone. The continuous reverse flow of air is transported into the core of the hydrocyclone in turn feeding and preserving the air-core. In the LBM-VOF model the gas phase is modelled as an empty region as a result of not being assigned a fluid equation. As a result of this modelling assumption, the gas phase does not have a velocity field. By assigning a backflow volume fraction of air condition at the outlets’ reverse flow sites, the volume fraction of air is set to unity if the velocity at an outlet face is normal into

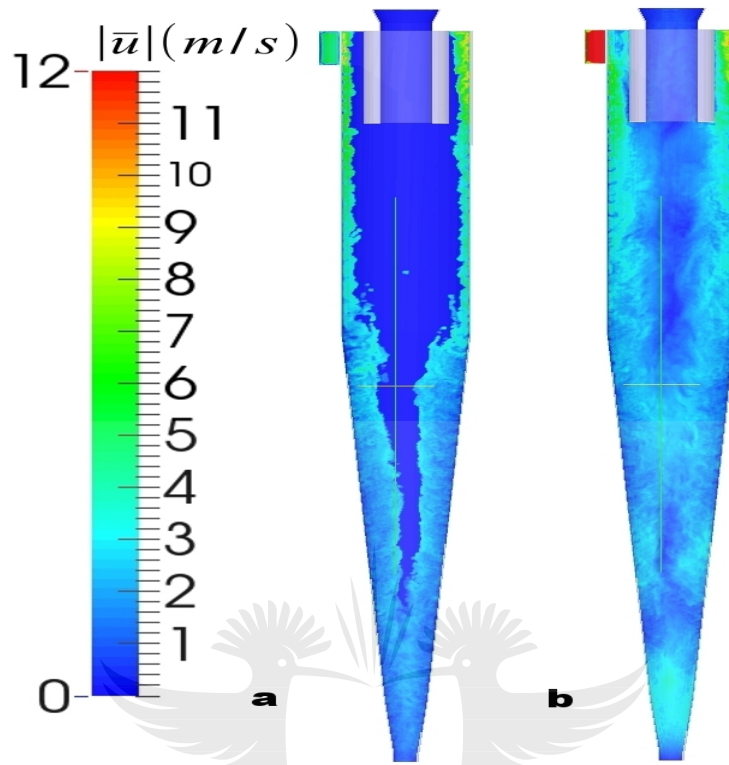


Figure 6.21: Contours coloured by velocity magnitude ($|u|/m/s$) on the plane $x = 0$ from the LBM-VOF model at flow-time a) $t = 0.5s$, b) $t = 2.0s$

the boundary (reverse flow). However, once the volume fraction of air at that site is changed to unity that site no longer has a velocity and the air cannot be transported into the hydrocyclone. Thus, it cannot feed the hydrocyclone with a continuous supply of air leading to the dissipation of the air-core as seen in Figure 6.20.

Despite the maturity of the Palabos library, the LBM-VOF implementation is relatively new, with basic boundary condition implementations for the outlets when coupled with the LBM-VOF model. Thus, the pressure outlet conditions are not fully implemented with the LBM-VOF model. As a result the outlet boundaries do not behave as a proper pressure outlet when coupled with the LBM-VOF model in Palabos. As seen in Figure 6.21, the water flows to the underflow first. However, in a hydrocyclone the water should initially experience a short-cut flow whereby the water is separated into two fluid streams with the larger mass fraction of water being forced into the barrel,

Table 6.4: Air-Core Model Mass Flow Rate Comparisons for LBM-VOF Model

Outlet α_{air}	m_{under} (kg/s)	m_{over} (kg/s)	$m_{under,exp}$ (kg/s)	$m_{over,exp}$ (kg/s)	$ Error_{under} $ (%)	$ Error_{over} $ (%)
0.5	0.51	4.50	$0.85^{+0.09+0.06}_{-0.11-0.06}$	$4.38^{+1.01+0.54}_{-0.49-0.54}$	39	3
1	0.43	4.14	$0.85^{+0.09+0.06}_{-0.11-0.06}$	$4.38^{+1.01+0.54}_{-0.49-0.54}$	51	6

through the vortex finder and out through the overflow.

If the volume fraction of air at the outlet was varied between $\alpha_{air} = 0$ and $\alpha_{air} = 1$ the same result is achieved apart from two subtle differences. The first difference is that when the volume fraction of air is greater than 0 there is a volume of air at the overflow waiting to be entrained into the domain. Furthermore at approximately 0.5s flow-time there is a column of air near the overflow, apart from the air bubbles in the domain. This can be seen in Figure 6.22. However, for the reasons given above the air-core disappears once the model has reached steady state ($t = 2s$).

Although, the LBM-VOF model could not predict air-core formation, it did offer reasonable predictions for the mass flow rate at the overflow and underflow. Table 6.4 shows the accuracy of the model predictions against experiment. From this it implies that if α_{air} is fixed at 0.5 at the outlet the best results are achieved. The results in Table 6.4 are based on the average values in the “quasi” - steady-state period of the simulations.

Figure 6.23 indicates that if α_{air} is fixed at 0.5 at the outlets the predicted mass flow rate at the overflow remains within the maximum and minimum mass flow rates determined by experiment during the “quasi” - steady-state period of the simulations. However, the model predictions, when α_{air} is fixed at 1 at the outlets, does not stay within these bounds and has random unphysical spikes in the mass flow rate.

Both models under-predict the mass flow rate at the underflow in relation to experiment as seen in Figure 6.24. However, in both cases the underflow predictions are of similar accuracy to the NS based model predictions, specifically the Eulerian model predictions. This may be an indication that a higher mesh density needs to be used in the underflow region in both the

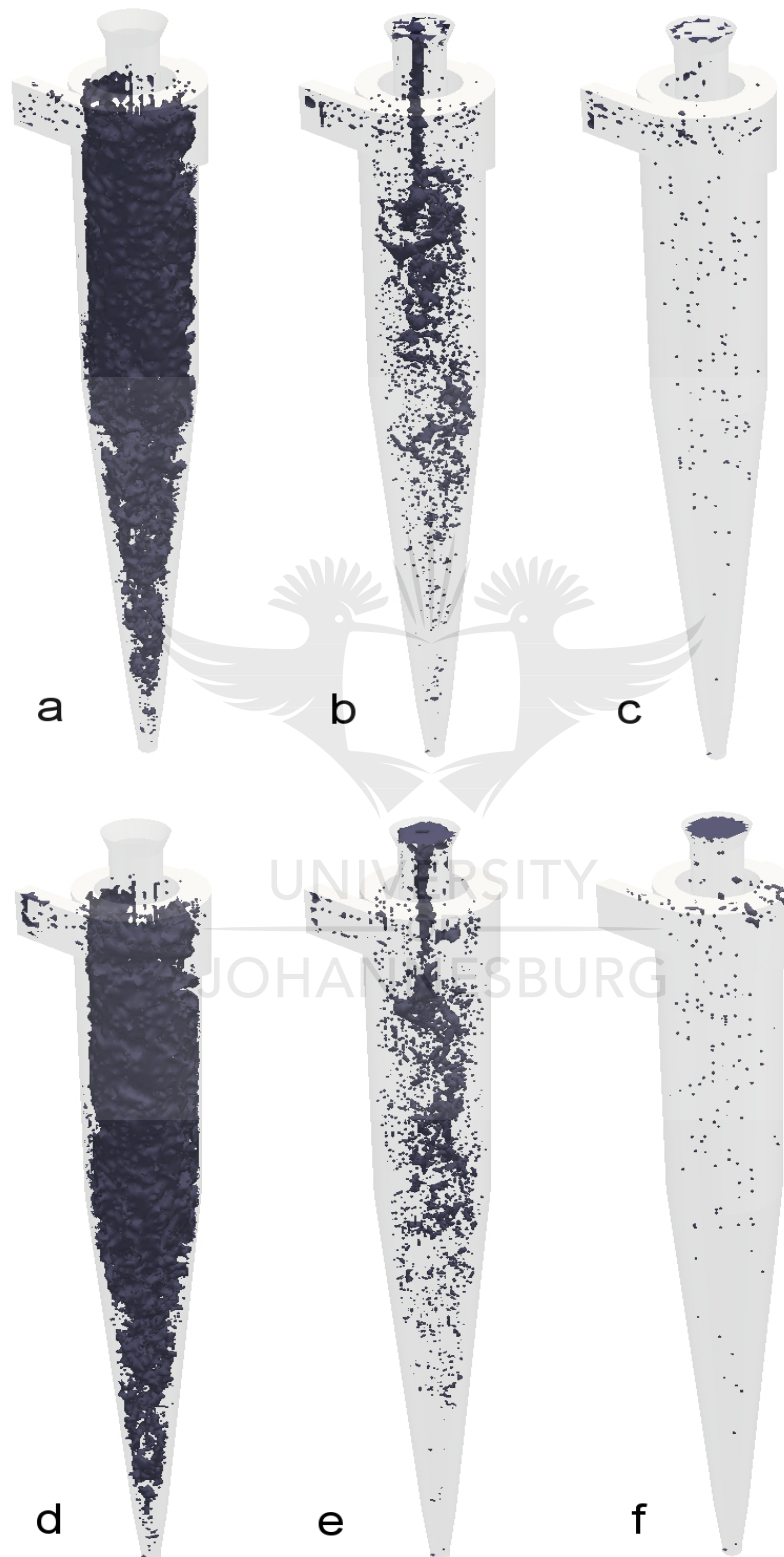


Figure 6.22: Iso-Surface of volume fraction of air from the LBM-VOF model: a) $\alpha_{air} = 0.5$ at $t = 0.5s$, b) $\alpha_{air} = 0.5$ at $t = 1s$, c) $\alpha_{air} = 0.5$ at $t = 2s$, d) $\alpha_{air} = 1$ at $t = 0.5s$, e) $\alpha_{air} = 1$ at $t = 1s$ and f) $\alpha_{air} = 1$ at $t = 2s$

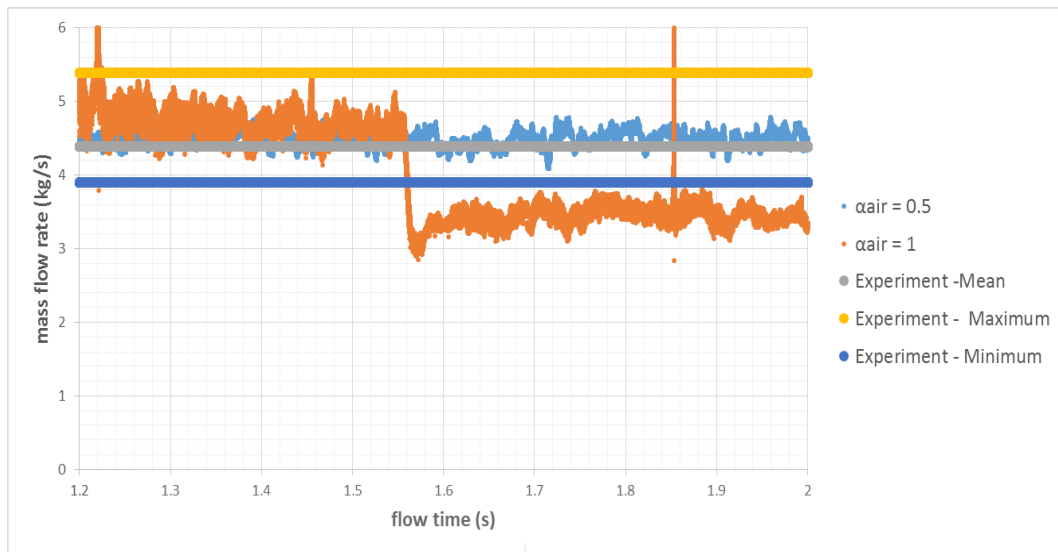


Figure 6.23: Overflow mass flow rate as predicted by the LBM based models for α_{air} at the outlets set at 1 and 0.5

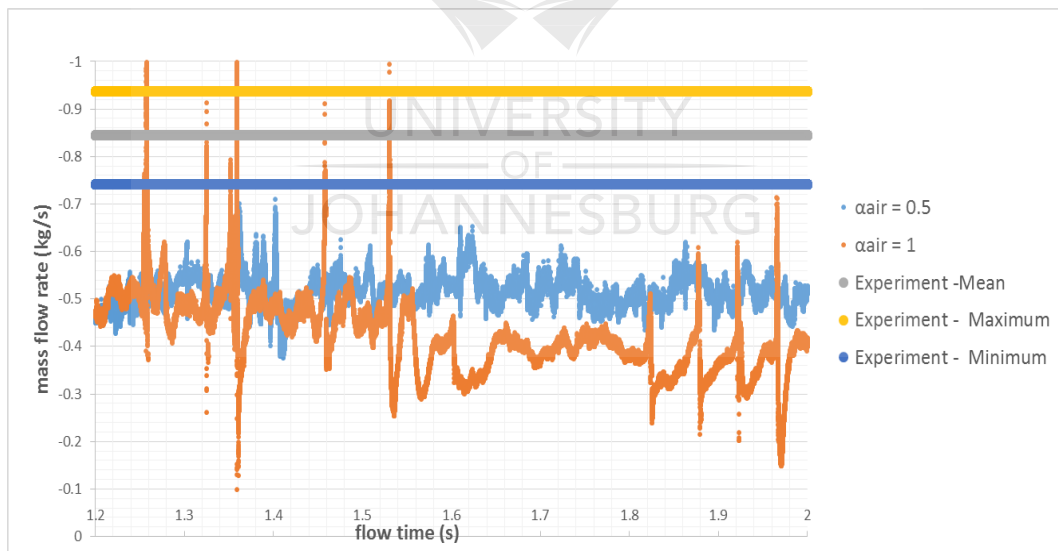


Figure 6.24: Underflow mass flow rate as predicted by the LBM based models for α_{air} at the outlets set at 1 and 0.5

NS and LBM approaches.

The LBM-VOF models required significant computational effort. A simulation using a cell size of 3.9mm (287 595 cells) with a time step size of 1ns took approximately 38 hours to complete on 64 cores with 80GB RAM. A simulation using a cell size of 0.97mm (16 455 200 cells) with a time step size of 1ns took approximately 240 hours to complete on 128 cores with 160GB RAM. As a result of this, the model with α_{air} fixed at 0 was run at various cell sizes and the results presented are for the fine mesh (0.97mm) and the models with α_{air} fixed at 0.5 and 1 were run on the coarse mesh (3.9mm). However, the results presented were not qualitatively and quantitatively affected by the mesh.

The LBM-VOF model failed to capture the key physics of air-core formation in the hydrocyclone. Furthermore, the LBM-VOF model proved impractical from a computational efficiency perspective. However, an initial single phase implementation of the LBM to the hydrocyclone captured the key physics, namely, the early short-cut flow as well as the suction pressure profile in the core of the hydrocyclone. The single phase implementation of the LBM to the hydrocyclone proved computationally efficient and provided a computational advantage over the NS based implementation of the single phase flow.

6.1.3.1 Single Phase Flow Model Predictions

A single phase LBM model of the hydrocyclone was implemented prior to the air-core and particle modelling to ensure that the LBM could model the basic water flow field before implementing the air-core and particle models, respectively. The results indicate that the LBM model was able to reproduce the same physics as the NS based model. In this section a comparison of the LBM and NS based models of the single phase water flow field will be made. It should be noted that at this point in the study the hydrocyclone used was the same as that used in Appendix B. The boundary conditions are the same as in Chapter 3 and Chapter 4.

The models were implemented on three mesh sizes for each approach. For the NS based model the mesh sizes used were 5mm ($\approx 120\ 000$ cells), 2.5mm ($\approx 760\ 000$ cells) and 1.25mm ($\approx 7\ 400\ 000$ cells). The mesh sizes used for the LBM models were 4.4mm ($\approx 237\ 000$ cells), 2.2mm ($\approx 1\ 760\ 000$ cells) and 1.1mm ($\approx 7\ 400\ 000$ cells). It should be noted that due to the non-body-

fitted mesh type used in the LBM, as described in Section 4.3 in Chapter 4, all the cells in the LBM were not fluid cells. The number of fluid cells for each mesh size in the LBM are 4.4mm (61 342 cells), 2.2mm (490 961 cells) and 1.1mm (3 926 800 cells). For the NS based models the time step size was kept constant at 10ms. For the LBM models the time step size was varied as a function of the cell size resulting in the following time step sizes 4.4mm ($\delta t = 106.22\text{ns}$), 2.2mm ($\delta t = 26.55\text{ns}$) and 1.1mm ($\delta t = 6.64\text{ns}$). For the comparison, the fine mesh results will be used, namely the 1.25mm mesh for the NS model and the 1.1mm mesh for the LBM model. In all the models the LES turbulence model was used.

As seen in Figure 6.25, the short-cut flow to the overflow is predicted by both the LBM and NS based models. Furthermore, a low-flow to the underflow can also be seen in both models. The LBM model shows good qualitative agreement with the NS based model. However, the LBM model predicts higher velocities near the intake as seen on the z - plane in Figure 6.26. Apart from the velocity difference near the intake region, both models offer similar velocity and flow field predictions. The comparability of the models are in-line with the observations reported in [28].

The low/suction pressure distribution in the core of the hydrocyclone is present in the LBM model as seen in Figure 6.27. Figure 6.27.b. is the clipped out suction pressure distribution in the core of the hydrocyclone. This indicates that the LBM single phase model can predict the correct conditions for air-core formation. This result was not displayed in [28] despite the relevance to appropriate and accurate modelling of hydrocyclones. The implementation of the pressure outlet in the LBM single phase model and the LBM-VOF model in Palabos is the main factor that leads to the inability of the LBM-VOF model to predict the short-cut flow and the low pressure region in the core of the hydrocyclone.

The pressure outlet boundaries in the single phase model were implemented using an off-lattice condition whereas with the LBM-VOF model they were implemented via an on-lattice option. The off-lattice implementation of the pressure appears to capture the flow separation to the overflow and underflow realistically as seen in the single phase flow model results. The LBM-VOF model in Palabos cannot accommodate an off-lattice pressure outlet boundary condition. Whilst, on-lattice pressure boundaries were implemented, for the overflow and underflow, in the LBM-VOF and LBM-VOF two-fluid

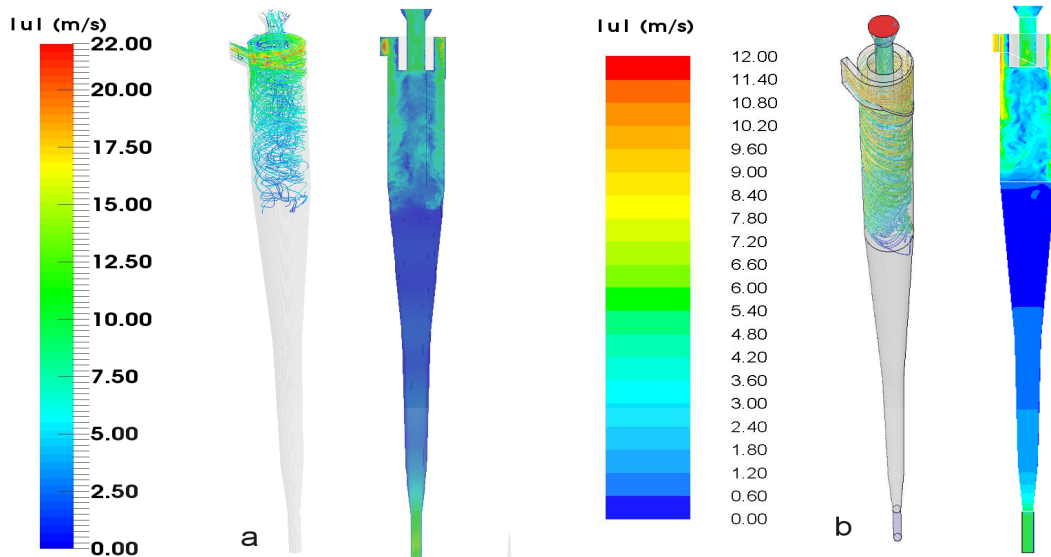


Figure 6.25: Pathlines reversed from the overflow and contours coloured by velocity magnitude ($|u|$ m/s) on the plane $x = 0$ at $t = 0.25$ s for the a) LBM single phase model and b) NS single phase model

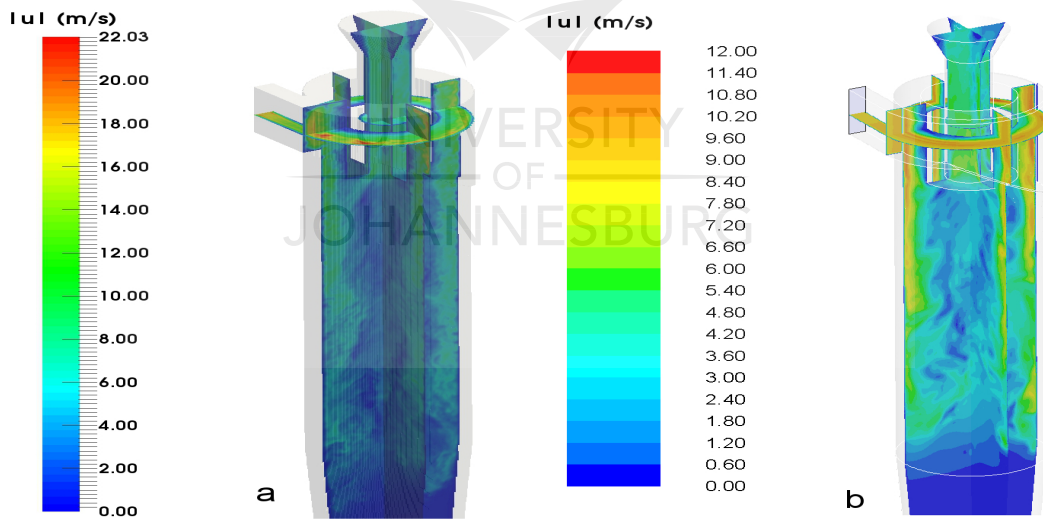


Figure 6.26: Contours coloured by velocity magnitude ($|u|$ m/s) on the planes $x = 0$, $y = 0$, $z = 0.25$ $t = 0.25$ s for the a) LBM single phase model and b) NS single phase model

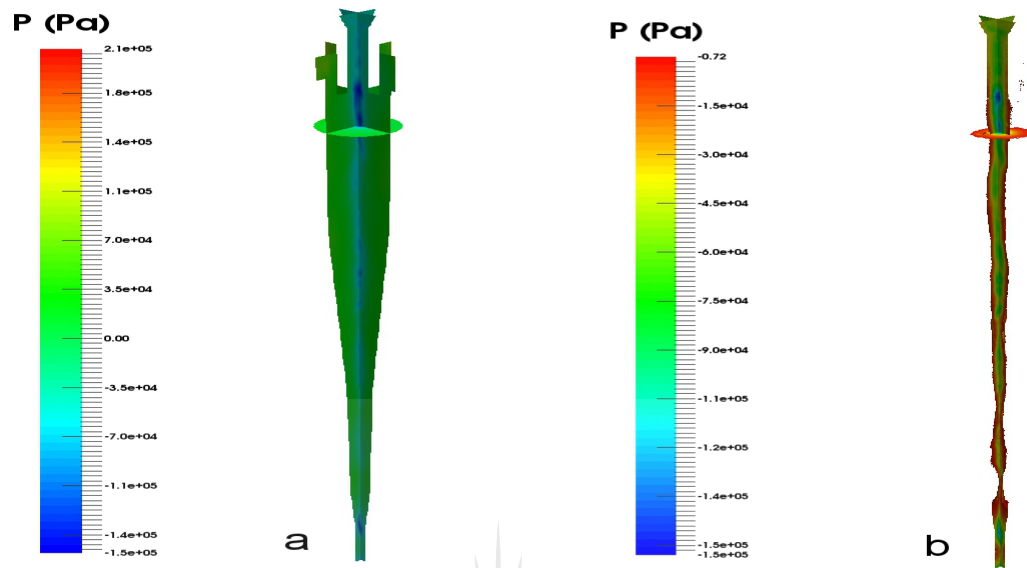


Figure 6.27: Low pressure region, as predicted by the LBM, in the core of the hydrocyclone from single phase simulation on the planes $x = 0$, $y = 0$, $z = 0$ at $t = 2$ s: a) full pressure distribution and b) clipped low pressure region

models, the outlet boundaries behaved as outflow boundaries as opposed to pressure boundaries.

A key point to note is that the LBM single phase model was significantly less computationally intensive than the NS based single phase model. The 1.25mm mesh NS model was solved on the Nehalem cluster at the CHPC. A total of 72 cores and 90GB of RAM was requested. In a period of 72 hours only 0.4324s flow-time was simulated. However, the LBM model was solved on a virtual machine on a desktop. Only 2 cores (4 threads) and 14GB RAM was made available to the virtual machine. The LBM solved 2s flow in under 146 hours. The LBM was also solved on 60 cores with 100GB RAM (requested) and took just over 65 hours to complete. This validates the statement made by LBM software developers that the LBM can produce “cluster like” results on a desktop, at least for complex single phase flows. This is due to the high level of parallelism inherent in the LBM [25]. However, as indicated in [25], the inherent parallelism of the LBM diminishes as the interaction strength in a model increases. Thus, once the air-core was modelled using the LBM-VOF model, the LBM lost it’s

computational advantage. This will be discussed further in Subsection 6.1.4.

6.1.3.2 LBM-VOF Two Fluid Model

The LBM-VOF two fluid model was implemented to account for the gas phase velocity field. However, this model was unstable at the high Reynolds Number flow in the hydrocyclone despite the use of a mesh with more than sixteen million lattices and a time step below one nanosecond. Thus, a multicomponent-multiphase (MCMP) LBM model that is suited to flows with high density ratio might be needed to capture the air-core physics. Alternatively, further improvements to the stability of the LBM-VOF two fluid model for high Reynolds Number flows might be able to provide suitable results. Thus, the MCMP model or an improved and stable LBM-VOF two fluid model with off-lattice pressure outlet boundaries might in future be suitable options to capture the air-core physics.

6.1.4 Computational Efficiency Comparison for Single Phase and Air-Core Models

Computational efficiency was measured based on three criterion, namely: walltime (time for model to run to completion), RAM usage and MCUPS. MCUPS is the number of cell time step updates per second. The MCUPS value for the LBM represents the number of lattice time step updates per second. MCUPS is a normalized metric that removes the bias of the hardware used, time step size and number of cells in the model providing a benchmark for the various models despite the difference in hardware used, time step size and cell count. The MCUPS metric similar to the performance metric used in [33].

For the single phase model, the LBM proved significantly more efficient (computationally). The results are based on the 1.25mm cell size for the NS models and a 1.1mm voxel size for the LBM model. The LBM-LES model was run on 60 cores with an upper RAM limit of 100GB and the NS-LES model was run on 72 cores with an upper RAM limit of 90GB. The NS models could

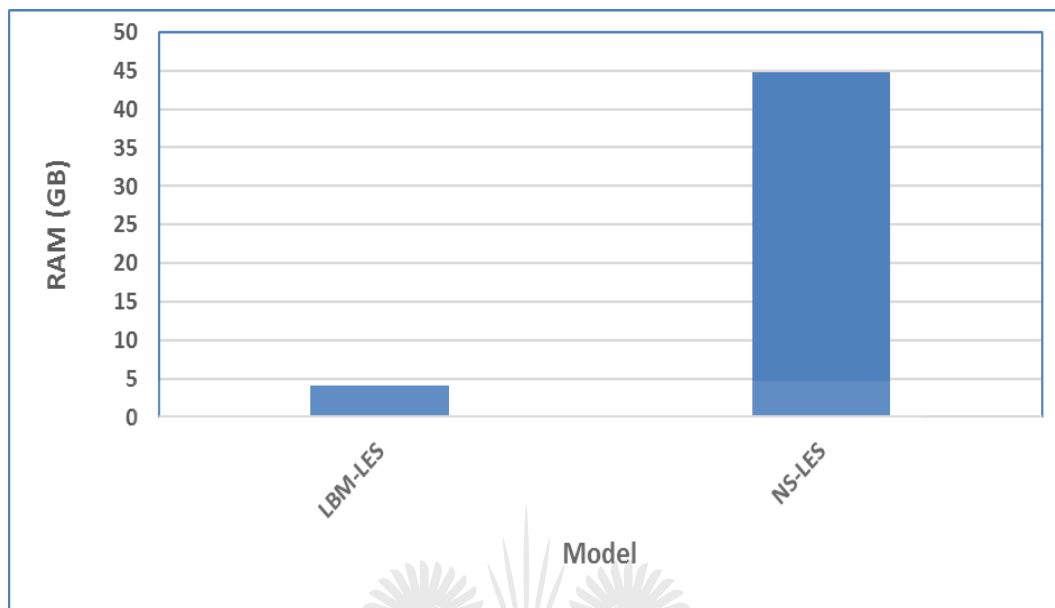


Figure 6.28: RAM usage for the LBM-LES and NS-LES single phase models

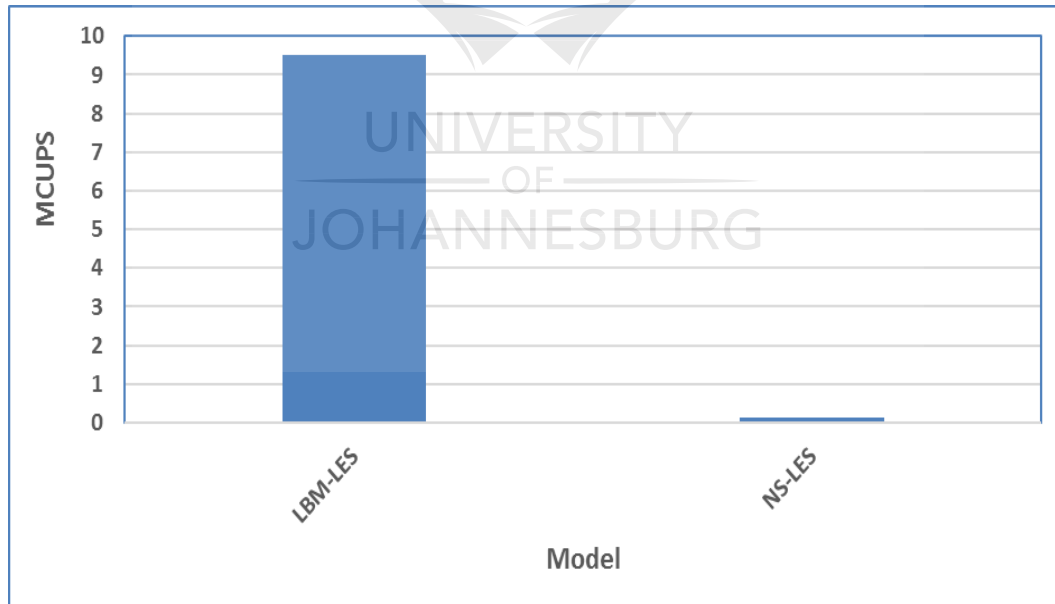


Figure 6.29: MCUPS based performance for the LBM-LES and NS-LES single phase models

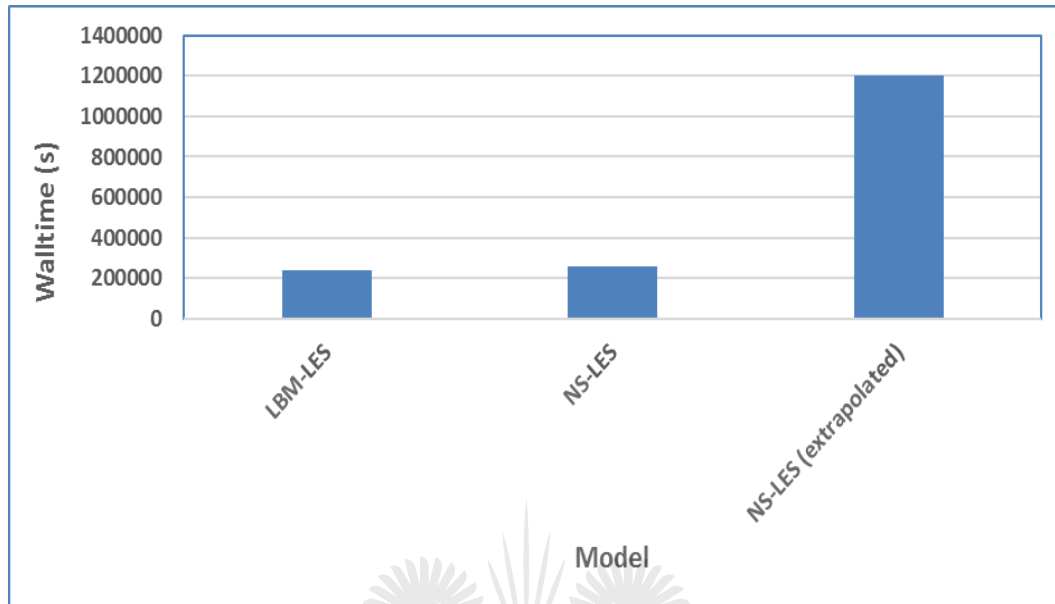


Figure 6.30: Walltime in seconds for the LBM-LES and NS-LES single phase models (on similar hardware)

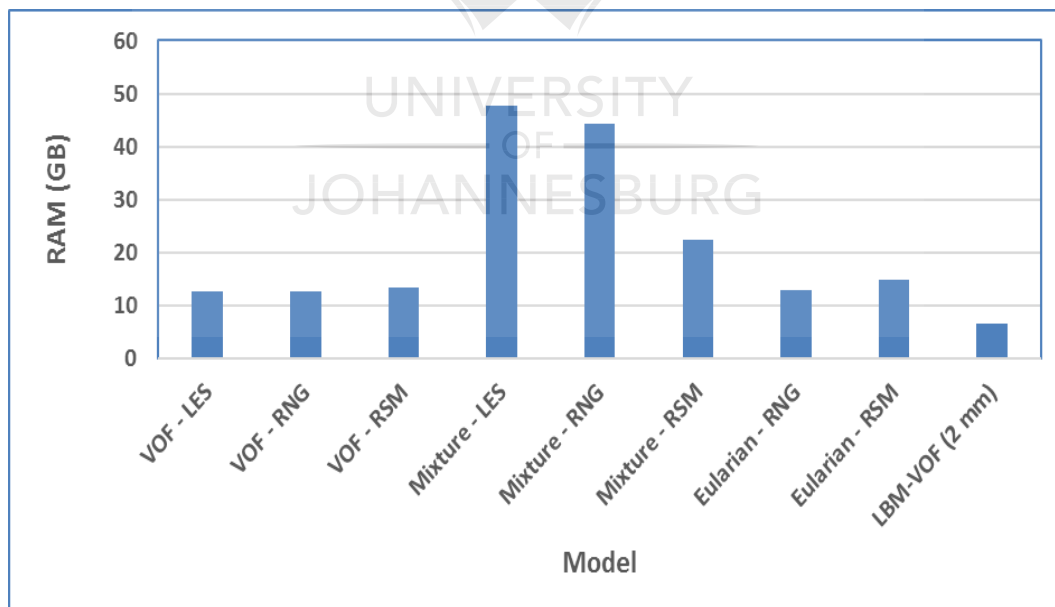


Figure 6.31: RAM usage for the air-core models

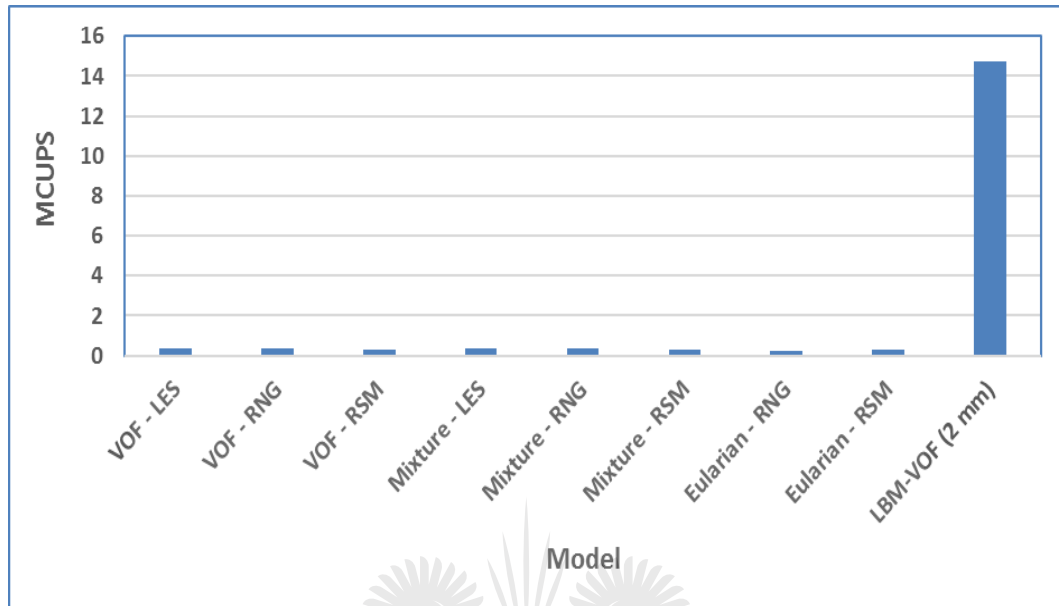


Figure 6.32: MCUPS based performance for the air-core models

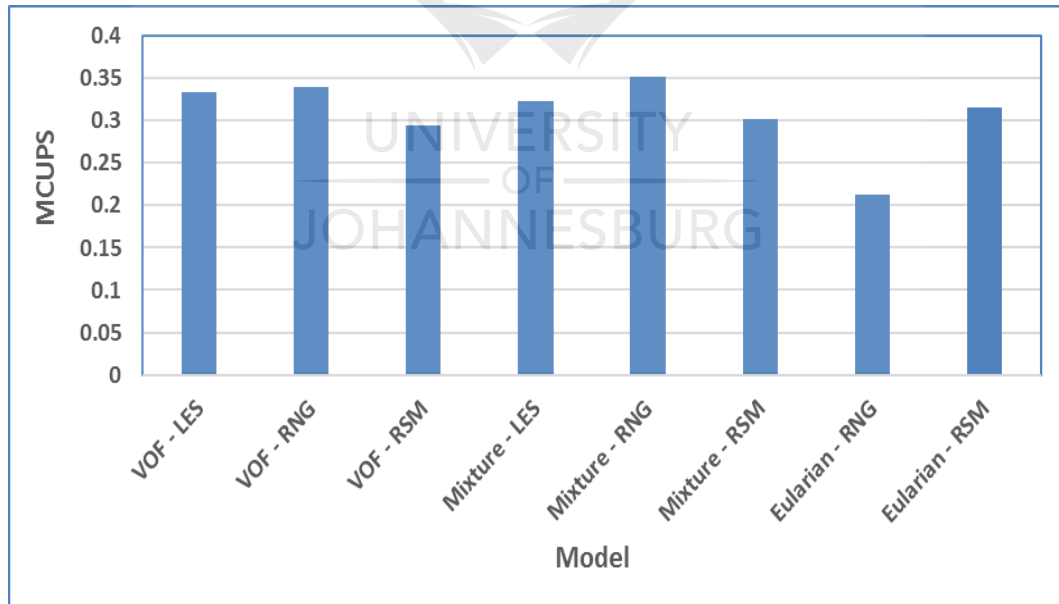


Figure 6.33: MCUPS based performance for the NS based air-core models (expanded view of part of Figure 6.32)

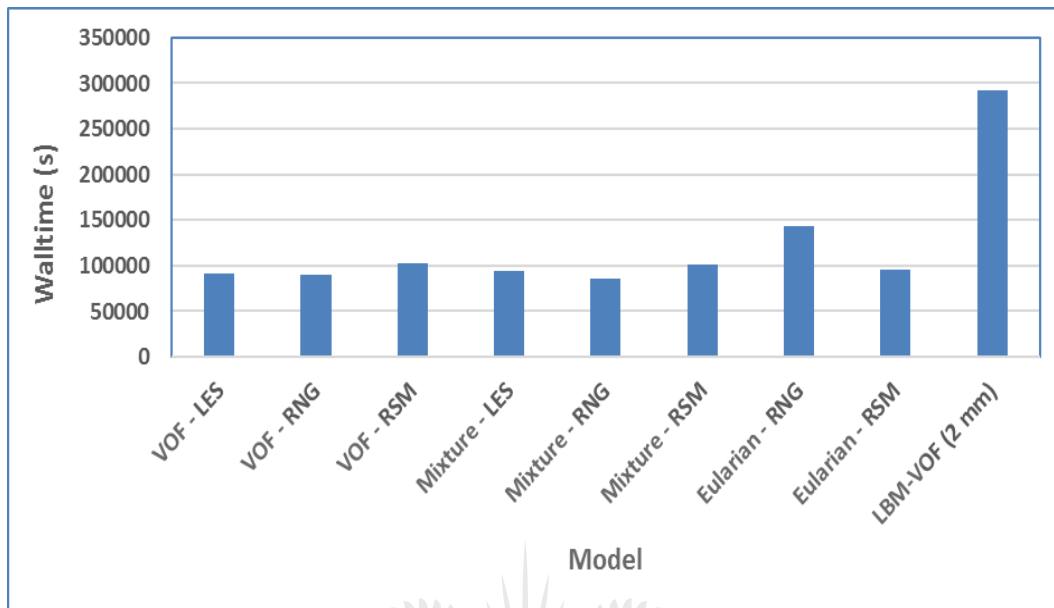


Figure 6.34: Walltime in seconds for the air-core models (on similar hardware)

not complete the full 2s flow-time calculation in 72 hours. Only 0.43s flow-time was computed in that time. Whereas, the LBM model completed the full 2s flow-time calculation in approximately 65 hours. The LBM also used significantly less RAM and had a higher MCUPS value than the NS model, as seen in Figures 6.28 and 6.29. The walltime comparisons for the models are given in Figure 6.30. An extrapolated walltime is given for the NS model to indicate the expected time for the full 2s flow-time calculation. Thus, it is clear that the LBM model is significantly more efficient (computationally) than the NS based model for single phase flow.

For the air-core models, the LBM proved significantly more efficient (computationally) in all aspects except walltime. The results are based on the 2.5mm cell size for the NS models and a 2mm voxel size for the LBM model. All the models were run on 64 cores with an upper RAM limit of 80GB. Once again, the LBM also used significantly less RAM and had a higher MCUPS value than the all the NS models, as seen in Figures 6.31 and 6.32. A comparison of the MCUPS for only the NS models, as seen in Figure 6.33, reveals that the mixture model provides the worst performance. All three performance metrics reveals a small difference in computational efficiency for

the VOF and Eulerian models.

The walltime comparisons for the models are given in Figure 6.34, highlighting the significantly larger walltime requirement for the LBM-VOF model. The MCUPS for the LBM-VOF model was between 42 - 70 times larger than that of the NS based models. However, the LBM-VOF model required a time step size that was 50 times smaller than the NS based models. Thus, the MCUPS gain, when using the LBM-VOF model, was offset by the requirement for significantly smaller time step sizes. Therefore, if the NS based models and LBM-VOF models had the same cell count the NS based models and the LBM-VOF models would have had similar walltimes. However, the LBM-VOF model cell count, for a similar cell size, was three times the cell count for the NS based models. Thus, the LBM-VOF model required between 2 - 3.4 times longer to run the simulation.

6.2 Particle Model Predictions

The discussion of the simulation results continues with the particle interaction and separation modelling. In this discussion the effect of the particles on the air-core will be highlighted. Furthermore, the model predictions of separation efficiency and outlet PSDs will be benchmarked to the experimental measurements.

6.2.1 Effect of Particles on the Air-Core and Water Phase

In Table 6.5 the average mass flow rate of water at the underflow and overflow as predicted by the NS based VOF-DEM models are presented. Furthermore, the respective tables present the error between the predictions and experiment for the average mass flow rate at the underflow and overflow. The results are based on the fine mesh (2.5mm cell size) results. This is further shown in Figures 6.35 and 6.36, the water mass flow rate predictions remain within bounds of the experiment for the overflow and underflow water mass flow rate predictions. However, the LES model does exhibit noticeable spikes in the both the overflow and underflow water mass flow rates which are well below the minimum or well above the maximum values measured

Table 6.5: NS-DEM Water Mass Flow Rate Model Comparisons

Model	m_{under} (kg/s)	m_{over} (kg/s)	$m_{under,exp}$ (kg/s)	$m_{over,exp}$ (kg/s)	$ Error_{under} $ (%)	$ Error_{over} $ (%)
VOF-DEM (LES)	0.41	4.78	$0.85^{+0.09+0.06}_{-0.11-0.06}$	$4.38^{+1.01+0.54}_{-0.49-0.54}$	49	10
VOF-DEM (RSM)	0.79	4.44	$0.85^{+0.09+0.06}_{-0.11-0.06}$	$4.38^{+1.01+0.54}_{-0.49-0.54}$	7	2

of experimentally. Thus, the results in Table 6.5 as well as Figures 6.35 - 6.36 indicates that the VOF-DEM model, with the RSM, provides the most accurate predictions in relation to experiment in terms of the water mass flow rate at the outlets .

The above result is counter-intuitive as it would be expected that the LES results should be more accurate than the RSM results particularly in a complex turbulent flow such as in a hydrocyclone because LES models resolve a larger range of turbulent eddies whereas the RSM models a larger range of turbulent eddies. However, the results in the above models are on meshes that are still too coarse for accurate LES models to provide acceptable results. Due to the excessive computing time required to produce LES based results on meshes that are suitably fine was out of reach in this study, thus, it will be reserved for future work. However, it is useful for practitioners, which need to produce CFD results on coarse meshes, to know that RSM based models can produce results that are within acceptable limits.

Based on a comparison of the air-core model predictions and the particle model predictions it can be seen that the NS based models produce results that show good agreement with the experimental measurements, particularly for the underflow. The underflow error reduced by 60% for the RSM and 29% for the LES by introducing particles. The overflow error reduced by 5% for both the RSM and the LES by introducing particles. The error between the CFD and experiment of 7% for the underflow water mass flow rate and 2% for the overflow water mass flow rate as presented in Table 6.5 is within acceptable limits. In the case of the air-core models in Section 6.1 the boundary conditions and operating parameters were based on the experimental results presented in Chapter 5. The experimental results in Chapter 5 were obtained from experiments that included particles. However, in the models in Section 6.1 the particle phase is neglected. Thus, the particle-fluid interaction must have a significant impact on the water phase and on the air-core and it can be concluded that the large difference between the CFD



Figure 6.35: Overflow water mass flow rate as predicted by the NS based VOF-DEM models

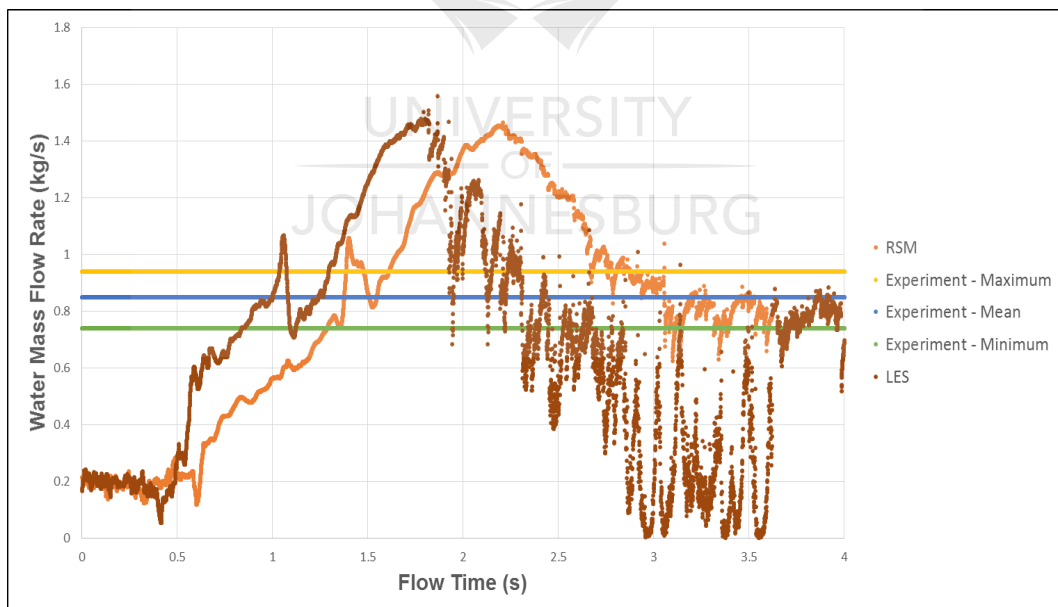


Figure 6.36: Underflow water mass flow rate as predicted by the NS based VOF-DEM models

predictions and experiment as noted in Section 6.1 are due to the fact that the particle phase was neglected in the air-core models. Therefore, future validation of air-core models should be done using experiments whereby the particles are not included in the experiment so that the air-core models can be compared directly to experiments that are free of the bias of the effect of the particle phase on the water phase and air-core.

In Appendix C it is shown that mesh independence was not achieved for the NS based VOF-DEM models. However, from the above results it can be seen that the 2.5mm mesh is sufficient to produce results that are comparable to experiment, in terms of the water mass flow rate. Furthermore, the 4s of modelled flow-time for the 2.5mm mesh simulations had a walltime of over 220 hours (over 9 days) to run on 64 cores on the Nehalem cluster. The walltime for the equivalent model on the 3.75mm model took 120 hours (5 days) to run on the same resources. Thus, a further refinement would have taken approximately 18 days to run. Based on the time constraints this was not feasible.

The NS based VOF-DEM models predict the suppression of the air-core as seen in Figure 6.37. This is a real phenomenon in hydrocyclones known as surging. In the case of surging the particles accumulate in the hydrocyclone in the cone area specifically. This accumulation of particles causes the water velocity and the swirl in that region to decrease rapidly resulting in a rise in pressure in the core of the hydrocyclone. The rise in pressure removes the low pressure region which is the primary mechanism for air-core formation. The concentration of particles and subsequent decrease in velocity and swirl and the rise in pressure can be seen in Figures 6.38 - 6.40.

Whilst the VOF-DEM model predicts surging, it was not determined whether recovery from surging could be modelled. Based on the separation efficiency predictions, which are presented in the next subsection, complete recovery from surging would occur at approximately 16s of flow-time. Based on the run time of more than 9 days on 64 cores for 4s flow-time it would require approximately over 36 days to model 16s of flow-time. Thus, it was not possible, on the resources and within the time limits of the project, to verify whether the model would at 16s of flow-time demonstrate such an effect.

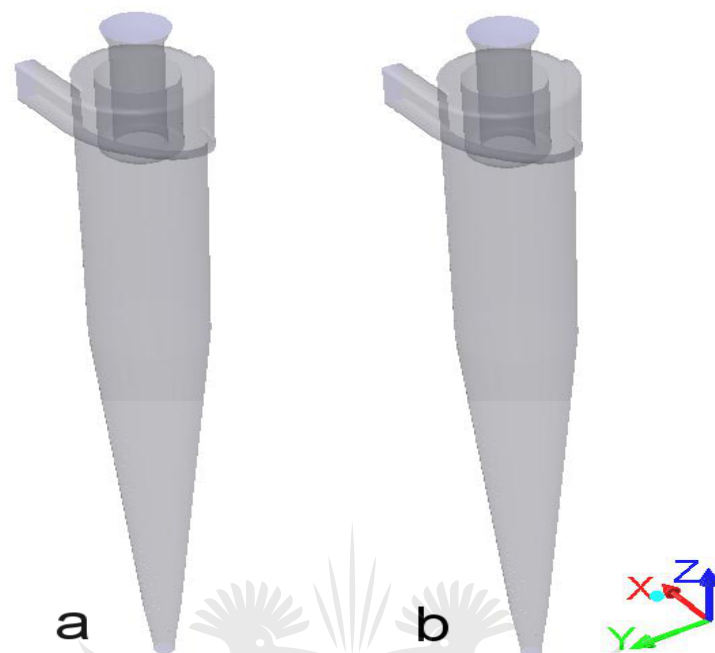


Figure 6.37: Iso-Surface of volume fraction of air from the VOF-DEM models at flow-time 4s: a) RSM and b) LES.

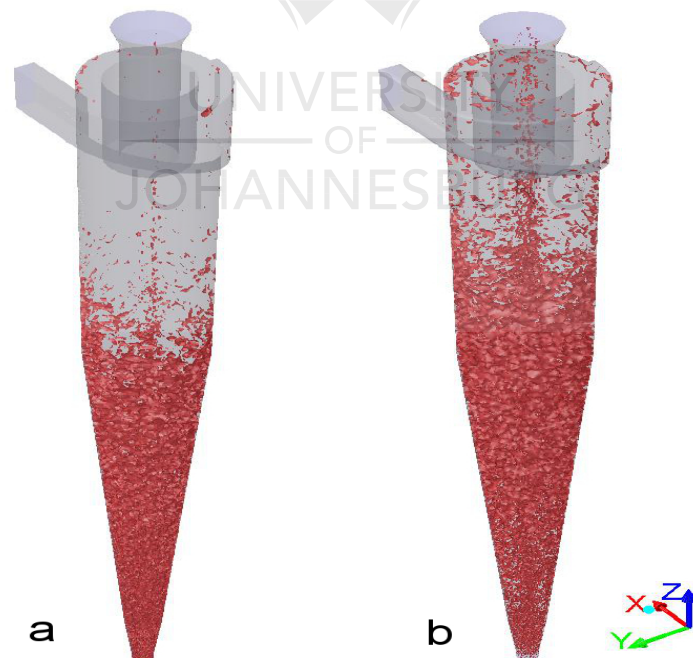


Figure 6.38: Iso-Surface of particle concentration above 600 kg/m^3 from the VOF-DEM models at flow-time 4s: a) RSM and b) LES.

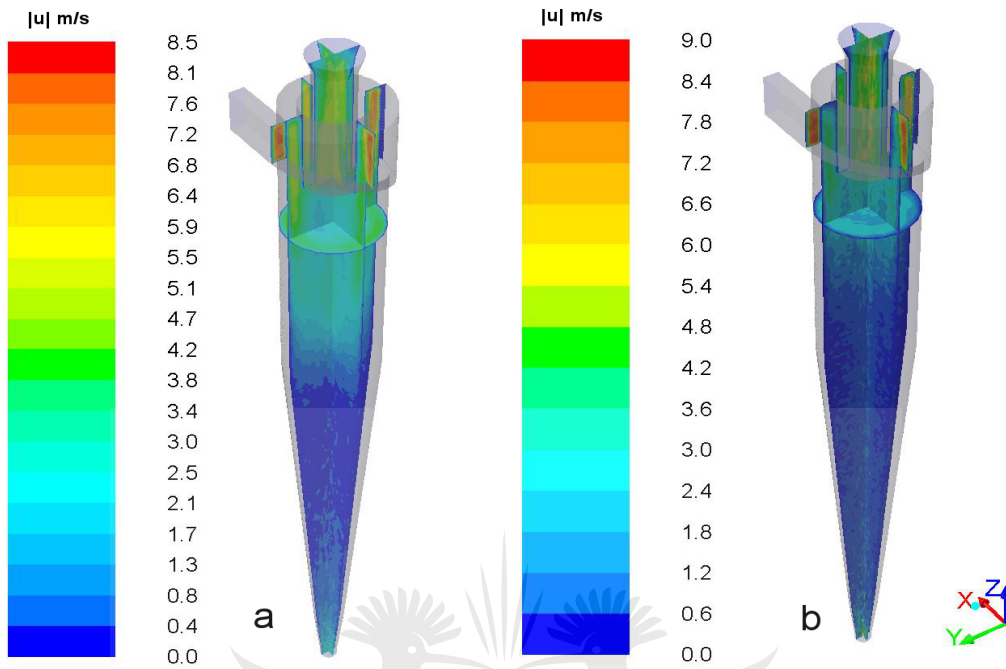


Figure 6.39: Contours coloured by velocity magnitude, on the planes $x = 0$, $y = 0$ and $z = 0$ from the VOF-DEM models at flow-time 4s: a) RSM and b) LES.

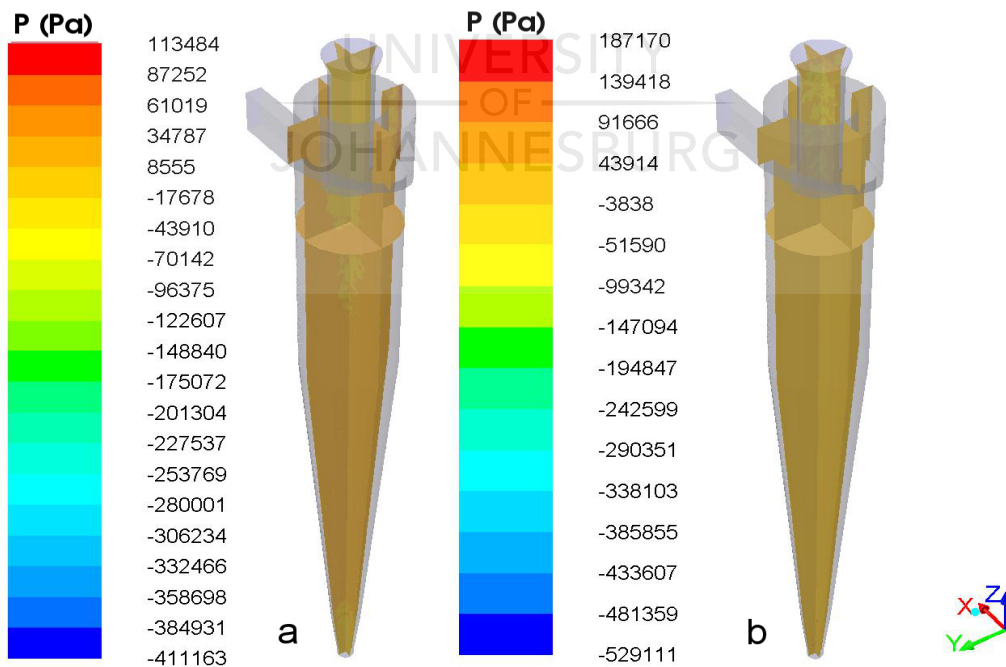


Figure 6.40: Contours coloured by static pressure, on the planes $x = 0$, $y = 0$ and $z = 0$ from the VOF-DEM models at flow-time 4s: a) RSM and b) LES.

Surging causes a significant change in the dynamic behaviour of the flow regime in the cyclone apart from the suppression of the air-core. Thus, the effect of the particles on the dynamic behaviour of the cyclonic flow was investigated by comparing the models with the particles against the corresponding air-core models. This was done in the case of the VOF and VOF-DEM models with both the RSM and LES turbulence models. The dynamic behaviour was investigated in terms of the tangential and axial velocities, the vorticity and pressure. This was done at four heights along the hydrocyclone, with varying y co-ordinates namely $z/H = 0.2$, $z/H = 0.4$, $z/H = 0.6$ and $z/H = 0.8$ to correspond with positions near the underflow, higher up in the cone, in the barrel near the cone and near the vortex finder respectively. In addition the pressure profiles were taken as a function of height in the core of the hydrocyclone. The position of the places where the profiles were investigated is shown Figure 6.41.

Under particle-free air-core formation the static and dynamic pressure are relatively constant along the height of the hydrocyclone. However, as seen in

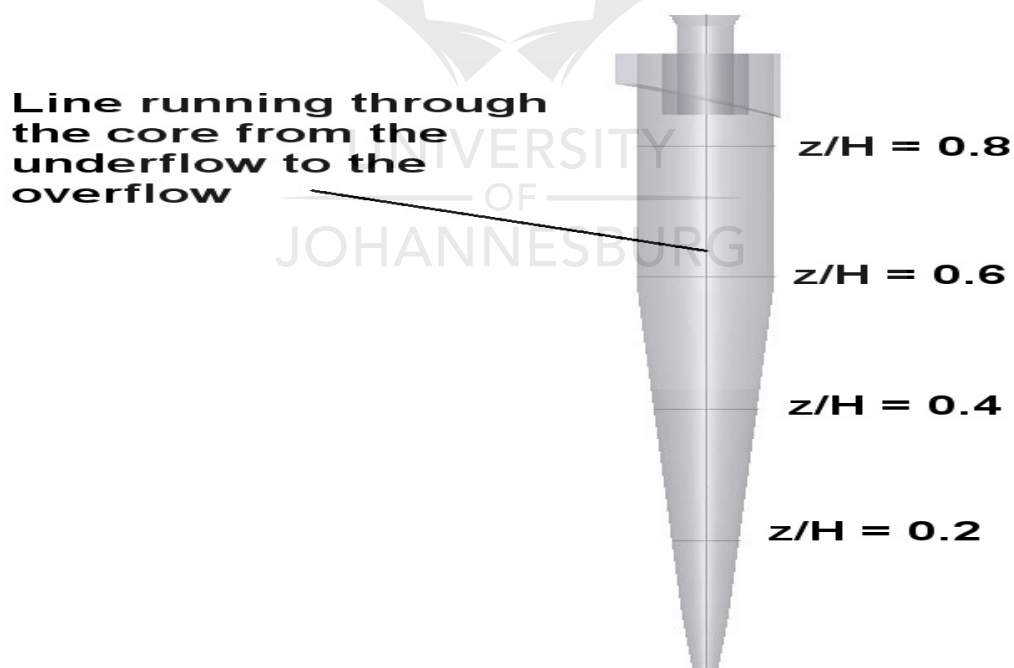


Figure 6.41: Positions where profiles were investigated.

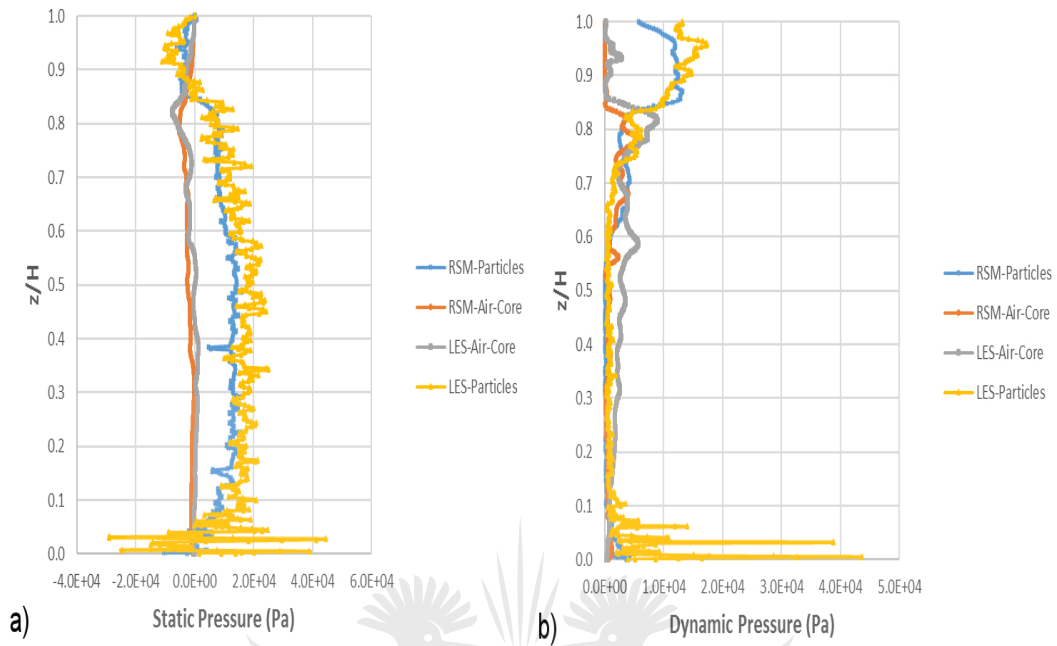


Figure 6.42: a) Static and b) dynamic pressure (Pa) as a function of the normalised z co-ordinate.

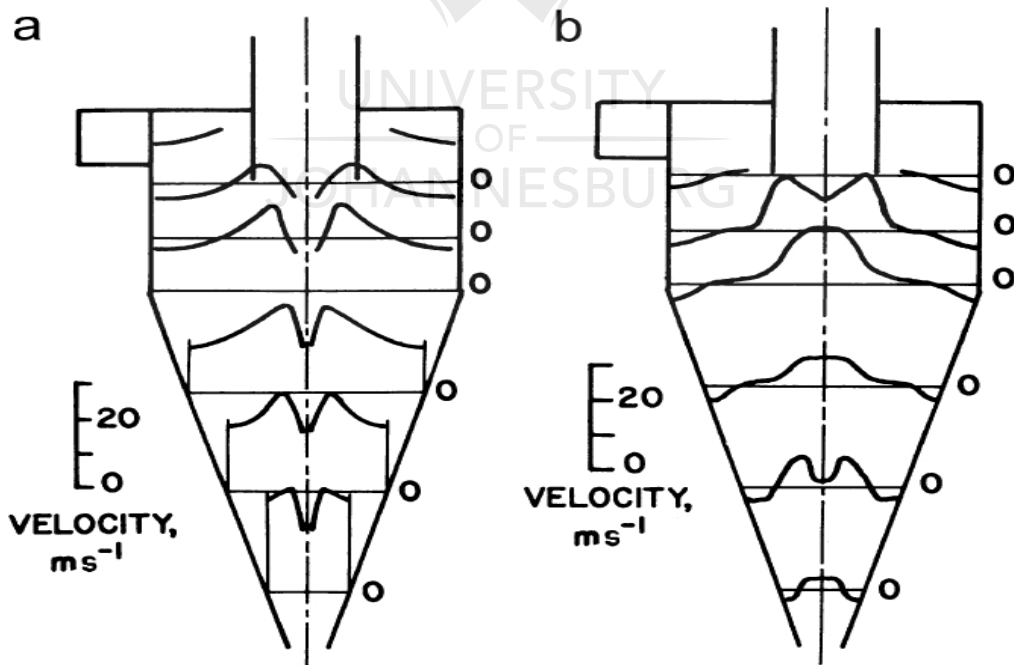


Figure 6.43: a) Tangential and b) axial velocities (m/s) as a function of the normalised y co-ordinate at various heights as reported in literature (adapted from [114]).

Figure 6.42, there is a noticeable drop in the static pressure and rise in the dynamic pressure near the vortex finder. The inclusion of particles, to the point of surging, causes a significant rise in the static pressure from the area near the vortex finder to the underflow and a significant rise in the dynamic pressure from the vortex finder to the overflow as seen in Figure 6.42. Apart from the apparent suppression of the air-core this significant change in the pressure distribution leads a significant impact on the velocity profiles and the vorticity in the hydrocyclone. The LES model display excessive noise in the pressure distributions near the underflow during surging which may be part of the reason why the LES model predictions were less accurate than the RSM model. However, this may be related to the coarse mesh in the underflow region. As indicated previously, it is expected that the LES model should provide more accurate results than the LES model when the mesh is refined further.

Figure 6.43 presents the expected tangential and axial velocity profiles during air-core formation and non-surging based particle loading in the hydrocyclone [114]. The tangential and axial velocity profiles predicted by the VOF air-core models, as seen in Figure 6.44, matches the expected profiles as reported in literature. Under particle-free air-core formation the peak tangential velocities remain constant relatively along the height of the hydrocyclone. The axial velocities are also relatively constant along the height of the hydrocyclone apart from near the underflow. Figure 6.44 indicates that the RSM model predicts a peak tangential velocity that is up to 20% lower and a peak axial that is up to 70% lower than the corresponding predictions by the LES model. Furthermore, the LES model more accurately represents the axial velocity profile near the underflow ($z/H = 0.2$).

When surging occurs the tangential and axial velocities undergo significant attenuation. As seen in Figure 6.44 the only noticeable fluid motion occurs near the vortex finder ($z/H = 0.8$). This is once again due to the high concentration of particles in the rest of the hydrocyclone (as shown in Figures 6.38 and 6.39). Despite the attenuated velocity, the models still predict the “M” shaped tangential velocity profile as seen in Figure 6.44.a. at $z/H = 0.8$.

The attenuated velocity should result in attenuation of the vorticity. The subsequent attenuation of the vorticity, due to surging, can be seen in Figure 6.45. In the case of particle-free air-core formation the vorticity peaks near

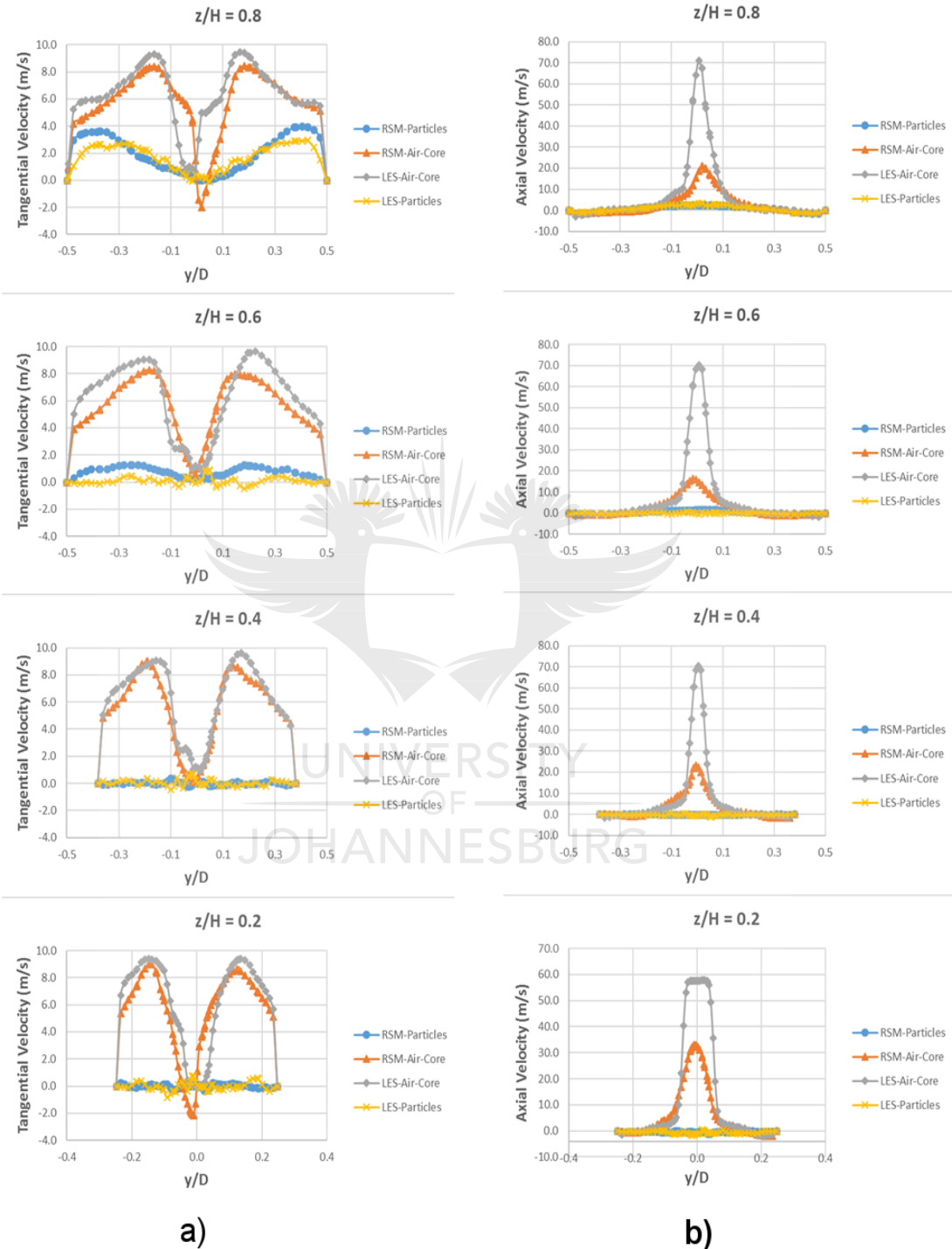


Figure 6.44: a) Tangential and b) axial velocities (m/s) as a function of the normalised y co-ordinate at various heights.

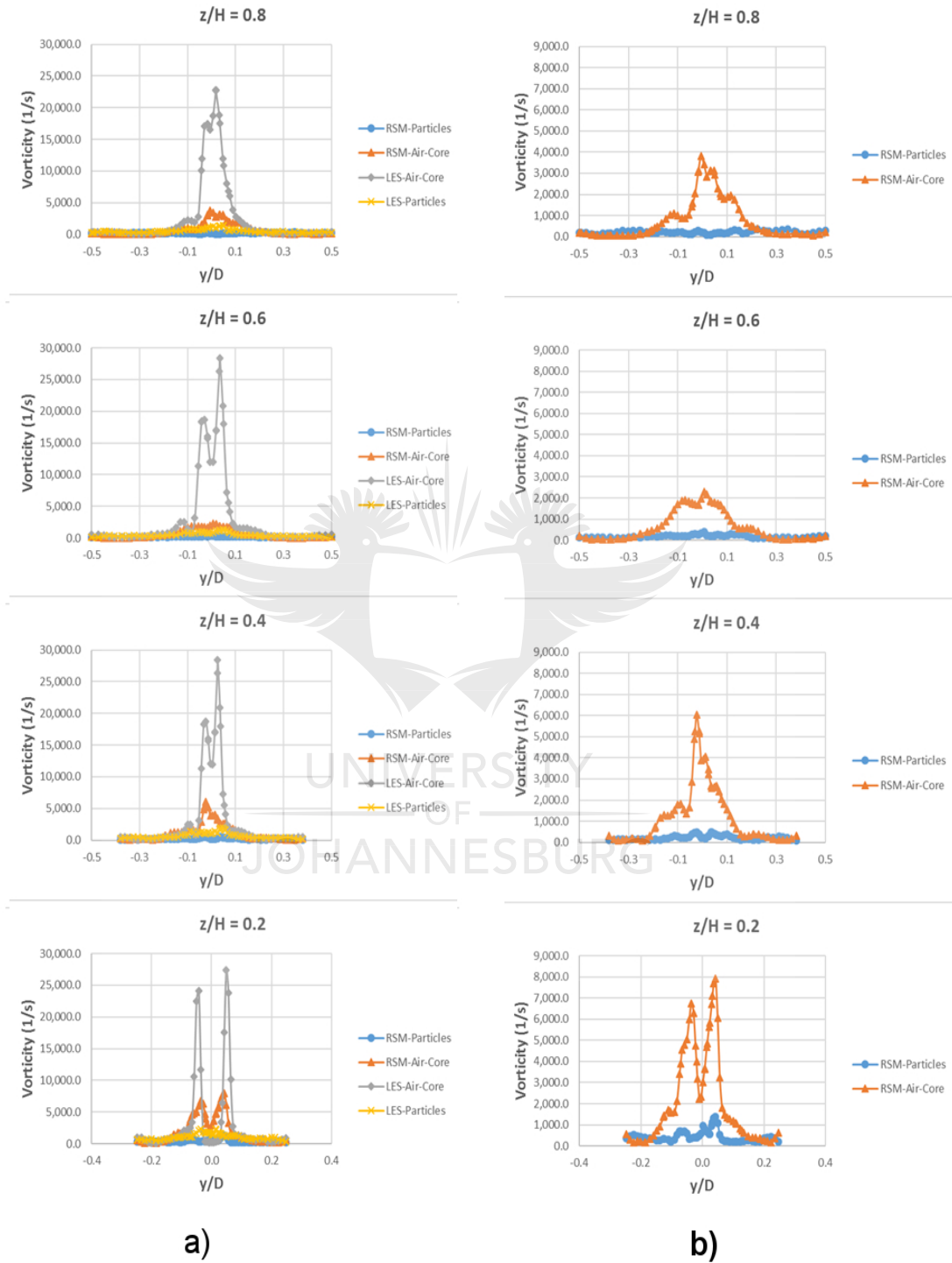


Figure 6.45: Vorticity magnitude (1/s) for the a) RSM and LES models and b) the RSM model as a function of the normalised y co-ordinate at various heights.

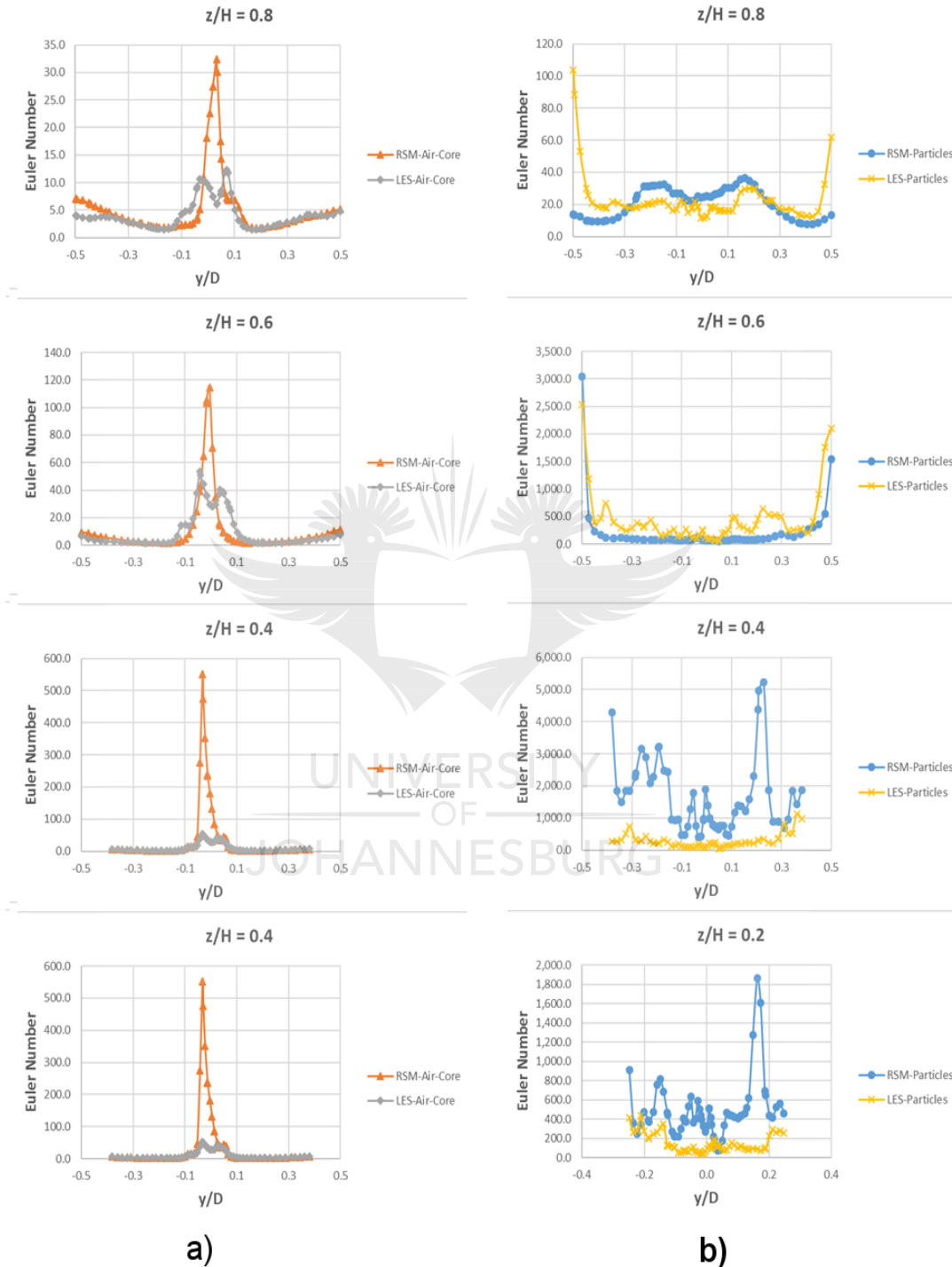


Figure 6.46: Euler Number for the a) air-core models and b) the particle models as a function of the normalised y co-ordinate at various heights.

the air-water interface due to the high level of separation in that region. The inclusion of the particles, to the point of surging, attenuates the vorticity in that region subsequently breaking down the cyclonic separation. The LES model predicts a vorticity that is up to an order of magnitude higher than the RSM models.

The breakdown in the cyclonic separation can be described by the Euler number. The variation of the Euler number at various heights is given in Figure 6.46. The Euler number was calculated as the ratio between the pressure drop from the inlet to the outlets and the dynamic pressure:

$$Eu = \frac{\Delta P}{(\rho v^2)/2}. \quad (6.1)$$

For both the LES and RSM models the flow in the core of the hydrocyclone is driven primarily by the pressure drop as seen by the high Euler Number in the core of the hydrocyclone in Figure 6.46.a. Whereas the flow near the wall is primarily driven by the gravitational and centrifugal force induced momentum as seen by the significantly lower Euler Number in the core of the hydrocyclone in Figure 6.46.a. This effect is somewhat reversed when the particles are added and surging occurs as seen in Figure 6.46.b. When surging occurs the Euler number rises near the walls and attenuates near the core leading to a break down in the balance between the pressure and momentum based separation in the core and near the wall of the hydrocyclone. The breakdown in the cyclonic separation leads to a reduced separation efficiency as discussed in the next section.

6.2.2 PSD and Separation Efficiency Predictions

The VOF-DEM models were sampled at the underflow and overflow to reconstruct the model predictions of the PSD at the outlets. A comparison of the model predictions of the PSD at the underflow and the overflow are given in Figures 6.47 and 6.48. Figure 6.47 illustrates poor PSD predictions from the VOF-DEM, with the LES. This is expected when considering the poor predictions from the LES highlighted in subsection 6.2.1. From Figure 6.47 it can be seen that the VOF-DEM, with RSM, provided an underflow

PSD prediction that is in good agreement with experiment. However, there is a noticeable deviation in the model PSD and experimental measurements in the range of $10\mu\text{m}$ and $400\mu\text{m}$.

The reason for the deviation is related to the inlet PSD. Figure 6.49 illustrates the comparison between the experimentally measured PSD, the Rosin-Rammler fit which was specified at the inlet boundary condition and the actual PSD that Fluent impressed at the inlet. Whilst the Rosin-Rammler fit matched the experimental measurements, sampling of the inlet PSD revealed that Fluent did not reconstruct the inlet PSD, accurately, as specified at the inlet boundary condition. Furthermore, it should be noted that the deviation between the experimentally measured PSD and the actual PSD that Fluent impressed at the inlet deviates significantly in the $10\mu\text{m}$ - $400\mu\text{m}$ range. This difference would produce the deviation noticed in PSD predictions from experiment, as seen in Figure 6.47, in the $10\mu\text{m}$ - $400\mu\text{m}$ range.

Both models did not provide accurate PSD predictions for the overflow. The poor overflow PSD predictions are possibly related to the separation efficiency. As mentioned previously surging occurs, in the cone, as predicted by the model. Due to surging the mass accumulated particles in the domain increases as a function of time as seen in Figure 6.50. From Figure 6.50, the recovery from surging is seen by the decrease in the accumulation of particles after 3.5s. Furthermore, the separation efficiency also rises over time as seen in Figure 6.51. By extrapolating the separation efficiency based on the data from the modelled 4s of flow-time, it is approximated that the separation efficiency would match experiment at 16s of flow-time, as seen in Figure 6.52.

The extrapolation appears to predict an efficiency above 100% after 17s of flow-time. However, this will not occur and the maximum separation efficiency would be 100% because the assumption (of no accumulation of particles) made when calculating the separation efficiency prevents this from occurring. If there is no mass flow of particles to the overflow then the separation efficiency would be 100% and if there is no mass flow of particles to the underflow the separation efficiency will be 0%. If the particle mass flow is split between the outlets then the separation efficiency will be bounded between 0% and 100%. Thus, if the trend in Figure 6.52 is achieved, then the separation efficiency predictions of the VOF-DEM, with RSM, model would

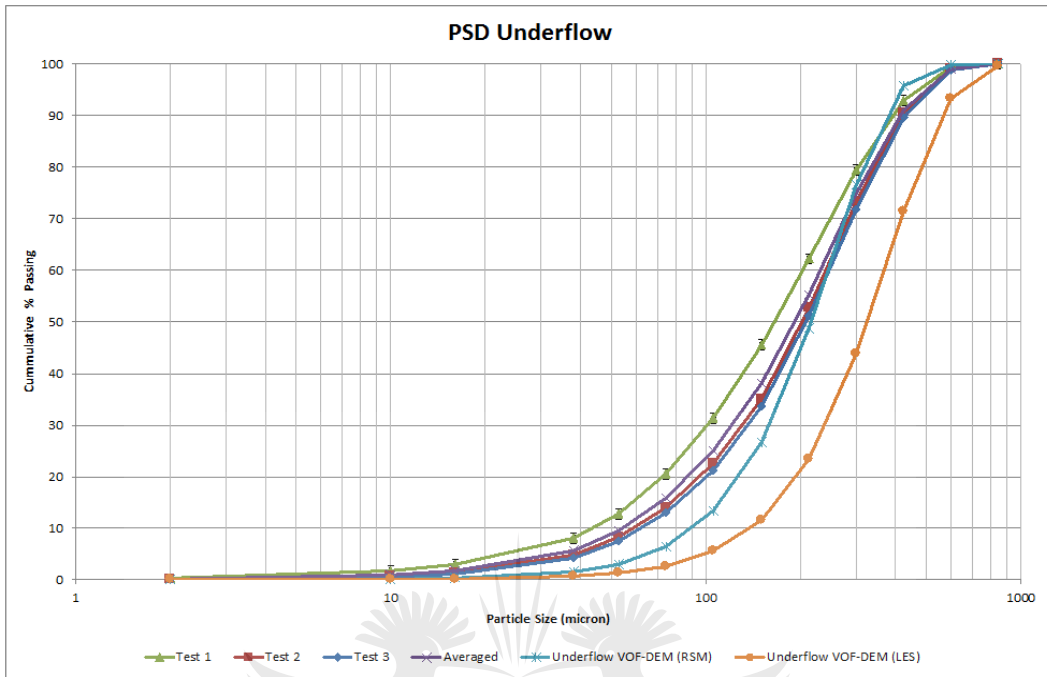


Figure 6.47: Underflow PSD - Comparison between Fluent predictions and experimental measurements

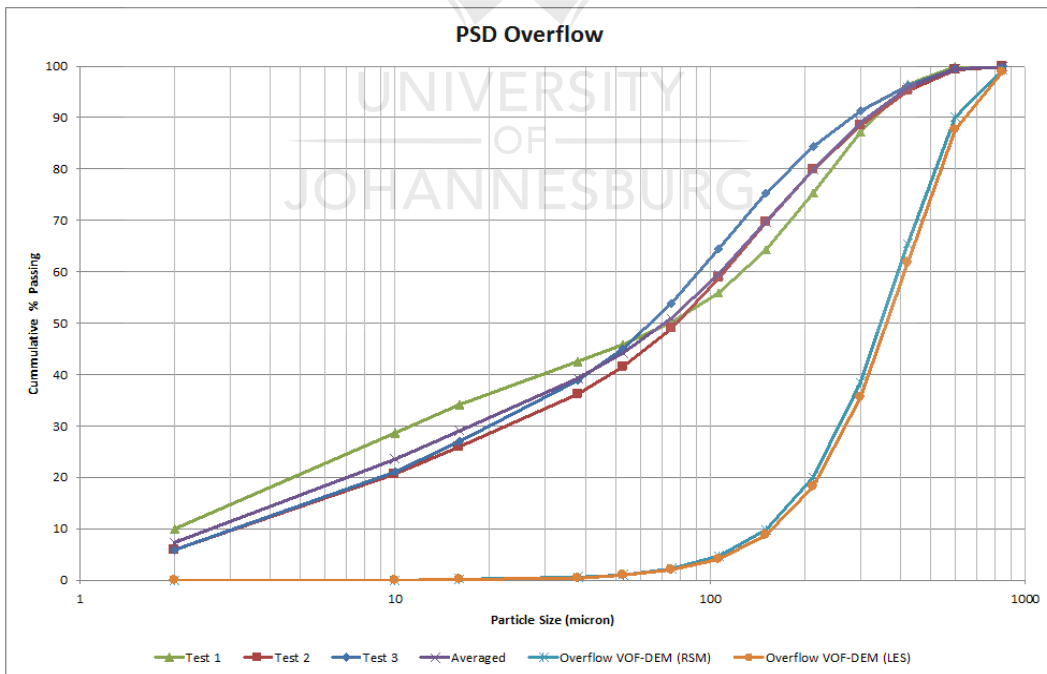


Figure 6.48: Overflow PSD - Comparison between Fluent predictions and all experimental measurements

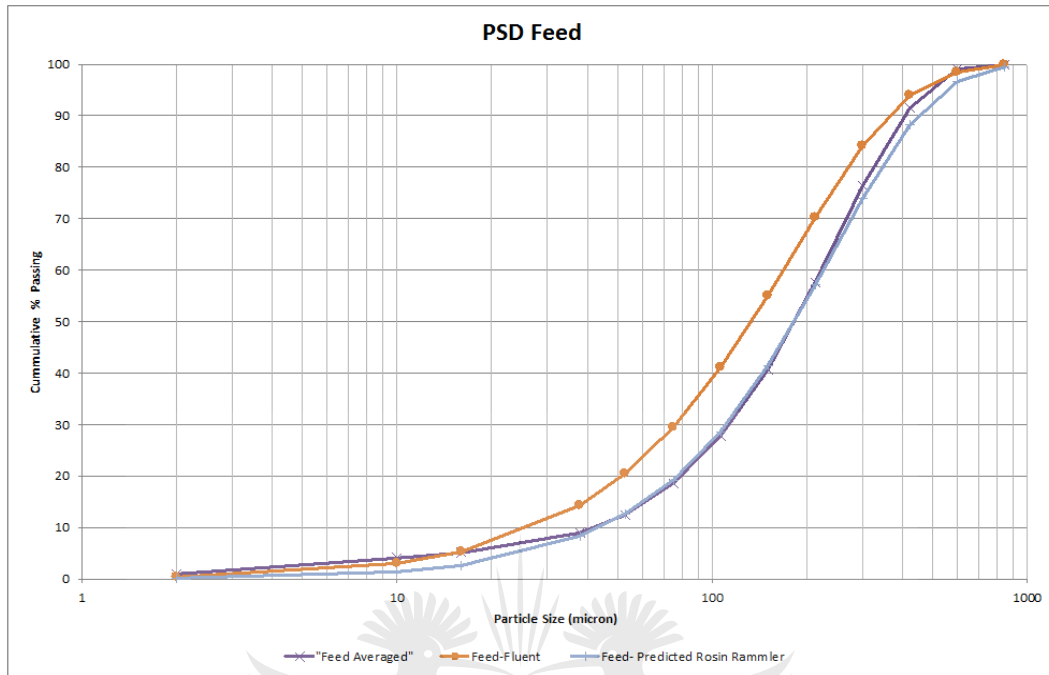


Figure 6.49: Feed PSD - Comparison between Fluent predictions and average experimental measurements

match the experimental measurements.

During the time of surging short-cut flow tends to occur as observed, previously, in Figure 6.39. This short-cut flow caused the models to predict a large mass of particles to exit through the overflow. Separation efficiency calculated under the assumption of no accumulation of particles and is given by Equation C.2. Thus, a high mass of particles at the overflow will lead to a low separation efficiency. This high mass flow of particles to the overflow does not occur under normal operating conditions and could in turn affect the overflow PSD¹.

As mentioned previously, based on the run time for modelling 4s flow-time it was not possible to model a full 16s of flow-time on the resources and within the time limits of the project. Thus, the investigation on the modelling of

¹The results on the separation efficiency and accumulation of particles were based on the VOF-DEM model, with RSM, on the 5mm mesh. However, these results are representative of the results for the other models and mesh refinements

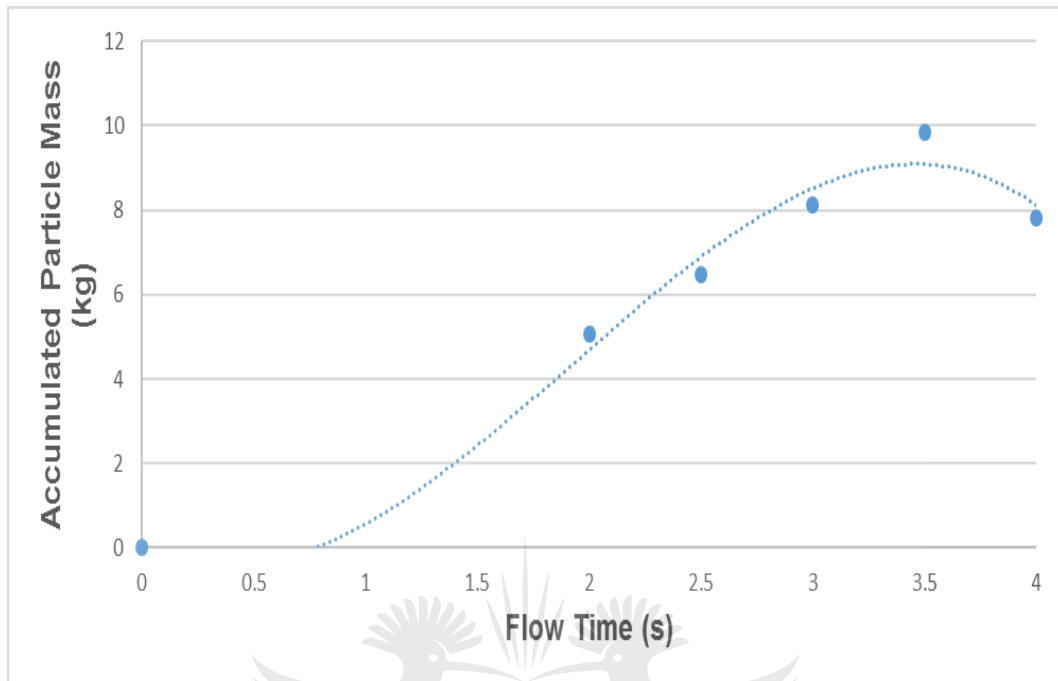


Figure 6.50: The Accumulation of particles

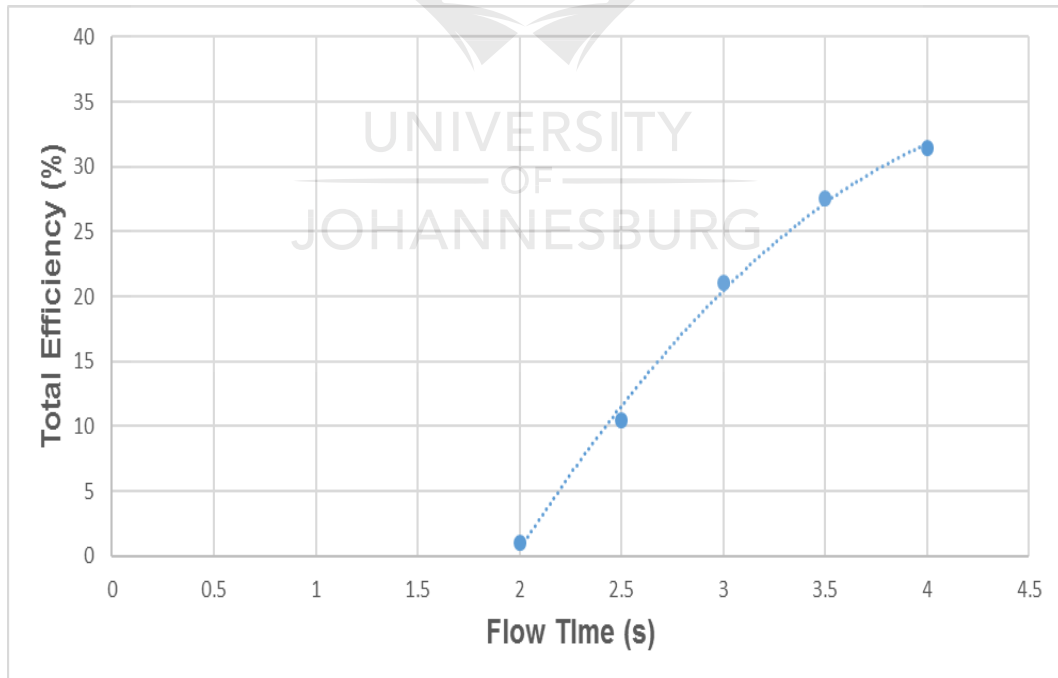


Figure 6.51: VOF-DEM (RSM) separation efficiency predictions

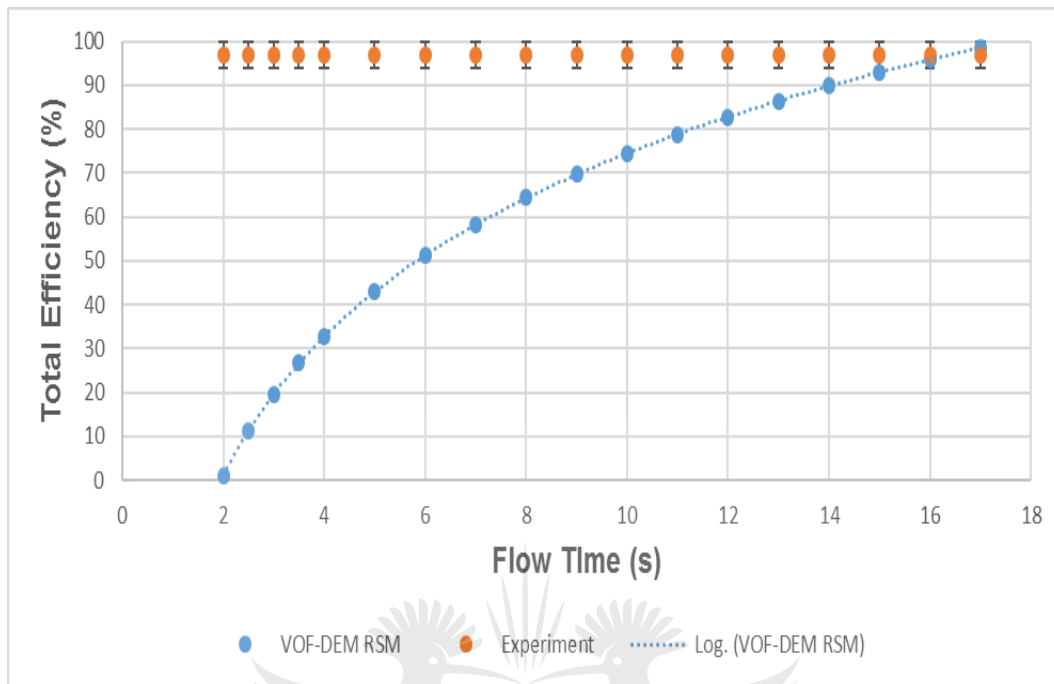


Figure 6.52: Extrapolation of the separation efficiency predictions

complete recovery from surging will be reserved as future work.

6.2.3 Eulerian DDPM-DEM and LBM-VOF Particle Model Predictions

For the LBM-VOF particle models, the point particle and the Verlet particle approach were both used. For the point particle approach, the particle inherits the local fluid velocity. For the Verlet particle approach, Equation 4.17 is solved to obtain the particle velocity. However, for stability reasons the virtual mass and pressure gradient forces, in Equation 4.17, were neglected in the Verlet particle model.

Due to stability issues the Eulerian model was only solved on the 5mm mesh. Furthermore, the Eulerian model could not complete the full 4s flow-time calculation due to stability issues. The LBM-VOF particle models could only be run on the 3.9mm mesh and could not complete the 4s flow-time due

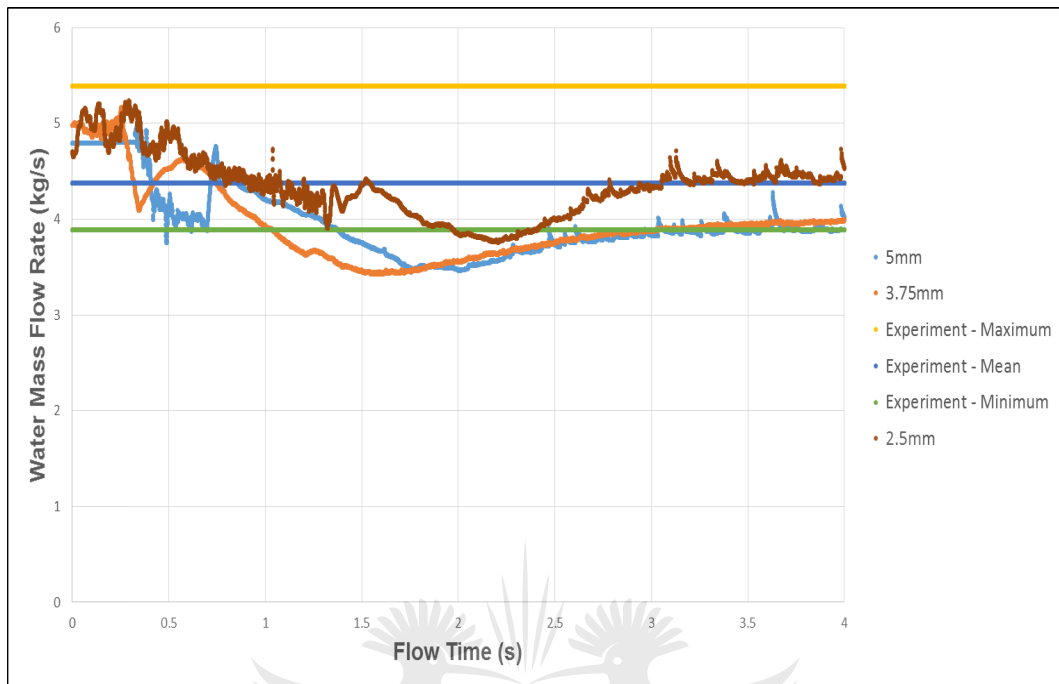


Figure 6.53: Overflow water mass flow rate as predicted by the VOF-DEM models, with RSM, for different mesh sizes

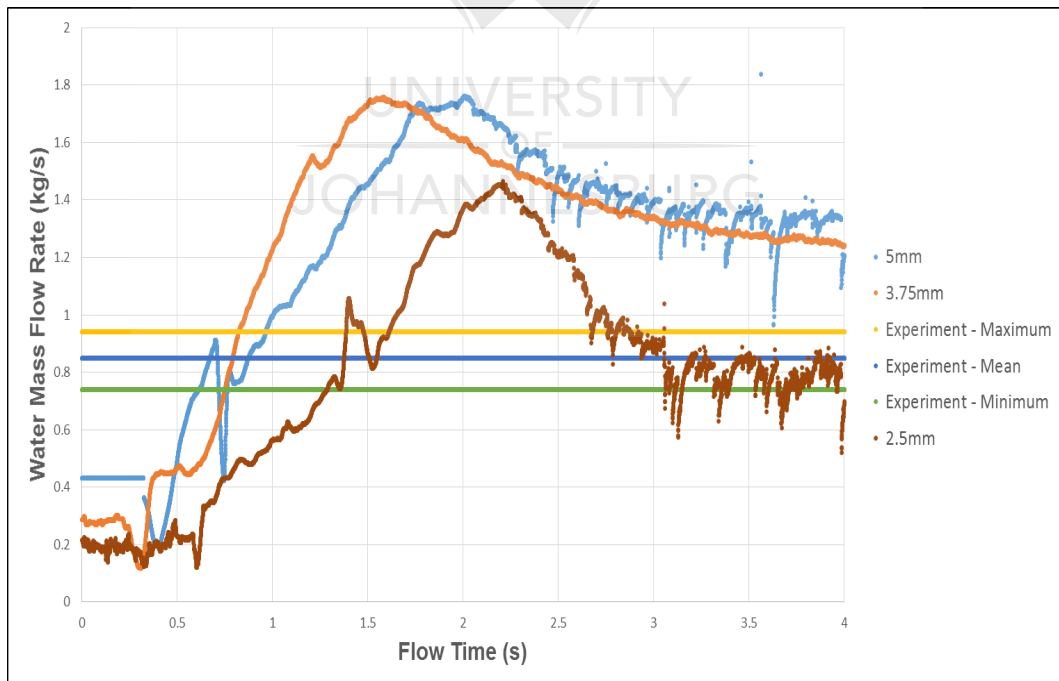


Figure 6.54: Underflow water mass flow rate as predicted by the VOF-DEM models, with RSM, for different mesh sizes

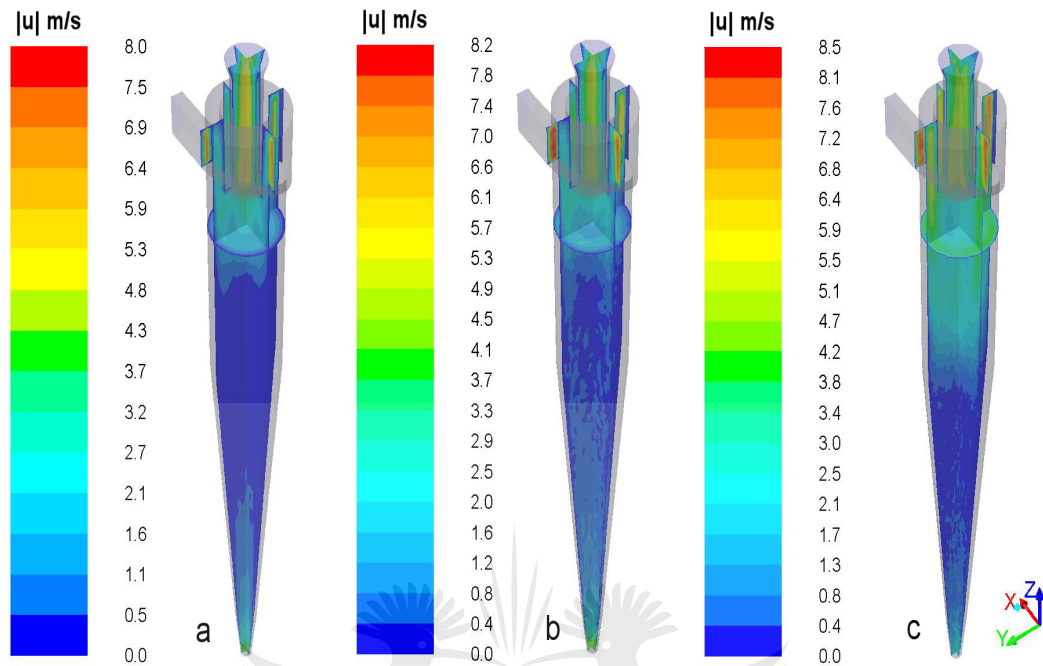


Figure 6.55: Contours coloured by velocity magnitude ($|u|$ m/s) on the planes $x = 0$, $y = 0$, $z = 0$ from the VOF-DEM (RSM) model at flow-time = 4s for the a) 5mm, b) 3.75mm and c) 2.5mm mesh sizes

to the extended shut-down of the cluster. Thus, the Eulerian and LBM-VOF particle models will be compared to the VOF-DEM, with RSM, on the 5mm mesh. The comparisons will be based on the first 1.5s of flow-time for the Eulerian and LBM-VOF particle models. The VOF-DEM, with LES, will not be used for comparison because it showed poor correlation with experimental measurements as discussed previously.

The VOF-DEM, with RSM, did not show mesh independence as discussed in Appendix C. However, the coarser mesh predictions for the VOF-DEM, with RSM, show qualitative and in some cases quantitative agreement with the fine mesh solution. Qualitative agreement in the overflow and underflow water mass flow rates is shown, for the different mesh sizes, in Figures 6.53 and 6.54 respectively.

Quantitative agreement is shown by the maximum velocity as shown on the

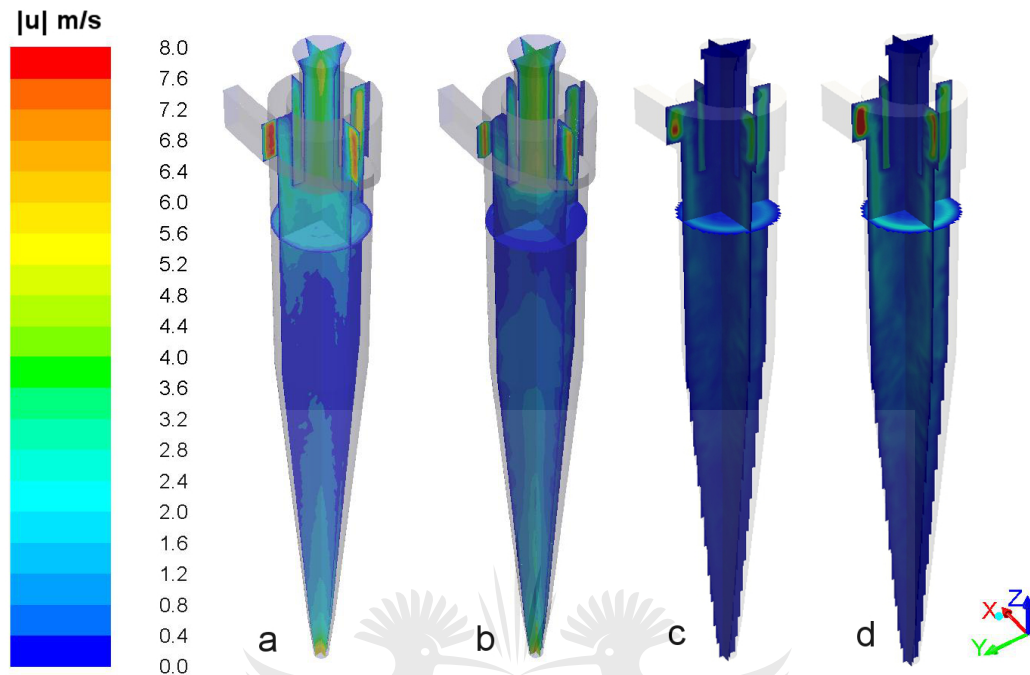


Figure 6.56: Contours coloured by velocity magnitude ($|u|$ m/s) on the planes $x = 0$, $y = 0$, $z = 0$ at $t = 1.5$ s from the a) VOF-DEM (RSM), b) Eulerian DDPM-DEM (RSM), c) LBM-VOF Verlet particle and d) LBM-VOF Point particle models

scale in Figure 6.55. Furthermore, qualitative agreement is shown in Figure 6.55. Thus, it is acceptable to compare the Eulerian DDPM-DEM and LBM-VOF particle model predictions to the VOF-DEM, with RSM, model predictions on the 5mm.

The velocity contours are shown in Figure 6.56. Whilst the maximum velocity is comparable for all the models, there are key features that illustrate noticeably different predictions. The short-cut flow is most evident in the Eulerian case. Apart from that, the Eulerian and the VOF-DEM model exhibit similar velocity profiles. This is not unexpected because at this point the air-core disappeared in the Eulerian DDPM-DEM model as well. Thus, both the VOF-DEM and the Eulerian DDPM-DEM models have essentially reduced to single phase flow with the same turbulence model, solver settings and boundary conditions, with only the initial conditions (the original air-core based solutions) being different. Thus, it is expected that the Eulerian DDPM-DEM and VOF-DEM model would produce similar results during

the period of surging.

The LBM-VOF particle models display noticeably different predictions from the NS based models, particularly in the region of the vortex finder, barrel, cone and spigot. This is primarily related to the behaviour of the pressure outlets behaving as outflow boundaries as discussed in the case of the air-core modelling. This is most notable in the significantly lower velocities in the region near the overflow and underflow, when comparing to the NS based models, as seen in Figure 6.56.

The LBM-VOF Verlet particle model has lower fluid velocities than the LBM-VOF Point particle model near the intake, in the barrel and the cone. This is related to the momentum transfer from the particle to the fluid and vice versa. In the Point particle model the particle does not transfer momentum to the fluid. However, in the case of the Verlet particle model the particle to fluid momentum transfer does occur. Furthermore, the momentum transfer due to drag and gravity from the fluid to the particle as well as the momentum transfer from the particles to the fluid as a result of particle-particle and particle-wall collisions would affect the flow field in this way. The effect of particles on the water velocity field was reported in [2] and is the same as the above results.

A comparison of the PSDs at the underflow and overflow shows that the LBM-VOF Verlet particle model provides the most accurate results against experiments, as seen in Figures 6.57 and 6.58. All of the models display noticeable error in comparison to experiment. However, these results are based on the solutions at a flow-time of 1.5s. Based on the VOF-DEM results, presented earlier, the underflow predictions are comparable to experiment at 4s of flow-time and the overflow results may require a significantly larger modelled flow-time to achieve comparability to experiment. However, the VOF-DEM, with RSM, was shown to match experiment with reasonable accuracy. Thus, the results in Figures 6.57 and 6.58 can be used for comparison against experimental measurements and the VOF-DEM model at the 1.5s flow-time.

From Figure 6.57 the LBM-VOF Verlet particle model and the LBM-VOF Point particle model show comparable results. The Eulerian DDPM-DEM model predicts only the $2\mu\text{m}$ particles leaving the underflow. Based on Figure 6.58, the LBM-VOF Verlet particle model shows the most accurate predictions in comparison to experiment and there is a noticeable difference in

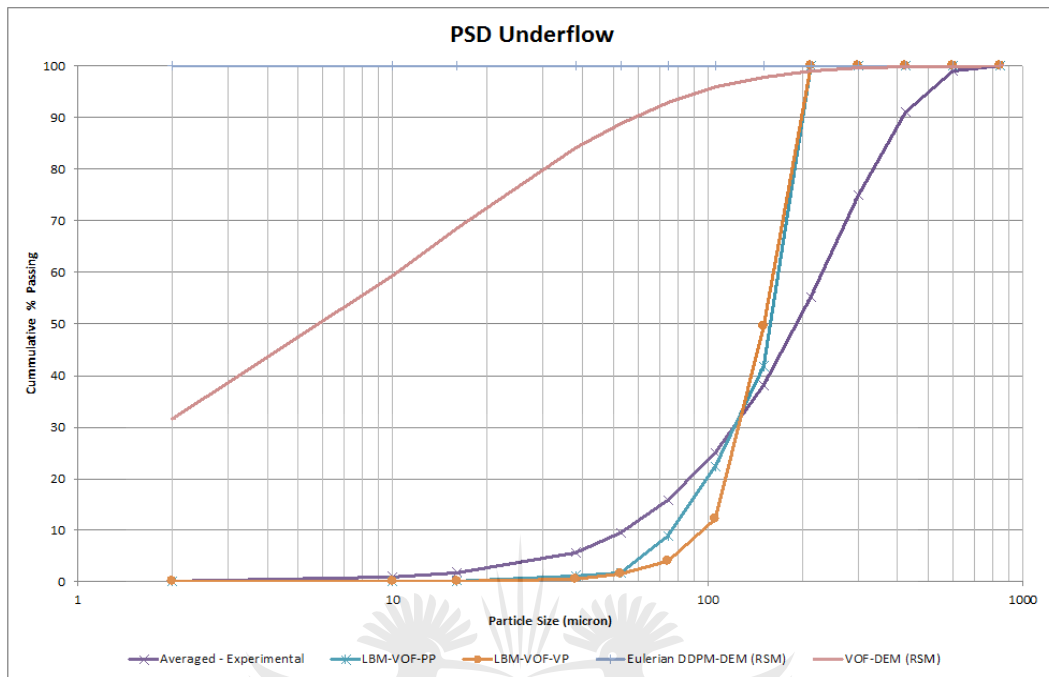


Figure 6.57: Underflow PSD - Comparison between Eulerian DDPM-DEM, VOF-DEM (RSM) and LBM-VOF particle models with experimental measurements

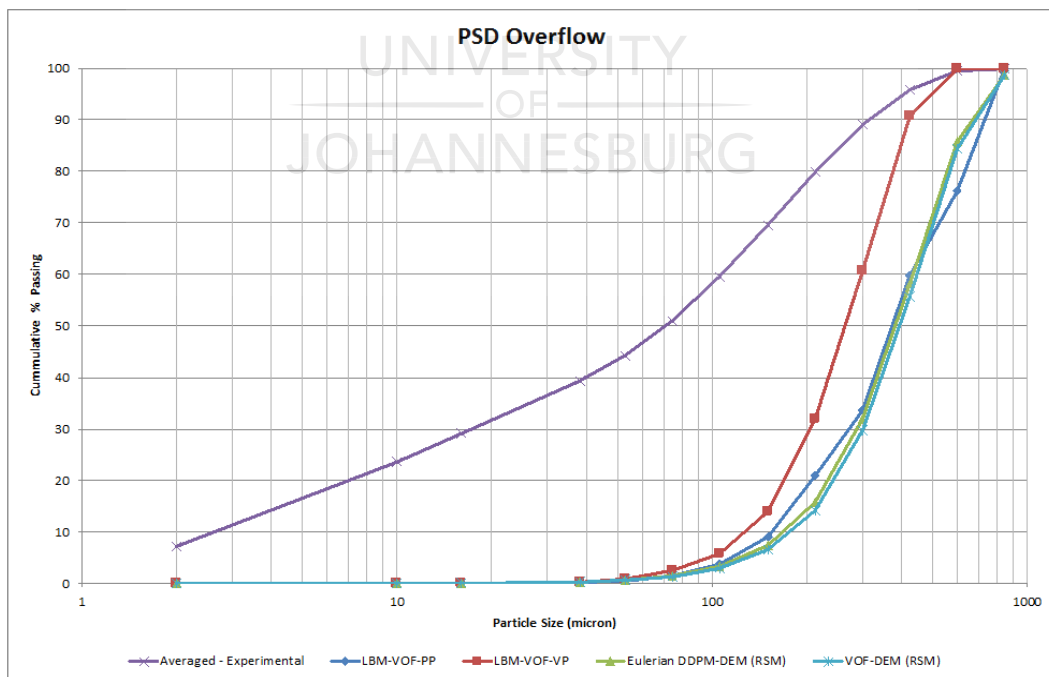


Figure 6.58: Overflow PSD - Comparison between Eulerian DDPM-DEM, VOF-DEM (RSM) and LBM-VOF particle models with experimental measurements

predictions between the LBM-VOF models. For the overflow, the Eulerian DDPM-DEM, VOF-DEM and the LBM-VOF Point particle model predictions are almost identical.

6.2.4 Computational Efficiency Comparison for Particle Models

For the particle models, the NS based VOF-DEM model, with the RSM, proved significantly more computationally efficient than the other NS based models. The results are based on the 5mm cell size for the NS models and a 3.9mm voxel size for the LBM model. In addition, the results for the VOF-DEM, with RSM on the 3.75mm mesh are presented to facilitate an appropriate comparison to the LBM model. All the models were run on 64 cores with an upper RAM limit of 60GB. In the case of the particle models the LBM-VOF (Point particle) model used significantly more RAM, as seen in Figure 6.59, which is contrary to the cases of the single phase and the air-core models. The LBM-VOF -VOF (Point particle) model, as in the previous cases, had a higher MCUPS value than the all the NS based models, as seen in Figure 6.60. A comparison of the MCUPS for only the NS models, as seen in Figure 6.61, reveals that the Eulerian DDPM-DEM model provides the worst performance.

The Eulerian models could not complete the full 4s flow-time calculation due to stability issues and the LBM-VOF (Point particle) model could not complete due to the extended shut-down of the cluster. An estimated walltime for the Eulerian and LBM models, based on extrapolation, is compared to the walltime requirements for the VOF-DEM models in Figure 6.62. The walltime comparisons in Figure 6.62 indicate that the Eulerian DDPM-DEM model is the worst performing model. However, the LBM model is comparable to the VOF-DEM model, with the RSM. Thus, it is clear that, contrary to the cases of single phase flow and the air-core modelling, the LBM model is not significantly more computationally efficient than the NS based models except in terms of MCUPS. In the case of the particle separation modelling the VOF-DEM model is the most computationally efficient and the Eulerian DDPM-DEM model is the least computationally efficient.

The LBM-VOF (Verlet particle) model could not be run on the cluster due

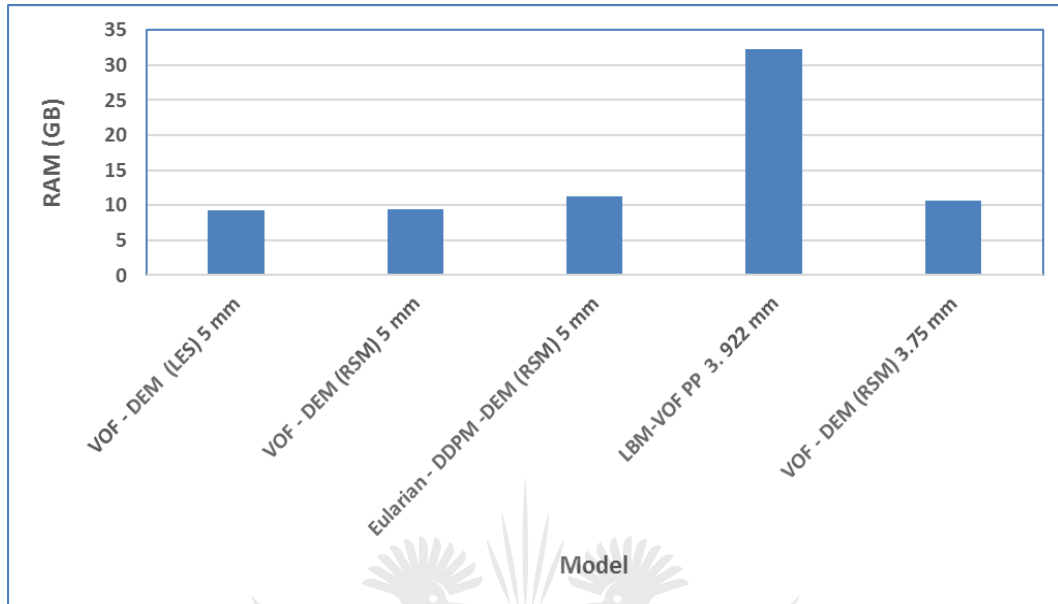


Figure 6.59: RAM usage for the particle models

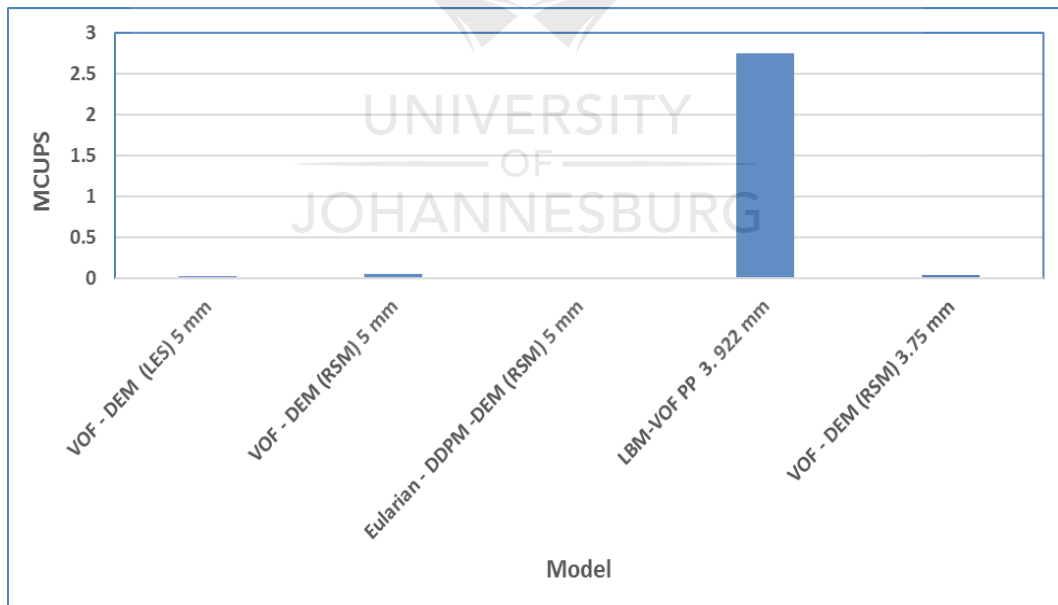


Figure 6.60: MCUPS based performance for the particle models

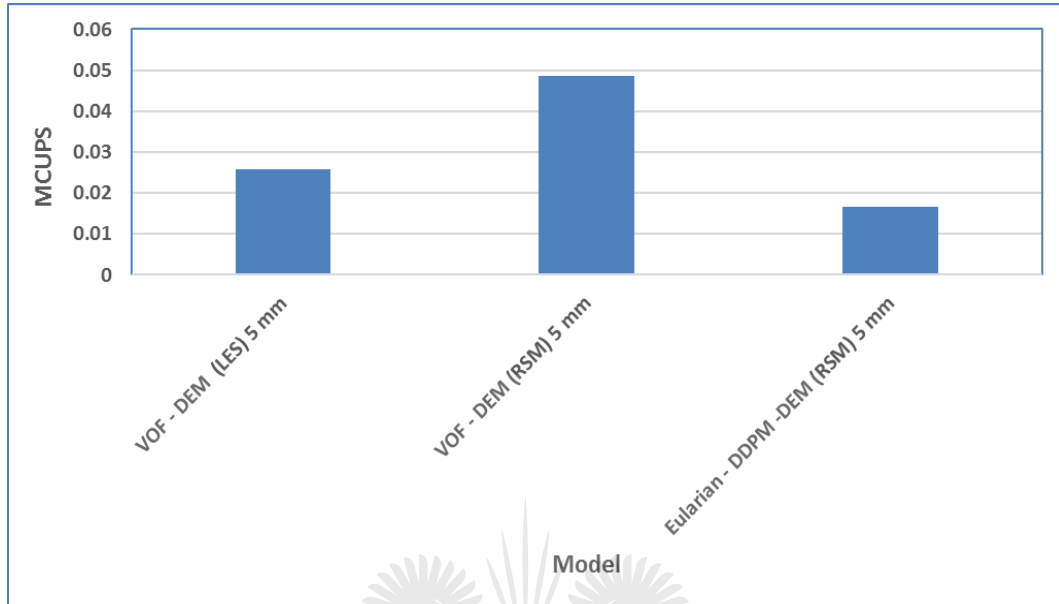


Figure 6.61: MCUPS based performance for the NS based particle models (expanded view of part of Figure 6.60)

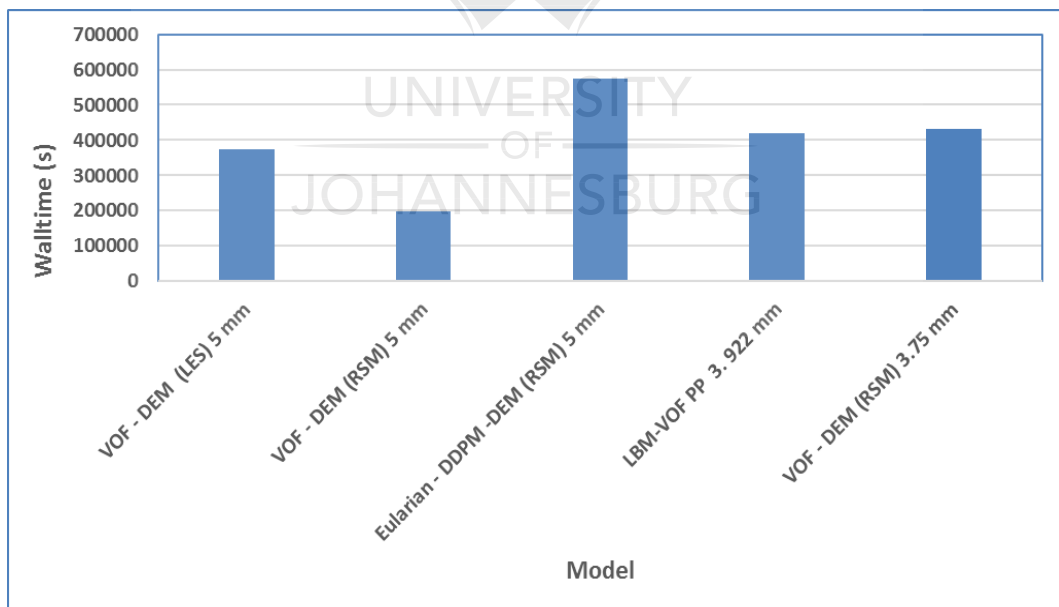


Figure 6.62: Walltime in seconds for the particle models

to the extended shut-down of the cluster. Thus, it was run on the 2 core (4 thread) virtual machine on a desktop. The LBM-VOF (Verlet particle) model used only 3GB of RAM. However, the model took approximately 18 and a half days to complete 1.5s of flow-time. Thus, an actual computational efficiency comparison of the LBM-VOF (Verlet particle) model could not be completed. However, the LBM-VOF (Verlet particle) model did not show any computational efficiency gains over the LBM-VOF (Point particle) model in early tests. Thus, it can be said, with confidence, that it had no computational efficiency gain over the VOF-DEM based models.

6.2.5 Linearisation of the DPM Source Terms in the NS Based Models

The VOF-DEM models provided numerical stability issues when the mesh was refined. Thus, as per the recommendation of Qfinsoft (the local ANSYS support) the DPM source terms were linearised and node based averaging of the DPM source terms was used to provide numerical stability. According to the ANSYS Theory Guide [13] and the ANSYS User Guide [14], using the default approach only distributes the DPM source terms to the local fluid cell whereas using node based averaging of the DPM source terms results in a non-localised distribution of the DPM source terms to the neighbouring fluid cell nodes. This results in less dependency between the DPM simulations and the mesh which in turn results in improved numerical stability [13, 14]. ANSYS [14], states that numerical stability can be improved by linearisation of the DPM source terms.

The use of node based averaging and linearisation of the DPM source terms resulted in improved numerical stability. However, this change did not have any noticeable effect on the computational efficiency of the models or on the predictions. Thus, it is advisable to linearise the DPM source and to use node based averaging of the DPM source terms to improve numerical stability.

6.3 Summary

In this chapter a detailed discussion of the simulation results is presented. Furthermore, the model results are benchmarked to each other as well as to

the experimental measurements. The models are also benchmarked to each other in terms of computational efficiency.

The LBM model was compared to the NS based model for single phase flow with LES to model turbulence. Based on literature regarding single phase flow in cyclones [28, 29] it is expected that the LBM model should provide predictions that are comparable to or more accurate than the NS based models. It is expected that both models should predict the low pressure region in the core of the cyclone that is the precursor to air-core formation and which is pivotal to effective separation. Furthermore, it is expected that both models should predict a highly swirling turbulent flow that leads to a separation of the primary (intake) fluid stream into two secondary streams, namely the spiral stream that flows from the inlet to the underflow along the wall and the spiral stream that flows to the centre of the hydrocyclone and upwards through the vortex finder and to the overflow [38].

Both the LBM and NS based models predicted the expected physics and show qualitative agreement. The only notable difference is that the LBM model predicts higher velocities near the intake apart from which both models offer similar velocity and flow field predictions. It is expected that the LBM model would provide a higher computational efficiency due to its inherent parallelism. The results indicate that, for single phase flow, the LBM does indeed exhibit a significantly higher computational efficiency than the NS based model.

A full comparison of the predictions of the NS based VOF, ASM and Eulerian models as well as the LBM-VOF and LBM two-fluid VOF models for air-core formation modelling was done. The expected physics to be captured by the models is the pressure drop between the inlet and the outlets (overflow and underflow) and the rotational motion of the fluid which produces a low pressure region in the core of the hydrocyclone along its central axis [6, 38]. It is expected that this low pressure region should result in air ingress from the underflow and the overflow which should be entrained in the main flow and forms an upward rotating column of air in the area of the low pressure region [6, 38].

The VOF, ASM and Eulerian models are all suitable for modelling the primary mechanisms of air-core formation. However, the Eulerian has a distinct advantage over the VOF and ASM models which is that the Eulerian model does not use the shared velocity formulation. Instead the Eulerian model models the phases as interpenetrating continua which should result in the

prediction of an air-core free-surface with less false diffusion due to the more accurate resolution of momentum transfer at the air-core free -surface. This should also lead to better predictions of the water mass flow rate split. It is expected that the LBM-VOF model should provide comparable predictions with the NS based VOF model and that the LBM-VOF two-fluid model should provide predictions comparable to the Eulerian model. In terms of computational efficiency it is expected that the Eulerian and LBM-VOF two-fluid models should be the least computationally efficient models, whereas the LBM-VOF, VOF and ASM models should be the most computationally efficient. It is known that the Eulerian and LBM-VOF two-fluid model may exhibit numerical instabilities.

The results indicate that the NS based models predict the primary mechanisms of air-core formation whilst the LBM-VOF model does not predict air-core formation. The Eulerian model provided the predictions of the air-core free-surface with the least amount of false diffusion In terms of mass flow rate predictions at the outlets the Eulerian model provides the best predictions when benchmarked to experiment. The ASM model provides the worst predictions. Whilst the LBM-VOF model could not predict air-core formation, the mass flow predictions at the outlets are of similar accuracy as the Eulerian models when compared to the experimental measurements.

The Eulerian model posed difficulties in terms of numerical stability as expected. The LBM-VOF two-fluid model was unstable and could not provide meaningful predictions, as expected, due to it's known instability as high Reynolds numbers. The LBM-VOF model was more computationally efficient in all aspects, except walltime for air-core modelling. The poor performance of the LBM-VOF model, in terms of walltime, was due to the fact that the LBM-VOF model required a 50 times smaller time step size than the NS based models.

The particle model results indicate that the NS based VOF-DEM, with RSM, model provides water mass flow rate predictions at the outlet that compare well with the experimental measurements. The phenomenological and physics based discussion of the modification of the dynamic behaviour of the cyclonic flow before particles are added and after particles are added and surging occurs revealed that the primary cyclonic separation mechanisms break down during surging and results in air-core suppression. The Separation efficiency predictions would require an additional 12s (a total of 16s) of modelled flow-time to match the experimental measurements. However, this is not feasible under the resource and time constraints of this study.

The underflow PSD predictions also matches the experimental measurements whilst the overflow PSD predictions does not match the experimental measurements.

The Eulerian DDPM-DEM and the LBM-VOF Point particle models provided similar result to the VOF-DEM, with RSM, model whereas the LBM-VOF Verlet particle model provided the most accurate results when benchmarked to the experimental measurements. The ASM model provides the worst predictions. The LBM particle models have no gain over the NS based models in terms of computational efficiency.

The turbulence models used, to provide closure to the RANS equations, were the RNG $k - \epsilon$ model and the RSM. For the LES approach the static Smagorinsky LES model was used. A turbulence sensitivity was done to determine which was the most accurate turbulence model in relation to the experimental results. The RNG $k - \epsilon$ model was used to provide a stable initial solution to the RSM as it generally provides more accurate predictions for highly swirling flows than the standard and realizable $k - \epsilon$ models [13,86]. The RNG $k\epsilon$ model is a two equation model and uses the Boussinesq hypothesis to calculate the Reynolds Stresses, thus, it is an isotropic turbulence model [13,86]. However, cyclonic flows exhibit largely anisotropic turbulence due to the high swirl and flow separation. Thus, it is expected that the RSM model should provide superior predictions to the RNG $k - \epsilon$ model because the RSM overcomes the limitation of the isotropic turbulence limitation of the two equation models solving the Reynold Stress transport equations. The LES model is expected to provide the best predictions of all the models because it resolves a larger range of turbulent eddies whereas the RSM models a larger range of turbulent eddies.

The results indicate that the accuracy of the LES model predictions increased whereas the accuracy of the RSM model predictions decreased as the mesh was refined. This indicates that as the mesh is refined further, the LES model may produce superior predictions. The LES model did not exhibit superior predictions for air-core and particle modelling. This is counter-intuitive as it would be expected that the LES results should be more accurate than the RSM results. However, the results in the above models are on meshes that are still too coarse for accurate LES models to provide acceptable results. To produce LES based results on meshes that are suitably fine was out of reach in this study due to the excessive computing time required, thus, it will be reserved for future work. However, it is useful for practitioners, which need to produce CFD results on coarse meshes, to know that RSM based models

can produce results that are within acceptable limits. The results indicate that on the coarse mesh the RNG $k - \epsilon$ is a better model and not the RSM and on only medium meshes is the RSM superior.



Chapter 7

Conclusions and Recommendations

The aim in this study was to compare the predictions of the NS and LBM based models of the multiphase flow interactions hydrocyclone to determine if either or both of the approaches can produce results which are comparable to experimental measurements. Thus, predictions from CFD models of a hydrocyclone, based on both the NS and LBM approach, were implemented and compared to each other as well as to experimental measurements (mass flow rates and PSDs). The models included both single phase flow and the multiphase flow in a hydrocyclone. The multiphase models were implemented to capture the multiphase interactions related to the air-core formation and particle-fluid, particle-particle and particle-wall interactions. The models were compared on the basis of the accuracy of the predictions against experimental measurements as well as on the basis of computational efficiency. The experimental measurements were done on a full scale 100mm hydrocyclone under normal plant operating conditions.

The NS based VOF, ASM and the Eulerian models were used to model the air-core. In terms of the LBM the LBM-VOF and LBM two-fluid VOF models were used to model the air-core. The DEM model was combined with the VOF and Eulerian models to predict particle interactions. In terms of the LBM the Point and Verlet particle classes were used LBM to model the particle interactions. The NS based models used three different turbulence models, namely: the RSM, RNG $k - \epsilon$ model and the LES model. The LBM

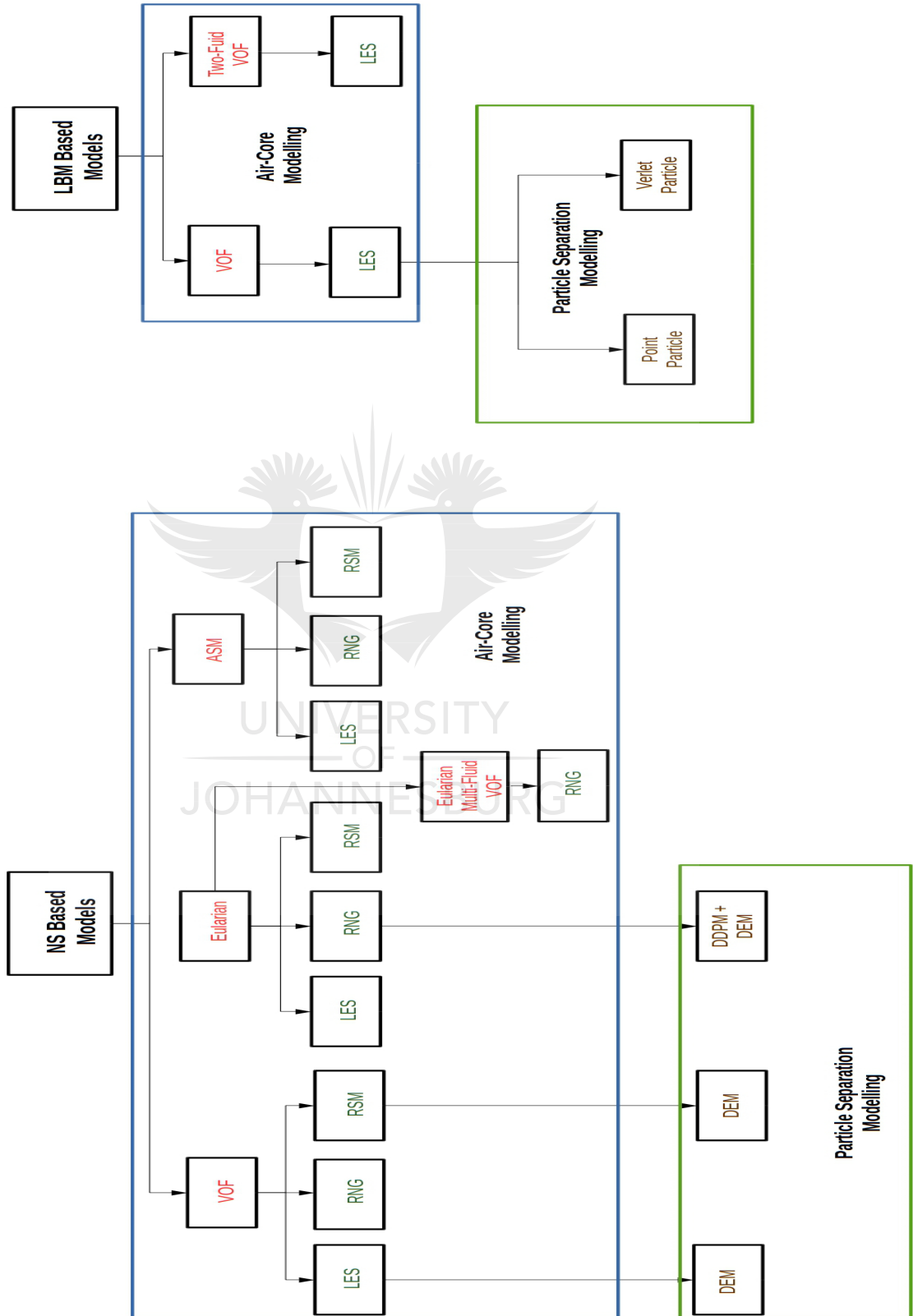


Figure 7.1: Summary of computational models used in the study

models used the LES model to account for turbulence. The implemented models are summarised in Figure 7.1. A full mesh sensitivity study was done to ensure that all the models achieved mesh independence.

7.1 Outcomes from the Study

In this study a full comparison of the predictions of the NS based VOF, ASM and Eulerian models as well as the LBM-VOF and LBM two-fluid VOF models for air-core formation modelling was done. The two-step process used in the literature for air-core modelling, which is to model the single phase first then model the air-core, was reduced to a one step process in this study. This was done by initialising the entire domain with $\alpha_{air} = 1$. This ensured that the air-core always formed, in the case of the NS based models, and that the transient air-core formation was captured directly.

All of the NS based models predictions of the mass flow rate at the overflow were in good agreement with the experimental measurements. However, there was a significant under-prediction of the underflow mass flow rate in all cases. Whilst the LBM-VOF model could not predict the formation of the air-core it did exhibit accurate predictions of the overflow mass flow rate. The LBM-VOF suffered from the same under-prediction of the underflow mass flow rate as in the case of the NS based models. The results indicate that the Eulerian model provides superior predictions, in comparison to the other NS based models for air-core modelling. The ASM model provided the worst predictions of the NS based models. The LBM-VOF model predictions of the underflow and overflow mass flow rates were comparable to the Eulerian model.

The Eulerian model provided numerical stability issues, particularly as the mesh was refined. The numerical instability in the case of the Eulerian model was related to the high velocity region ($> 20\text{m/s}$) in the core of the hydrocyclone. The impact of this high velocity region on the numerical stability was reduced by ensuring that the cell aspect ratios in that region were below 10 (and ideally below 5). The VOF and ASM models were not susceptible to the numerical instability caused by the high velocity region and high aspect ratio cells in the core of the hydrocyclone.

The NS based models predicted air-core formation whilst the LBM-VOF

model could not predict air-core formation. The Eulerian model provided the predictions of the air-core shape with the least amount of false diffusion, whereas the ASM model produced the air-core shape with the most false diffusion. The suppression of the air-core in the LBM-VOF model was related to the way in which Palabos implemented the pressure boundary in the LBM-VOF model and because the air-phase is modelled as an ‘empty’ region which does not solve the gas phase velocity field in the Palabos implementation of the LBM-VOF model. The pressure boundary in the LBM-VOF model in Palabos is an on-lattice boundary which behaves as an outflow boundary. However, to obtain the low pressure region in the core, which is the primary mechanism for air-core formation, an off-lattice pressure boundary would be ideal in this case. The LBM-VOF model did indicate that air was present at the outlets, however, the air could not be entrained in the main flow in order for the air-core to form because the air-phase velocity field was not solved. Thus, the LBM-VOF two fluid model was used to overcome the issue of the air-phase velocity field. Due to instability at high Reynolds number flows, as is the case in this study, the LBM-VOF two-fluid model could not provide meaningful predictions.

Despite the issues experienced with the LBM models in terms of air-core formation, the LBM model predictions were comparable to the NS based models for single phase flow. The LBM model produced the low pressure region in the core of the hydrocyclone when modelling single phase flow because the off-lattice pressure boundary was used.

The NS models were used to determine the best turbulence model to be used. On course meshes, for air-core formation, the RNG $k-\epsilon$ turbulence model produced the most accurate results. However, on fine meshes the RSM model produced the better results. The LES model may require significantly finer meshes than used in this study to produce results comparable to the RSM.

Furthermore, a comparison of the computational efficiency of the models was done based on RAM usage, walltime and MCUPS. The LBM was more computationally efficient in all aspects for single phase flow. The LBM was more computationally efficient in all aspects, except walltime for air-core modelling. The poor performance of the LBM-VOF model, in terms of walltime, was due to the fact that the LBM-VOF model required a 50 times smaller time step size than the NS based models.

The VOF-DEM model predictions were comparable to experiment in terms

of the underflow and overflow water mass flow rates. The under-prediction of the underflow mass flow rate was resolved by the addition of particles. The RSM turbulence model showed superior predictions over the LES model. Whilst mesh independence was not achieved, the VOF-DEM model, with the RSM produced results that were within 2% and 7% of experimental measurements in terms of the underflow and overflow mass flow rates, respectively. This result is only valid in the case of coarse meshes. It is expected that the LES results should be more accurate than the RSM results. However, the results in the above models are on meshes that are still too coarse for accurate LES models to provide acceptable results. The LES model may require significantly finer meshes than used in this study to produce results comparable or superior to the RSM. To produce LES based results on meshes that are suitably fine was out of reach in this study due to the excessive computing time required, thus, it will be reserved for future work.

The phenomenological and physics based discussion of the modification of the dynamic behaviour of the cyclonic flow before particles are added and after particles are added and surging occurs revealed that the primary cyclonic separation mechanisms break down during surging and results in air-core suppression. The separation efficiency predictions did not match experiment after 4s of modelled flow-time. However, an extrapolation of the separation efficiency as a function of flow-time, revealed that the model prediction of separation efficiency would match experimental measurements after 16s of modelled flow-time. This observation is speculative at this point. To prove that this observation is true requires additional modelling which requires the current models to run in excess of available computer resources at present. However, due to the resource and time limitations on the study, it was not possible to model this length of flow-time. Furthermore, the under-prediction of the separation efficiency was related to the fact that the model predicted that the system was in the state of surging, which led to an accumulation of particles in the cone. The results indicate that at 3.5s of modelled flow-time the state of surging began to diminish by virtue of a reduction the accumulation of the particles. The surging resulted in the suppression of the air-core.

The VOF-DEM, with RSM, model PSD predictions at the underflow were in good agreement with the experimental measurements, however, the overflow PSD predictions showed noticeable divergence from experiment. The difference in the overflow PSDs may due the impact of surging on the overflow. The VOF-DEM, with LES, showed poor agreement with experimental measurements in terms of the underflow and overflow predictions. Sampling of

the inlet in the VOF-DEM models revealed a notable difference between the specified PSD at the inlet and the PSD that was impressed at the inlet by the software in ANSYS Fluent.

A comparison of the VOF-DEM (RSM), Eulerian DDPM-DEM, LBM-VOF Point particle and the LBM-VOF Verlet particle models with experimental measurements, indicated that the NS based models provided comparable predictions to each other, with minor differences. Similarly the LBM-VOF particles models provided comparable predictions to each other, with minor differences. However, the LBM-VOF models showed superior predictions, in comparison to the NS based models and experimental measurements, in terms of the underflow PSD predictions. The LBM-VOF Point particle model and the NS based models had near identical overflow PSD predictions. The LBM-VOF Verlet particle model provided the most accurate overflow PSD predictions from all of the models.

The Eulerian DDPM-DEM model was the least computationally efficient of all the particle models. The LBM-VOF Point particle and the VOF-DEM (RSM) model showed comparable computational efficiency. However, the LBM-VOF Point particle model required more RAM and had a higher MCUPS value. The LBM-VOF Verlet particle models computational efficiency could not be gauged due to an extended shut-down of the CHPC. However, early test indicated that it was less computationally efficient than the LBM-VOF Point particle model and subsequently less computationally efficient than the VOF-DEM (RSM) model. However, no conclusions can be made as to the computational efficiency of the LBM-VOF Verlet particle model in relation to the Eulerian DDPM-DEM model.

The Eulerian model exhibited further problems with maintaining numerical stability when introducing particles. This issue was not investigated further, due to the time limitations of the study. The VOF-DEM models also exhibited problems with maintaining numerical stability when introducing particle. This was resolved by linearisation and node based averaging of the DPM source terms, as per the recommendations of Qfinsoft and [13,14]. The linearisation and node based averaging of the DPM source terms did not resolve the numerical stability issued encountered with the Eulerian DDPM-DEM model.

7.2 Validation of Research Hypothesis and Answers to Research Questions

The primary research hypothesis was:

The LBM can adequately resolve the multiphase interactions, thus predicting separation, in a hydrocyclone with greater accuracy and computational efficiency than CFD-DEM.

The expectations of any valid LBM solution that would validate the hypothesis would be to provide predictions of water mass flow rates at the outlets, air-core formation and particle separation that when benchmarked against the experimental measurements are more accurate than the NS based CFD/CFD-DEM models. In addition, the valid LBM solution should be more efficient (computationally) than the NS based CFD/CFD-DEM models.

The accuracy of the LBM model predictions of water mass flow rate at the overflow and underflow were similar to the NS based Eulerian model and superior to the NS based VOF and ASM models. In terms of air-core formation, the LBM was unable to model air-core formation, whereas the all NS based models were able to predict air-core formation. Thus, the water-air interactions could not be captured by the LBM models. The LBM Verlet particle model was able to predict particle separation, and subsequently particle interactions within a hydrocyclone more accurately than the NS based VOF-DEM and Eulerian DDPM-DEM models when benchmarked against experiment.

The LBM model was significantly more computationally efficient than the NS model in terms of walltime, RAM usage and MCUPS for single phase flow. For air-core modelling the LBM was computationally more efficient than the NS based models in terms of in terms of RAM usage and MCUPS but was less efficient than the NS models in terms of walltime. The LBM showed comparable computational efficiency for particle separation modelling to the to the VOF-DEM (RSM) model, however, the LBM model had a higher RAM usage.

Thus, in terms of water mass flow rates at the outlets, particle separation modelling and computational efficiency the hypothesis does hold. However,

in terms of air-core formation the hypothesis does not hold.

The research hypothesis was probed further in the form of a number of research questions which are as follows, with corresponding answers:

- *Can the CFD-DEM and LBM accurately resolve the multiphase interactions in a hydrocyclone?*

Answer: The CFD-DEM models were able to accurately model both air-core formation and the particle separation, and subsequently the particle interactions in a hydrocyclone. The LBM models could not predict air-core formation. However, the LBM was able to predict the particle separation, and subsequently the particle interactions in a hydrocyclone, more accurately than the NS based models. The LBM and NS based models produce comparable results for single phase flow modelling.

- *Can the CFD-DEM and LBM provide accurate predictions of separation in a hydrocyclone?*

Answer: The CFD-DEM and LBM models are able to provide accurate predictions of separation in a hydrocyclone. However, it may be necessary to model at least 16s of flow-time to determine if the NS based models can predict the full recovery from surging and the re-formation of the air-core as well as to determine if the LBM and NS based models can provide more accurate overflow PSD predictions.

- *Can the LBM give more accurate predictions, than CFD-DEM, of separation in a hydrocyclone?*

Answer: The LBM was able to predict the particle separation in a hydrocyclone, more accurately than the NS based models. This was the case if the Verlet particle class was used in the LBM and not in the case where the Point particle class was used.

- *Is the LBM more computationally efficient, than the CFD-DEM, in predicting multiphase interactions and separation in a hydrocyclone?*

Answer: The LBM is more computationally efficient than the NS model for single phase flow and air-core modelling. However, the LBM requires lower time step sizes than the NS based model to produce comparable results. The LBM model is comparable to the NS based models, in terms of computational efficiency, for particle modelling.

- *From the VOF, mixture, algebraic slip, Eulerian-Eulerian multiphase,*

Eulerian-Eulerian VOF, LBM-VOF and LBM two-fluid VOF models which provides the most accurate predictions of air-core formation in a hydrocyclone?

Answer: It is expected that the Eulerian model should predict an air-core free-surface with less false diffusion and better predictions of the water mass flow rate split. It is expected that the LBM-VOF model should provide comparable predictions with the NS based VOF model and that the LBM-VOF two-fluid model should provide predictions comparable to the Eulerian model. The Eulerian model provides superior predictions, in comparison to experiment, than the other models for modelling of air-core formation. The Eulerian VOF provides identical predictions to the standard Eulerian model. The LBM-VOF and LBM two-fluid VOF models could not predict air-core formation. The ASM model provides the least accurate solution of all the NS based approaches. On coarse meshes the RNG $k-\epsilon$ turbulence model produced the most accurate results. However, on fine meshes the RSM model produced the better results. The LES model requires significantly finer meshes than used in this study to produce results superior to the RSM.

- *Based on NS CFD models, does surface tension have a significant effect on air-core formation in hydrocyclones?*

Answer: Surface tension does not have a significant effect on air-core formation in hydrocyclones. Surface tension has a small but noticeable effect on the mass flow at the underflow and overflow, thus, it would be advisable to specify the surface tension coefficient based on whether hydrophilic or hydrophobic particles are being modelled. However, in light of the comparisons of the accuracy of the model predictions against experimental measurement, the effect of surface tension on the air-core is well below the maximum error in the model predictions. Thus, this effect, whilst noticeable, is not considered significant.

7.3 Contributions Arising from the Study

The key contributions from this study are as follows:

- The implementation, comparison and validation of the three main NS based multiphase models for air-core modelling; namely the VOF, ASM

and Eulerian-Eulerian models; in a hydrocyclone. Previous studies used either one of the models, but the full comparison to determine which model is the most accurate for air-core modelling has not been done in the literature.

- The implementation and validation of the LBM-VOF and LBM-VOF two-fluid model for modelling air-core modelling in a hydrocyclone.
- The comparison of the computational efficiency of the three main NS based multiphase models; namely the VOF, ASM and Eulerian-Eulerian models; and the LBM-VOF models for air-core modelling in a hydrocyclone.
- The implementation, comparison and validation of a VOF-DEM, an Eulerian DDPM-DEM, a LBM-VOF Point particle and a LBM-VOF Verlet particle model for modelling particle interactions and separation in a hydrocyclone.
- The phenomenological and physics based discussion of the modification of the dynamic behaviour of the cyclonic flow before particles are added and after particles are added and surging occurs.
- The comparison of the computational efficiency of a VOF-DEM, an Eulerian DDPM-DEM, a LBM-VOF Point particle and a LBM-VOF Verlet particle model for modelling particle interactions and separation in a hydrocyclone.
- The provision of a list of implementation tips that are necessary for successful modelling of hydrocyclones but are not mentioned in the literature. The list contains advice on meshing guidelines, physics specification and solver setup.

7.4 Recommendations and Future Work

The following recommendations are made for future work, either to overcome some of the problems discovered in this study or to further investigate promising areas revealed in this study:

- The development of a stabilisation method for the LBM two-fluid VOF model, when modelling high-Reynolds number flows and incorporate

an off-lattice boundary condition for the LBM two-fluid VOF model to predict air-core formation in hydrocyclones using the LBM.

- The development of a MCMP LBM model to allow modelling of air-core formation in hydrocyclones using the LBM.
- The implementation of a more physically sound DEM model, with particle rotation, as in [2, 3] to both the NS based models and the LBM model and compare the predictions to the DEM model in this study.
- The incorporation of more granular interactions in the Eulerian DDPM-DEM model, namely: solid shear-stress, turbulence dispersion, granular temperature and solids pressure.
- The implement of an IB-LBM model to account for localised fluid flow around particles.
- To port the LBM code to GPU based architectures to facilitate computational efficiency comparisons to the LBM model running on only a CPU.
- The use of PEPT to provide experimental data for particle trajectories as well as the fluid and particle velocity fields.
- An investigation of the reason for the difference in the specified PSD at the inlet and the PSD that is impressed at the inlet by the software in ANSYS Fluent.
- To model the transient flow effects that are common in practical hydrocyclones such as surging and recovery from surging and the subsequent re-formation of the air-core.

Bibliography

- [1] M. Narasimha, M. S. Brennan, and P. N. Holtham, “CFD modeling of hydrocyclones: prediction of particle size segregation,” *Minerals Engineering*, vol. 39, no. 0, pp. 173 – 183, 2012. [Online]. Available: <http://www.sciencedirect.com/science/article/pii/S0892687512002014>
- [2] K. W. Chu, B. Wang, A. B. Yu, and A. Vince, “CFD-DEM modelling of multiphase flow in dense medium cyclones,” *Powder Technology*, vol. 193, pp. 235–247, 2009.
- [3] K. W. Chu, B. Wang, D. L. Xu, Y. X. Chen, and A. B. Yu, “CFD-DEM simulation of the gas-solid flow in a cyclone separator,” *Chemical Engineering Science*, vol. 66, pp. 834–847, 2011.
- [4] R. Postma and A. Hoffmann, “The use of swirl tubes for dedusting,” in *World Congress on Particle Technology 3: A Four-day Symposium Incorporating the 3rd Biennial Particle Technology Forum of the AIChE Held at The Brighton Centre, UK, 6-9 July 1998*, ser. ECI Symposium Series, C. Proceedings, I. of Chemical Engineers (Great Britain), and A. I. of Chemical Engineers. Particle Technology Forum. n, Eds., vol. (1998). The Brighton Centre, UK: Institution of Chemical Engineers, IChemE, July 1998. [Online]. Available: <http://web.ift.uib.no/~hoffmann/papershtml/part98rf.pdf>
- [5] H. E. Van den Akker, “Toward a truly multiscale computational strategy for simulating turbulent two-phase flow processes,” *Industrial and Engineering Chemistry Research*, vol. 49, pp. 10 780–10 797, 2010.
- [6] M. Narasimha, M. Brennan, and P. N. Holtham, “Large Eddy Simulation of hydrocyclone-prediction of air-core diameter and shape,” *International Journal of Mineral Processing*, vol. 80, pp. 1–14, 2006.

- [7] J. A. Delgadillo and R. K. Rajamani, “Computational fluid dynamics prediction of the air-core in hydrocyclones,” *International Journal of Computational Fluid Dynamics*, vol. 23, pp. 189–197, 2009.
- [8] M. Brennan, P. Holtham, and M. Narasimha, “CFD modelling of cyclone separators: validation against plant hydrodynamic performance,” in *Seventh International Conference on CFD in the Minerals and Process Industries*, P. Witt and M. Schwarz, Eds. Melbourne, Australia: CSIRO, December 2009. [Online]. Available: http://www.cfd.com.au/cfd_conf09/PDFs/106BRE.pdf
- [9] M. Narasimha, M. S. Brennan, P. N. Holtham, A. Purchase, and T. J. Napier-Munn, “Large Eddy Simulation of a dense medium cyclone - prediction of medium segregation and coal partitioning,” in *Fifth International Conference on CFD in the Minerals and Process Industries*. Melbourne, Australia: CSIRO, December 2006. [Online]. Available: http://www.cfd.com.au/cfd_conf06/PDFs/047Man.pdf
- [10] K. H. Versteeg and W. Malalasekera, *An Introduction to Computational Fluid Dynamics : The Finite Volume Method*, 1st ed. Essex: Longman Scientific and Technical, 1995.
- [11] J. B. Joshi and V. V. Ranade, “Computational fluid dynamics for designing process equipment: expectations, current status, and path forward,” *Industrial & Engineering Chemistry Research*, vol. 42, pp. 1115–1128, 2003.
- [12] B. Wang, K. W. Chu, A. B. Yu, and A. Vince, “Modeling the multiphase flow in a dense medium cyclone,” *Industrial & Engineering Chemistry Research*, vol. 48, no. 7, pp. 3628–3639, 2009. [Online]. Available: <http://dx.doi.org/10.1021/ie801175c>
- [13] ANSYS Fluent Technical Staff, *ANSYS Fluent 16.0 Theory Guide*, ANSYS Inc., Canonsburg, PA USA, January 2015.
- [14] —, *ANSYS Fluent 16.0. Users Guide*, ANSYS Inc., Canonsburg, PA : USA, January 2015.
- [15] J. T. Cornelissen, F. Taghipour, R. Escudié, N. Ellis, and J. R. Grace, “CFD modelling of a liquid-solid fluidized bed,” *Chemical Engineering Science*, vol. 62, pp. 6334–6348, 2007.

- [16] J. Cui, X. Chen, X. Gong, and G. Yu, "Numerical study of gas-solid flow in a radial-inlet structure cyclone separator," *Industrial & Engineering Chemistry Research*, vol. 49, pp. 5450–5460, 2010.
- [17] C. Bhasker, "Flow simulation in industrial cyclone separator," *Advances in Engineering Software*, vol. 41, pp. 220–228, 2010.
- [18] K. Elsayed and C. Lacor, "Modeling, analysis and optimization of air-cyclones using artificial neural network, response surface methodology and CFD simulation approaches," *Powder Technology*, vol. 212, pp. 115–133, 2011.
- [19] H. Yoshida, Y. Nishimura, K. Fukui, and T. Yamamoto, "Effect of apex cone shape on fine particle classification of gas-cyclone," *Powder Technology*, vol. 204, pp. 54–62, 2010.
- [20] K. U. Bhaskar, Y. R. Murthy, M. R. Raju, S. Tiwari, J. K. Srivastava, and N. Ramakrishnan, "CFD simulation and experimental validation studies on hydrocyclone," *Minerals Engineering*, vol. 20, pp. 60–71, 2007.
- [21] Y.-F. Chang, C. G. Ilea, Ø. L. Aasen, and A. C. Hoffman, "Particle flow in a hydrocyclone investigated by positron emission particle tracking," *Chemical Engineering Science*, vol. 66, pp. 4203–4211, 2011.
- [22] Y. Zhao, Y. Ding, C. Wu, and Y. Cheng, "Numerical simulation of hydrodynamics in downers using a CFD-DEM coupled approach," *Powder Technology*, vol. 199, pp. 2–12, 2010.
- [23] G. B. Marin, Ed., *Advances in Chemical Engineering*, 1st ed. Academic Press, December 2006, vol. 31.
- [24] Z. Guo and C. Shu, *Advances in Computational Fluid Dynamics Vol. 3: Lattice Boltzmann Method and its' Applications in Engineering*, 1st ed. Singapore: World Scientific Publishing Co. Pte. Ltd., 2013.
- [25] M. C. Sukop and J. D. T. Thorne, *Lattice Boltzmann Modelling: An Introduction for Geoscientists and Engineers*, 2nd ed. Miami, FL: Springer-Verlag, 2006.
- [26] L. Wang, B. Zhang, X. Wang, W. Ge, and J. Li, "Lattice Boltzmann based discrete simulation for gas-solid fluidization," *Chemical Engineering Science*, vol. 101, pp. 228–239, 2013.

- [27] H. Gao, H. Li, and L.-P. Wang, "Lattice Boltzmann simulation of turbulent flow laden with finite-size particles," *Computers & Mathematics with Applications*, vol. 65, no. 2, pp. 194 – 210, 2013, special Issue on Mesoscopic Methods in Engineering and Science (ICMMES-2010, Edmonton, Canada). [Online]. Available: <http://www.sciencedirect.com/science/article/pii/S0898122111005074>
- [28] G. Gronald and J. J. Derksen, "Simulating turbulent swirling flow in a gas cyclone: A comparison of various modeling approaches," *Powder Technology*, vol. 205, pp. 160–171, 2011.
- [29] S. Pirker, C. Goniva, C. Kloss, S. Puttinger, J. Houben, and S. Schneiderbauer, "Application of a hybrid Lattice Boltzmann-finite volume turbulence model to cyclone short-cut flow," *Powder Technology*, vol. 235, pp. 572–580, 2013. [Online]. Available: <http://dx.doi.org/10.1016/j.powtec.2012.10.035>
- [30] J. J. Derksen, S. Sundaresan, and H. E. A. van den Akker, "Simulation of mass-loading effects in gas-solid cyclone separators," *Powder Technology*, vol. 163, no. 12, pp. 59 – 68, 2006, Fluidization and Fluid Particle Systems Papers chosen by the AIChE Area 3b Committee on Fluidization and Fluid Particle Systems, drawn from a selection of papers presented at the 2004 AIChE Annual Meeting held in Austin, 7-12 November 2004. [Online]. Available: <http://www.sciencedirect.com/science/article/pii/S0032591006000222>
- [31] H. P. Zhu, Z. Y. Zhou, R. Y. Yang, and A. B. Yu, "Discrete particle simulation of particulate systems: a review of major applications and findings," *Chemical Engineering Science*, vol. 63, pp. 5728–5770, 2008.
- [32] F. Muggli, L. Chatagny, and J. Latt, "Lattice Boltzmann method for the simulation of laminar mixers," in *Proceedings of the 14th European conference on mixing, Warsaw, 2012*. [Online]. Available: <http://mixing14.eu/program.php>
- [33] J. Habich, "Performance Evaluation of Numeric Compute Kernels on nVIDIA GPUs," Masters dissertation, Friedrich-Alexander-Universität Erlangen-Nürnberg Institut Für Informatik, January 2008. [Online]. Available: https://www10.informatik.uni-erlangen.de/Publications/Theses/2008/Habich_MA08.pdf
- [34] ANSYS, Inc., *ANSYS Fluent 16.0 [DVD-ROM]*., Canonsburg, PA : USA, January 2015. [Online]. Available: <http://www.ansys.com>

- [35] Flowkit Ltd., *Palabos 1.4r1.*, Lausanne: Switzerland, May 2013. [Online]. Available: <http://www.palabos.org>
- [36] T. Pöschel and T. Schwager, *Computational Granular Dynamics: Models and Algorithms*, 1st ed. Heidelberg, New York: Springer-Berlin, 2005.
- [37] S.-H. Chiang, D. He, and Y. Feng, “Liquid - Solids Separation,” in *Handbook of Fluidization and Fluid-Particle Systems*, 1st ed., W.-C. Yang, Ed. USA: Marcel Dekker, Inc., 2003, ch. 28.
- [38] W.-C. Yang, Ed., *Handbook of Fluidization and Fluid-Particle Systems*, 1st ed. USA: Marcel Dekker, Inc., 2003.
- [39] A. Davailles, E. Climent, and F. Bourgeois, “Fundamental understanding of swirling flow pattern in hydrocyclones,” *Separation and Purification Technology*, vol. 92, pp. 386 – 400, 2012.
- [40] A. A. Vegini, H. F. Meier, J. J. Iess, and M. Mori, “Computational fluid dynamics (CFD) analysis of cyclone separators connected in series,” *Industrial & Engineering Chemistry Research*, vol. 47, pp. 192–200, 2008.
- [41] F. J. de Souza, R. de Vasconcelos Salvo, and D. A. de Moro Martins, “Large Eddy Simulation of the gas-particle flow in cyclone separators,” *Separation and Purification Technology*, vol. 94, no. 0, pp. 61 – 70, 2012, CO2 Capture and Storage. [Online]. Available: <http://www.sciencedirect.com/science/article/pii/S1383586612002171>
- [42] C. Corts and A. Gil, “Modeling the gas and particle flow inside cyclone separators,” *Progress in Energy and Combustion Science*, vol. 33, no. 5, pp. 409 – 452, 2007. [Online]. Available: <http://www.sciencedirect.com/science/article/pii/S036012850700010X>
- [43] M. J. V. Goldschmidt, R. Beetstra, and J. A. M. Kuipers, “Hydrodynamic modelling of dense gas-fluidised beds: comparison and validation of 3D discrete particle and continuum models,” *Powder Technology*, vol. 142, no. 1, pp. 23 – 47, 2004. [Online]. Available: <http://www.sciencedirect.com/science/article/pii/S0032591004000804>
- [44] —, “Hydrodynamic modelling of dense gas-fluidised beds: Comparison of the kinetic theory of granular flow with 3D hard-sphere discrete particle simulations,” *Chemical Engineering Science*,

- vol. 57, no. 11, pp. 2059 – 2075, 2002. [Online]. Available: <http://www.sciencedirect.com/science/article/pii/S0009250902000829>
- [45] C. H. Ibsen, E. Helland, B. H. Hjertager, T. Solberg, L. Tadriss, and R. Occelli, “Comparison of multifluid and discrete particle modelling in numerical predictions of gas particle flow in circulating fluidised beds,” *Powder Technology*, vol. 149, no. 1, pp. 29 – 41, 2004. [Online]. Available: <http://www.sciencedirect.com/science/article/pii/S0032591004004127>
- [46] K. Nageswararao, D. Wiseman, and T. Napier-Munn, “Two empirical hydrocyclone models revisited,” *Minerals Engineering*, vol. 17, no. 5, pp. 671 – 687, 2004, hydrocyclones '03. [Online]. Available: <http://www.sciencedirect.com/science/article/pii/S0892687504000731>
- [47] K. W. Chu and A. B. Yu, “Numerical simulation of complex particle-fluid flows,” *Powder Technology*, vol. 179, no. 3, pp. 104 – 114, 2008, WCPT5 Papers presented at the 5th World Conference of Particle Technology (WCPT5), Orlando, Florida, April 23-27 2006 5th World Conference of Particle Technology (WCPT5). [Online]. Available: <http://www.sciencedirect.com/science/article/pii/S0032591007003129>
- [48] Y.-D. Hsu, H. M. Chein, T. M. Chen, and C.-J. Tsai, “Axial flow cyclone for segregation and collection of ultrafine particles: theoretical and experimental study,” *Environmental Science and Technology*, vol. 39, pp. 1299–1308, 2005.
- [49] J. P. K. Seville, A. Ingram, X. Fan, and D. J. Parker, “Chapter 4 positron emission imaging in chemical engineering,” in *Characterization of Flow, Particles and Interfaces*, ser. Advances in Chemical Engineering, J. Li, Ed. Academic Press, 2009, vol. 37, pp. 149 – 178. [Online]. Available: <http://www.sciencedirect.com/science/article/pii/S0065237709037041>
- [50] A. C. Hoffmann, C. Dechsiri, F. van de Piel, and H. G. Dehling, “PET investigation of a fluidized particle: spatial and temporal resolution and short term motion,” *Measurement Science and Technology*, vol. 16, pp. 851–858, 2005.
- [51] C. R. Bemrose, P. Fowles, M. R. Hawkesworth, and M. A. O’Dwyer, “Application of positron emission tomography to particulate flow measurement in chemical engineering processes,” *Nuclear Instruments and Methods in Physics Research*, vol. A273, pp. 874–880, 1988.

- [52] T. W. Leadbeater, D. J. Parker, and J. Gargiuli, "Positron imaging systems for studying particulate, granular and multiphase flows," *Particuoology*, vol. 10, pp. 146–153, 2012.
- [53] C. W. Chan, J. Seville, X. Fan, and J. Baeyens, "Particle motion in L-valve as observed by positron emission particle tracking," *Powder Technology*, vol. 193, pp. 137–149, 2009.
- [54] M. V. de Velden, J. Baeyens, J. P. K. Seville, and X. Fan, "The solids flow in the riser of a circulating fluidised bed (CFB) viewed by positron emission particle tracking (PEPT)," *Powder Technology*, vol. 183, pp. 290–296, 2008.
- [55] C. W. Chan, A. Brems, S. Mahmoudi, J. Baeyens, J. Seville, D. Parker, T. Leadbeater, and J. Gargiuli, "PEPT study of particle motion for different riser exit geometries," *Particuoology*, vol. 8, pp. 623–630, 2010.
- [56] Positron Imaging Centre Staff, University of Birmingham, "Positron Emission Particle Tracking (PEPT)," [Accessed: February 7, 2012]. [Online]. Available: <http://www.np.ph.bham.ac.uk/pic/pept>
- [57] —, "Physics of PET and PEPT," [Accessed: February 7, 2012]. [Online]. Available: [http://www.np.ph.bham.ac.uk/pic/pept\\$physics](http://www.np.ph.bham.ac.uk/pic/pept/$physics)
- [58] T. J. Olson and R. V. Ommen, "Optimizing hydrocyclone design using advanced CFD model," *Minerals Engineering*, vol. 17, no. 5, pp. 713 – 720, 2004, hydrocyclones '03. [Online]. Available: <http://www.sciencedirect.com/science/article/pii/S0892687504000688>
- [59] M. Narasimha, M. S. Brennan, P. N. Holtham, and T. J. Napier-Munn, "A comprehensive CFD model of dense medium cyclone performance," *Minerals Engineering*, vol. 20, no. 4, pp. 414 – 426, 2007, SPECIAL ISSUE: Selected papers from Ultrafine Grinding 06 and Hydrocyclones 06, held in Falmouth, UK in June 2006. [Online]. Available: <http://www.sciencedirect.com/science/article/pii/S0892687506002494>
- [60] E. A. Sadaati, *CFD Modelling Courses: Modelling Discrete Phase*, Lecture, Sharif University of Technology. [Online]. Available: <http://www.petrodanesh.com/Virtual%20Education/Mechanics/ANSYS-FLUENT/Modeling%20Discrete%20Phase.ppsx>
- [61] M. Bhamjee, S. H. Connell, and A. L. Nel, "The effect of surface tension on air-core formation in a hydrocyclone," in *Ninth*

- South African Conference on Computational and Applied Mechanics, Somerset West, 14 - 16 January 2014, SACAM 2014*, J. Hoffmann and J. van der Spuy, Eds. Stellenbosch, South Africa: SAAM, January 2014. [Online]. Available: <http://www.sacam2014.co.za/>
- [62] H. Meier, A. Vegini, and M. Mori, “Four-phase Eulerian-Eulerian model for prediction of multiphase flow in cyclones,” *The Journal of Computational Multiphase Flows*, vol. 3, pp. 93–106, June 2011. [Online]. Available: <http://multi-science.metapress.com/content/4174684N614G2257>
- [63] S. Krishnan, “A solution for every multiphase challenge,” in *Confidence by Design Workshop*, ANSYS Inc. Chicago, IL: ANSYS Inc., June 2012, conference Presentation. [Online]. Available: <http://www.ansys.com/staticassets/ANSYS/Conference/Confidence/Chicago/Downloads/a-solution-for-every-multiphase-challenge.pdf>
- [64] M. Thies, “Lattice Boltzmann modeling with free surfaces applied to formation of metal foams,” Doctoral thesis, Der Technischen Fakultät der Universität Erlangen-Nürnberg zur Erlangung des Grades, 2005.
- [65] T. Pohl, “High performance simulation of free surface flows using the Lattice Boltzmann Method,” Doctoral thesis, Der Technischen Fakultät der Universität Erlangen-Nürnberg zur Erlangung des Grades, 2008.
- [66] C. Körner, M. Thies, T. Hofmann, N. Thürey, and U. Råde, “Lattice Boltzmann model for free surface flow for modeling foaming,” *Journal of Statistical Physics*, vol. 121, no. 1-2, pp. 179–196, 2005. [Online]. Available: <http://dx.doi.org/10.1007/s10955-005-8879-8>
- [67] P. A. Cundall and O. D. L. Strack, “A discrete numerical model for granular assemblies,” *Géotechnique*, vol. 29, pp. 47 – 64, March 1979. [Online]. Available: <http://www.icevirtuallibrary.com/content/article/10.1680/geot.1979.29.1.47>
- [68] J. R. Third and C. R. Müller, “Coupled LBM-DEM simulations of gas fluidised beds,” in *The 14th International Conference on Fluidization From Fundamentals to Products*, ser. ECI Symposium Series, J. Kuipers, R. Mudde, J. van Ommen, and N. Deen, Eds., vol. (2013). NH Conference Centre Leeuwenhorst Noordwijkerhout, The Netherlands: ECI Digital Archives, May 2013. [Online]. Available: http://dc.engconfintl.org/fluidization_xiv/97

- [69] A. J. C. Ladd and R. Verberg, “Lattice-Boltzmann simulations of particle-fluid suspensions,” *Journal of Statistical Physics*, vol. 104, pp. 1191–1251, 2001.
- [70] N. Nhan-Quyen and A. J. C. Ladd, “Sedimentation of hard-sphere suspensions at low Reynolds Number,” *Journal of Fluid Mechanics*, vol. 525, pp. 73–104, 2 2005. [Online]. Available: http://journals.cambridge.org/article_S0022112004002563
- [71] Z. Yu and L.-S. Fan, “Lattice Boltzmann method for simulating particlefluid interactions,” *Particuology*, vol. 8, no. 6, pp. 539 – 543, 2010, special Issue In Honor of Professor Mooson Kwauk on his 90th Birthday. [Online]. Available: <http://www.sciencedirect.com/science/article/pii/S1674200110001343>
- [72] J. Lee and A. J. C. Ladd, “Particle dynamics and pattern formation in a rotating suspension,” *Journal of Fluid Mechanics*, vol. 577, pp. 183–209, 4 2007. [Online]. Available: http://journals.cambridge.org/article_S002211200700465X
- [73] A. J. C. Ladd, “Numerical simulations of particulate suspensions via a discretized Boltzmann equation. Part 1. Theoretical foundation,” *Journal of Fluid Mechanics*, vol. 271, pp. 285–309, 7 1994. [Online]. Available: http://journals.cambridge.org/article_S0022112094001771
- [74] —, “Numerical simulations of particulate suspensions via a discretized Boltzmann equation. Part 2. Numerical results,” *Journal of Fluid Mechanics*, vol. 271, pp. 311–339, 7 1994. [Online]. Available: http://journals.cambridge.org/article_S0022112094001783
- [75] L. Wang, B. Zhang, X. Wang, W. Ge, and J. Li, “Lattice Boltzmann based discrete simulation for gassolid fluidization,” *Chemical Engineering Science*, vol. 101, no. 0, pp. 228 – 239, 2013. [Online]. Available: <http://www.sciencedirect.com/science/article/pii/S0009250913004260>
- [76] K. Ota, K. Suzuki, and T. Inamuro, “Lift generation by a two-dimensional symmetric flapping wing: immersed boundary-Lattice Boltzmann simulations,” *Fluid Dynamics Research*, vol. 44, no. 4, p. 045504, 2012. [Online]. Available: <http://stacks.iop.org/1873-7005/44/i=4/a=045504>
- [77] S. Chen, Z. Liu, B. Shi, and C. Zheng, “Computation of gas-solid flows by finite difference Boltzmann equation,” *Applied Mathematics and*

- Computation*, vol. 173, no. 1, pp. 33 – 49, 2006. [Online]. Available: <http://www.sciencedirect.com/science/article/pii/S0096300305003000>
- [78] R. O. Fox, “A quadrature-based third-order moment method for dilute gas-particle flows,” *Journal of Computational Physics*, vol. 227, no. 12, pp. 6313 – 6350, 2008. [Online]. Available: <http://www.sciencedirect.com/science/article/pii/S0021999108001599>
- [79] K. Luo, J. Fan, and J. Feng, “Simulations of particle dispersion around multiple circular cylinders via an immersed boundary method,” *The Journal of Computational Multiphase Flows*, vol. 3, pp. 57 – 70, June 2011. [Online]. Available: <http://multi-science.metapress.com/content/3196N26729747511>
- [80] N. Govender, D. N. Wilke, S. Kok, and R. Els, “Development of a convex polyhedral discrete element simulation framework for nVIDIA Kepler based GPUs,” *Journal of Computational and Applied Mathematics*, vol. 270, no. 0, pp. 386 – 400, 2014, fourth International Conference on Finite Element Methods in Engineering and Sciences (FEMTEC 2013). [Online]. Available: <http://www.sciencedirect.com/science/article/pii/S037704271300705X>
- [81] Y. Zhao, “Lattice Boltzmann based PDE solver on the GPU,” *The Visual Computer*, vol. 24, no. 5, pp. 323–333, 2008. [Online]. Available: <http://dx.doi.org/10.1007/s00371-007-0191-y>
- [82] S. V. Patankar, *Numerical Heat Transfer and Fluid Flow*, 1st ed. Minnesota: Hemisphere Publishing Corporation, 1980.
- [83] R. Ansorge, *Mathematical Models of Fluid Dynamics: Modelling, Theory, Basic Numerical Facts An Introduction*, 1st ed. Hamburg: WILEY-VCH GmbH & Co. KGaA, Weinheim, Inc., 2003.
- [84] D. Kuzmin, *Introduction to Computational Fluid Dynamics, Lecture 1 - Lecture 11*, University of Dortmund - Institute of Applied Mathematics. [Online]. Available: <http://www.mathematik.uni-dortmund.de/~kuzmin/cfdintro/cfd.html>
- [85] R. D. Blevins, *Applied Fluid Dynamics Handbook*, 1st ed. NY: Van Nostrand Reinhold Company, Inc., 1984.
- [86] A. Bakker, *Applied Computational Fluid Dynamics: Lecture 10 - Turbulence Models, Lecture*, Lecture, Dartmouth University. [Online]. Available: <http://www.bakker.org/dartmouth06/engs150/10-rans.pdf>

- [87] D. C. Wilcox, *Turbulence Modelling for CFD*, 2nd ed. Glendale, CA: Griffin Printing, Inc., 1994.
- [88] A. Bakker, *Applied Computational Fluid Dynamics: Lecture 12 - Large Eddy Simulation, Lecture*, Lecture, Dartmouth University. [Online]. Available: <http://www.bakker.org/dartmouth06/engs150/12-les.pdf>
- [89] S. A. Morsi and A. J. Alexander, “An investigation of particle trajectories in two-phase flow systems,” *Journal of Fluid Mechanics*, vol. 55, pp. 193–208, 9 1972. [Online]. Available: http://journals.cambridge.org/article_S0022112072001806
- [90] G. Iaccarino, *Computational Methods in Fluid Dynamics using Commercial CFD Codes Lecture Notes: Solution Methods for the Incompressible Navier-Stokes Equations*, Standard University - Center for Turbulence Research. [Online]. Available: <http://web.stanford.edu/class/me469b/handouts/incompressible.pdf>
- [91] H. Y. Ling, L. Q. W. Yong, and T. G. Hai, “Lattice Boltzmann Method and its applications in engineering thermophysics,” *Chinese Sci. Bull.*, vol. 54, pp. 4117–4134, 2009.
- [92] S. Chen, G. D. Doolen, and K. G. Eggert, “Lattice-Boltzmann a versatile tool for multiphase fluid dynamics and other complicated flows,” *Los Alamos Science*, no. 22, pp. 99–111, 1994. [Online]. Available: <http://library.lanl.gov/cgi-bin/getfile?22-10.pdf>
- [93] G. Peng, H. Xi, C. Duncan, and S.-H. Chou, “Finite volume scheme for the Lattice Boltzmann Method on unstructured meshes,” *Phys. Rev. E*, vol. 59, pp. 4675–4682, Apr 1999. [Online]. Available: <http://link.aps.org/doi/10.1103/PhysRevE.59.4675>
- [94] M. Stiebler, J. Tölke and M. Krafczyk, “An upwind discretization scheme for the finite volume Lattice Boltzmann Method,” *Computers & Fluids*, vol. 35, no. 89, pp. 814 – 819, 2006, proceedings of the First International Conference for Mesoscopic Methods in Engineering and Science. [Online]. Available: <http://www.sciencedirect.com/science/article/pii/S004579300500143X>
- [95] OpenLB Project, *OpenLB*, Mannheim: Germany, August 2014. [Online]. Available: <http://www.openlb.net>
- [96] Kitware, Inc, *Paraview 4.0.1*, NY: USA. [Online]. Available: <http://www.paraview.org>

- [97] Dassault Systèmes SolidWorks Corporation, *Solidworks 2012-2013. [DVD-ROM]*., Waltham, MA: USA.
- [98] Visual Computing Lab - Istituto di Scienza e Tecnologie dell'Informazione "A. Faedo", *MeshLab v1.3.2*, Pisa: Italy, August 2012. [Online]. Available: <http://meshlab.sourceforge.net/>
- [99] M. Hecht and J. Harting, "Implementation of on-site velocity boundary conditions for $D3Q19$ Lattice Boltzmann simulations," *Journal of Statistical Mechanics: Theory and Experiment*, vol. 2010, no. 01, p. P01018, 2010. [Online]. Available: <http://stacks.iop.org/1742-5468/2010/i=01/a=P01018>
- [100] S. Geller, S. Uphoff, and M. Krafczyk, "Turbulent jet computations based on MRT and cascaded Lattice Boltzmann models," *Computers & Mathematics with Applications*, vol. 65, no. 12, pp. 1956 – 1966, 2013. [Online]. Available: <http://www.sciencedirect.com/science/article/pii/S0898122113002198>
- [101] R. W. Nash, H. B. Carver, M. O. Bernabeu, J. Hetherington, D. Groen, T. Krüger, and P. V. Coveney, "Choice of boundary condition for Lattice-Boltzmann simulation of moderate-Reynolds-Number flow in complex domains," *Phys. Rev. E*, vol. 89, p. 023303, Feb 2014. [Online]. Available: <http://link.aps.org/doi/10.1103/PhysRevE.89.023303>
- [102] S. K. Kang and Y. A. Hassan, "The Effect of lattice models within the Lattice Boltzmann Method in the simulation of wall-bounded turbulent flows," *Journal of Computational Physics*, vol. 232, no. 1, pp. 100 – 117, 2013. [Online]. Available: <http://www.sciencedirect.com/science/article/pii/S0021999112003968>
- [103] H. Yu, S. S. Girimaji, and L. Luo, "DNS and LES of decaying isotropic turbulence with and without frame rotation using Lattice Boltzmann Method," *Journal of Computational Physics*, vol. 209, pp. 599–616, 2005.
- [104] C. M. Teixeira, "Incorporating turbulence models into the Lattice-Boltzmann Method," *Int. J. Mod. Phys. C*, vol. 9, pp. 1159–1175, 1998.
- [105] O. Filippova, S. Succi, F. Mazzocco, C. Arrighetti, G. Bella, and D. Hnel, "Multiscale lattice boltzmann schemes with turbulence modeling," *Journal of Computational Physics*, vol. 170, no. 2, pp. 812 – 829, 2001. [Online]. Available: <http://www.sciencedirect.com/science/article/pii/S0021999101967646>

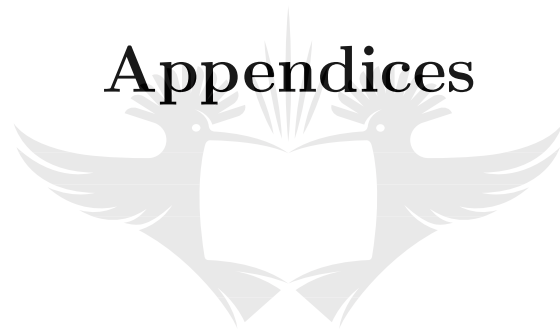
- [106] O. Malaspinas and P. Sagaut, “Consistent subgrid scale modelling for Lattice Boltzmann Method,” *Journal of Fluid Mechanics*, vol. 700, pp. 514–542, 2012. [Online]. Available: <http://dx.doi.org/10.1017/jfm.2012.155>
- [107] P. Sagaut, “Toward advanced subgrid models for Lattice-Boltzmann-based Large-Eddy Simulation: Theoretical formulations,” *Computers & Mathematics with Applications*, vol. 59, no. 7, pp. 2194 – 2199, 2010, mesoscopic Methods in Engineering and Science International Conferences on Mesoscopic Methods in Engineering and Science. [Online]. Available: <http://www.sciencedirect.com/science/article/pii/S0898122109006385>
- [108] Z. Guo, C. Zheng, and B. Shi, “An extrapolation method for boundary conditions in Lattice Boltzmann Method,” *Phys. Fluids*, vol. 14, pp. 2007–2010, 2002.
- [109] M. Bhamjee, S. H. Connell, and A. L. Nel, “An investigation into the applicability of the Lattice Boltzmann Method to modelling of the flow in a hydrocyclone,” in *Ninth South African Conference on Computational and Applied Mechanics, Somerset West, 14 - 16 January 2014, SACAM 2014*, J. Hoffmann and J. van der Spuy, Eds. Stellenbosch, South Africa: SAAM, January 2014. [Online]. Available: <http://www.sacam2014.co.za/>
- [110] J. Latt, “Choice of units in Lattice Boltzmann simulations,” *LBMMethod.org Documentation Project*, 2008. [Online]. Available: http://wiki.palabos.org/_media/howtos:lbunits.pdf
- [111] “Multotec Pty Ltd.” [Accessed: June 3, 2014]. [Online]. Available: <http://www.multotec.com>
- [112] “Multotec Pty Ltd.- South African Branch,” [Accessed: June 3, 2014]. [Online]. Available: <http://www.multotec.co.za>
- [113] Malvern Technical Staff, “Mastersizer 2000,” [Accessed: June 3, 2014]. [Online]. Available: <http://www.malvern.com/en/products/product-range/mastersizer-range/mastersizer-2000/default.aspx>
- [114] S. Benavides, *Cyclone Separators Physics behind them and how they work*, Lecture, Fakultet for Ingeniørvitenskap, Institutt for petroleumsteknologi og anvendt geofysikk. [Online]. Available: <http://www.ipt.ntnu.no/~jsg/student/prosjekt/2012BenavidesEmne.pdf>

- [115] R. H. Perry, D. W. Green, and J. O. Maloney, Eds., *Perry's Chemical Engineers Handbook*, 7th ed. USA: McGraw-Hill, 1997.
- [116] M. Pell and J. B. Dunson, "Gas-Solid Operations and Equipment," in *Perry's Chemical Engineers Handbook*, 7th ed., R. H. Perry, D. W. Green, and J. O. Maloney, Eds. USA: McGraw-Hill, 1997, ch. 17.
- [117] D. A. Dahlstrom, R. C. Bennett, E. Robert G, P. Harriott, T. Laros, W. Leung, S. A. Miller, B. Morey, J. Y. Oldshue, G. Priday, C. E. Silverblatt, J. S. Slottee, and J. C. Smith, "Liquid-Solid Operations and Equipment," in *Perry's Chemical Engineers Handbook*, 7th ed., R. H. Perry, D. W. Green, and J. O. Maloney, Eds. USA: McGraw-Hill, 1997, ch. 18.
- [118] K. V. S. Sastry, H. C. R. Hogg, T. L. Jespen, F. Knoll, B. Parekh, R. K. Rajamani, T. Sorenson, I. Wechsler, C. McCleary, and D. B. Todd, "Solid-Solid Operations and Equipment," in *Perry's Chemical Engineers Handbook*, 7th ed., R. H. Perry, D. W. Green, and J. O. Maloney, Eds. USA: McGraw-Hill, 1997, ch. 19.
- [119] S. Yue-Tao, S. Feng-zhong, and T. Wen-Quan, "An experimental study of gas-solid flow around helically finned tube," *Applied Thermal Engineering*, vol. 28, pp. 1563–1571, 2008.
- [120] R. A. Williams, "Landmarks in the application of electrical tomography in particle science and technology," *Particuology*, vol. 8, pp. 493–497, 2010.
- [121] J. Doucet, F. Bertrand, and J. Chaouki, "An extended radioactive particle tracking method for systems with irregular moving boundaries," *Powder Technology*, vol. 181, pp. 195–204, 2008.
- [122] B. Wang, K. W. Chu, A. B. Yu, and A. Vince, "electrostatics generation in a small cyclone separator," *Industrial & Engineering Chemistry Research*, vol. 48, pp. 185–190, 2009.
- [123] P. J. Roache, "Perspective: A method for uniform reporting of grid refinement studies," *Journal of Fluids Engineering*, vol. 116, pp. 405–413, 1994.
- [124] P. Gauglitz, L. A. Mahoney, J. Blanchard, and J. A. Bamberger, "Surface tension estimates for droplet formation in slurries with low concentrations of hydrophobic particles, polymer flocculants or surface-active contaminants," Pacific Northwest National

- Laboratory, Richland, WA : USA, Tech. Rep., June 2011. [Online]. Available: http://www.pnnl.gov/main/publications/external/technical_reports/PNNL-20466.pdf
- [125] *Palabos User Guide*, Flowkit Ltd., Lausanne: Switzerland, 2011. [Online]. Available: <http://www.palabos.org/documentation/userguide/>
- [126] Z. Guo, C. Zheng, and B. Shi, “Discrete lattice effects on the forcing term in the Lattice Boltzmann Method,” *Phys. Rev. E*, vol. 65, April 2002.
- [127] N.-R. Koosukuntla, “Towards development of a multiphase simulation model using Lattice Boltzmann Method (LBM),” Masters dissertation, Mechanical Engineering, University of Toledo, December 2011. [Online]. Available: https://etd.ohiolink.edu/ap/10?0::NO:10:P10_ACCESSION_NUM:toledo1321629685
- [128] X. He, X. Shan, and G. D. Doolen, “Discrete Boltzmann equation model for nonideal gases,” *Phys. Rev. E*, vol. 57, pp. R13–R16, Jan 1998. [Online]. Available: <http://link.aps.org/doi/10.1103/PhysRevE.57.R13>
- [129] Q. Zou and X. He, “On pressure and velocity boundary conditions for the Lattice Boltzmann BGK model,” *Physics of Fluids (1994-present)*, vol. 9, no. 6, pp. 1591–1598, 1997. [Online]. Available: <http://scitation.aip.org/content/aip/journal/pof2/9/6/10.1063/1.869307>
- [130] J.-Y. Yang, L.-H. Hung, and S.-H. Hu, “Semiclassical lattice hydrodynamics of rarefied channel flows,” *Applied Mathematics and Computation*, vol. 217, no. 11, pp. 5151 – 5159, 2011, special issue on Fluid Flow and Heat Transfer. [Online]. Available: <http://www.sciencedirect.com/science/article/pii/S0096300310008805>
- [131] P. A. Skordos, “Initial and boundary conditions for the Lattice Boltzmann Method,” *Phys. Rev. E*, vol. 48, pp. 4823–4842, Dec 1993. [Online]. Available: <http://link.aps.org/doi/10.1103/PhysRevE.48.4823>
- [132] Y. J. Huang, O. J. Nydal, and Y. Wang, “Body fitted link-cell algorithm for particulate flow simulation in curved pipeline domain,” *Applied Mathematical Modelling*, vol. 37, no. 5, pp. 3504 – 3512, 2013. [Online]. Available: <http://www.sciencedirect.com/science/article/pii/S0307904X1200457X>

- [133] H. Wang, H. Zhao, Z. Guo, and C. Zheng, “Numerical simulation of particle capture process of fibrous filters using Lattice Boltzmann two-phase flow model,” *Powder Technology*, vol. 227, no. 0, pp. 111 – 122, 2012, emerging Particle Technology. [Online]. Available: <http://www.sciencedirect.com/science/article/pii/S0032591011007418>
- [134] S. Geller, M. Krafczyk, J. Tölke, S. Turek and J. Hron, “Benchmark computations based on Lattice-Boltzmann, finite element and finite volume methods for laminar flows,” *Computers & Fluids*, vol. 35, no. 89, pp. 888 – 897, 2006, proceedings of the First International Conference for Mesoscopic Methods in Engineering and Science. [Online]. Available: <http://www.sciencedirect.com/science/article/pii/S0045793005001519>
- [135] T. Lee and C.-L. Lin, “A stable discretization of the Lattice Boltzmann equation for simulation of incompressible two-phase flows at high density ratio,” *Journal of Computational Physics*, vol. 206, no. 1, pp. 16 – 47, 2005. [Online]. Available: <http://www.sciencedirect.com/science/article/pii/S0021999104004929>
- [136] E. W. Weisstein, “Permutation Tensor.” [Online]. Available: <http://mathworld.wolfram.com/PermutationTensor.html>

Appendices



UNIVERSITY
OF
JOHANNESBURG

Appendix A

Malvern Mastersizer Particle Size Analyser Performance Verification Certificate

UNIVERSITY
OF
JOHANNESBURG

APPENDIX A. MASTERSIZER PSA PERFORMANCE VERIFICATION 190



Performance Verification Certificate
Mastersizer Series Sample Dispersion Units


Test date:	14 August 2013
Tester:	N.Fernandes
Mastersizer Serial No:	MAL100574
SDU serial No:	MAL110087
Sample Lot No:	163193
Test ref:	13002482

<p>Valid Product</p> <p><input type="radio"/> DIF2021</p> <p><input type="radio"/> Hydro S / S+ / SM</p> <p><input type="radio"/> DIF2012</p> <p><input type="radio"/> QS-M / MU (with 1000ml beaker)</p> <p><input checked="" type="radio"/> Hydro 2000G</p> <p><input type="radio"/> Hydro2000M/MU (1000ml beaker)</p> <p><input type="radio"/> Hydro2000 uP</p> <p><input type="radio"/> Hydro2000S with Autosampler 2000</p> <p><input type="radio"/> Hydro2000G with Autosampler 2000</p>	<p>Valid QAS</p> <p><input type="radio"/> QAS3001</p> <p><input type="radio"/> QAS3001B</p> <p><input checked="" type="radio"/> QAS3002</p> <p><input type="radio"/> QAS3004</p>
<p><input type="radio"/> MAM2460/1</p> <p><input type="radio"/> Scirocco 2000 ceramic</p> <p><input type="radio"/> Scirocco 2000 steel</p> <p><input type="radio"/> EDA2000</p> <p><input type="radio"/> EDA2001</p> <p><input type="radio"/> Spraytec wet unit</p>	

Test Results:

	Dv10	Dv50	Dv90
Tol % plus	5.0%	3.0%	5.0%
Tol% minus	5.0%	3.0%	5.0%
+Tol limit	39.044	63.706	94.471
Target	37.185	61.850	89.972
-Tol limit	35.326	59.995	85.473
RESULTS	37.524	61.747	90.584
Check>	0.9117% PASS	-0.1665% PASS	0.6802% PASS
OBSC%	19.43%	12.18% < 30.0%	PASS
RESIDUAL%	0.58%	< 2.0%	PASS
OQ Pass or Fail:	PASS		

I certify that the measurement results documented here were performed according to the performance verification procedure reference PVSQAS18.doc

Tester Signature:  Date: 13 August 2013

I certify that I witnessed the tester performing the PV on the date shown, and that the results appear to be correctly performed and recorded.

Customer Signature: _____ Date: _____

Certificate: PVCQAS18.XLS

APPENDIX A. MASTERSIZER PSA PERFORMANCE VERIFICATION 191



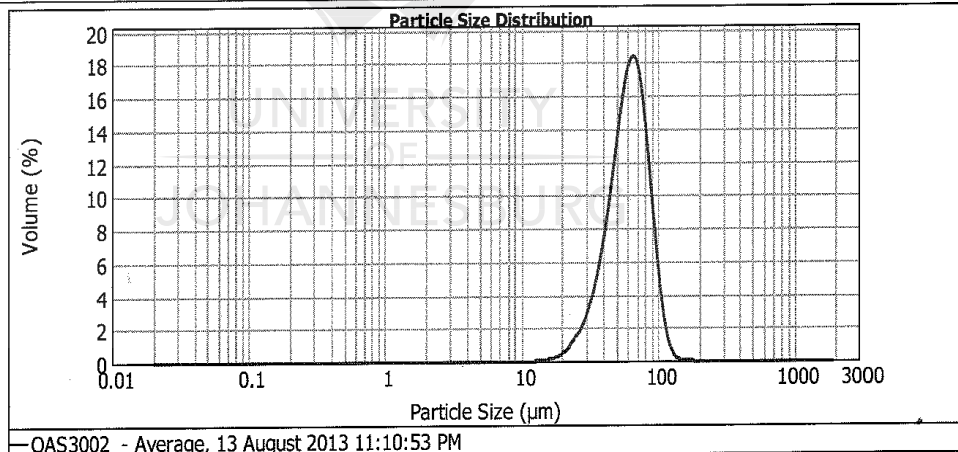
Result Analysis Report

Sample Name: QAS3002 - Average **SOP Name:** **Measured:** 13 August 2013 11:10:53 PM
Sample Source & type: Malvern **Measured by:** Christinar **Analysed:** 13 August 2013 11:10:54 PM
Sample bulk lot ref: 163193 **Result Source:** Averaged

Particle Name: Polystyrene latex **Accessory Name:** Hydro 2000G (A) **Analysis model:** Single narrow mode (spherical) **Sensitivity:** Enhanced
Particle RI: 1.590 **Absorption:** 0 **Size range:** 0.020 to 2000.000 μm **Obscuration:** 19.43 %
Dispersant Name: Water **Dispersant RI:** 1.330 **Residual:** 0.580 % **Result Emulation:** Off

Concentration: 0.1682 %Vol **Span :** 0.859 **Uniformity:** 0.271 **Result units:** Volume
Specific Surface Area: 0.102 m^2/g **Surface Weighted Mean D[3,2]:** 55.952 μm **Vol. Weighted Mean D[4,3]:** 63.250 μm

d(0.1): 37.524 μm **d(0.5):** 61.747 μm **d(0.9):** 90.584 μm



Size (µm)	Volume in %	Size (µm)	Volume in %	Size (µm)	Volume in %	Size (µm)	Volume in %	Size (µm)	Volume in %	Size (µm)	Volume in %
0.010	0.00	0.105	0.00	1.096	0.00	11.482	0.00	120.226	0.69	1258.925	0.00
0.011	0.00	0.120	0.00	1.259	0.00	13.183	0.04	138.038	0.08	1445.440	0.00
0.013	0.00	0.138	0.00	1.445	0.00	15.136	0.10	156.489	0.02	1609.587	0.00
0.015	0.00	0.158	0.00	1.660	0.00	17.378	0.24	181.970	0.00	1905.461	0.00
0.017	0.00	0.182	0.00	1.905	0.00	19.953	1.11	208.930	0.00	2187.762	0.00
0.020	0.00	0.209	0.00	2.188	0.00	22.909	3.28	239.893	0.00	2511.886	0.00
0.023	0.00	0.240	0.00	2.512	0.00	26.303	1.97	275.423	0.00	2884.032	0.00
0.026	0.00	0.275	0.00	2.884	0.00	30.200	5.25	316.228	0.00	3311.311	0.00
0.030	0.00	0.316	0.00	3.311	0.00	34.674	8.06	363.078	0.00	3801.894	0.00
0.035	0.00	0.363	0.00	3.802	0.00	38.811	11.98	416.869	0.00	4365.158	0.00
0.040	0.00	0.417	0.00	4.365	0.00	45.709	14.93	478.630	0.00	5011.872	0.00
0.046	0.00	0.479	0.00	5.012	0.00	52.481	16.63	549.541	0.00	5754.389	0.00
0.052	0.00	0.550	0.00	5.754	0.00	60.256	15.37	630.957	0.00	6606.934	0.00
0.060	0.00	0.631	0.00	6.607	0.00	68.183	11.33	724.436	0.00	7585.776	0.00
0.068	0.00	0.724	0.00	7.589	0.00	78.433	6.38	831.764	0.00	8709.636	0.00
0.079	0.00	0.832	0.00	8.710	0.00	91.201	2.50	954.993	0.00	10000.000	0.00
0.091	0.00	0.955	0.00	10.000	0.00	104.713		1066.478	0.00		
0.105	0.00	1.086	0.00	11.482	0.00	120.226		1258.925	0.00		

Operator notes: BN: 02
Ref: 13002482



Performance verification certificate
Mastersizer 2000 optical unit

Tester name: N.Fernandes Test: 13002482 Serial No.
 Test date: 14-Aug-13 MS 2000: MAL100574
 Hydro: MAL1022838

9um (nominal) Type No. 2009		Packaging lot: 41491				2009 batch
	Dv10	Dv50	Dv90	Resid%	Obsc%	
Tol%	5.0%	2.0%	5.0%			<input type="radio"/> 001
+Tol%	8.416	9.068	10.115	0.75%	13.00%	<input type="radio"/> 002
Target	8.016	8.891	9.634			<input type="radio"/> 003
-Tol%	7.616	8.713	9.153	0.00%	7.00%	<input type="radio"/> 004 to 010
RESULTS	8.087	8.911	9.630	0.40%	7.32%	<input checked="" type="radio"/> 011 to 014
Outcome	0.886%	0.228%	-0.042%			
	✓	✓	✓	✓	✓	✓

1um (nominal) Type No. 4009		Packaging lot: 39568				4009 batch
	Dv10	Dv50	Dv90	Resid%	Obsc%	
Tol%	5.0%	2.0%	5.0%			<input type="radio"/> 021
+Tol%	0.970	1.035	1.184	1.50%	6.00%	<input type="radio"/> 022 to 028
Target	0.924	1.015	1.128			<input type="radio"/> 029 to 035
-Tol%	0.878	0.995	1.072	0.00%	4.00%	<input checked="" type="radio"/> 036
RESULTS	0.927	1.019	1.131	0.34%	5.71%	
Outcome	0.325%	0.394%	0.266%			
	✓	✓	✓	✓	✓	✓

0.3um (nominal) Type No. 3300 (Note 1)		Packaging lot: 41796				3300 batch
	Dv10	Dv50	Dv90	Resid%	Obsc%	
Tol%	6.0%	3.0%	6.0%			<input type="radio"/> 021
+Tol%	0.289	0.304	0.349	3.50%	4.50%	<input type="radio"/> 022
Target	0.273	0.296	0.330			<input type="radio"/> 023 to 028
-Tol%	0.257	0.288	0.311	0.00%	2.50%	<input type="radio"/> 029 to 031
RESULTS	0.270	0.289	0.322	2.00%	4.02%	<input checked="" type="radio"/> 032 to 035
Outcome	-1.099%	-2.365%	-2.424%			
	✓	✓	✓	✓	✓	✓

The performance verification of this product has PASSED ✓

I certify that the measurement results documented here were performed according to the formal procedure reference **OQSMS2K44 OQ Specification.doc**
 Signatures
 Tester: *[Signature]*
 Date: 14 August 2013

I certify that I witnessed the tester performing the test on the date shown, which appeared to be correctly performed and recorded. I have been provided with, and accept, this Certificate and the Result Evidence as a record of the procedure.
 Recipient: _____
 Date: 14 August 2013

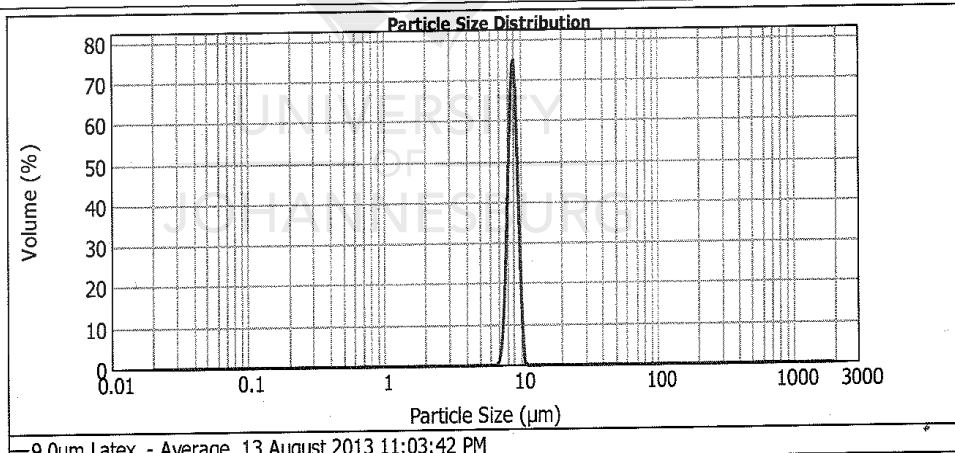


Result Analysis Report

Sample Name: 9.0um Latex - Average
Sample Source & type: Thermo
Sample bulk lot ref: 41491
SOP Name:
Measured by: Christinar
Result Source: Averaged
Measured: 13 August 2013 11:03:42 PM
Analysed: 13 August 2013 11:03:43 PM

Particle Name: Polystyrene latex
Particle RI: 1.590
Dispersant Name: Water
Accessory Name: Hydro 2000G (A)
Absorption: 0
Dispersant RI: 1.330
Analysis model: Single narrow mode (spherical)
Size range: 0.020 to 2000.000 um
Residual: 0.396 %
Sensitivity: Enhanced
Obscuration: 7.32 %
Result Emulation: Off
Concentration: 0.0089 %Vol
Span : 0.173
Uniformity: 0.0614
Result units: Volume
Specific Surface Area: 0.647 m²/g
Surface Weighted Mean D[3,2]: 8.832 um
Vol. Weighted Mean D[4,3]: 8.877 um

d(0.1): 8.087 um d(0.5): 8.911 um d(0.9): 9.630 um



— 9.0um Latex - Average, 13 August 2013 11:03:42 PM

Size (µm)	Volume in %	Size (µm)	Volume in %	Size (µm)	Volume in %	Size (µm)	Volume in %	Size (µm)	Volume in %
0.010	0.00	0.109	0.00	1.096	0.00	11.482	0.00	1258.925	0.00
0.011	0.00	0.120	0.00	1.239	0.00	13.183	0.00	1445.440	0.00
0.013	0.00	0.138	0.00	1.445	0.00	15.136	0.00	1658.587	0.00
0.015	0.00	0.156	0.00	1.660	0.00	17.378	0.00	1905.481	0.00
0.017	0.00	0.182	0.00	1.905	0.00	19.953	0.00	2187.782	0.00
0.020	0.00	0.209	0.00	2.188	0.00	22.909	0.00	2511.886	0.00
0.023	0.00	0.240	0.00	2.512	0.00	26.303	0.00	2884.032	0.00
0.026	0.00	0.275	0.00	2.884	0.00	30.200	0.00	3311.311	0.00
0.030	0.00	0.316	0.00	3.311	0.00	34.674	0.00	3801.884	0.00
0.035	0.00	0.363	0.00	3.802	0.00	39.811	0.00	4363.158	0.00
0.040	0.00	0.417	0.00	4.365	0.00	45.709	0.00	5011.872	0.00
0.046	0.00	0.479	0.00	5.012	0.00	52.481	0.00	5754.389	0.00
0.052	0.00	0.550	0.00	5.754	0.00	60.258	0.00	6603.934	0.00
0.060	0.00	0.631	0.00	6.607	0.97	69.163	0.00	7585.776	0.00
0.069	0.00	0.724	0.00	7.586	36.63	79.433	0.00	8708.636	0.00
0.079	0.00	0.832	0.00	8.710	61.85	91.201	0.00	10000.000	0.00
0.091	0.00	0.955	0.00	10.000	61.85	104.713	0.00		
0.105	0.00	1.096	0.00	11.482	0.45	120.226	0.00		

Operator notes: BN: 2009-013
 Ref: 13002482

APPENDIX A. MASTERSIZER PSA PERFORMANCE VERIFICATION 194



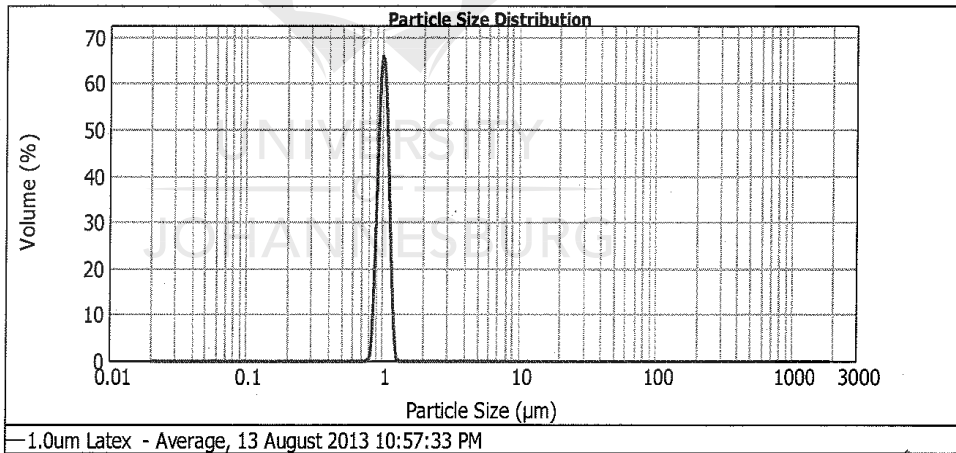
Result Analysis Report

Sample Name: 1.0um Latex - Average
SOP Name:
Measured: 13 August 2013 10:57:33 PM
Sample Source & type: Thermo
Measured by: Christinar
Analysed: 13 August 2013 10:57:34 PM
Sample bulk lot ref: 39568
Result Source: Averaged

Particle Name: Polystyrene latex
Accessory Name: Hydro 2000G (A)
Analysis model: Single narrow mode (spherical)
Sensitivity: Enhanced
Particle RI: 1.590
Absorption: 0
Size range: 0.020 to 2000.000 um
Obscuration: 5.71 %
Dispersant Name: Water
Dispersant RI: 1.330
Residual: 0.335 %
Result Emulation: Off

Concentration: 0.0006 %Vol
Span : 0.200
Uniformity: 0.0767
Result units: Volume
Specific Surface Area: 5.61 m²/g
Surface Weighted Mean D[3,2]: 1.019 um
Vol. Weighted Mean D[4,3]: 1.025 um

d(0.1): 0.927 um d(0.5): 1.019 um d(0.9): 1.131 um



Size (µm)	Volume in %	Size (µm)	Volume in %	Size (µm)	Volume in %	Size (µm)	Volume in %	Size (µm)	Volume in %	Size (µm)	Volume in %
0.010	0.00	0.105	0.00	1.036	19.43	11.482	0.00	120.226	0.00	1258.925	0.00
0.011	0.00	0.120	0.00	1.259	0.00	13.183	0.00	138.036	0.00	1445.440	0.00
0.013	0.00	0.138	0.00	1.445	0.00	15.136	0.00	158.489	0.00	1658.587	0.00
0.015	0.00	0.158	0.00	1.660	0.00	17.378	0.00	181.970	0.00	1905.461	0.00
0.017	0.00	0.182	0.00	1.905	0.00	19.953	0.00	208.930	0.00	2187.762	0.00
0.020	0.00	0.209	0.00	2.188	0.00	22.909	0.00	238.883	0.00	2511.866	0.00
0.023	0.00	0.240	0.00	2.512	0.00	26.303	0.00	275.423	0.00	2884.032	0.00
0.026	0.00	0.275	0.00	2.884	0.00	30.200	0.00	316.226	0.00	3311.311	0.00
0.030	0.00	0.316	0.00	3.311	0.00	34.674	0.00	363.078	0.00	3801.894	0.00
0.035	0.00	0.363	0.00	3.802	0.00	39.811	0.00	416.869	0.00	4366.158	0.00
0.040	0.00	0.417	0.00	4.365	0.00	45.703	0.00	478.630	0.00	5011.872	0.00
0.046	0.00	0.479	0.00	5.012	0.00	52.481	0.00	548.541	0.00	5754.989	0.00
0.052	0.00	0.550	0.00	5.754	0.00	60.259	0.00	630.957	0.00	6606.994	0.00
0.060	0.00	0.631	0.00	6.607	0.00	69.183	0.00	724.436	0.00	7585.776	0.00
0.069	0.00	0.724	0.00	7.586	0.00	79.433	0.00	831.764	0.00	8709.635	0.00
0.079	0.00	0.832	0.00	8.710	0.00	91.201	0.00	954.993	0.00	10000.000	0.00
0.091	0.00	0.955	20.46	10.000	0.00	104.713	0.00	1096.478	0.00		
0.105	0.00	1.093	60.11	11.482	0.00	120.226	0.00	1258.925	0.00		

Operator notes: BN: 4009-034
 Ref: 13002482

APPENDIX A. MASTERSIZER PSA PERFORMANCE VERIFICATION 195



Result Analysis Report

Sample Name:
300nm Latex - Average

Sample Source & type:
Thermo

Sample bulk lot ref:
41796

SOP Name:

Measured by:
Christinar

Result Source:
Averaged

Measured:
13 August 2013 10:51:27 PM

Analysed:
13 August 2013 10:51:28 PM

Particle Name:
Polystyrene latex

Particle Ri:
1.590

Dispersant Name:
Water

Accessory Name:
Hydro 2000G (A)

Absorption:
0

Dispersant Ri:
1.330

Analysis model:
Single narrow mode (spherical)

Size range:
0.020 to 2000.000 um

Residual:
2.002 %

Sensitivity:
Enhanced

Obscuration:
4.02 %

Result Emulation:
Off

Concentration:
0.0016 %Vol

Span :
0.180

Uniformity:
0.0399

Result units:
Volume

Specific Surface Area:
19.7 m²/g

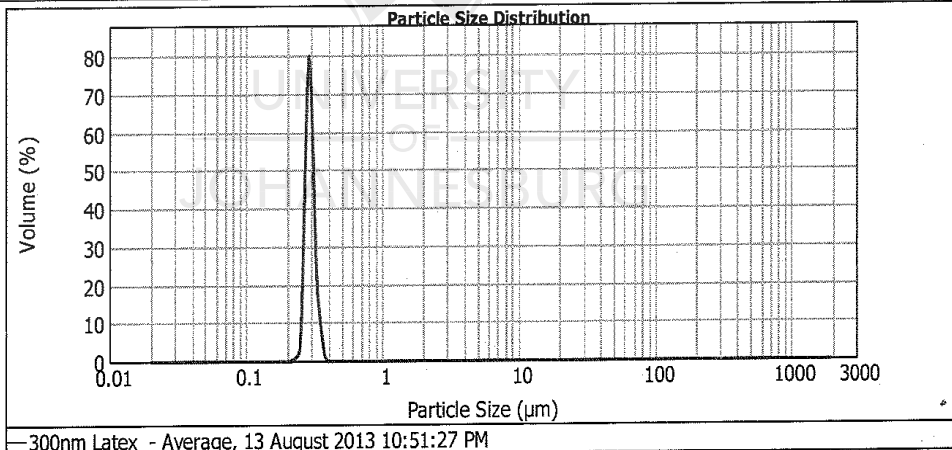
Surface Weighted Mean D[3,2]:
0.291 um

Vol. Weighted Mean D[4,3]:
0.292 um

d(0.1): 0.270 um

d(0.5): 0.289 um

d(0.9): 0.322 um



Size (µm)	Volume In %	Size (µm)	Volume In %	Size (µm)	Volume In %	Size (µm)	Volume In %	Size (µm)	Volume In %	Size (µm)	Volume In %
0.010	0.00	0.105	0.00	1.095	0.00	11.482	0.00	120.226	0.00	1258.925	0.00
0.011	0.00	0.120	0.00	1.259	0.00	13.183	0.00	138.038	0.00	1445.440	0.00
0.013	0.00	0.138	0.00	1.445	0.00	15.136	0.00	158.489	0.00	1659.587	0.00
0.015	0.00	0.158	0.00	1.660	0.00	17.378	0.00	181.970	0.00	1905.461	0.00
0.017	0.00	0.182	0.00	1.905	0.00	19.953	0.00	208.930	0.00	2187.762	0.00
0.020	0.00	0.209	0.00	2.188	0.00	22.909	0.00	239.883	0.00	2511.866	0.00
0.023	0.00	0.240	0.00	2.512	0.00	26.303	0.00	275.423	0.00	2884.032	0.00
0.026	0.00	0.275	19.21	2.884	0.00	30.200	0.00	316.228	0.00	3311.311	0.00
0.030	0.00	0.316	67.81	3.311	0.00	34.674	0.00	363.076	0.00	3801.894	0.00
0.035	0.00	0.363	12.71	3.802	0.00	39.811	0.00	416.999	0.00	4365.158	0.00
0.040	0.00	0.417	0.01	4.365	0.00	45.708	0.00	478.630	0.00	5011.872	0.00
0.046	0.00	0.479	0.00	5.012	0.00	52.461	0.00	549.541	0.00	5754.369	0.00
0.052	0.00	0.550	0.00	5.754	0.00	60.256	0.00	630.967	0.00	6606.934	0.00
0.060	0.00	0.631	0.00	6.607	0.00	69.163	0.00	724.436	0.00	7585.776	0.00
0.069	0.00	0.724	0.00	7.586	0.00	79.433	0.00	831.764	0.00	8709.636	0.00
0.079	0.00	0.832	0.00	8.710	0.00	91.201	0.00	954.983	0.00	10000.000	0.00
0.091	0.00	0.965	0.00	10.000	0.00	104.713	0.00	1096.478	0.00		
0.105	0.00	1.095	0.00	11.482	0.00	120.226	0.00	1258.925	0.00		

Operator notes: BN: 3300-035
Ref: 13002482

Appendix B

The Effect of Surface Tension on Air-Core Formation

Gauglitz *et al.* [124] illustrated that entrained hydrophilic particles, such as gold, have no effect on the surface tension of water, whereas, entrained hydrophobic particles reduce the surface tension of water. The work of Gauglitz *et al.* [124] implies that the effect the entrained particles have on the surface tension of the carrier medium may have an effect on the air-core. However, the effect of varying surface tension on the air-core has not been considered in the literature. Furthermore, insufficient detail is provided, in the literature, on how surface tension was included in the models. Thus, the purpose of this study is to propose a model for incorporating surface tension in a CFD model of air-core formation in a hydrocyclone. Furthermore, the effect of varying surface tension on air-core formation in a hydrocyclone will be investigated.

Three cases were modelled in this research: no surface tension, pure water, and water with reduced surface tension. Thus, the second case models the effect of surface tension when using pure water or water with entrained hydrophilic particles. The final case models the effect of surface tension when using water with hydrophobic particles.

Table B.1: Old VV100 Hydrocyclone dimensions

D_c (mm)	H (mm)	D_{overflow} (mm)	$D_{\text{underflow}}$ (mm)	h (mm)	l (mm)	s (mm)	a (mm)	b (mm)
100	1250	75	20	895	80	100	13	45

B.1 Model, Boundary Conditions and Solver Setup

The results in this appendix were obtained during the preliminary modelling of a hydrocyclone for this study and were published as a conference paper [61]. Initially Multotec Pty Ltd. provided a hydrocyclone with dimensions as given in Table B.1. Thus, the initial models were done on the version in Figure 3.1 and Table B.1. Multotec Pty Ltd. changed the hydrocyclone to a different version of the VV100 for the experimental work. The experimental work and final models were done on a more recent version as given in Figure 3.1 and Table 3.1.

The NS based models computational grid (mesh), for this part of the study, was constructed with a cell size of 5mm in all regions using the sweep and multizone meshing schemes. However, the inlet has a sloping and reducing section which was meshed using the tetrahedral cell type with a cell size of 5mm. For the final models the entire mesh was hexahedral. The mesh consisted of 123908 cells.

The model used was the VOF model as per Chapter 3. The particle model was not included in this preliminary study. The differences in this model as compared to the final model as presented in Chapter 3 was that only the RSM turbulence model was used.

The solver setup for the models were identical to that presented in Chapter 3, Section 3.5 except that the transient discretisation used in this preliminary study was first order as opposed to the bounded second order implicit scheme used in the final models. The fixed time step size in all cases was $\Delta t = 10^{-4}$ s. This time step size resulted in the models converging in 5 - 15 iterations per time step. Larger time step sizes results in a CFL number greater than 0.7 which leads to instability and divergence.

The CFL condition posed convergence difficulties in the final model. Thus, instead of applying a varying time step size in the final models the implicit volume fraction formulation option was used as opposed to the explicit option used in this preliminary study. The transient formulation was first order implicit. The boundary conditions were identical to the final model.

B.2 Results and Conclusions

The change in the velocity field and pressure distribution of the water phase is negligible in all three cases. For the cases with surface tension the increase and decrease in water mass flow at the overflow and underflow, respectively, is also negligible. Thus, surface tension has little impact on the water phase.

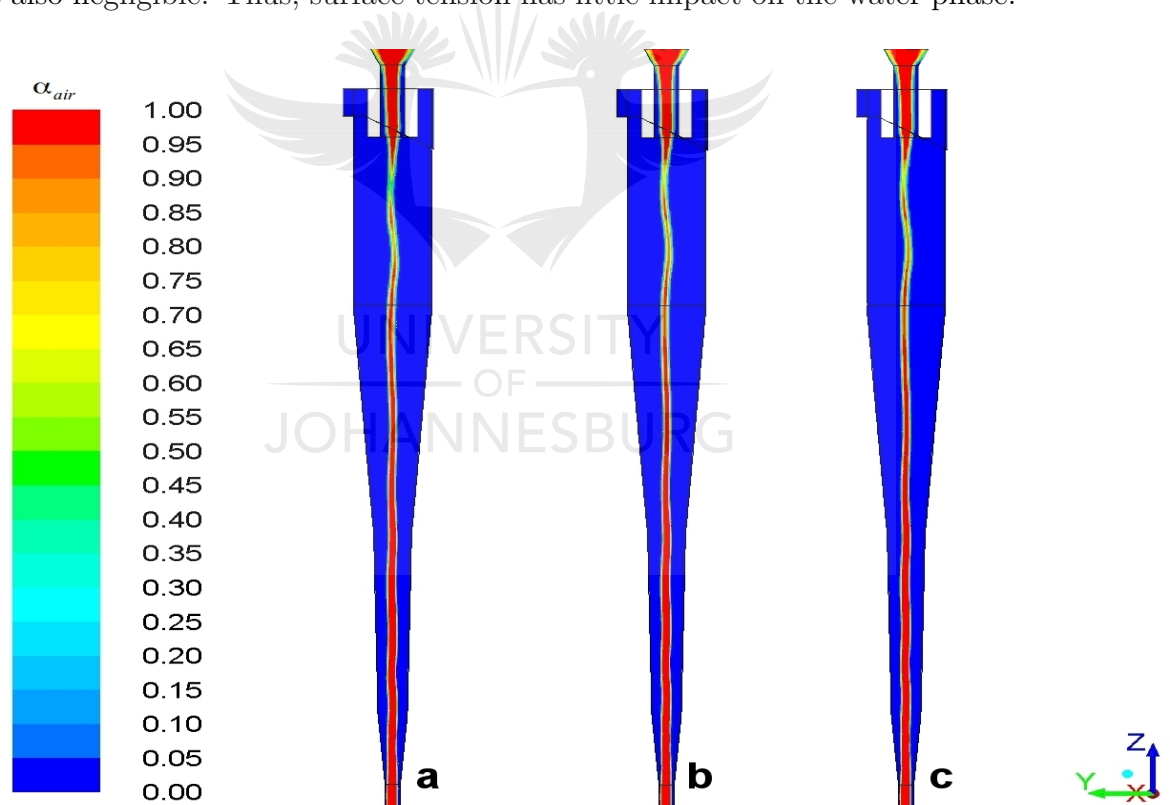


Figure B.1: Contours coloured by volume fraction of air (α_{air}), on the plane $x = 0$, for the case with a) no surface tension b) reduced surface tension and c) surface tension of pure water

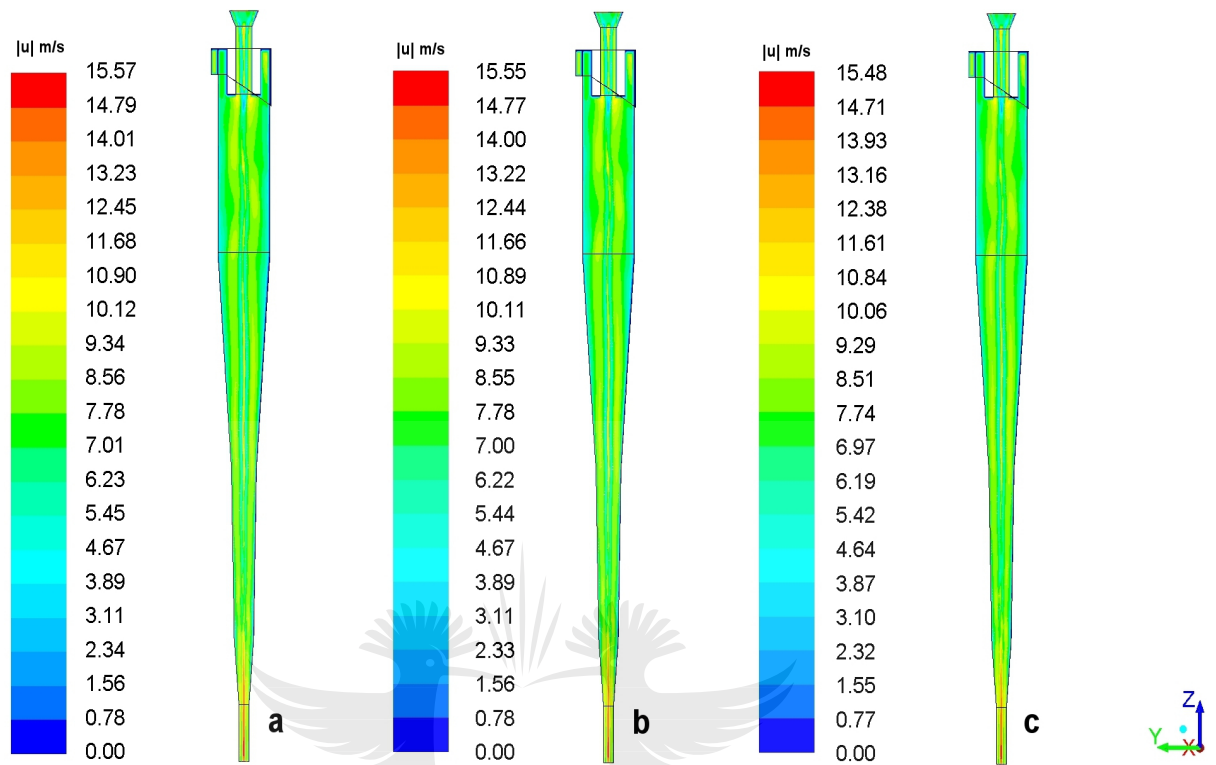


Figure B.2: Contours coloured by velocity magnitude ($|\mathbf{u}|$ (m/s)), on the plane $x = 0$, for the case with a) no surface tension b) reduced surface tension and c) surface tension of pure water

The air-core size and position is the same in all three cases as seen in Figure B.1. However, the maximum velocity of the air phase at the underflow is lower in the models with surface tension. The case with reduced surface tension has a higher maximum air velocity, at the underflow, than the case for pure water. The above can be seen in Figure B.2, by looking at the maximum velocity as per the colour-map. The maximum velocities occur at the underflow. The decrease in the maximum velocity in the air phase, with increasing surface tension, is expected because the increasing surface tension acts as a damping force for the air-core. As a result, the air-core formation is slower in the case with surface tension of pure water. However, the velocity difference is not significant as the maximum difference is less than 1%.

The approach of simulating the water phase without the presence of air and then adding the air phase when the single phase solution reached steady

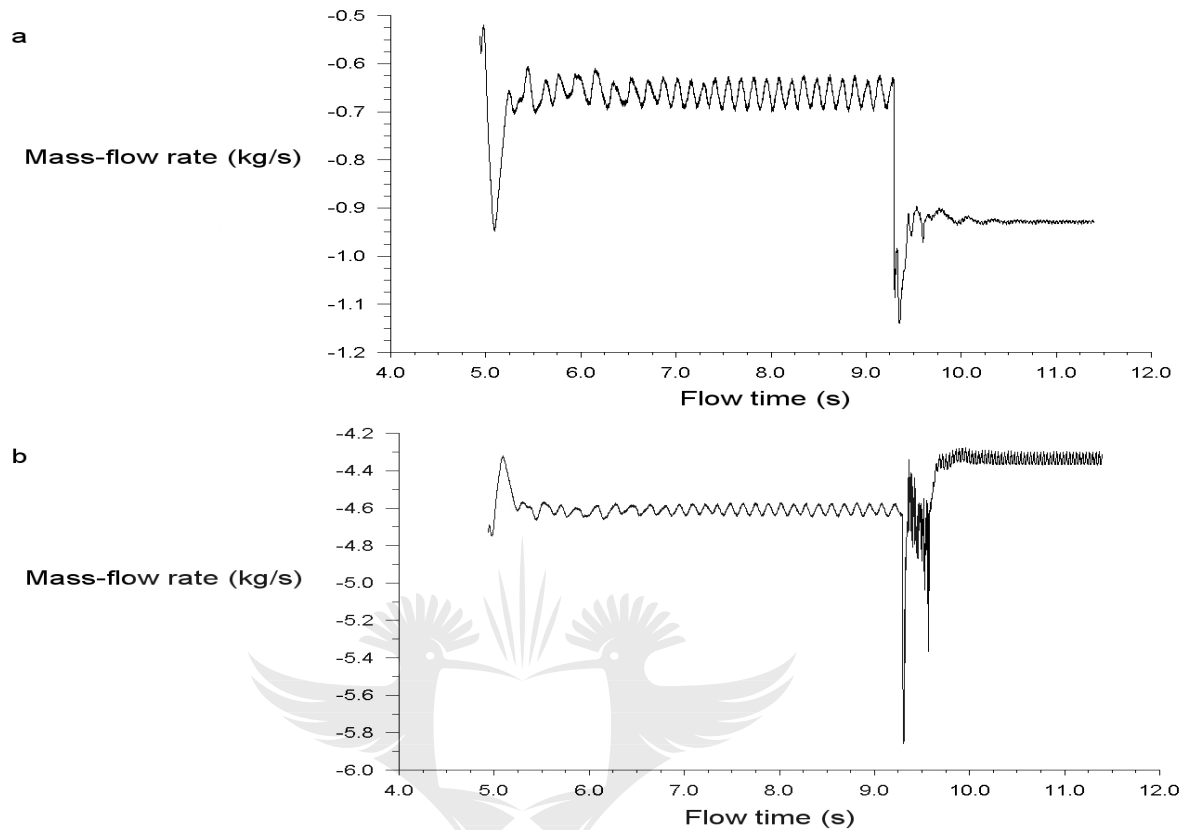


Figure B.3: mass flow rate at the a) underflow and b) overflow

state was used. This shows the effect of the air phase on the water phase at the underflow and overflow. When the system reaches steady state the mass flow rate at the underflow and overflow still exhibits oscillatory behaviour with a fixed period and amplitude as seen in Figure B.3. This quasi-steady behaviour is present with or without the air-core.

The air-core does have a significant impact on the mass flow on the underflow and overflow. The air-core formation reduces the period and amplitude of the mass flow rate at both outlets. This can be seen in Figure B.3. Furthermore, the introduction of the air-core results in a noticeable drop in the average mass flow-rate at the overflow and an increased flow rate at the underflow, as seen in Figure B.3. It should be noted that ANSYS Fluent [13,14,34] defines a negative mass flow rate as leaving through the boundary and positive mass flow rate as reverse flow, thus, Figure B.3 shows the mass flow rate of fluid

leaving the domain.

Surface tension appears to have a small but noticeable effect on the mass flow at the underflow and overflow. The air mass flow for the case of pure water, relative to the case with no surface tension, increases by approximately 1% at the overflow and decreases by approximately 3% at the underflow. In the case with reduced surface tension, relative to the case with no surface tension, the air mass flow increases by approximately 1% at the overflow and decreases by approximately 3% at the underflow. However, in light of the comparison between the CFD and experiment in Chapter 6, it can be seen that the mass flow rate dependence on surface tension is within the fluctuations in the mass flow rate about the mean mass flow rate and within the experimental error. Thus, the effect of surface tension on the mass flow at the underflow and overflow, whilst noticeable, is not significant.



Appendix C

Mesh Sensitivity Study

C.1 NS based Air-Core Models

The three NS based models, namely the ASM, the VOF and the Eulerian models were implemented on varying meshes (cell sizes) to determine mesh independence. The cell sizes set at 5mm ($\approx 120\,000$ cells), 2.5mm ($\approx 760\,000$ cells) and 1.25mm ($\approx 7\,400\,000$ cells). Overflow and underflow mass flow rates were used as the metric. As seen in Figures C.1 - C.4 the VOF and ASM models achieved mesh independence on the 1.25mm cell size.

The Eulerian model did not achieve mesh independence due to complications with numerical stability and convergence as the cell size decreased, as seen in Figures C.5 and C.6. Thus, the finest mesh used with converged results, for the Eulerian model, was the 2.5mm cell size. The numerical stability and convergence requirements of the Eulerian model are discussed in detail in Section 6.1.2.

It should be noted that the RNG turbulence model (for both VOF and ASM) requires further mesh refinement as seen in Figures C.1 - C.4. However, the RNG model was a stepping stone to achieve stable results with the RSM, the RNG models were not refined further.

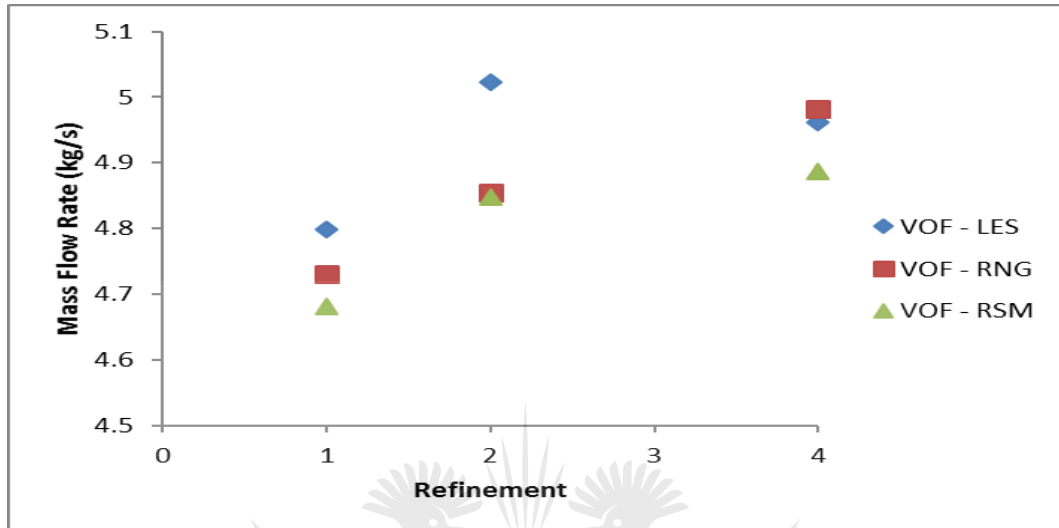


Figure C.1: VOF model mesh sensitivity - overflow mass flow rate

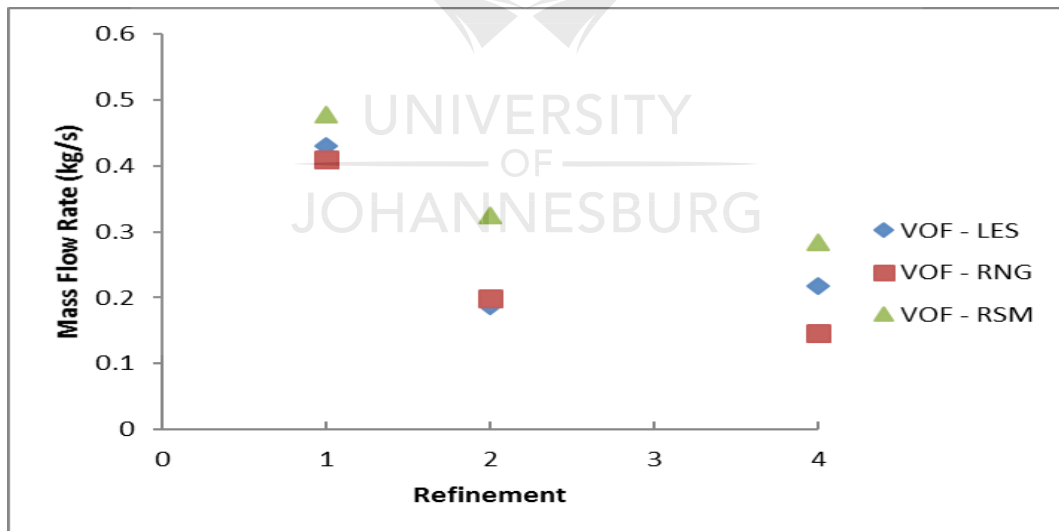


Figure C.2: VOF model mesh sensitivity - underflow mass flow rate

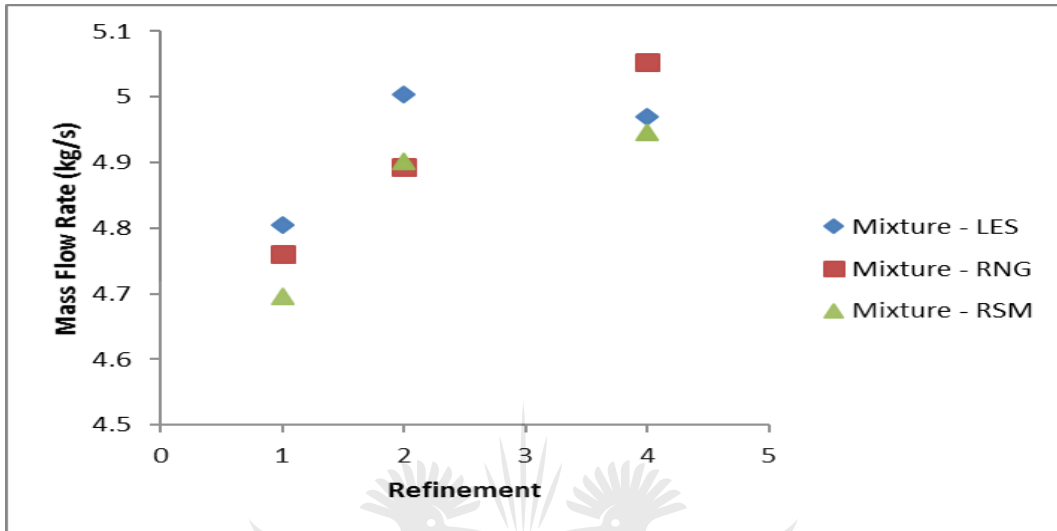


Figure C.3: Mixture model mesh sensitivity - overflow mass flow rate

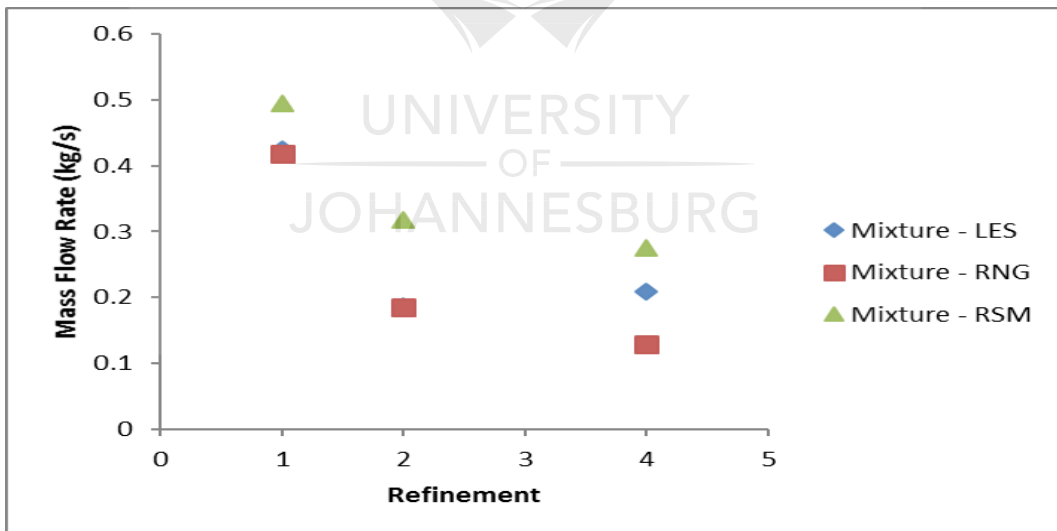


Figure C.4: Mixture model mesh sensitivity - underflow mass flow rate

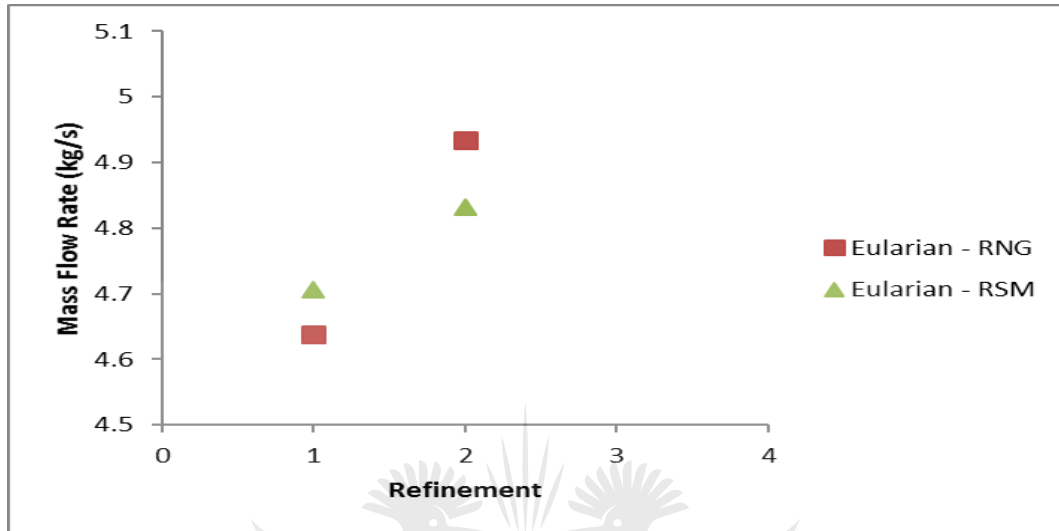


Figure C.5: Eulerian model mesh sensitivity - overflow mass flow rate

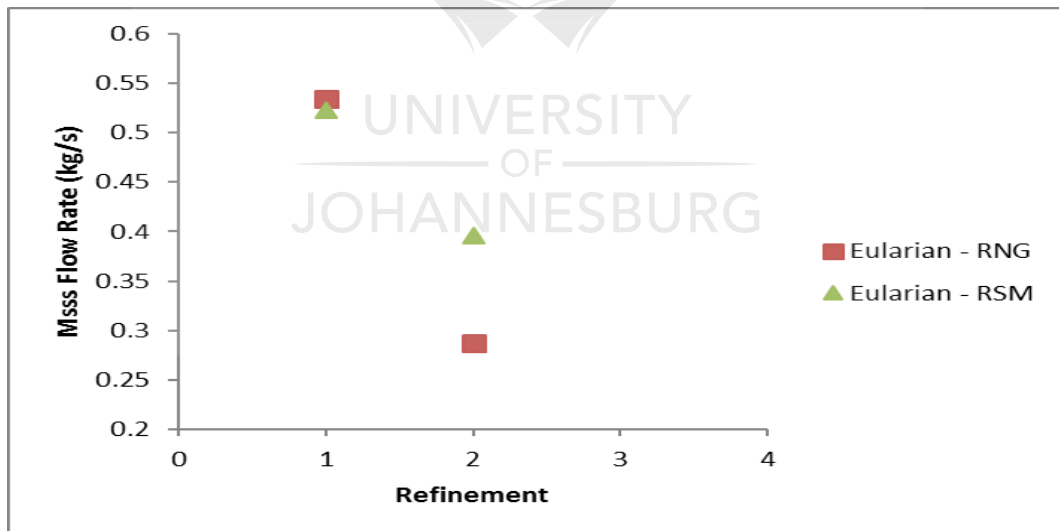


Figure C.6: Eulerian model mesh sensitivity - underflow mass flow rate

C.2 NS based Particle Models

The NS based VOF-DEM models were implemented on varying meshes (cell sizes) to determine mesh independence. The cell sizes set at 5mm ($\approx 120\ 000$ cells), 3.75mm ($\approx 215\ 000$ cells) and 2.5mm ($\approx 760\ 000$ cells). The models were initially tested on the 1.25mm mesh. However, the addition of the particles (and the DEM) increased the run times significantly. The time to complete 0.05s flow-time on the 1.25mm mesh was in the region of a day on 64 cores on the CHPC cluster. Thus, it was not possible within the time (and resource limits) of this study to run the full model with the DEM on the 1.25mm mesh. Thus, the intermediate cell size of 3.75mm was used to provide a third mesh size for the mesh sensitivity study. The total efficiency as well as the overflow and underflow mass flow rates were used as the metric. The total efficiency is defined as [37]:

$$E_T = \frac{m_{p,underflow}}{m_{p,feed}}(100) \quad (C.1)$$

The total efficiency is calculated based on the assumption of no accumulation of solids in the hydrocyclone [37]. Thus, the mass of particles at the feed was approximated as the sum of the mass of particles at overflow and the underflow. Therefore, the above equation was simplified to the following:

$$E_T = \frac{m_{p,underflow}}{(m_{p,underflow} + m_{p,overflow})}(100) \quad (C.2)$$

The Eulerian DDPM-DEM model, could not be run on the 3.75mm and 2.5mm meshes due to the numerical instabilities and convergence difficulties discussed in Chapter 6. The numerical stability and convergence requirements of the Eulerian model as discussed in Section 6.1.2 were determined after the particle models were completed. Thus, due to the time limitations of the study, it could not be applied to the Eulerian DDPM-DEM model on the finer meshes.

It should be noted that the RNG turbulence model was not used in this part of the study because it was only used to provide a stable initial solution for the RSM model when modelling the air-core. The stable RSM VOF (and Eulerian) solutions were used as the initial solution for the particle models.

As seen in Figures C.7 - C.9 the VOF-DEM models did not achieve mesh independence. The metrics were shown to fluctuate as the mesh was refined. Furthermore, the three data points do not provide a trend to approximate at which cell size mesh independence would be achieved. Thus, a further refinement needs to be made to determine mesh independence. However, due to the time (and resource) limitations of the study, this could not be done. However, the results in chapter 6 (specifically Section 6.2) illustrate that the 2.5mm mesh was sufficient to facilitate meaningful comparisons to experiment. Furthermore, the results in chapter 6 (specifically Section 6.2) illustrate that the 5mm mesh was sufficient to facilitate meaningful comparisons between the VOF-DEM, Eulerian DDPM-DEM and the LBM-VOF Particle models.

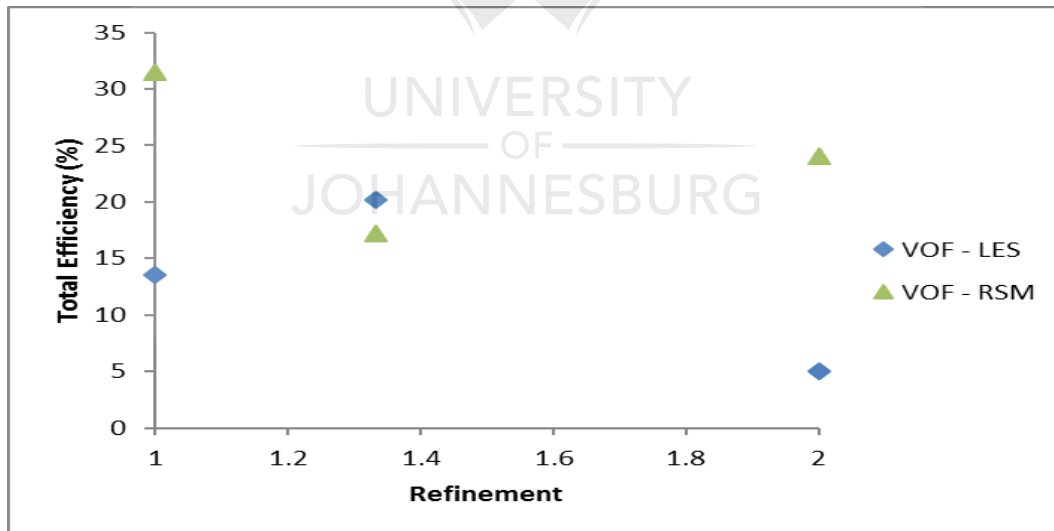


Figure C.7: VOF-DEM model mesh sensitivity - total efficiency

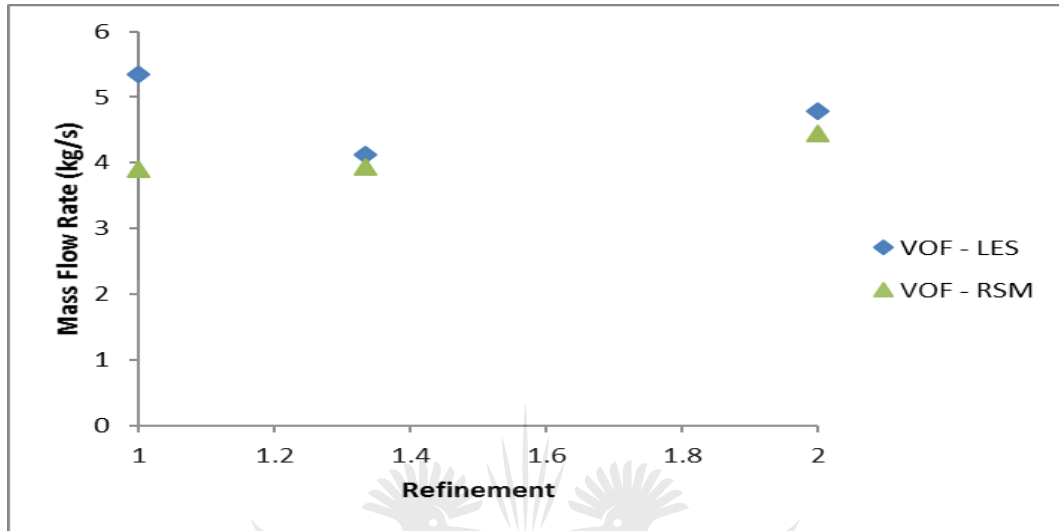


Figure C.8: VOF-DEM model mesh sensitivity - overflow mass flow rate

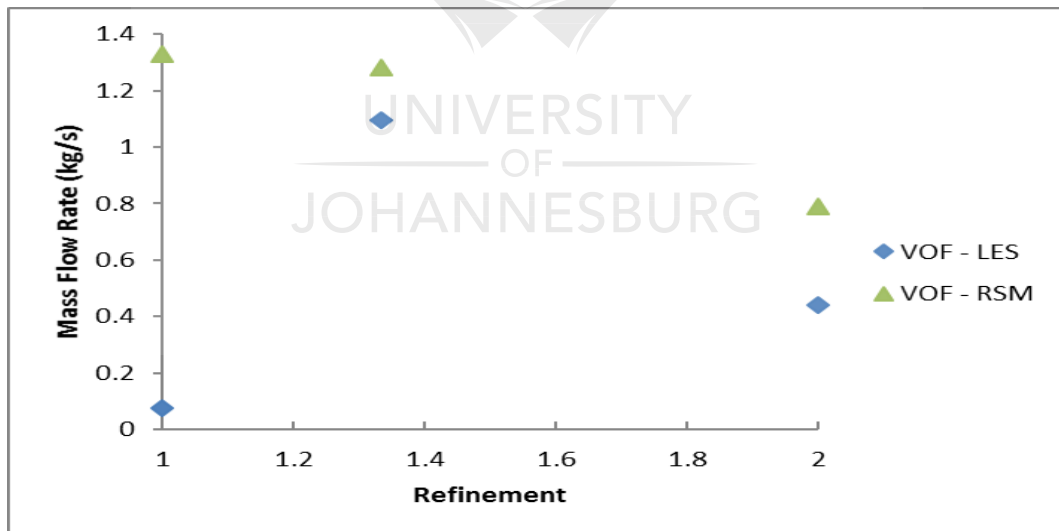


Figure C.9: VOF-DEM model mesh sensitivity - underflow mass flow rate

Appendix D

List of Does and Don'ts when Modelling Hydrocyclones

This appendix contains a list of does and don'ts with regards to modelling hydrocyclones using both the NS based and LBM based approaches. This list is based on the findings from the study. This list contains implementation tips that are necessary for successful modelling but are not mentioned in the literature. The list contains advice on meshing guidelines, physics specification and solver setup.

D.1 Meshing Guidelines

D.1.1 NS based Models

- The NS based models require a hexahedral mesh and not a tetrahedral mesh. Tetrahedral meshes provide unreliable and unstable results particularly with air-core modelling and more specifically when the water-air interface is present in a tetrahedral cell.
- Aspect ratio's must be kept below 10 (and ideally below 5) to ensure stability in the computation and to ensure accurate underflow predictions. If this is not adhered to, an excessively high velocity region forms in the core of the hydrocyclone causing numerical instability and poor underflow predictions.

- For initial runs on a poor quality mesh, use the VOF model as it is less susceptible to the numerical instability as mentioned above.
- For high quality meshes, use the Eulerian model.

D.1.2 LBM based Models

- The LBM is more mesh sensitive than the NS based approach. The only guideline for the LBM based model and meshing is that the LBM models requires larger meshes and smaller time step sizes than the NS based models.

D.2 Physics Specification

D.2.1 NS based Models

- For a coarse mesh use the RNG $k - \epsilon$ model.
- For finer meshes use the RSM or LES models.
- It is necessary to impress a radial equilibrium pressure distribution.
- For single phase models, use the LBM-LES model.
- Use the VOF model for air-core formation over the mixture model for coarse or fine meshes.
- The Eulerian model is the best model for air-core formation modelling.
- Do not inject particles at every fluid flow time step. Stagger the injections across multiple fluid-flow time steps. This allows the fluid to resolve the momentum transfer from the particles to the fluid, and vice-versa, before the next injection.
- Model approximately 2s flow-time to capture a steady state single phase and a steady state air-core solution. However, the particle models only achieve steady state after a further 4s of flow-time modelling. Despite achieving a steady state solution in the particle model, the model should be run for at least 8 times the flow-time required to

achieve a steady state single phase and a steady state air-core solution to achieve separation predictions comparable to experiment.

- Consider using the Eulerian granular model over a VOF-DEM model to overcome unphysical behaviour when the particles volume fraction (particularly in the cone) exceeds the packing limit.
- For air-core modelling initialise the entire domain with a $\alpha_{air} = 1$. This will ensure that the air-core forms.

D.2.2 LBM based Models

- Do not use the LBM model proposed in this study to model air-core formation.

D.3 Solver Setup

D.3.1 NS based Models

- Use the QUICK discretisation scheme as opposed to second order upwind.
- The segregated solver does not always work, thus, use the coupled solver.
- The CFL number should be kept below 1 to ensure stability and convergence of 5 - 15 iteration per time step.
- If using the explicit VOF solver keep the CFL number below 0.7.
- The explicit VOF solver convergence issues can be overcome by using the implicit solver instead

D.3.2 LBM based Models

- Specify the spatial and temporal resolutions to ensure that $0.5 < \tau < 1$.